

BRNO UNIVERSITY OF TECHNOLOGY

Faculty of Electrical Engineering
and Communication

DOCTORAL THESIS

Brno, 2017

Ing. Michal Mrnka



BRNO UNIVERSITY OF TECHNOLOGY

VYSOKÉ UČENÍ TECHNICKÉ V BRNĚ

FACULTY OF ELECTRICAL ENGINEERING AND COMMUNICATION

FAKULTA ELEKTROTECHNIKY
A KOMUNIKAČNÍCH TECHNOLOGIÍ

DEPARTMENT OF RADIO ELECTRONICS

ÚSTAV RADIOELEKTRONIKY

PERFORATED DIELECTRICS AND HIGHER-ORDER MODE DIELECTRIC RESONATOR ANTENNAS

PERFOROVANÁ DIELEKTRIKA A DIELEKTRICKÉ REZONÁTOROVÉ ANTÉNY S VYŠŠÍMI MÓDY

DOCTORAL THESIS

DIZERTAČNÍ PRÁCE

AUTHOR

AUTOR PRÁCE

Ing. Michal Mrnka

SUPERVISOR

ŠKOLITEL

prof. Dr. Ing. Zbyněk Raida

BRNO 2017

ABSTRACT

The thesis deals with the excitation of higher-order modes in the rectangular and cylindrical dielectric resonator antennas for gain enhancement purpose. The properties and limitations of the antenna elements are studied numerically. Mutual coupling between the higher-order mode dielectric resonators is examined and the results prove the elements to be suitable for antenna array applications. For perforated dielectrics, an analytical model of effective permittivity that respects its anisotropic properties is proposed. The model is based on the Maxwell Garnett approximation of inhomogeneous media. Surface waves on perforated substrates are then studied and the validity of the analytical model is verified also in this case. The dielectric resonator antennas embedded in perforated substrates are studied and certain degradations in antenna properties are pointed out.

KEYWORDS

dielectric resonator antenna, directive antenna, mutual coupling, higher-order mode, perforated dielectrics

ABSTRAKT

Práce se zabývá buzením vyšších módů v kvádrových a válcových dielektrických rezonátorových anténách pro účely zvýšení zisku. Pomocí numerických simulací jsou studovány vlastnosti a limity anténních prvků. Je zkoumána vzájemná vazba mezi dielektrickými rezonátorovými anténami pracujícími s vyššími vidy a na základě výsledků je možno usuzovat o vhodnosti těchto prvků k popužití v anténních řadách. V práci je popsán analytický model efektivní permitivity perforovaných dielektrik, který respektuje anizotropní povahu tohoto materiálu. Model je založen na Maxwell Garnettově aproximaci nehomogenních materiálů. Dále jsou studovány povrchové vlny na perforovaných substrátech a je ověřena použitelnost teoretického modelu i v tomto případě. Nakonec jsou studovány dielektrické rezonátorové antény vytvořené pomocí perforací v dielektrickém substrátu a je demonstrováno zhoršení určitých vlastností takových antén.

KLÍČOVÁ SLOVA

dielektrická rezonátorová anténa, směrová anténa, vzájemná vazba, vyšší mód, perforovaná dielektrika

MRNKA, Michal. *Perforated dielectrics and higher-order mode dielectric resonator antennas*. Brno, 2017, 171 p. Doctoral thesis. Brno University of Technology, Faculty of Electrical Engineering and Communication, Department of Radio Electronics. Advised by prof. Dr. Ing. Zbyněk Raida

DECLARATION

I declare that I have written the Doctoral Thesis titled “Perforated dielectrics and higher-order mode dielectric resonator antennas” independently, under the guidance of the advisor and using exclusively the technical references and other sources of information cited in the thesis and listed in the comprehensive bibliography at the end of the thesis.

As the author I furthermore declare that, with respect to the creation of this Doctoral Thesis, I have not infringed any copyright or violated anyone’s personal and/or ownership rights. In this context, I am fully aware of the consequences of breaking Regulation § 11 of the Copyright Act No. 121/2000 Coll. of the Czech Republic, as amended, and of any breach of rights related to intellectual property or introduced within amendments to relevant Acts such as the Intellectual Property Act or the Criminal Code, Act No. 40/2009 Coll., Section 2, Head VI, Part 4.

Brno

.....

author’s signature

ACKNOWLEDGEMENT

First of all, I would like to express my sincere appreciation to my supervisor prof. Zbyněk Raida for creating the professional and material framework without which this thesis would not have been written. I am obliged to prof. Raida for all the opportunities and invaluable advises that he has given me during my doctoral studies. For all the time and effort, that he has invested in me, I want to thank doc. Jaroslav Láčák, with whom I could discuss any matter related to my thesis, work, or in fact anything I was interested in and did not fully understand by myself. Also, I want to acknowledge the past and the present colleagues from the office SC6.46, namely J. Vélím, M. Cupal, M. Kotol, D. Krutílek, M. Kufa and V. Hebelka. Our discussions and our common after-lunch simulations in CS helped me to deal with and to overcome many complicated situations. For his help during my short term scientific mission in Košice I want to thank Ing. Jan Schneider. Next, I want to thank my boss from ERA company Dr. Antonín Heřmánek for providing me enough time that was necessary to finish this thesis. Although not directly connected to the thesis, I want to express my gratitude to Frank Schäfer and all the guys with the Microwave laboratory at the Max Planck Institute for Radio Astronomy for welcoming me in Bonn during my almost one year internship which gave me a lot for my future career. Last but not least I would like to express my gratitude to my family for all the support during not only my university studies, but in fact during my whole life. Nevertheless, the only person without whom there is no chance that this thesis would have ever come to existence is my girlfriend Dominika, who has, during the last four years, heard about antennas and electromagnetics much more that she had ever expected. Thank you.

Brno

.....

author's signature



Faculty of Electrical Engineering
and Communication
Brno University of Technology
Purkynova 118, CZ-61200 Brno
Czech Republic
<http://www.six.feec.vutbr.cz>

ACKNOWLEDGEMENT

Research described in this Doctoral Thesis has been implemented in the laboratories supported by the SIX project; reg. no. CZ.1.05/2.1.00/03.0072, operational program Výzkum a vývoj pro inovace.

Brno

.....

author's signature



EVROPSKÁ UNIE
EVROPSKÝ FOND PRO REGIONÁLNÍ ROZVOJ
INVESTICE DO VAŠÍ BUDOUCNOSTI



Contents

Introduction	9
1 State of the Art	11
1.1 Dielectric Resonator Antennas	11
1.2 Electromagnetic Modes in Dielectric Resonators	12
1.3 Gain Enhancement of a Single Element DRA	15
1.4 Mutual Coupling in DRA Arrays	17
1.5 Perforated Dielectrics	18
2 Objectives	21
3 Enhanced Gain Higher-Order Mode Dielectric Resonator Antennas	23
3.1 Rectangular Directive DRA	24
3.1.1 Dielectric Waveguide Model	25
3.1.2 Antenna Configurations	27
3.1.3 Infinite Ground Plane DRAs	28
3.1.4 Finite Ground Plane Effects	34
3.1.5 Square, TE_{133} Mode DRA Design	36
3.1.6 Numerical Results	37
3.1.7 Experimental Results	38
3.2 Cylindrical Directive DRA	42
3.2.1 High Gain Cylindrical DRA Concept	43
3.2.2 Parametric Study	46
3.2.3 Prototype and Measurement	47
3.3 Gain Improvement of HO Mode DRA by Thin Air Gap	50
3.3.1 Antenna Configuration	51
3.3.2 Numerical Study	51
3.3.3 Prototype and Measurements	52
3.4 Low Temperature Co-Fired Ceramics for Millimeter Wave Directive DRA Design	56

3.4.1	Millimeter-Wave Directive Cylindrical DRA Based on Low-Loss LTCC 9K7 Green Tape	57
3.4.2	Antenna Design	58
3.4.3	Prototype and Measurements	59
3.5	Summary	63
4	Mutual Coupling in Higher-Order Mode DRA Arrays	64
4.1	Mutual Coupling Between Dielectric Resonator Antennas Excited with Their Fundamental Modes	66
4.2	Mutual Coupling Between Rectangular Resonators Operating with TE_{113} and TE_{115} Mode	67
4.2.1	Design and Performance of a Single TE_{113} and TE_{115} Mode Elements	68
4.2.2	Coupling Between the Resonators in TE_{113} Mode	71
4.2.3	Coupling Between the Resonators in TE_{115} Mode	74
4.2.4	Designs for Experimental Verification	77
4.2.5	Experimental Verification	78
4.3	Mutual Coupling Between Rectangular Resonators Operating with TE_{133} Mode	80
4.3.1	Single Element Characteristics	82
4.3.2	Coupling Between the Resonators in TE_{133} Mode	83
4.3.3	Design for Experimental Verification	84
4.3.4	Experimental Verification	84
4.4	Summary	85
5	Perforated Dielectrics	87
5.1	Perforated Dielectrics	88
5.1.1	Basic Nomenclature	89
5.1.2	Porous Materials and the Theory of Homogenization	90
5.1.3	Anisotropic Materials	93
5.1.4	Classification of Perforated Substrates as Uniaxial Media	95
5.1.5	Determining Effective Relative Permittivity Tensor for Plane Waves	97
5.1.6	Results	110
5.2	Surface Wave Propagation in Perforated Substrates	110
5.2.1	Surface Waves on Dielectric Slabs	111
5.2.2	Determining Effective Relative Permittivity for TM/TE Waves from Unit Cell Analysis	115

5.2.3	Determining Effective Relative Permittivity for TM/ TE Waves from Scattering Parameters of Macroscopic Model	119
5.2.4	Summary	120
5.3	Perforated Dielectric Resonator Antennas	122
5.3.1	Single Element Perforated DRA	122
5.3.2	Mutual Coupling Between Perforated DRA Elements	129
5.3.3	Design for Manufacturing	131
5.3.4	Experimental Validation	133
5.3.5	Summary	136
	Conclusions	137
	References	140
	List of Figures	155
	List of Tables	166
	List of symbols, physical constants and abbreviations	167
	Curriculum Vitae	168
	List of Selected Publications	171

Introduction

The first dielectric resonator antenna (DRA), proposed by Long et. al. in 1980s, showed that if the dielectric resonator, well known from microwave circuits, is excited with an appropriate electromagnetic mode, the resonator can become an antenna with very high radiation efficiency and some other unique characteristics even if high dielectric constant material is used for its fabrication.

To list some of the advantages we can mention for example high radiation efficiency, compact size, ease of excitation and a relatively large impedance bandwidth when compared to other resonant antenna elements. Very important design parameter which influences all the properties of the DRA is the dielectric constant of the resonator. In the last decade new ceramic materials with very high ϵ_r (above 100) and with very low dielectric losses even deep in the millimeter wave regions became available. Very compact devices can be built from high dielectric constant materials; on the other hand their bandwidth is inversely proportional to the dielectric constant value. Hence the most compact designs often suffer from very narrowband operation bandwidth. Moreover, the fabrication process required for building the DRAs is in general more complex compared to other elements such as microstrip antennas. Increased costs are thus result of the more complex fabrication if small volume manufacturing is in question. Nevertheless, in the high volume production the costs can be significantly reduced.

One very promising application area for dielectric resonator antennas is their deployment at millimeter or even at sub-millimeter wave frequency bands. Their main advantages over the other more conventional elements are their very low conduction losses and the immunity from surface wave excitation. With today's dielectric materials, the overall losses of the antennas can therefore be kept at very reasonable levels. However, the usage of dielectric materials in antenna design in the millimeter wave and terahertz frequency regions is nothing new; dielectric lenses have been probably the most widely used terahertz antenna elements, but only a few resonating elements from dielectrics has been proposed to operate at such high frequencies so far.

In the last 30 years, many properties of the dielectric resonator antennas have

been studied and understood. New techniques for increasing the bandwidth, introducing multiple resonances, minimizing the dimensions etc. have been proposed. If the higher gain of the antenna was required, it was necessary to use a DRA array with element number based on the desired gain. Only recently the gain increase of the single radiating element became of interest.

Chapter 1 of this thesis describes the current state-of-the-art in the area of dielectric resonator antennas (DRA), DRA arrays and perforated DRAs. We discuss the basics of the DRAs, their basic shapes and feeding schemes, their resonant behavior and the electromagnetic modes that can be generated within the resonators. Two different approaches to increase the gain of the single element DRA are discussed. We follow by summarizing the research results in the area of DRA arrays and we focus primarily on the mutual coupling between two DRA elements. The third sub-area discussed in this thesis is an advanced manufacturing technique for DRA fabrication based on the perforated microwave substrates. The objectives of the dissertation thesis are presented in Chapter 2. Chapters 3, 4, and 5 present the core of this thesis and they deal with the higher-order (HO) modes for gain enhancement, mutual coupling between HO mode DRA elements and with the perforated dielectrics and perforated DRAs, respectively.

Chapter 1

State of the Art

Brief introduction into the field of dielectric resonator antennas (DRAs) is given in this chapter. The focus is drawn to the various electromagnetic modes that can be created inside the resonator and their corresponding radiation patterns. Next, two strategies to increase the gain of a single element DRA are discussed and their advantages and disadvantages are pointed out. Next, we give a summary of current state of the art in the DRA array analysis and design as well as in the perforated dielectrics and perforated DRA design.

1.1 Dielectric Resonator Antennas

Until 1980s the dielectric resonators with high quality factors Q had been used as circuit elements in microwave filters and oscillators designs only [1–3] but the utilization of the electromagnetic (EM) fields escaping the resonator was firstly proposed by Long. et. al. in 1982 [4]. Ever since then, the interest of researchers in this type of the new antenna element has grown rapidly and the number of publications dedicated to the DRA field still grows annually. Very good reference materials on the nowadays broad area of DRAs can be found in [5–8]. Application oriented review of the current state of the art can be found in recently published article [9].

The operation of the DRA is based on the excitation of the proper electromagnetic (EM) mode inside the dielectric resonator. If the relative permittivity of the resonator is reduced as compared to the resonators in the microwave circuits, it is easier for EM radiation to escape the resonator; thus the relative permittivity lies mostly between 5 and 30, if the resonator is to be used as an efficient radiator. Three main shapes of the resonators have been studied analytically and experimentally (i.e. cylindrical [4], rectangular [10] and hemispherical [11, 12]), but other shapes based on notches [13], combination of the shapes, stacking up the resonators

[14, 15] etc. have been proposed in order to improve the performance of the simple shaped DRAs. Moreover, introducing inhomogeneity [16], [17] and anisotropy [18–20] has also revealed certain improvement in the DRA performance mostly in the terms of the input impedance and the directivity. Combination of the anisotropic structure and the higher-order mode excitation inside a DRA has been presented recently in [21].

Although, the DRA can be excited by a plethora of excitation schemes [5] the most frequently used solution is the excitation by an aperture coupled microstrip line [22]. This solution provides symmetrically placed excitation, reasonable bandwidth and simple fabrication. In certain applications DRA feeding by an aperture in a Surface Integrated Waveguide (SIW) might be more advantageous [23]. Even half-mode SIW has been already used to excite the DRAs [24].

The simplest analytical method to analyze the DRA behavior is based on the magnetic wall model [1], [4], [5]. In the model, all the air-dielectric interfaces are considered perfect magnetic conductors (PMC) and the eigenmode problem is then solved for the dielectric cavity. Results of this approach are the resonant frequencies and field distributions of the individual modes. By knowing the electric field distribution of the particular mode, we can derive its approximate radiation pattern by calculating the magnetic currents flowing on the walls considering the component of the electric field tangential to the wall surface. Then the antenna radiation pattern is directly determined by the far field transformation of the magnetic currents. The similarity of the DRA analysis with the aperture antennas analysis [25] is obvious.

It must be emphasized that the magnetic wall model is only approximate and its applicability is determined by the difference of the dielectric constants of the resonator and its surrounding. In other words, this approach does not take radiation losses into account; hence it can give considerable errors if the resonator is used as an antenna element. Nevertheless, even in the antenna applications, the model can provide very good first approximation of the required results [4]. The advantage of the magnetic wall model is that the structure is analyzed only with respect to the field distributions, i.e. the coupling mechanism is not part of the analysis and the design of the resonator and the feeding scheme can be separated at the early stage of the design process.

1.2 Electromagnetic Modes in Dielectric Resonators

A dielectric resonator can resonate with infinite number of modes, but for a specific combination of material properties, dimensions and operating frequency only a finite

number of potentially existing modes is allowed to be excited.

A simple cylindrical DRA is in the majority of cases excited either with the transverse magnetic $TM_{01\delta}$ (also designated as TM_{011}) mode providing vertical electric dipole-like radiation pattern or with the hybrid electromagnetic $HEM_{11\delta}$ (also known as HEM_{111}) mode which provides radiation pattern similar to the horizontally placed magnetic dipole [5],[8]. Equivalent modes with analogous radiation patterns can be excited in the rectangular DRA as shown in [5] and [26].

Nevertheless, in the last decade, many higher-order modes have been identified and successfully excited. In particular, Avadanei et al. in [27] and [28] showed which modes can be excited in a cylindrically shaped DRA of high dielectric constant $\epsilon_r=82.7$ in case the resonator was fed by a centrally placed and off center placed slot in the ground plane. The resonant frequencies, radiation patterns and efficiencies of these modes were discussed and compared. Provided the modes are spaced closely in the frequency spectrum and show similar radiation patterns and if lower dielectric material is used for the antenna construction, the wideband operation can be achieved for increasing the antenna impedance bandwidth. In this case, the higher-order mode/modes is/are excited in addition to the low-order mode. For example a DRA described in [29] operated with two hybrid modes $TE_{\delta 11}$ (sometimes designated as TE_{111}) and $TE_{\delta 13}$ (TE_{113}) over an impedance bandwidth exceeding 40 %.

Multiband operation can be achieved if the modes are further away in the frequency spectrum; by adjusting the geometry of the resonator and/or the excitation scheme multiple modes can be excited at different frequencies of interest. If an omnidirectional radiation pattern is desired at two various frequencies, the lower frequency can be covered with TM_{011} mode of a cylindrical resonator and the higher frequency with the TM_{012} mode of the same resonator. Such a design was presented by Yong et al. in [30] and the antenna was able to cover the 3.5 GHz WiMAX and the 5.8 GHz WLAN bands with similar omnidirectional radiation patterns. Dual band DRA antennas based on the dual mode operation with broadside radiation patterns were analyzed by Fang in his doctoral thesis [31]. Fang focused mainly on the rectangular DRAs operating with the TE_{111} and TE_{113} modes and he proposed design formulas for calculation of the dual band DRA dimensions in case the operating frequency, dielectric constant and dimension ratios were given [32]. A cylindrical DRA with dual band operation and a broadside radiation pattern in both frequency bands was developed by Sun and Leung in [33]. They used a cylindrical resonator operating in the HEM_{111} and HEM_{113} modes to provide broadside radiation patterns at 1.8 GHz and 2.4 GHz.

Multiband operation can be also used with modes providing different radiation patterns and resonating at different frequencies (with different polarizations) like in

[34]. In this paper, a cylindrical DRA with circularly polarized broadside radiation pattern and a linearly polarized omnidirectional radiation pattern was designed. The broadside circularly polarized radiation pattern was generated by two orthogonal $\text{HEM}_{11\delta}$ modes at 1.575 GHz (GPS L1 carrier) and the omnidirectional linearly polarized radiation pattern was generated by $\text{TM}_{01\delta}$ mode at 2.45 GHz (WLAN).

Stand alone utilization of the higher-order modes in DRAs was proposed only recently with the main motivation being the increase of the DRA gain. On the contrary, the multiband/wideband structures utilized the higher-order modes in addition to the low-order modes. Nevertheless, the antennas working exclusively with the higher order mode suffer mostly from relatively narrow impedance bandwidth. However, no research focusing on the increase of the bandwidth of these antennas has been documented so far. Another unexplored research directions are the generation of the circular polarization in this radiators by techniques known from conventional DRA design and the utilization of the high gain DRA elements in the array antennas. Studies of mutual coupling between antenna elements operating with higher order modes are lacking; such studies are important since they must precede the effective DRA antenna array design [8], [35].

Dielectric resonator antennas are in general considered advantageous at millimeter wavelengths [24, 36–39] compared to metallic resonant radiators such as microstrip antennas due to the higher impedance bandwidth and higher radiation efficiency; according to the [40] the radiation efficiency of a DRA is about 15% higher than the efficiency of a microstrip antenna at 35 GHz. Besides introducing the multiband/wideband operation and increasing the gain, the higher-order modes can be utilized for millimeter-wave antenna design. Micromachining techniques can be used to fabricate small resonators operating at mm-wave bands with high accuracy as shown in the on-chip 60 GHz antenna design presented in [41]. Low Temperature Co-fired Ceramics technology was used for design presented in [42] to build a 4 by 4 antenna array operating in 60 GHz band. Both linear and circular polarization half-mode SIW fed 60 GHz DRAs were successfully designed in [24].

To support a higher-order mode the structure must be geometrically larger than a structure operating with the low order mode; such a larger structure might be easier to fabricate. Two antennas based on this idea were proposed by Pan, Leung and Luk in [43]. The antennas used TE_{115} and TE_{119} modes in a rectangular DRA with the operating frequency 24 GHz. Enhanced gain on-chip DRA for D-band (135 GHz) utilizing half-mode cavity feeding structure was presented in [44]; the peak measured realized gain was only about 7.5 dBi.

There have been published several designs showing successful utilization of DRA elements as single element radiators and also as reflectarrays in terahertz bands [45–47]. Interesting design, in which the DRA element was used as a director of

quasi Yagi-Uda 340 GHz on-chip antenna [48] resulted in 10 dBi gain and radiation efficiency of 80%. The antenna was designed in $0.13\mu\text{m}$ SiGe BiCMOS technology. After substitution of the metallic ground plane with more convenient full dielectric structures due to plasmonic losses, the DRAs seem to be usable even in the optical regime; the work [49] shows designs at 474 THz frequency. More information on scalability of DRAs to optical region and on optical nano-antennas can be found in [50] and [51].

1.3 Gain Enhancement of a Single Element DRA

A cylindrically shaped resonator, operating with the low-order hybrid electromagnetic mode HEM_{111} placed above a sufficiently large ground plane, is probably the most frequently used DRA configuration [4]. This mode generates a broadside radiation pattern with linear polarization and a gain of about 5 dBi.

Several approaches have been suggested to increase the gain of the DRAs. Arraying of single element DRAs [8] is probably the most versatile method in which the gain value can be directly controlled by the number of elements in the array. Nevertheless, increased size, complexity and costs of the resultant antenna are the main disadvantages.

Altering a single element DRA can be used in cases, where medium gains up to around 10 dBi are sufficient. In general, two tactics to increase the gain of the single element DRA exist. First, additional structures can be placed in the vicinity of the resonator operating in the low order mode thus forming a more geometrically complex structure. In the second approach, the gain boost is provided by the introduction of higher order modes into the simple shape dielectric resonator.

The gain enhancement of a single resonator DRA is a relatively new approach, the first research papers dealing with this topic were published during the year 2004.

The first approach, which utilizes the DRA operating in the low-order mode (mostly the HEM_{111} mode of the cylindrical resonator) and its radiation characteristics are changed by introducing additional structures/elements in its close vicinity. During experimentations with the stacked DRA structures [14, 15] certain possibility to alter the antenna gain was discovered. First systematic design of a directive DRA based on this technique was demonstrated in [52] where the DRA operating in the low-order mode was extended by additional resonators to form a structure resembling a Yagi-Uda antenna. The achieved gains were 7.8 dBi and 8.7 dBi corresponding to the two (i.e. one active element and one director) and three element structure (one active element and two directors), respectively. Nevertheless, the antennas were not fabricated and all the results corresponded to the simulations. Nasimuddin and Eselle used a shape modification of the DRA ground plane [53]; the

ground plane was altered into the shape of a surface mounted short horn increasing the gain of the DRA to 9.8 dBi at 5.95 GHz with 10 dB return loss bandwidth of 3.2%. Mushroom-like electromagnetic bandgap (EBG) structure with a circular symmetry was used in [54] to enhance the gain of a cylindrical DRA to about 8.3 dBi. Particularly, the rectangular hybrid DRA antenna based on a superstrate described in [55] provided peak gain of 14.44 dBi and gain above 11 dBi in the complete ISM band at 60 GHz. Circularly polarized aperture coupled DRA operating at 31 GHz with frequency selective surface based superstrate layer for gain enhancement was proposed with in [56] with maximum gain of 15.5 dBi.

It should be mentioned that a higher complexity and an increased size are the common disadvantages of the directive DRA antennas based on this approach.

An alternative to the above described approach is to excite a suitable higher order mode in the single element DRA. Some of the modes documented over the last years exhibit relatively high radiation efficiencies with the gain up to about 10 dBi. The obvious advantages are the more compact dimensions and considerably reduced complexity of the final antenna; on the other hand, narrower impedance bandwidth is the main shortcoming.

The second strategy utilizes the higher-order radiating modes in a single dielectric resonator. This approach has already been adopted in both rectangular and cylindrical DRAs. Petosa and Thirakoune in [57] and [58] showed that a DRA based on higher-order TE_{113} and TE_{115} modes in a rectangular resonator can achieve gains of 8.2 dBi and 10.2 dBi, respectively. The structure operating in TE_{115} mode [58] required a maximum resonator dimension of about $1.1\lambda_0$ when built from dielectric material with relative permittivity $\epsilon_r = 10$, where λ_0 is the free space wavelength. Guha et al. [59–61] managed to excite higher-order $HEM_{12\delta}$ mode in a cylindrical resonator by introducing an air-filled cavity in the ground plane below the resonator. This way, peak gain of about 10 dBi was achieved but only in a relatively narrow impedance bandwidth.

Despite the reduced impedance bandwidth, the DRAs based on the second approach seem to be suitable for array applications. However, no DRA array design based on these structures has been proposed in the open literature so far.

1.4 Mutual Coupling in DRA Arrays

In general, mutual coupling among array elements can be responsible for radiation pattern distortions as well as for gain reduction that cannot be predicted by an array factor and pattern multiplication principle. Such distortions can be present in case of both, receiving and transmitting mode of the antenna array [25]. Moreover, it can alter the input impedance of array elements (and also introduces mutual impedance) and thus cause impedance mismatch at the element terminals. The coupling level is influenced by the properties of single elements (directivity, sidelobes etc.), feeding network and last, but not least, by the separation distance between the neighboring elements. In the most designs of DRA arrays, the separation distance between two elements lies between $0.5\lambda_0$ and $1\lambda_0$. Since the coupling level is proportional to the separation distance, very simple solution to eliminate it is to increase the separation between the elements. Even though, we are able to minimize all the negative effects of mutual coupling with this solution, the inter-element separation has also influence on the generation of grating lobes and hence large separations are impractical if the large sidelobe levels are to be avoided. The selection of the separation distance is therefore a tradeoff between small mutual coupling and good side lobe level performance.

Mutual coupling between two DRAs was studied for the first time in [62]. The authors theoretically derived the mutual impedances and calculated mutual coupling for two hemispherical dielectric resonators operating in broadside TE_{111} mode and fed by a probe. Since hemispherical DRA is the only shape for which analytical field solution exists, mutual coupling between rectangular and cylindrical DRAs has been studied only numerically and experimentally in numerous papers, where authors used either short current probe [63–66] or more frequently an aperture [67–71] for feeding the dielectric resonators. In this way, it was possible to account for other coupling mechanisms, most importantly the direct coupling between feeds of the resonators. In all the works, the resonators were excited with fundamental broadside radiated modes, i.e. HEM_{111} for cylindrical resonators and TE_{111} in case of rectangular resonators. Several techniques have already been proposed to decrease the mutual coupling among the array elements, these methods mostly work with some sort of metasurfaces [72] or defected ground plane [73].

The results of the literature investigations can be roughly generalized as follows. The coupling in the H-plane of the resonators is stronger, if the element spacing is smaller than approximately $0.5\lambda_0$. With increasing the spacing, the E-plane coupling becomes stronger as it decays with spacing more steadily. At spacing $0.5\lambda_0$ the transmission coefficient between two cylindrical aperture-fed dielectric resonators ($\epsilon_r \approx 10$) is approximately about -12 dB in the E-plane and about -15 dB in the

H-plane [67, 68, 70]. At $1\lambda_0$ spacing we can expect, for the same resonators, the transmission coefficient of about -20 dB in the E-plane and about -30 dB in the H-plane [67, 68]. In case of probe-fed resonators [64] with separation distance $0.5\lambda_0$ the transmission between resonators in their E-plane is -11.4 dB and in the H-plane -15.5 dB according to [64]. At spacing $1\lambda_0$ the transmission coefficient decreases to -17.8 dB for E-plane and -28.0 dB for the H-plane.

Since the introduction of the DRAs as array elements, plethora of papers devoted to research and development of DRA arrays has been published, concerning various shapes of the resonators and various feeding schemes, such as apertures, direct microstrip lines, waveguides, substrate integrated waveguides and dielectric image guides ranging from radio up to terahertz frequencies operating with linear and circular polarization. For several interesting examples see e.g. [5, 7, 38, 42, 45, 74–77].

1.5 Perforated Dielectrics

One of the main reasons why DRAs are not more widely used in the design of (sub-)mm wave antennas and arrays is the complexity of fabrication and mechanical adjustment of individual elements on the correct positions. This problem is even more pronounced if large arrays consisting of hundreds or even thousands of elements are to be assembled. One of the potential solutions is to utilize perforations in classical microwave substrates. The DRA element is created in the volume without the perforation (island of unperforated dielectrics), whereas the part of the substrate with perforations (air filled holes of certain radius and period) acts as a low permittivity material surrounding the resonator, which in best case is air.

The perforations in substrates as means of relative permittivity reduction were successfully used in microstrip antenna design [78] to suppress the surface wave propagation on thick dielectric substrates with large relative permittivities. The main negative effects of surface waves are gain reduction and ripples in radiation pattern due to diffraction of the energy at the substrate edges.

The perforations can also serve as Electromagnetic Band Gap (EBG) structures if the period and diameter of perforations is comparable to the wavelength at given frequency. Such application was proposed in e.g. [79] and [80]. Again, the purpose was to suppress the surface wave propagation in high permittivity dielectric substrates. Nevertheless, the surface waves are in this case suppressed also by the reduced effective relative permittivity. Moreover, for antenna array applications, this technique is not suitable due to considerable size of the perforations.

The same concept of using perforations to control the effective permittivity was deployed by Patrovsky and Wu in [81] and [82] for design of so-called Substrate

Integrated Image Guide (SIIG). The SIIG is a variation on standard dielectric image guide [83–85] with improved fabrication precision, design flexibility and with lower assembly costs.

In [86], the authors proposed linearly tapered slot antennas for 30 GHz and 94 GHz bands on synthesized low permittivity substrate. To lower the permittivity, air perforations were used. Another interesting design was introduced by Patrovsky and Wu in [87]. In the paper, a planar dielectric rod antenna formed on the same layer with SIIG feeding [82] was proposed for 94 GHz band. Another SIIG fed antenna array for 94 GHz band directly integrated on semiconductor wafer was presented in [88]. Recently, Mondal and Wu published a paper [89] describing a leaky wave antenna based on dielectric layer with periodic perforations and fed by SIIG covering 96 – 108 GHz frequency band. Review article [90] summarizes the substrate integrated image lines and their variations as well as devices based on them.

The perforated single element DR antenna was firstly described by Petosa, Ittipiboon and Thirakoune in [91]. The authors then extended the concept for larger two-dimensional array antennas in [92] and [5]. Comparison between performance of perforated DRA array and patch antenna array of the same size at frequency 24.5 GHz can be found in [93]. The DRA array provided about 1 dB higher gain and 22 % larger impedance bandwidth with the same number of array elements.

Utilization of air perforations in single element as well as in array DRA design became rather popular since its introduction. Zhang and Kishk in [94] deployed perforated dielectric rods to keep the DRA elements properly aligned at 10 GHz frequency. In their design, the perforated dielectric layer did not fill all the space among the elements, but only narrow single-hole thick rods were used. Furthermore, Kishk et al. in [95] used several rings of different size perforations to increase impedance bandwidth of single element circular, probe-fed DRA to almost 27 %. Hybrid dual frequency, two port antenna for 5.2 and 24 GHz bands with excellent isolation was proposed by Sun and Leung in [96]. The authors used slot for radiation in 5 GHz band and substrate integrated DRA element, using air perforations and metalized vias. Successful application of perforations was utilized in [97] for an array of recently proposed dense dielectric patch antennas [98] operating at 60 GHz.

In [99], a single substrate layer DRA based on perforations was fed by a substrate integrated waveguide (two-layer structure) at 35 GHz, however, the authors did not give any credit to any of the work described in this chapter, and the original contribution of their paper was questionable.

Another application in which perforated dielectrics are used is the area of reflectarrays and transmitarrays. In [100] wideband single dielectric layer transmitarray of perforations with varying period and size was described. The antenna was opti-

mized for X-band with peak gain approximately 27 dBi. In the paper, the authors designed a reflectarray based on the same principle. In case of the reflectarray, the gain was increased to 28 dBi; however, -1 dB gain bandwidth was reduced from 35.5 % to only about 7.5 %. Another reflectarray design based on perforated dielectric substrate was proposed in [101]. Again, the authors varied the density and diameters of air perforations, to control effective permittivity of the dielectric layer. Similar design, but with elaborate analysis and for Ka band was presented by Tahseen and Kishk in [102].

Vast area where air perforations are used to control the electromagnetic properties of the dielectric objects is radio optics and transformation optics. Designs of various dielectric lenses were described in e.g. [103–105]. In [103] and [104], the authors used a single layer perforated dielectric material with different distribution of perforations. Additionally, Kishk et al. in [105] deployed variable number of layers within the area of the lens. Examples of transformation optics devices based on controlling the effective relative permittivity with the air perforations can be found in e.g. [106, 107].

Chapter 2

Objectives

The previous, state-of-the-art section briefly summarized how can the HO modes improve the characteristics of the conventional dielectric resonator antennas in terms of the impedance bandwidth and the radiation pattern. The attention was mostly drawn to the gain enhancement of the single element DRAs, mutual coupling between DRA elements and to perforated DRAs. The main objectives of this dissertation thesis resulting from the performed review are formulated in this section. The objectives can be divided into three main research areas.

Objective 1

Proposing an original directive DRA element based on the excitation of the higher-order modes.

Radiation patterns of the potentially promising higher order modes will be examined and based on the field distributions, suitable mode (or combination of multiple modes) should be utilized to build a high gain DRA antenna element. From manufacturing point of view it is desirable that the element is simple shaped (cylinder, rectangular parallelepiped). Since the higher order modes mostly suffer from the narrowband operation, the techniques used for bandwidth enhancement of the conventional DRAs will be tested whether they can provide any bandwidth improvement of the high gain DRA element. If they can, the tradeoff between the impedance bandwidth and the radiation properties will be found. For this reason, various shapes, dielectric materials and feeding schemes will be tested.

Objective 2

Research of mutual coupling between the higher-order mode DRA elements.

The mutual coupling between two cylindrical (rectangular) high-gain DRA elements will be examined numerically and experimentally and the attention will be

focused on linearly polarized elements. The result will be a set of recommendations for minimum element spacing as well as the consideration of HO mode excitation as a mutual coupling reduction technique.

Objective 3

Research and description of the anisotropic behavior of the perforated dielectric substrates. The excitation of surface waves on such substrates and evaluation of possible DRA performance deterioration.

The perforated substrates are to be examined, first, as unbounded perforated dielectrics for which the components of the permittivity tensor will be derived. In this way, theoretical, polarization sensitive model of a homogenous equivalent model based on a quasi-static approximation will be given. Such a model can better suit specific applications with different propagation directions. Secondly, the analysis will be extended to surface waves on grounded dielectric substrates and the effective relative permittivity determination for TE and TM cases. At last, we evaluate the deterioration of DRA performance designed and fabricated using air perforations. The effects of perforated dielectric layer surrounding the resonator on radiation patterns as well as on mutual coupling between antenna elements will be evaluated.

Chapter 3

Enhanced Gain Higher-Order Mode Dielectric Resonator Antennas

It has been described in the previous chapter that a suitable, higher order mode excited inside a dielectric resonator antenna can increase its directivity whereas keeping its radiation efficiency high. As a result, gain of the antenna is enhanced. The authors have previously worked only with modes that were described by increased index number in one direction of the resonator achieving maximum gains of up to 10 dBi [58]. We turn our attention to higher modes with larger index numbers in two directions, which inevitably makes the geometry of the antenna electrically larger.

Hybrid electromagnetic mode HEM_{133} of cylindrical dielectric resonator and transverse electric mode TE_{133} of rectangular resonators with square footprint are investigated numerically as well as experimentally. These two modes provide very similar radiation patterns with three main lobes and relatively high directivity. The level of two of the sidelobes can be significantly reduced by suitably designing the size of the ground plane as well as by introducing a small air gap between the resonator and its ground plane, redirecting more energy towards the broadside lobe. Since the size of the air gap turns out to be an important design parameter of our HO mode antennas, we deal with it in a separate section (see 3.3).

We first analyze the properties of the antennas based on the TE_{133} mode with an infinite ground plane and after that we examine the effects of the finiteness of the ground plane. A comparison with the fundamental broadside mode of cylindrical resonator HEM_{111} is made, since it suffers from significant ground plane effects as well. The performance of both cylindrical and rectangular DRAs is verified by measurements. The antenna prototypes are built by stacking up layers of etched

microwave substrates.

The values of gain and impedance bandwidth of the rectangular elements are examined as functions of the width/length to height ratio. Results of the antenna optimization either on maximum gain or on maximum impedance bandwidth are provided. We do not perform the same analysis for the cylindrical antennas as there are sufficient reasons to believe, the element behaves similarly.

In case of electrically oversized resonators with circular and square footprints we partially excite also the nearby modes, which have in some situation positive effects on both gain and bandwidth. For miniaturization, we also examine the performance of the reduced size elements with suppressed excitation of modes other than the desired TE_{133} mode of rectangular resonator

Since the DRAs are very interesting millimeter (and sub-millimeter) wave elements, in section 3.4 we turn our attention to a more advanced fabrication technique for resonator's manufacturing. We use Low Temperature Co-fired Ceramics (LTCC) with very low losses to build a resonator for 26 GHz antenna. In simulations, we compare antennas based on two different LTCC materials, one cheap and suitable for rather lower frequency regions and one more expensive but dedicated for utilization up to 100 GHz. The antenna based on mm-wave LTCC material is assembled and measured with extremely good agreement between simulation and experimental results which is caused by higher accuracy in shape control in LTCC process.

3.1 Rectangular Directive DRA

As it has been shown by Petosa et al. [58], the higher order TE modes (TE_{113} and TE_{115}) of rectangular resonators can provide more directive radiation patterns compared to the fundamental broadside radiating mode TE_{111} . Nevertheless, even the directivity of the fundamental mode can be enhanced by a factor up to 2 dB by decreasing the size of the ground plane and constructively utilizing the ground plane edge diffraction.

Very interesting can be the excitation of modes with two modal indexes larger than 1. In this way, we end up with resonators with larger footprint compared to modes described in [58]. In this section, we focus on TE_{133} , which, as it turns out provide directive radiation pattern. We examine its behavior above infinite as well as above finite ground plane. Furthermore, we conduct parametric study and find optimal dimensions maximizing the broadside gain.

3.1.1 Dielectric Waveguide Model

The analytical model of rectangular DRAs suitable of derivation of field distributions as well as for obtaining approximate resonant frequency is based on the dielectric waveguide model (DWM) equations [10]. In the model, we assume a standing wave in one direction of a short section of a dielectric waveguide. The outcomes of this model can be easily verified by any EM field simulation software supporting eigenmode analysis. Referring to Fig. 3.1. we can write for the field components of the TE_{111}^y mode:

$$H_x = \frac{k_x k_y}{j\omega\mu_0} A \sin k_x x \sin k_y y \cos k_z z, \quad (3.1)$$

$$H_y = \frac{k_x^2 + k_z^2}{j\omega\mu_0} A \cos k_x x \cos k_y y \cos k_z z, \quad (3.2)$$

$$H_z = \frac{k_z k_y}{j\omega\mu_0} A \cos k_x x \sin k_y y \sin k_z z, \quad (3.3)$$

$$E_x = A k_z \cos k_x x \cos k_y y \sin k_z z, \quad (3.4)$$

$$E_z = -A k_x \sin k_x x \cos k_y y \cos k_z z, \quad (3.5)$$

$$E_y = 0. \quad (3.6)$$

Substituting the air-dielectric interfaces in x and z directions by a perfect magnetic wall boundary condition (PMC) enables us to write for the wavenumbers k_x and k_z :

$$k_x = m \frac{\pi}{d}, k_z = n \frac{\pi}{2h}, \quad (3.7)$$

where m, n are half-wave field variation along y and z direction, respectively. And the resonant frequency is found by solving the following transcendent equations for k_y

$$k_y \tan \frac{k_y d}{2} = \sqrt{(\epsilon_r - 1)k_0^2 - k_y^2}, \quad (3.8)$$

using the separation equation relating together the wavenumbers in all directions and the free space wavenumber

$$k_x^2 + k_y^2 + k_z^2 = \epsilon_r k_0^2. \quad (3.9)$$

By solving the transcendental equation 3.8 with the aid of 3.7 and 3.9 we can find the theoretical resonant frequencies of modes of interest. Due to the periodicity

of tan function, the equation 3.8 suggest infinite number of possible modes, hence the equation allows us to determine also the resonant frequencies of the HO modes.

The comparison between analytically and numerically (CST) computed resonant frequencies of modes TE_{111} and TE_{133} is given in table 3.1.

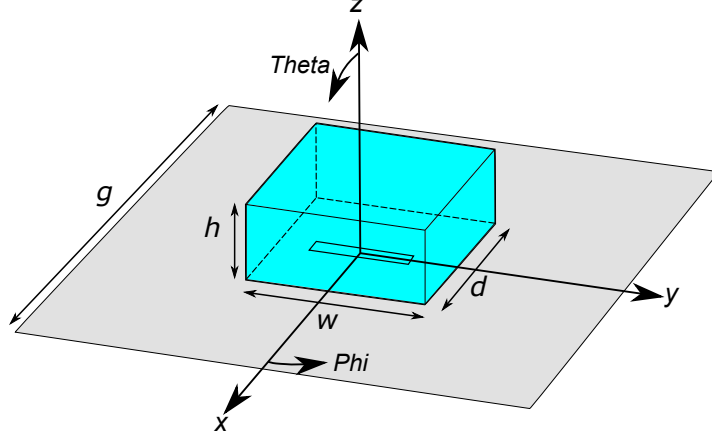


Fig. 3.1: General geometry of a DRA including a feeding aperture. Orientation of the aperture determines if TE_{mnp}^x or TE_{mnp}^y mode is excited. In this case the excitation of TE_{mnp}^y modes would be supported. For simplification, we first assume ground plane to be infinite $g \rightarrow \infty$.

Tab. 3.1: Comparison between the resonant frequency results of theoretical DWM and eigenmode analysis in CST. Relative permittivity of the resonator $\epsilon_r = 6.15$, $h = 10$ mm.

d (mm)	Analytical f_r		Numerical f_r	
	TE_{111}	TE_{133}	TE_{111}	TE_{133}
5	12.46	37.39	12.49	37.43
8	8.14	24.42	8.16	24.44
11	6.27	18.81	6.29	18.85
14	5.27	15.81	5.29	15.84
17	4.67	14.00	4.69	14.03
20	4.27	12.81	4.29	12.85

At this point we should explain the notation of the modal indexes. We follow the simplified notation according to [10], in which, for the rectangular resonators, the lowest order modes are designated as TE_{111}^x , TE_{111}^y and TE_{111}^z , depending on the alignment of equivalent magnetic monopole (i.e. axis x , y , or z). According to Fig. 3.1 and equations 3.7 we have full half-wave field variations (i.e. π rad) along directions x and z ; however, the phase variation in y direction is determined

from solving eq. 3.8 and is equal to π rad only if the permittivity of the resonator is infinite (for the lowest order mode). For real materials, only fraction of a half-wave is present along given direction (i.e. y direction for TE_{111}^y mode) and we can designate the lowest order modes as $\text{TE}_{\delta 11}^x$, $\text{TE}_{1\delta 1}^y$ and $\text{TE}_{11\delta}^z$, where δ is given for $\text{TE}_{1\delta 1}^y$ mode as:

$$\delta = \frac{k_y}{\pi/w}. \quad (3.10)$$

In this notation, the higher order modes in y direction are denoted as $\text{TE}_{1(\delta+p)1}$, where $p = 1, 2, 3, \dots$ and the same applies for the other directions.

Similar notation can be introduced also for cylindrical DRAs. Nevertheless, we stick to the simplified notation in that case as well.

3.1.2 Antenna Configurations

During the analysis, we use three different antenna models varying by their level of model simplification. All three models are based on the dielectric resonator placed on top of a conductive ground plane and fed by an aperture inside the plane. The ground plane is in addition backed by a dielectric substrate with thickness $h = 1.524$ mm and relative permittivity $\varepsilon_r = 3.38$.

The first model includes an infinite ground plane and is fed by a discrete port. In this way, we can deal with the radiation characteristics of the DRA elements without the additional finite ground plane effects (edge diffraction). Moreover, thanks to the discrete port excitation we can use two symmetry planes during simulations, thus reducing the computational domain to $\frac{1}{4}$ of the original model.

The second model differs from the first one only by the inclusion of the ground plane edges – we thus examine the finite ground plane effects for reduced set of geometrical configurations. The model is physically larger and requires more meshcells than the first model. Nevertheless, we can still simulate only one quarter of the full computational volume.

In the third case, the model is fed by a realistic feeding structure; we use standard microstrip line for this purpose. The line is deposited on top of the dielectric substrate corresponding with its properties to Arlon 25N with thickness 1.524 mm. Since in this case, the model is no longer symmetric according to yz plane, we can use only one symmetry plane, reducing the computational domain only by a $\frac{1}{2}$ factor.

We start with resonators with square footprint, since this geometry has only two degrees of freedom: height h and width w . Size reduction in y direction follows resulting in antenna with rectangular footprint. With rectangular geometry, we can further suppress additional modes that are excited inside the square resonators. As the other modes help to increase impedance bandwidth quite significantly, the change of geometry to rectangular is used only to examine the characteristics of the

isolated TE_{133} mode and to show, how the size of the antenna can be reduced if one sacrifices the impedance bandwidth.

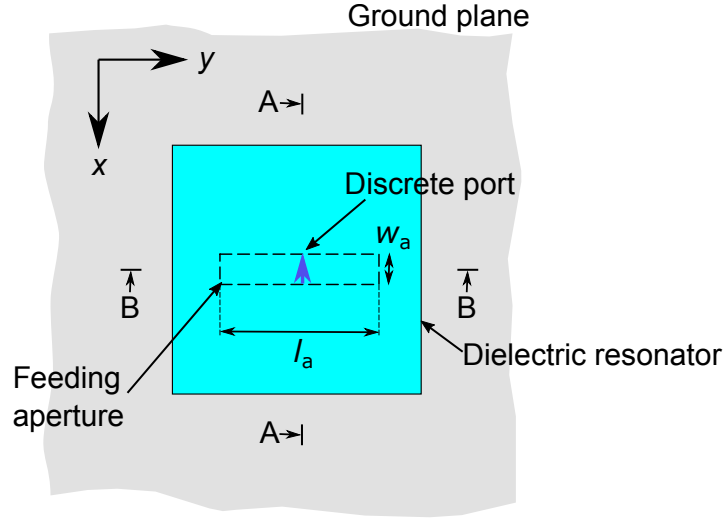


Fig. 3.2: Detail on the aperture feeding of the resonator. The input impedance of the discrete port in the simulations is set to 50Ω .

3.1.3 Infinite Ground Plane DRAs

Rectangular resonators have in general three degrees of freedom considering the design process, height h , width w and length d (see Fig. 3.1). In order to make the analysis systematic, we present characteristics in the following manner. We first select a certain height of the resonator h between 11 and 15 mm. Then, using DWM we determine the dimensions of a square footprint resonator ($w = d$) for resonant frequency $f_r \approx 10$ GHz. Afterwards, we fix the dimension w and we gradually change the length d from 5 mm up to $d = w$. For these dimensions, we examine input port reflection coefficient, maximum gain and radiation patterns in the E- and in the H-planes. According to the Fig. 3.1, E-plane corresponds to the $\phi = 0^\circ$ and H-plane to $\phi = 90^\circ$. The resonator is fed by a centrally placed aperture with dimensions $l_a = 9$ mm and $w_a = 1.5$ mm and the aperture is excited by a discrete port with input impedance 50Ω . The visualization of electromagnetic field components corresponding to the TE_{133} mode can be found in figures 3.3 to 3.5

For parametric study, we use simplified model of DRA above infinite ground plane with aperture, fed by a discrete port. The properties of the dielectric resonator are $\epsilon_r = 6.15$ and $\tan\delta = 0.003$ corresponding to Arlon 600 substrate from which the resonators are built in section 3.1.7. However, in this section we still consider the resonators to be built from single piece of dielectric material. The size of the ground plane (the distance of PML boundaries from the resonator) must be chosen large

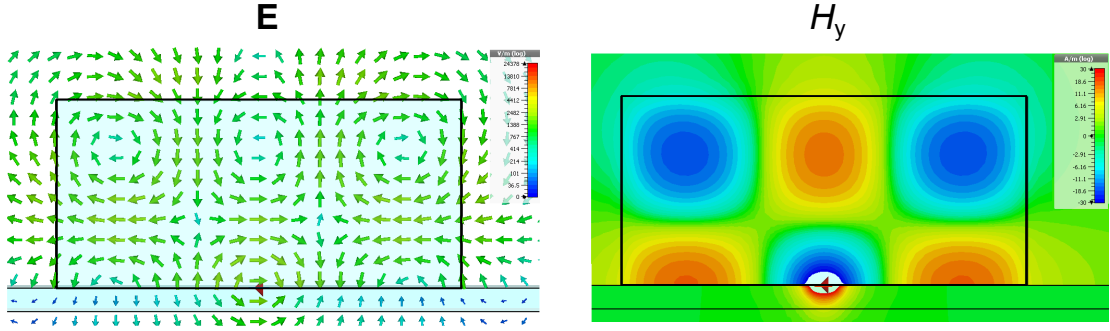


Fig. 3.3: Electric and magnetic fields in A-A cross section of the resonator (see Fig. 3.1).

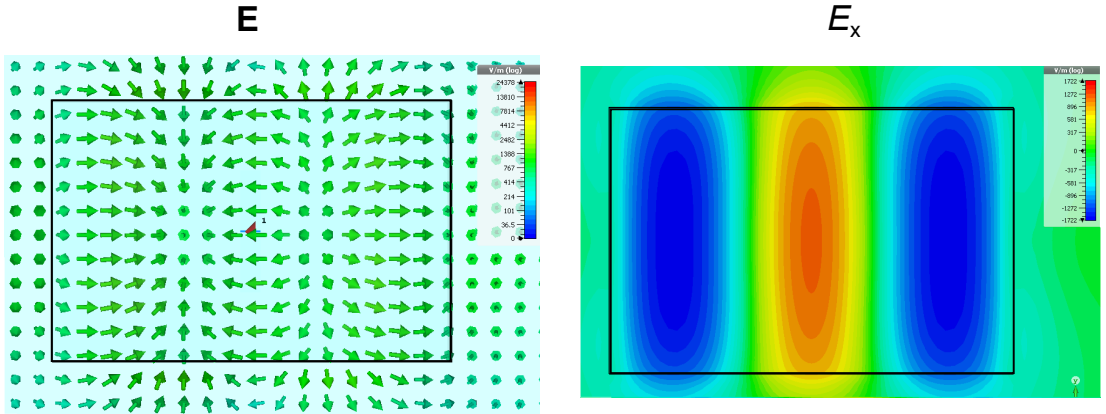


Fig. 3.4: Electric field distribution on the top wall of the resonator.

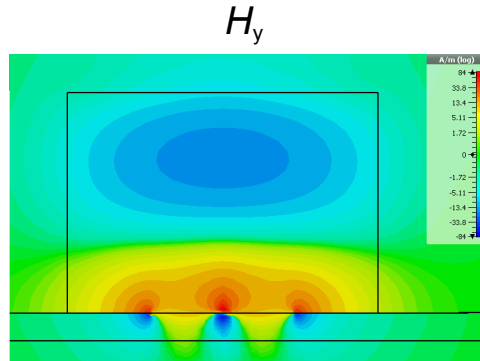


Fig. 3.5: Magnetic field distribution (H_y component) in the B-B cross section of the resonator.

enough not to influence the field distribution inside the resonator and the surface currents on the ground plane. In our simulations the size of the square ground plane is $g \approx 3\lambda_0$.

For h larger than circa 15 mm, TE_{115} and TE_{133} mode resonant frequencies are rather close and the radiation patterns of these modes cannot be separated. For this reason, we do not give any results for these dimensions. For larger h it is not possible to excite the desired TE_{133} mode efficiently. We can see the effects of partial excitation of TE_{115} mode in curves for $h = 15$ mm (see Fig. 3.10).

Since we do not change the size of the feeding aperture throughout the parametric study, we can expect that the level of impedance matching between the discrete port and the TE_{133} mode of the resonator is not always optimal. This can be seen e.g. in Fig. 3.10 where we could improve matching to the TE_{133} mode by adjusting size of the aperture. Nevertheless, we can at this point neglect the impedance matching loss as we are mainly interested in gain (not realized gain) and radiation patterns of the antennas. We decide for the fixed aperture size due to the slight influence of the aperture dimensions on the achievable gain.

In several reflection coefficient characteristics (see Fig. 3.6 to 3.10) we can find several resonances at various frequencies belonging to other HO modes. Most often, the TE_{115} mode is excited and sometimes matching to this mode is much better than to our TE_{133} mode (see Fig. 3.10 - right). If the resonant frequencies of these modes are close to each other, the impedance bandwidth as well as the gain bandwidth can be improved (see e.g Fig. 3.10 right). However, since we are examining the characteristics of TE_{133} mode at this point, we do not proceed in research of combined mode DRAs in this section.

Dielectric losses as well as metallic losses are present in the model, therefore we are interested in the IEEE gain (Fig. 3.11) according to IEEE standards [108]. In the radiation patterns plots (see Fig. 3.12 to 3.14) we plot normalized gains vs. $theta$ angle. We use convention where angle $theta$ ranges between -180° and 180° ; however, because the resonator is in this section placed on top of an infinite ground plane, we plot only characteristics for $-90^\circ \leq theta \leq 90^\circ$ (i.e. the upper half space). The lower half space is not interesting since it would only show parasitic radiation of the slot, which is of no interest at this point. We obtain the maximum gain from TE_{133} mode to be above 10 dBi (see Fig. 3.11 for comparison).

The E-plane radiation patterns show three main lobes at $theta = 0^\circ$, and $theta = \pm 90^\circ$. For certain dimensions, another two sidelobes around angles $theta = \pm 45^\circ$ arise. We can assume that the finite ground plane reduces the radiation towards $theta = \pm 90^\circ$; however, radiation in these directions disqualify this element from 2D array applications (1D H-plane array should be possible as we show in chapter 4), where we cannot rely on edge diffraction between adjacent elements. However, additional structures could suppress the radiation in these directions.

The presence of the other, at this point, unwanted HO modes (e.g. TE_{115}) can be seen most clearly from Fig. 3.13 and 3.14. As the height of the resonator h increases, the resonant frequencies of TE_{133} and TE_{115} get closer, thus the influence of multi-mode excitation can be seen most clearly in Fig. 3.14, resulting in gain reduction in directions $theta = \pm 90^\circ$ of the E-plane (desirable) and increase of sidelobes in the H-plane (undesirable).

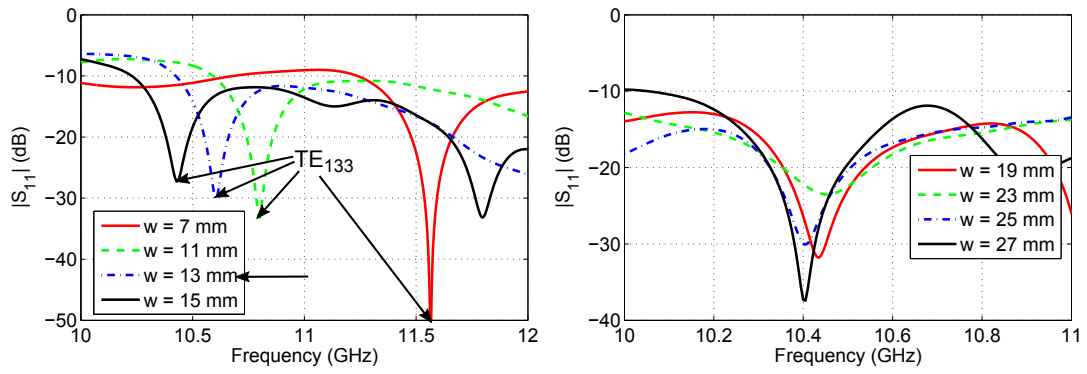


Fig. 3.6: Input port reflection coefficients showing resonances of the TE_{133} mode for resonators height $h = 11$ mm. As the footprint's shape of the resonator approaches square, the resonant frequency of TE_{133} mode varies more slowly (right). The resonance on the right for $w = 15$ mm is TE_{115} mode.

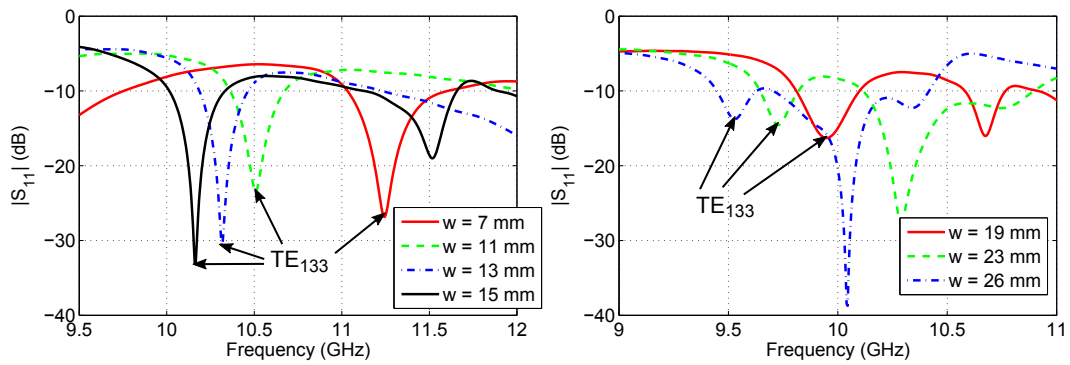


Fig. 3.7: Input port reflection coefficients showing resonances of TE_{133} mode and some additional higher modes for resonators height $h = 12$ mm. We can see that the additional resonances increase the impedance bandwidth of the antenna (right).

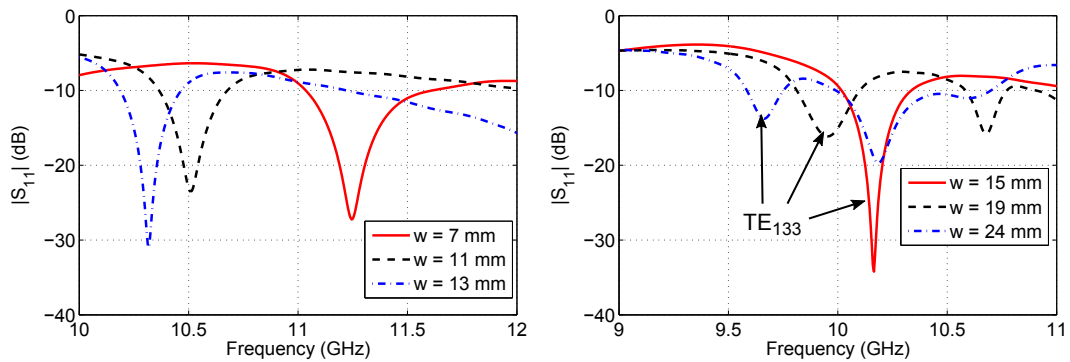


Fig. 3.8: Input port reflection coefficients showing resonances of TE_{133} mode $h = 13$ mm.

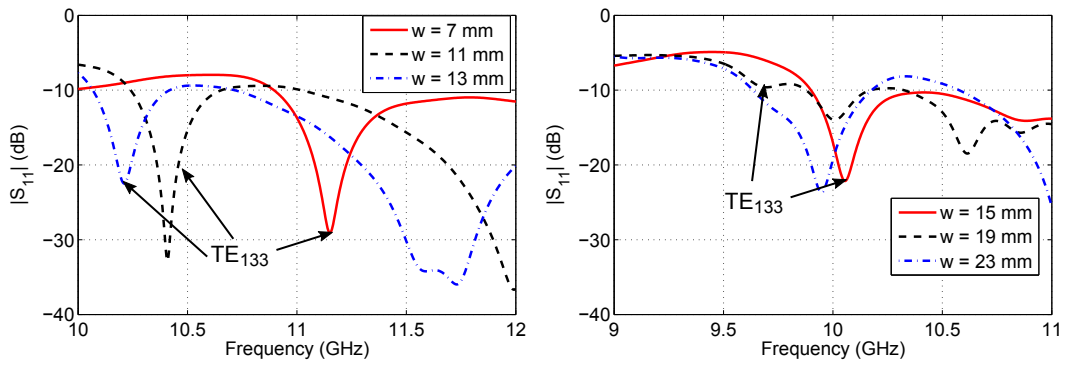


Fig. 3.9: Input port reflection coefficients showing resonances of TE_{133} mode for resonators height $h = 14$ mm.

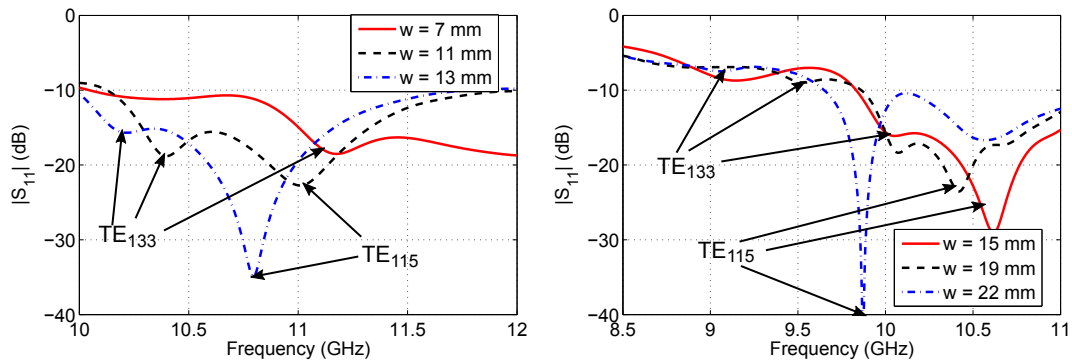


Fig. 3.10: Input port reflection coefficients showing resonances of TE_{133} mode $h = 15$ mm.

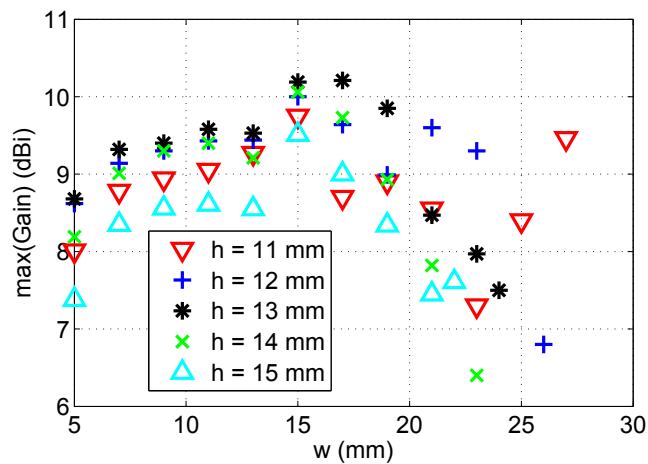


Fig. 3.11: Maximum gain corresponding to the TE_{133} mode as function of resonator's width w for various heights of the resonator (frequencies according to Fig. 3.6 to 3.10).

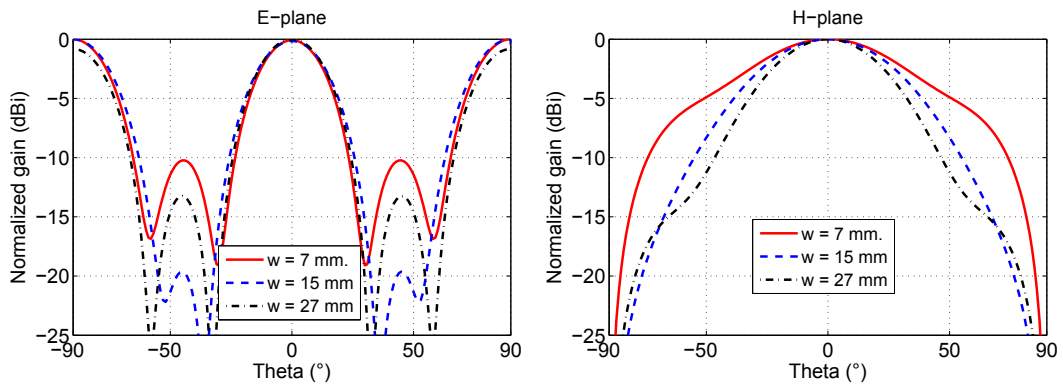


Fig. 3.12: Radiation patterns for resonator with height $h = 11$ mm and for various widths w . For frequencies see TE_{133} mode resonances in Fig. 3.6.

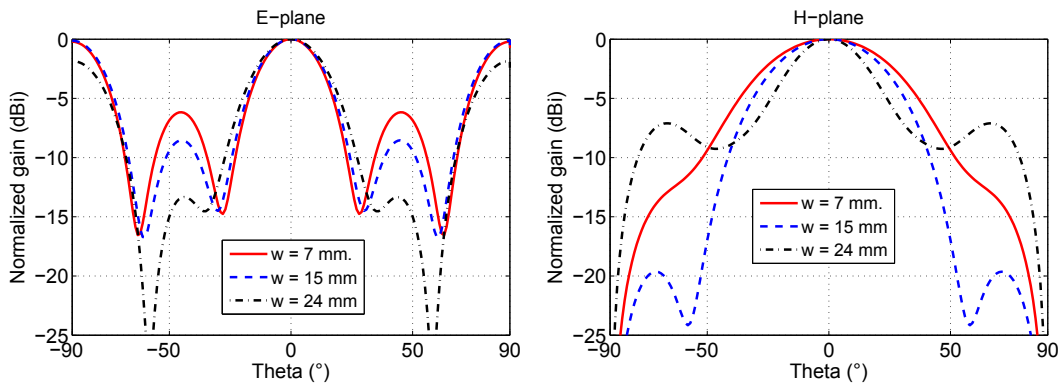


Fig. 3.13: Radiation patterns for resonator with height $h = 13$ mm and for various widths w . For frequencies see Fig. 3.8.

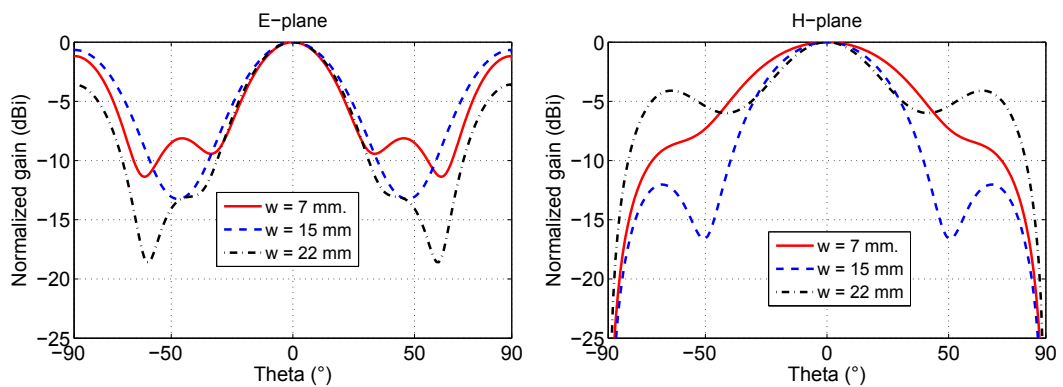


Fig. 3.14: Radiation patterns for resonator with height $h = 15$ mm and for various widths w . For frequencies see Fig. 3.10. In this case, the excitation of TE_{115} is the strongest, we can see it by reduced sidelobes in the E-plane at $\theta = \pm 90^\circ$ and increased sidelobes in the H-plane at circa $\pm 70^\circ$.

3.1.4 Finite Ground Plane Effects

It turns out that the size of the ground plane has a considerable effect on the radiation patterns as well as on the maximum achievable gain in the broadside direction (i.e. $\theta = 0^\circ$, see Fig. 3.1). This gain variation can be explained by the edge diffraction in the E-plane (i.e. xz plane in Fig. 3.1) due to two beams at the angles $\theta = \pm 90^\circ$, i.e. in the reflector plane (see e.g. Fig. 3.12). The gain maximum in the broadside direction is obtained when the direct and diffracted waves meet in phase in direction $\theta = 0^\circ$.

In the simulation model, we choose square shape of the ground plane with side length g . We gradually increase g and we observe how the gain in the broadside direction varies as a function of g . For visualization, we express g in free space wavelengths λ_0 . From Fig. 3.15 we can see, that the gain maxima (or minima) occur, whenever we increase g by approximately $2\lambda_0$ ($2\lambda_0$ is the period). The increase of g by $2\lambda_0$ corresponds to increase in distance between resonator's phase center and one of the edges by λ_0 .

The DR has in this case dimensions $h = 13$ mm, $d = 24$ mm, $w = 17$ mm (i.e. resonator with maximum gain). Next, we show radiation patterns for several ground plane sizes, showing increasing ripples, especially in the E-plane. The reason is clearly the two beams directing towards ground plane edges in the E-plane. In the H-plane, there is only a little radiation towards the edges. As the diffraction causes propagation of waves also in the directions corresponding to lower half-space (contrary to the section 3.1.3 for infinite plane) we are now interested in radiation patterns in full range of angle θ : $-180^\circ \leq \theta \leq 180^\circ$. However, due to the symmetry of radiation patterns we only show results for $0^\circ \leq \theta \leq 180^\circ$.

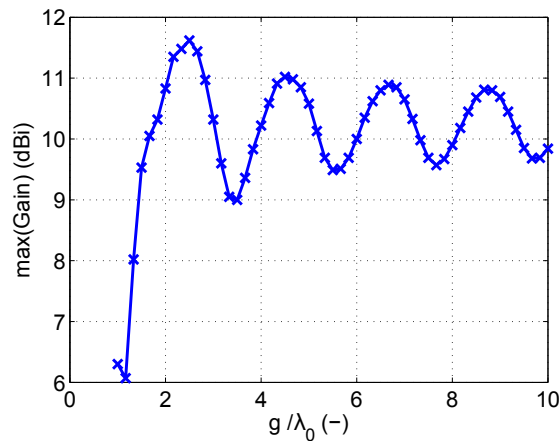


Fig. 3.15: Realized gain in direction $\theta = 0^\circ$ as a function of the ground plane size g at frequency 10 GHz. The period corresponds to approximately $2\lambda_0$.

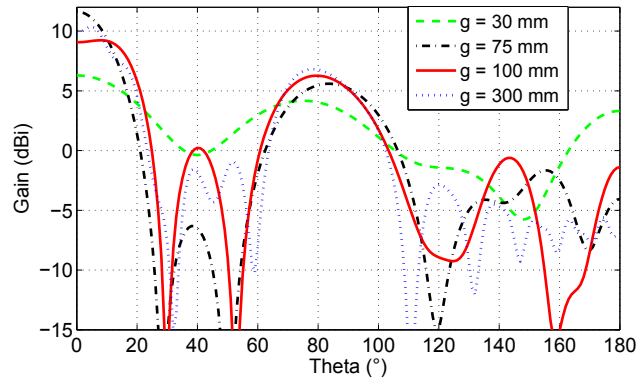


Fig. 3.16: E-plane radiation patterns at 10 GHz for four ground plane sizes $g = 30$, 75, 100 and 300 mm. With increasing g , the patterns are getting more rippled – i.e. interference between direct and diffracted waves.

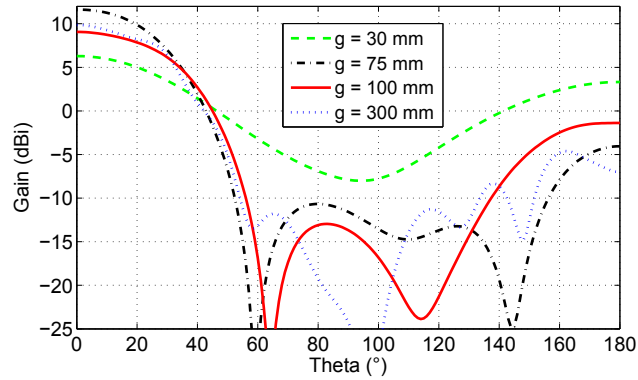


Fig. 3.17: H-plane radiation patterns at 10 GHz for four ground plane sizes $g = 30$, 75, 100 and 300 mm. We can see the H-plane patterns are less sensitive to the ground plane size.

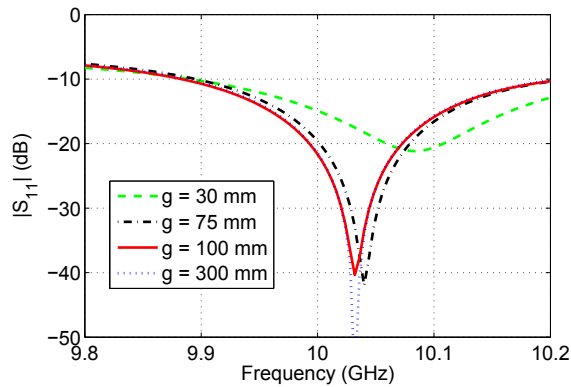


Fig. 3.18: Reflection coefficient for various ground plane sizes. We can see that only extremely small g can influence the reflection coefficient.

3.1.5 Square, TE_{133} Mode DRA Design

In the design, we work with a square footprint resonators and we excite dominantly TE_{133} mode of the resonator. However, as has been shown in previous sections, in square resonator, multiple modes can be excited and thus expand the impedance bandwidth of the antenna. After successful excitation of the TE_{133} mode, the impedance bandwidth and the radiation properties are compared for two resonators with different aspect ratios.

Since, the size of the ground plane has significant effect on the maximum achievable gain, we choose the size to maximize gain in the broadside direction. The antennas are optimized for application in the X-band with central frequency about 10.25 GHz. The antennas are fed by rectangular apertures, which determine the linear polarization.

Each of the antennas is configured as a rectangular dielectric resonator with a square footprint (i.e. width w and depth d are equal) above a conductive ground plane. Square shape of the ground plane is selected. The dielectric resonator is fed by an aperture coupling from a $50\ \Omega$ microstrip line. The relative permittivity of the resonator in the simulations is 6.15 and loss tangent $\tan\delta = 0.003$; these material parameters correspond to commercially available Arlon 600 microwave substrate and at this point we assume the resonator to be built from single piece of material. The substrate of the microstrip line is Arlon 25N with relative permittivity $\epsilon_r = 3.38$, loss tangent $\tan\delta = 0.003$ and height 1.524 mm. A microstrip parallel stub is used for impedance matching of the antenna. No air gap between the dielectric resonator and the ground plane is considered in simulations, even though the real material properties such as surface roughness might create very small air gap. This phenomenon is studied in detail in section 3.3. The geometry of the antenna with its alignment in spherical coordinate system is given in Fig. 3.19.

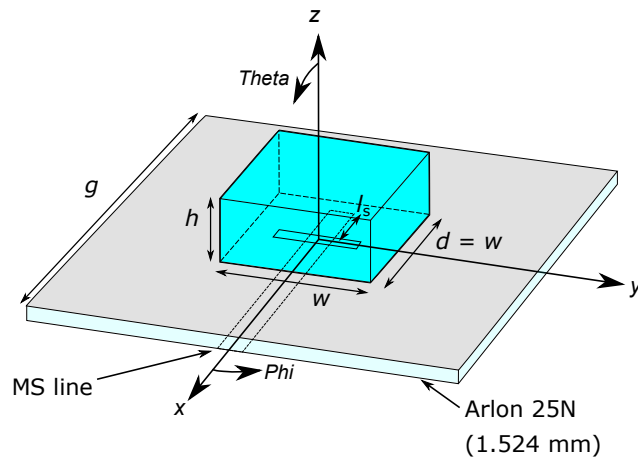


Fig. 3.19: Detail of the microstrip fed antenna.

3.1.6 Numerical Results

The suggested antenna is designed and its operation analyzed using full-wave EM simulation tool CST Microwave Studio. The initial set of resonator geometries is obtained by a so called magnetic wall method (i.e. numerical implementation of DWM). In our case, the method is done by performing modal analysis of the resonator in Eigenmode solver of CST MWS. In the simulations, all of the resonator's walls are set as perfect magnetic conductors (PMC), except the bottom wall which on the other hand is considered perfect electric conductor (PEC). This method does not take radiation losses into account and assumes vanishing tangential magnetic/electric fields on the resonator boundaries resulting in considerable errors, particularly if the resonator is based on a low permittivity material, just as in our case. Nevertheless, the resonant frequency error is in our case less than 5 %, providing sufficient accuracy for the design of initial geometry.

The resonator is brought into resonance with the desired mode at the center frequency 10.25 GHz for two aspect ratios (i.e. width to height ratio w/h), thus having a higher resonator with smaller footprint and a lower resonator with larger footprint. The aspect ratio influences the Q factor of the DRA and thus the antenna bandwidth. Nevertheless, in our case of square footprint resonator, two additional resonances at both sides of the desired frequency band occurs (most obvious are modes TE_{213} and TE_{115}), therefore increasing the impedance bandwidth significantly.

In our study, we are looking for the optimum aspect ratio to maximize the gain of the antenna. From this point of view, the optimum aspect ratio (resonator with this aspect ratio is designated as Resonator A) is found to be $w/h = 26.4 \text{ mm}/11.3 \text{ mm}$ and its frequency response of reflection coefficient is given in Fig. 3.20 and radiation patterns in E and H-plane are given in Fig. 3.21.

The second resonator is optimized for the best side lobe level performance. It is found out, that even though the higher resonator (designated as Resonator B) with aspect ratio $w/h = 22.7 \text{ mm}/13.4 \text{ mm}$ provides lower gain (about 0.5 dB), the side lobe levels are significantly decreased compared to the higher resonator (about 3.5 dB improvement).

The optimum ground plane size that maximizes the broadside gain is found by parametric analysis in which we sweep ground plane size g and observe gain in direction $\theta = 0^\circ$. The gain behaves as periodic function of g and thus the gain maxima are obtained for several ground plane sizes (approximately $g = 77 \text{ mm}$, 134 mm , 193 mm , 252 mm etc.) making the difference between two adjacent maxima (or minima) approximately 59 mm, which corresponds quite accurately to $2\lambda_0$ ($\lambda_0 = 58.5 \text{ mm}$).

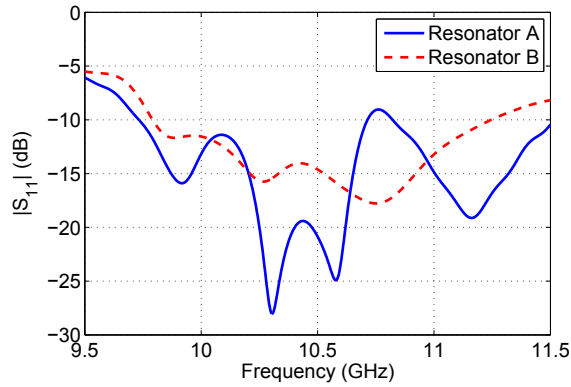


Fig. 3.20: Frequency response of the reflection coefficient of both resonators. The TE_{133} mode resonates at about 10.25 GHz.

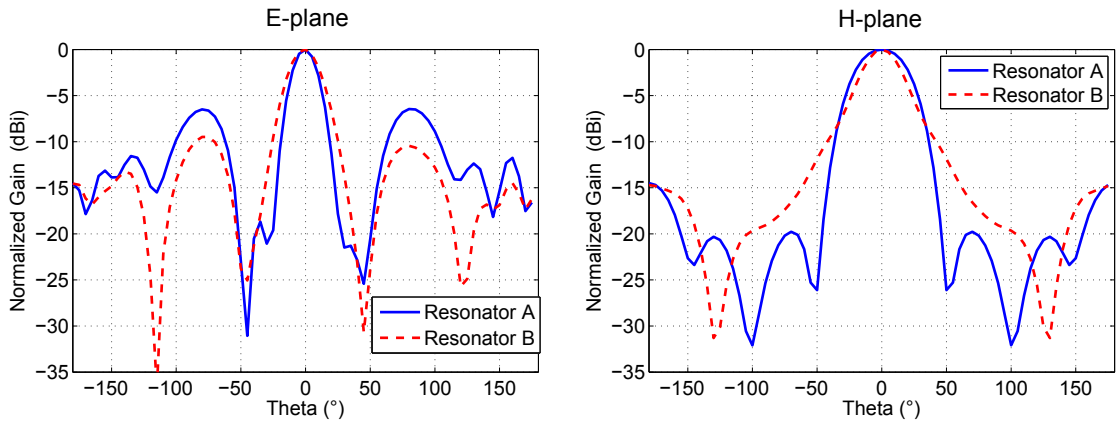


Fig. 3.21: E-plane (left) and H-plane (right) radiation patterns of both resonators at frequency 10.25 GHz.

3.1.7 Experimental Results

For experimental verification, we select resonator designated as resonator A that provide maximum gain at central frequency 10.25 GHz and which design has been described in the previous section.

In this section as well as throughout the whole thesis, we build the resonators by layering up conventional microwave substrates as described below. The antenna prototype is manufactured by assembling several layers of completely etched Arlon 600 substrate ($\epsilon_r = 6.15$, $\tan\delta = 0.003$) and the individual layers are held together by a special, double-sided duct tape with known electrical properties ($\epsilon_r \approx 3$). Due to the nature of the fabrication process, the height of the resonators must be an integer multiple of 1.575 mm (i.e. thickness of one layer of Arlon 600 substrate); in addition, the thickness of one layer of tape is about 50 μm , which also must be taken into account as it increases the overall height of the resonator. Considering these

additional requirements, the resonator is slightly redesigned and its final dimensions are given in the Tab. 3.2. The simplified view of the layered antenna can be seen in Fig. 3.22. The top view of the antenna with soldered SMA connector can be seen in photograph in Fig. 3.23. The final size of the ground plane of the manufactured antenna is $g = 77$ mm.

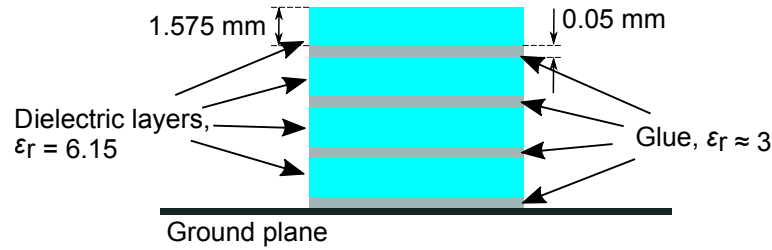


Fig. 3.22: Dielectric resonator created by several layers of dielectric substrate with interleaved glue layers. The proportions in the figure are exaggerated, glue layers are only circa $50 \mu\text{m}$ thick.

Tab. 3.2: Final dimensions of the antenna.

h (mm)	w (mm)	l_a (mm)	g (mm)
11.38	26.75	13.10	77

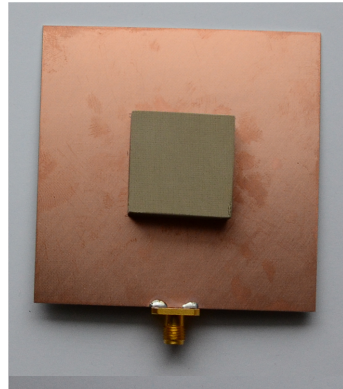


Fig. 3.23: Top view of the fabricated DR antenna with SMA connector.

The reflection coefficient frequency response is measured and the measured results of its magnitude are compared with simulation results of the redesigned resonator in Fig. 3.24. The differences might be explained by the absence of the SMA connector in the simulations but it is much more likely that the fabrication tolerances cause the discrepancy. The upshift of the resonant frequency can be explained by

small amounts of air trapped between the adjacent resonators layers, which slightly decrease the effective permittivity of the resonator.

The realized gain is measured at several frequencies and the results are given in Fig. 3.25. The enhanced gain region at the target frequency 10.25 GHz is therefore confirmed with maximum value 11.9 dBi.

Normalized radiation patterns in principal planes of the antenna are given in Fig. 3.26. The results confirm, that the higher-order mode resonator provide enhanced directivity; however, the side lobes are quite distinctive in the E-plane as predicted by simulations. The measured side lobe level is -7.7 dB compared to -6 dB obtained in simulations. One of the explanations that can at least partially explain this fact is the SMA connector that is placed in the E-plane of the antenna and that has not been part of the simulation model.

The maximum value of cross-polarization component is below -20 dB relative to the maximum value. Nulls in the measured patterns for the back lobe directions are caused by the properties of our measurement range, when line of sight between AUT and illuminating antenna is obscured for these angles by antenna scanner.

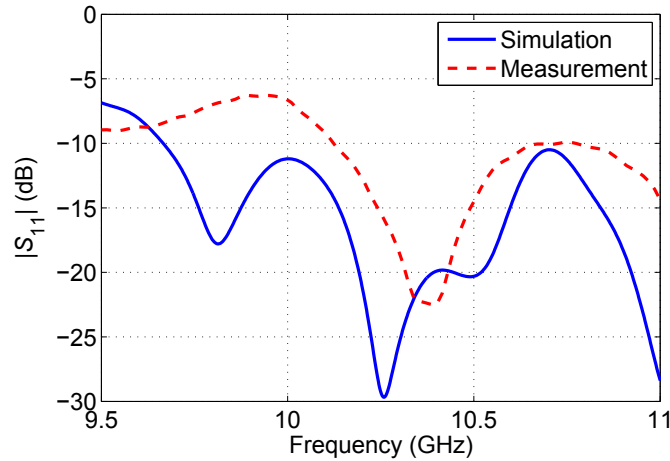


Fig. 3.24: Comparison between simulated and measured reflection coefficient. The measured results varied from simulated due to inaccurate fabrication.

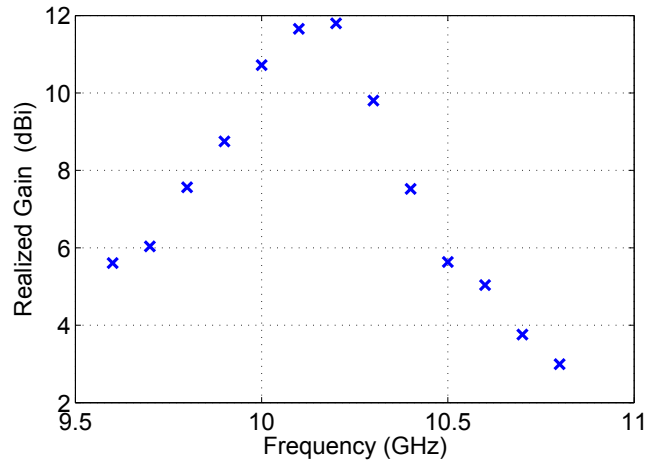


Fig. 3.25: Measured realized gain frequency response. Maximum achieved gain is 11.9 dBi.

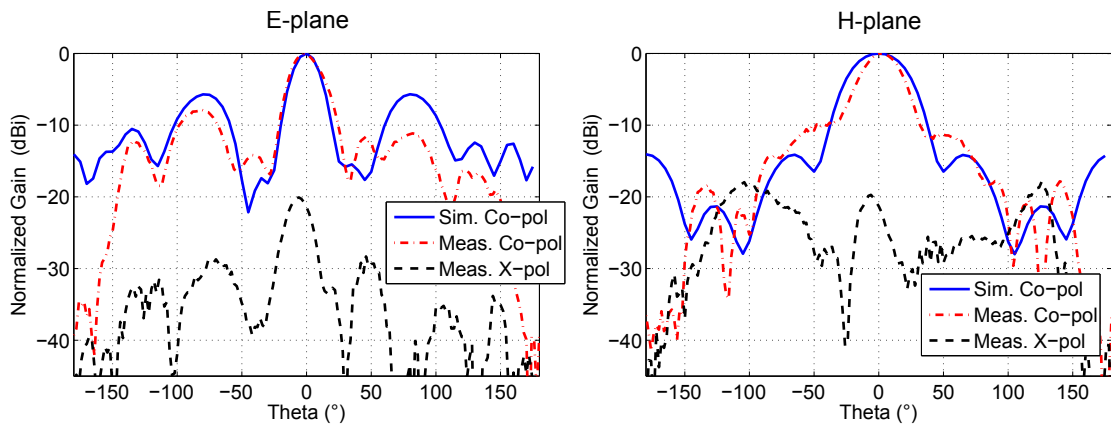


Fig. 3.26: Normalized radiation patterns in both principal planes (E-plane on the left, H-plane on the right). The absence of the measured back lobe (compared to simulations) is given by the nature of our measurement range. The shape of the cross-polarization pattern in the E-plane suggest slight misalignment of the antenna during measurements.

3.2 Cylindrical Directive DRA

In this part, we describe a DRA element based on the excitation of a higher-order hybrid electromagnetic HEM_{133} mode in a single cylindrical dielectric resonator to accomplish considerable gain enhancement. We observe partial excitation of the nearby HEM_{123} mode which slightly increase the gain, but more visibly the impedance bandwidth of the antenna. Similarly to conventional DRAs, where broadside radiating modes TE_{111} of rectangular and HEM_{111} of cylindrical resonator show very similar characteristics we can assume that HEM_{133} mode will resemble in performance the TE_{133} mode of rectangular resonator. Compared to rectangular resonator, the analysis and design of cylindrical resonators is more straightforward as the cylinders possess only two degrees of freedom (i.e. height and diameter) for selected relative permittivity.

Both HEM_{133} and HEM_{123} modes require neither special feeding schemes nor ground plane modifications and can be excited similarly to the well-known HEM_{111} (also denoted as $\text{HEM}_{11\delta}$) mode. The aperture coupling feed [22] is selected and optimized to avoid excitation of unwanted modes inside the resonator.

A parametric study in CST Microwave Studio is conducted to observe the behavior and to determine the limits of the proposed DRA. We focus on various diameter to height ratios (aspect ratio) as well as on ground plane size, which, as in case of rectangular DRA operating with TE_{133} mode has noticeable effect on the E-plane radiation patterns as well as on the broadside gain values.

The antenna is designed to operate over unlicensed ISM 5.8 GHz band (5.725 GHz - 5.875 GHz), but the concept might be more suitable at higher frequencies, where the resonator size can be less crucial. In section 3.3 we follow by study of an additional gain increase of the 5.8 GHz ISM band antenna by introducing an air gap between the resonator and its ground plane. We perform numerical and experimental parametric study in order to verify the additional gain increase of about 1.5 dB. The higher frequency operation is demonstrated in section 3.4 on millimeter-wave DRA resonating at central frequency about 26 GHz. For fabrication, we use advanced Low Temperature Co-fired Ceramic (LTCC) technology with very low losses. In simulations, we compare the performance of two electrically equivalent DRAs built from two various LTCC materials, one cheap, intended for low frequency PCB design and the other one, more expensive designated for high performance millimeter-wave PCB designs.

3.2.1 High Gain Cylindrical DRA Concept

The antenna is composed of a single cylindrical dielectric resonator placed above a circular conductive ground plane. The resonator is excited through a rectangular slot in the ground plane of a microstrip line according to Fig. 3.27. An aperture coupling feeding mechanism is selected to minimize the excitation of unwanted lower-order modes in the structure. Relative permittivity of the resonator in all simulations is 6.15. This value is selected due to availability of the material with the given ϵ_r . The substrate Arlon 25N with relative permittivity 3.38 is used in the feeding structure design.

Initial dimensions of the resonator (height h and diameter d according to Fig. 3.27) are found by the magnetic wall method using CST Eigenmode solver. All the walls are set as PMCs, except the bottom wall which is set to PEC and the resonator dimensions are obtained so that the resonant frequency of the target mode HEM_{133} is 5.8 GHz. In this way, we can also determine approximate resonant frequencies of nearby modes, particularly of HEM_{123} that is partially excited as well. Since the magnetic wall method does not take radiation losses of the resonator into account, considerably large inaccuracy is a result. Nevertheless, the method provides a reasonable initial approximation of dimensions that needs to be tuned and optimized afterwards. Full-wave transient solver of CST Microwave Studio is used for this purpose.

Figures 3.29 and Fig. 3.30 depict the simulated E-field and H-field distributions of the desired modes in several cross-sections (see Fig. 3.31) of the resonator as obtained from the modal analysis and as excited within the designed DRA at the target frequency 5.8 GHz. The comparison clearly shows the presence of the modes inside the DRA. Moreover, the modes are excited with quadrature phase shift which simplifies their identification.

The E-field oscillates predominantly in the x -axis direction (y -field components are symmetrical and thus cancel each other out) and thus the radiation is linearly polarized in the broadside direction (the direction along the z -axis). A relatively high gain radiator with radiation efficiency above 90 % can be obtained by carefully optimizing the resonator's size, dimensions of the aperture feed and the ground plane diameter.

Aperture coupling excitation scheme is selected to excite the desired modes in our DRA. This solution is preferred since the desired modes are of higher order and e.g. a probe feed would give rise to the excitation of unwanted TE/TM modes, deteriorating the near field distribution and resulting in main beam tilt and gain reduction. The aperture is fed by a 50Ω microstrip line placed on the other side of the ground plane as seen in Fig. 3.31. By placing the aperture symmetrically below

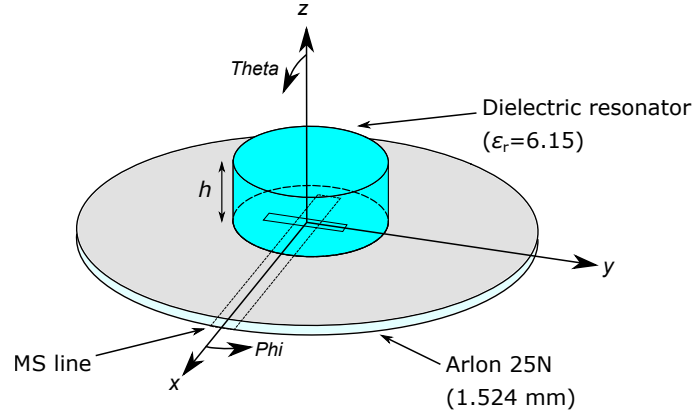


Fig. 3.27: Geometry of the aperture-fed cylindrical DRA and its alignment in the spherical coordinate system.



Fig. 3.28: Manufactured prototype of the high gain cylindrical DRA

the DRA and tuning its dimensions, we can excite both the desired modes with a single feed. Suitable values of parameters l_a , w_a and l_s must to be found; initial values are calculated using following equations:

$$l_a = \frac{0.4\lambda_0}{\sqrt{\varepsilon_e}}, \quad (3.11)$$

$$w_a = 0.2l_a, \quad (3.12)$$

$$l_s = \frac{\lambda_g}{4}, \quad (3.13)$$

where $\varepsilon_e = (\varepsilon_r + \varepsilon_s)/2$, ε_r and ε_s are relative permittivities of the DRA and the substrate, respectively and λ_g is the guided wavelength in the substrate. The length in 3.11 is selected, so that the half wave resonance of the slot is avoided. Nevertheless, we must work with a considerably longer slot for appropriate mode excitation.

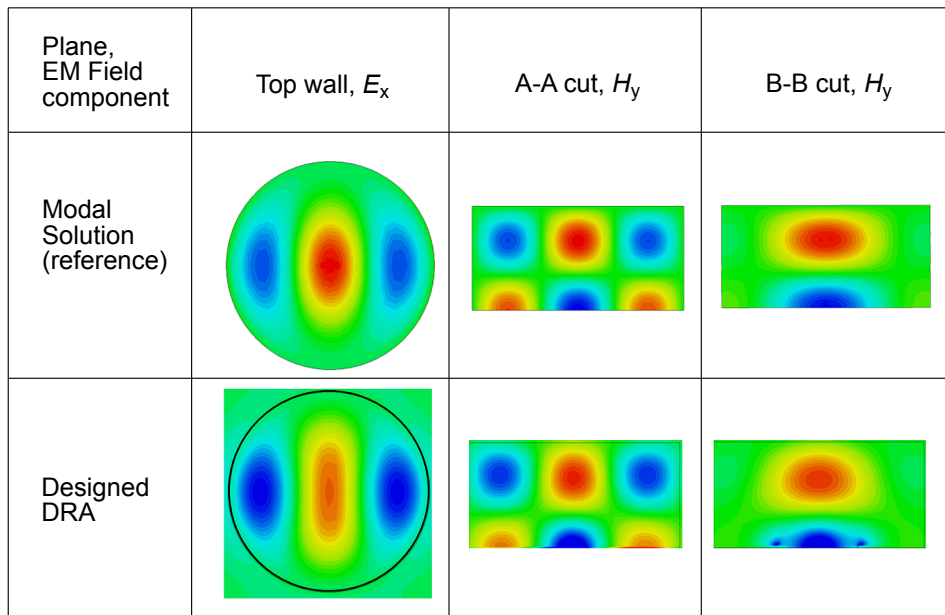


Fig. 3.29: E-field and H-field distributions of the HEM_{133} mode as obtained by the modal analysis and the same field components as excited in our DRA at 5.8 GHz. The phase difference between the visualized E and H-field is 180° . For plane cuts see Fig. 3.31.

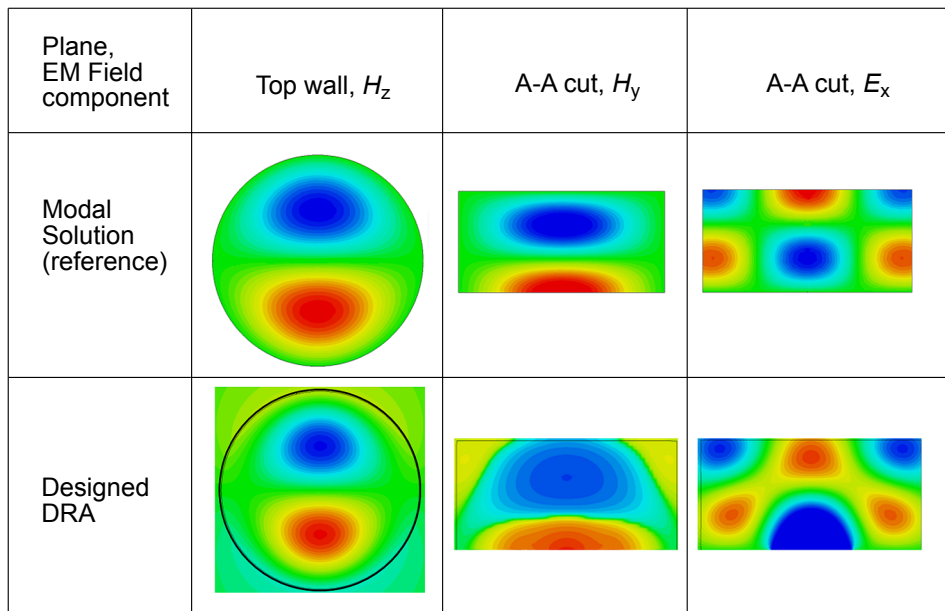


Fig. 3.30: E-field and H-field distributions of the HEM_{123} mode as obtained by the modal analysis and the same field components as excited in our DRA at 5.8 GHz. The phase difference between the visualized E and H-field is 180° . Moreover, the fields have 90° phase shift as compared to the fields in Fig. 3.29. For plane cuts see Fig. 3.31.

The result is that the back-lobe radiation is increased. However, this problem can be solved by using a stripline or a substrate integrated waveguide instead of the microstrip line. The optimum slot dimensions are found to be $l_a = 17.73$ mm, $w_a = 3.49$ mm with the stub length $l_s = 10.94$ mm.

3.2.2 Parametric Study

The influence of two main design parameters of the designed DRA on antenna performance is studied. Namely the resonator diameter d and the ground plane diameter g are varied and the resonant frequency, impedance bandwidth and maximum gain are observed.

Due to the restrictions of the antenna fabrication method, the height h must be an integral multiple of 1.575 mm only, which is the height of the Arlon substrate used for manufacturing (for details, see section 3.1.7). The optimum height h , providing the maximum gain is found to be 22.05 mm corresponding to 14 layers of the Arlon substrate. The desired resonant frequency was 5.8 GHz with the band of interest covering the frequency range 5.725-5.875 GHz (ISM band). The band of interest corresponds to a relative bandwidth of only 2.6 %. Throughout the parametric study, the dimensions of the feeding structure (i.e. the slot width w_a , its length l_a and the stub length l_s) are kept constant as well as the height h of the resonator.

The resonant frequency of the DRA and its impedance bandwidth are determined mostly by the dimensions of the resonator whereas its gain is in addition quite strongly influenced by the diameter of the ground plane. However, in case of very small ground plane, the input impedance is as well influenced by the diameter g . Figure 3.32 shows the frequency response of the reflection coefficient for several d values (the reference impedance is 50 Ω) with the ground plane size $g = 132.5$ mm. The height of the resonator h is fixed to the value 22.05 mm in all the plots.

Figure 3.33 depicts the frequency response of realized gain for several diameters of the resonator as well as for several ground plane sizes (see Fig. 3.33). The gain increases with the diameter of the ground plane to a certain point only, after which the gain is getting reduced with further increasing of the ground plane size. Such a behavior has already been documented in the literature for the dominant HEM_{111} mode [109]. In our case, this gain variation is caused by the edge diffraction in the E-plane (i.e. xz plane in Fig. 3.31) due to a relatively high side lobe levels in the reflector plane (see Fig. 3.37). The gain maximum is obtained if the direct and diffracted waves meet in phase in the broadside direction. In simulations, these maxima are obtained for several ground plane diameters (approximately 135 mm, 235 mm, 335 mm etc.) proving that the gain variation is caused by the diffraction, since the approximate ground plane diameter difference is $2\lambda_0$.

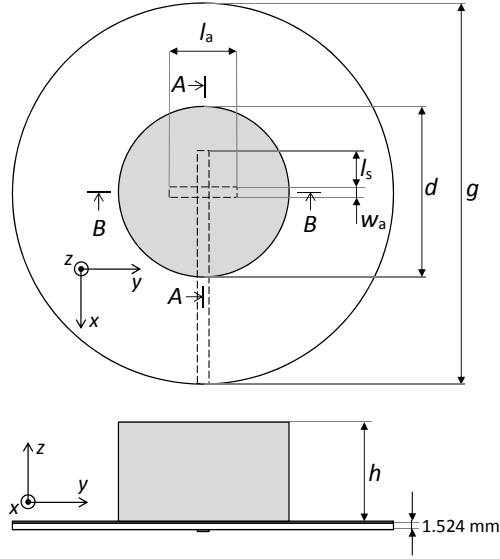


Fig. 3.31: Detail of the antenna geometry and the dimensions.

3.2.3 Prototype and Measurement

The antenna is fabricated by process described in section 3.1.7, in which we built the resonator by stacking up layers of a completely etched Arlon 600 substrate with $\epsilon_r = 6.15$, loss tangent $\tan\delta = 0.003$ and thickness 1.575 mm. The layers are held together by double sided duct tape of $65 \mu\text{m}$ thickness and relative permittivity 3, approximately. The resonant frequency must be slightly tuned by altering the resonator diameter to compensate the effect of 14 layers of the duct tape in between the dielectric layers. The final dimensions of the resonator are $h = 22.75$ mm corresponding to 14 layers of Arlon 600 substrate interleaved with 14 layers of duct tape. The diameter of the resonator is 44.1 mm and the diameter of the ground plane $g = 132.5$ mm.

The comparison between the simulated and measured magnitude of the reflection coefficient is depicted in Fig. 3.35; reasonable agreement can be observed. Simulations are conducted in the transient solver of CST Microwave Studio and measurement is done using a vector network analyzer. Next, radiation patterns and gain of the designed antenna are measured in an anechoic chamber. First, the realized gain frequency response is measured in the broadside direction; a maximum gain of 11.59 dBi is obtained at the frequency 5.82 GHz (Fig. 3.36). Radiation patterns in two orthogonal principal planes (xz , yz in Fig. 3.31) are measured at the frequency of maximum gain 5.82 GHz for co- and cross-polarization components (Fig. 3.37 and 3.38). The co-polarization component corresponded to the x axis and the cross-polarization to the y axis orientation as given in Fig. 3.31. From the results, we can see that the cross-polarization discrimination is better than 20 dB.

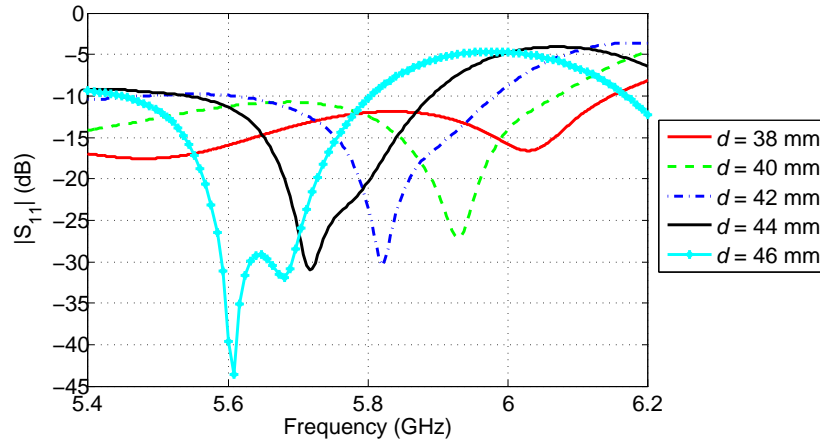


Fig. 3.32: Reflection coefficient vs. frequency for several diameters of the resonator.

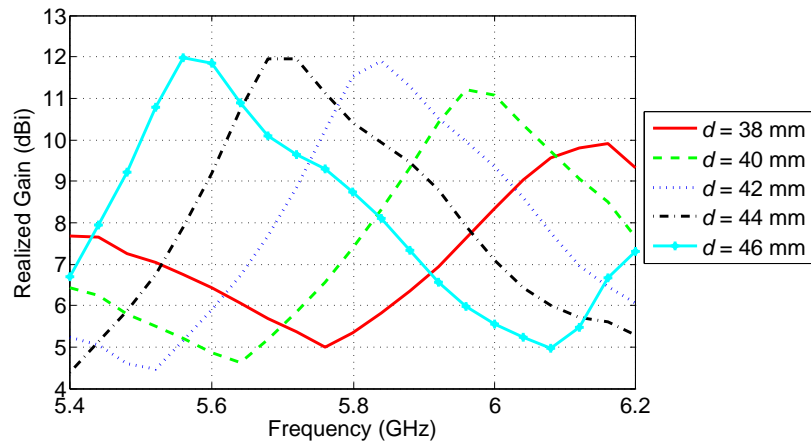


Fig. 3.33: Realized peak gain in the broadside direction vs. frequency for several diameters of the resonator.

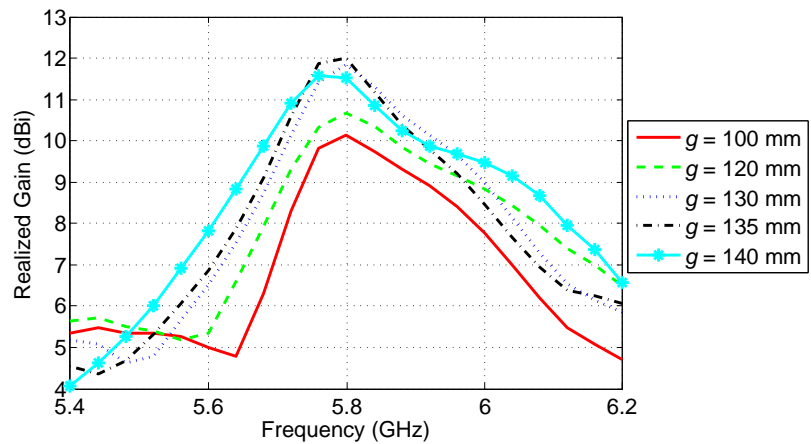


Fig. 3.34: Realized peak gain in the broadside direction vs. frequency with ground plane diameter as a parameter.

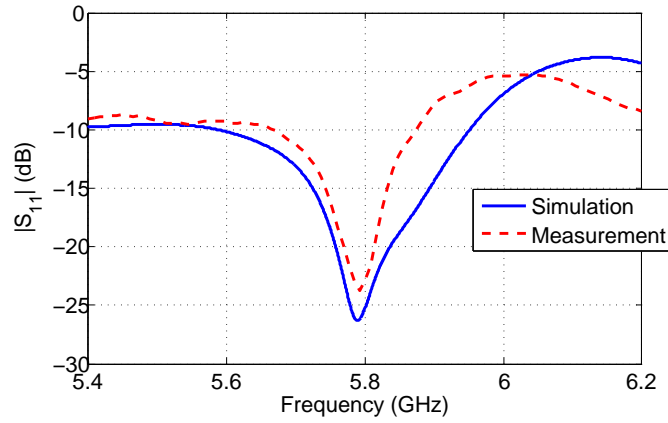


Fig. 3.35: Comparison between simulated and measured magnitude of the reflection coefficient.

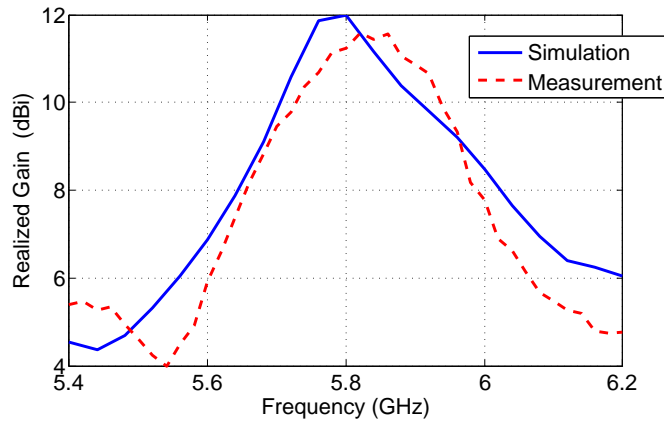


Fig. 3.36: Realized gain frequency response in the broadside direction – simulation vs. measurement.

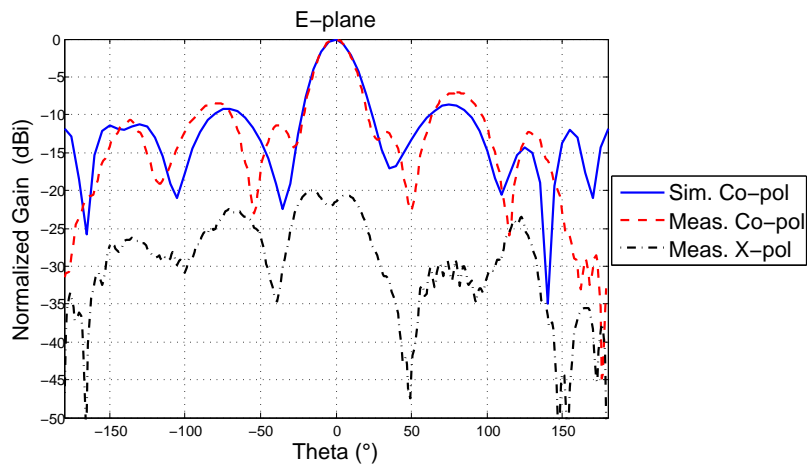


Fig. 3.37: Simulated and measured radiation patterns at 5.82 GHz in the E-plane, which corresponds to xz plane in Fig. 3.31.

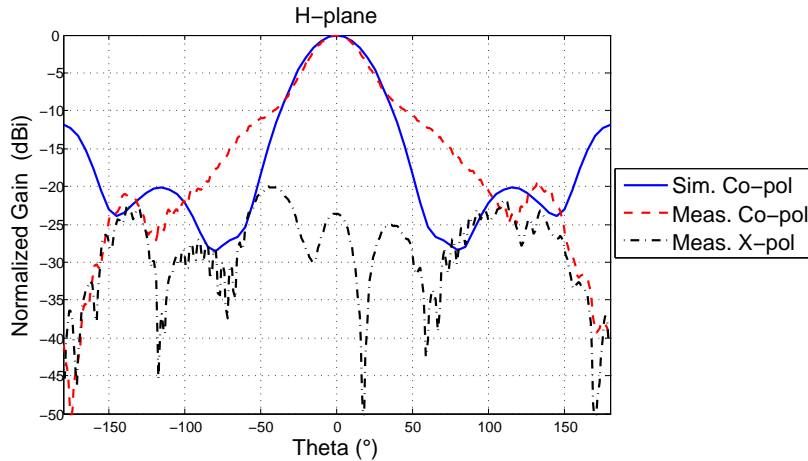


Fig. 3.38: Simulated and measured radiation patterns at 5.82 GHz in the H-plane, which corresponds to yz plane in Fig. 3.31.

3.3 Gain Improvement of HO Mode DRA by Thin Air Gap

Dielectric resonator antennas (DRA) are mostly configured as dielectric resonators situated above a conducting ground plane and excited by one of several suitable feeding schemes such as coaxial probe, aperture, microstrip etc. Introducing the air gap can have a significant impact on the performance of the DRA. Imperfect manufacturing process can result in small air gaps between the coaxial probe and the DR or between the DR and the conducting ground plane due to imperfect mechanical contacts (surface roughness). Effects of such imperfections have been numerically and experimentally studied in [16, 110, 111] for cylindrical DRA operating with the most frequently used $TM_{01\delta}$ and HEM_{111} modes. In fact, the air gap insertion has become a simple and popular way of increasing the impedance bandwidth of the DRA antennas [112], since it decreases the effective permittivity of the resonator.

So far, the attention has been mainly drawn to the gap influence on the input impedance and the Q-factor of the resonator, causing shift in the resonant frequency and change of impedance bandwidth, respectively. The gain variation due to the air gap between the cylindrical DRA operating in HEM_{111} mode was reported in [113]. The antenna gain was decreasing monotonously from about 5.8 dBi for no gap down to about 3 dBi for 0.5 mm gap at operating frequency 10.4 GHz.

We demonstrate by a numerical simulation and experiment, that a very small air gap between the ground plane and the dielectric resonator operating with certain higher order modes described in section 3.2 can in fact increase the gain of the antenna without significantly affecting the bandwidth.

3.3.1 Antenna Configuration

The test antenna geometry consists of a low permittivity cylindrical dielectric resonator (DR) with $\varepsilon_r = 6.15$ fed by aperture coupled microstrip line and placed on top of a ground plane (see 3.39). Small air gap of height h_2 between the ground plane and the dielectric resonator is introduced. The dielectric resonator is fed by a 50Ω microstrip line by aperture coupling method. The aperture is designed so that its resonance is avoided and the coupling to the DR is maximized. The antenna dimensions are first optimized to operate with higher order hybrid EM modes as demonstrated in previous section but without any air gap between the DR and the ground plane. The fields inside the resonator comprised dominantly of the combination of higher order modes HEM_{133} with partial excitation of HEM_{123} .

The dimensions of the resonator in both, numerical and experimental studies, are $h_1 = 22.75$ mm, $d = 44.1$ mm with ground plane diameter $g = 132.5$ mm, whereas the slot dimensions are $l_a = 17.73$ mm, $w_a = 3.49$ mm, and stub length $l_s = 10.94$ mm. The resonator is initially designed for resonant frequency 5.8 GHz considering no air gap between the resonator and ground plane. Based on previous studies [16, 110, 111], it is expected that the resonant frequency will shift upwards with introducing and extending the air gap.

3.3.2 Numerical Study

The original higher order mode DRA presented in 3.2 gives approximately 3.5 % impedance bandwidth with maximum gain of 11.59 dBi and relatively high side lobe levels of -8 dB.

In this study, only one parameter is swept, keeping the others unchanged. In simulations, we are varying only the air gap height h_2 from 0 mm up to 0.6 mm, observing variations in reflection coefficient and gain frequency response. The values of h_2 are very small if expressed in free space wavelengths, e.g. 0.6 mm corresponds to only $0.012\lambda_0$ at 5.8 GHz ($\lambda_0 = 51.7$ mm).

The air gap has expected influence on the resonance frequency value and the impedance bandwidth; however, the air gap for the antenna in our configuration enhances the gain by more than 1 dB (almost 1.7 dB). With increasing the air gap, the side lobe levels are slightly decreasing, thus the directivity values in the main beam of the antenna are improved, whereas the radiation efficiency stays approximately unchanged (above 90%). Impedance matching to the 50Ω microstrip line through the aperture is deteriorated as the air gap is increasing due to the change of the resonator's input impedance. However, by tuning the size of the coupling slot and stub, the impedance matching can be improved as well for the DRA with the air gap.

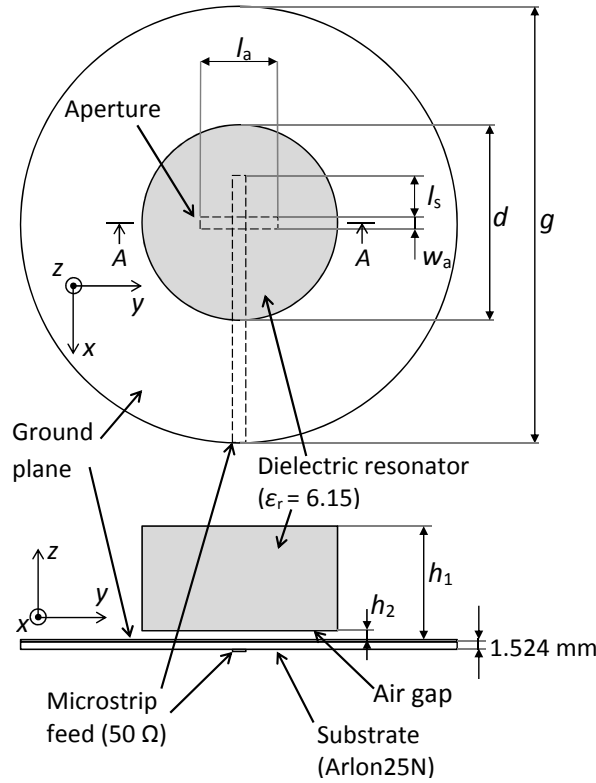


Fig. 3.39: The configuration of the examined DRA with incorporated air gap between the ground plane and the resonator.

3.3.3 Prototype and Measurements

We fabricate the resonator by stacking up etched layers of Arlon 600 substrate with $\epsilon_r = 6.15$, $\tan\delta = 0.003$, whereas for the feed Arlon 25N with $\epsilon_r = 3.38$, $\tan\delta = 0.0025$ is used. The thin air gap (h_2) is introduced by gluing together several layers of narrow strips of double sided duct tape. The resonator is attached to the ground plane with two narrow stripes of tape (see Fig. 3.46) resulting in total thickness of about 0.07, 0.2, 0.33 and 0.46 mm corresponding to one, two, three and four layers of tape, respectively.

The frequency response of realized gain (see Fig. 3.43) as well as the radiation patterns (Fig. 3.44 and 3.45) are measured only with the air gap of 0.07 mm and 0.33 mm, since the simulations shown the optimum height of the gap is somewhere around 0.4 mm (see Fig. 3.41). If we express these heights in terms of free space wavelengths ($\lambda_0 = 51.7$ mm at 5.8 GHz) we get $1.35 \cdot 10^{-3}\lambda_0$, $6.38 \cdot 10^{-3}\lambda_0$ and $7.74 \cdot 10^{-3}\lambda_0$ for heights 0.07 mm, 0.33 mm and 0.4 mm, respectively.

The resonant frequency is directly proportional to the height of the air gap. Since the input impedance of the resonator is changing with increasing the height of

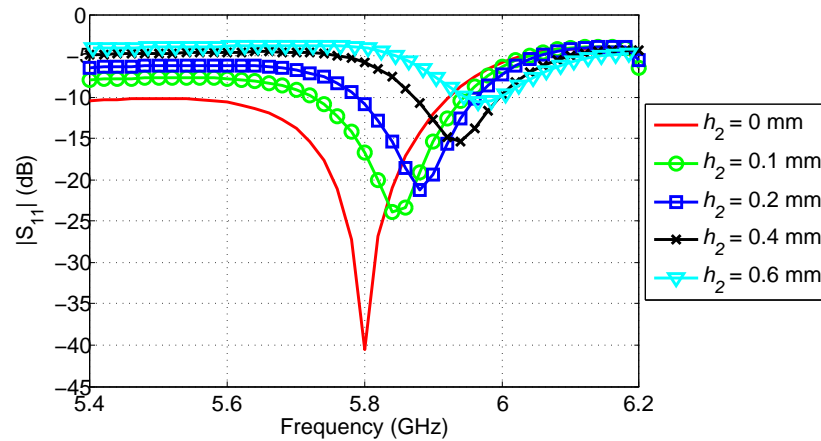


Fig. 3.40: Variation of the reflection coefficient with increasing the height of the air gap.

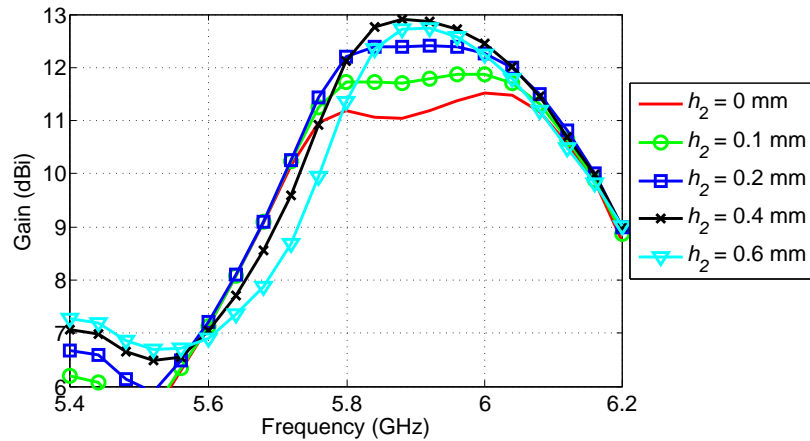


Fig. 3.41: Variation of the gain (IEEE gain) with increasing the size of the air gap.

the gap, the parallel stub matching becomes less effective as the gap is introduced. It follows, that the impedance matching level of the antenna with air the gap can be improved by additional tuning of the stub and coupling aperture dimensions; however, it is not attempted here. The results prove that a very thin air gap between the dielectric resonator and the ground plane can influence the radiation parameters of higher order mode. In this way gain increase from 11.6 dBi to 13.2 dBi can be achieved and simultaneously we can improve the side lobe level suppression. The realized gain of the antenna exceeds 10 dBi level in relative frequency bandwidth of about 5.1 %.

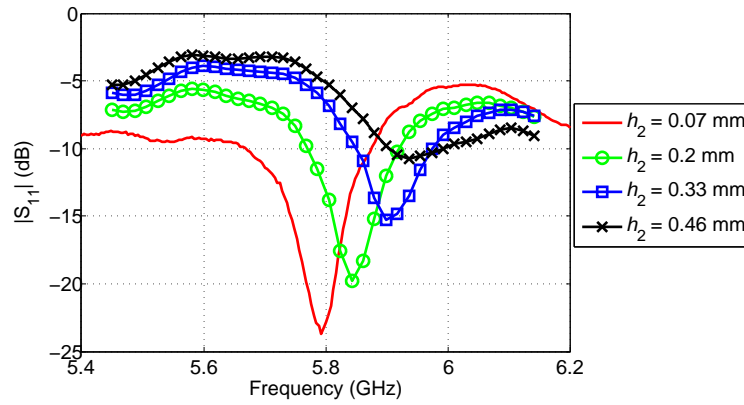


Fig. 3.42: Measured reflection coefficient for several thicknesses of the air gap between the ground plane and the resonator.

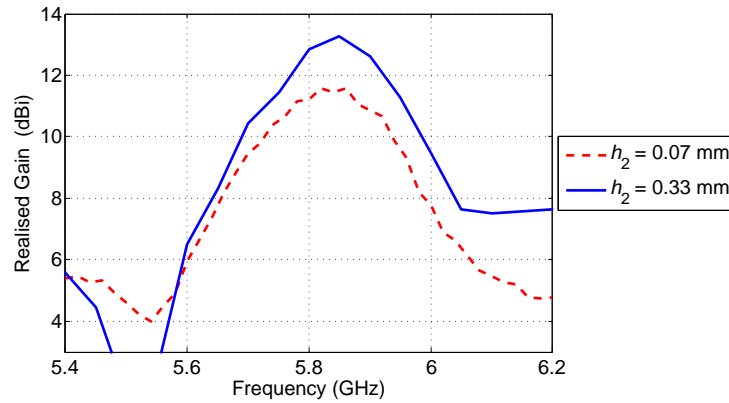


Fig. 3.43: Measured realized gain for two values of air gap height between the ground plane and the resonator. Gain boost of 1.6 dB can be seen.

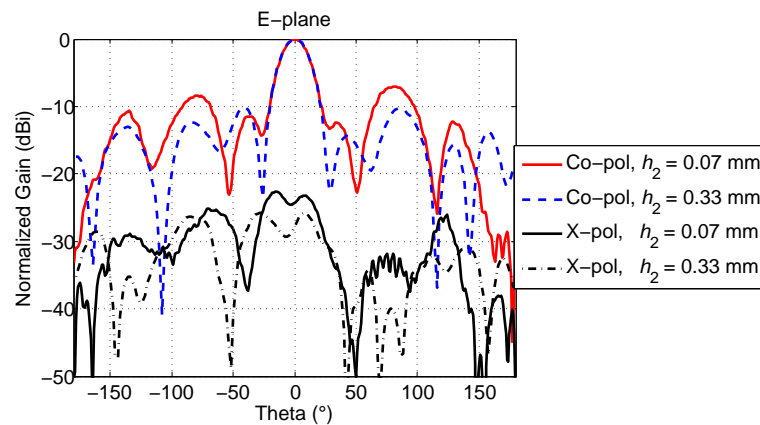


Fig. 3.44: E-plane radiation patterns (co- and cross-polarization) of the antenna for two different heights of the air gap at frequency 5.85 GHz.

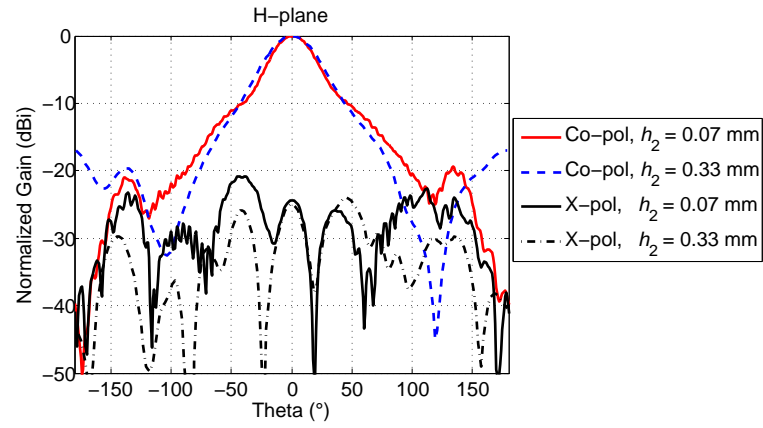


Fig. 3.45: H-plane radiation patterns (co- and cross-polarization) of the antenna for two different heights of the air gap at frequency 5.85 GHz.

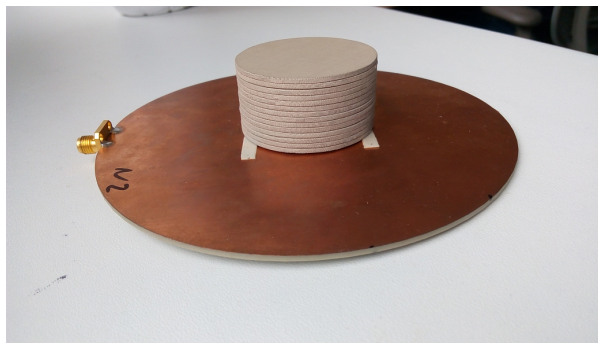


Fig. 3.46: DRA prototype with air gap introduced by stripes of duct tape on the left and right side of the resonator.

3.4 Low Temperature Co-Fired Ceramics for Millimeter Wave Directive DRA Design

Dielectric resonator antennas are very promising candidates for the deployment at millimeter and even sub-millimeter wave bands due to their inherently low conduction losses. In majority of applications the DRAs operate in one of their low-order modes producing radiation patterns comparable with short magnetic dipole with gain about 5 dBi. However, as the frequency increases, the dielectric losses can limit the radiation efficiency of the antenna. Low loss dielectrics must then be used if the radiation efficiency is to be kept high. One of the high-quality materials for millimeter-wave areas is Low Temperature Co-Fired Ceramics (LTCC) with excellent stability, mechanical and dielectric capabilities. Although LTCC is primarily intended for multilayer circuit board design, its permittivity and fabrication process capability makes it interesting also for DRA design [42]. Ultimately, the circuitry as well as the antenna can be fabricated in one processing step as single LTCC board.

This chapter deals with the development of a millimeter-wave LTCC based DRAs utilizing the antenna concept described in section 3.2, i.e. excitation of higher-order mode, dominantly HEM_{133} in cylindrical resonator at a center frequency of interest 25.5 GHz. The work should verify the suitability of the LTCC technology for building this type of a radiator. This technology is advantageous as it comes to the fabrication of more complex resonator shapes for very high frequency bands (millimeter waves), where it can be very difficult to meet the required tolerances with classical manufacturing methods. The shapes with increased complexity might provide improved impedance bandwidth, similarly to the basic DRAs. As substrate, we chose LTCC material, system Green Tape 9K7. Green Tape 9K7 is usually available in multiple thicknesses and is designed for use as an insulating layer in multichip multilayer modules, single chip packages, ceramic printed wiring boards and various millimeter-wave modules. Green Tape 9K7 shows very low loss tangent at millimeter wave bands and according to the manufacturer it is suitable for applications up to approximately 100 GHz [114].

In order to mitigate the losses and spurious radiation as much as possible the antenna is fed by a slot inside a substrate integrated waveguide (SIW). This solution decreases the losses compared to the microstrip line feed on one hand and on the other hand decrease the back-lobe radiation levels.

In simulations, we have experimented with much cheaper type of LTCC material called Green Tape 951 PX with $\epsilon_r = 7.8$ [115]; however, its performance rapidly deteriorates at higher frequencies. The loss tangent rises from 0.006 at 3 GHz to 0.014 at 10 GHz. The efficiency of the DRA drops to only about 48 % if the losses are so high. Moreover, we can assume even higher values of loss tangent at frequencies

above 20 GHz and thus the design in this frequency region would not be very useful from radiation efficiency point of view. Example of two manufactured resonators from Green Tape 951 can be seen in Fig. 3.47; slight misalignment of 200 μ m thick LTCC layers is obvious.

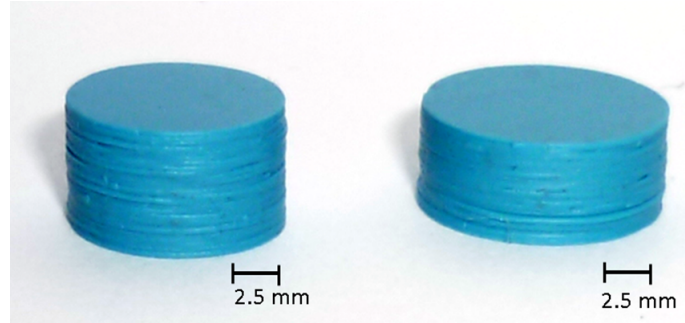


Fig. 3.47: Manufactured LTCC resonators for 24 GHz resonant frequency of HEM_{133} mode from DuPont Green Tape 951.

3.4.1 Millimeter-Wave Directive Cylindrical DRA Based on Low-Loss LTCC 9K7 Green Tape

The antenna is again configured as a cylindrical dielectric resonator from LTCC material (Green Tape 9K7) with electrical properties $\epsilon_r = 7.1$ and $\tan\delta = 0.0009$ as provided at 10 GHz, placed above a conducting ground plane of square footprint. The properties of LTCC during field simulations at 25.5 GHz are extrapolated utilizing the 3rd order electric dispersion model by “Constant fit tangent delta” option in CST MWS.

The radiating element of the antenna is based on the higher-order mode excitation inside a cylindrical dielectric resonator according to section 3.2, providing directive radiation pattern with good radiation efficiency, if the ground plane size is accordingly adjusted. The directivity in the broadside direction is affected by the edge diffraction in the E-plane and thus the maximum gain of the antenna is a periodic function of ground plane size. In this design, the resonator is fed by an aperture inside a SIW to minimize the back radiation inherent to the microstrip line fed aperture. For the feeding structure, Arlon 25N microwave substrate with relative permittivity $\epsilon_r = 3.38$, loss tangent $\tan\delta = 0.0025$ and thickness 0.762 mm is used. The fields in the aperture determine the linear polarization of the radiation produced by the antenna.

In addition, the losses inside the SIW feed are reduced compared to the microstrip line fed slot at such high frequency. However, further loss reduction (and increase of radiation efficiency) might be accomplished by using substrate with lower

loss tangent. The SIW is fed by a short section of a grounded coplanar waveguide (GCPW) line terminated with a linear taper connected to the SIW, efficiently transforming the quasi-transverse electromagnetic wave (QTEM) of the GCPW line into the transverse electric TE_{10} mode of the SIW. The electric and magnetic field distributions in cross-section of the resonator corresponding to the E-plane are visualized in Fig. 3.49 and Fig. 3.50. The fields can be identified as HEM_{133} mode; nevertheless, more detailed observation can show partial presence of HEM_{123} mode as showed in section 3.2.

3.4.2 Antenna Design

The antenna is initially designed for 25.5 GHz center frequency and the relative impedance bandwidth (BW) is expected to be quite small as shown in section 3.2. The fact that a low relative permittivity material is used to build the resonator does not help to provide larger BW since larger Q factor is associated with higher-order modes in general (compared to e.g. HEM_{111} mode). Achieving enhanced directivity while keeping high radiation efficiency and maintaining the impedance bandwidth is the main design goal.

The dimensions of the resonator (i.e. height h and diameter d) are first obtained by scaling down the DRA antenna designed in section 3.2 and subsequently followed by fine tuning. The magnetic wall model used for initial design, in which the dielectric-air interfaces are considered as perfect magnetic walls; gives in our case only about 3 % shift in the resonant frequency and therefore can be considered a good approximation for our purpose. The model predicts the resonant frequency to be somewhat higher; which is natural, since the lossy walls do not enforce the Dirichlet boundary condition ($H_t = 0$ A/m) at the dielectric-air interfaces.

The width of the SIW feed is calculated so that the waveguide has the cut-off frequency at about 18 GHz on a selected Arlon 25N substrate. In the first design steps, the SIW is modeled as a waveguide with full vertical walls instead of modeling individual vias which requires increased mesh complexity and eventually computation time. The SIW model with vias is included in simulations during tolerance analysis and final tuning. The coupling aperture length l_a , the width w_a and its distance from the shorted end of the substrate integrated waveguide l_s are determined for the resonator similarly as in case of microstrip fed aperture in section 3.2.

The SIW is connected to the input 50Ω GCPW line using linear taper with certain length and width at the SIW-GCPW connection, and the dimensions of the taper are obtained by optimization in CST.

The last design parameter is the size of the ground plane g , as it has been

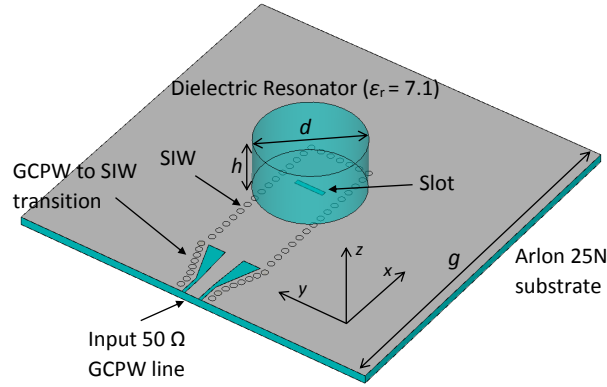


Fig. 3.48: Configuration of the proposed directive LTCC dielectric resonator antenna fed by an aperture in SIW.

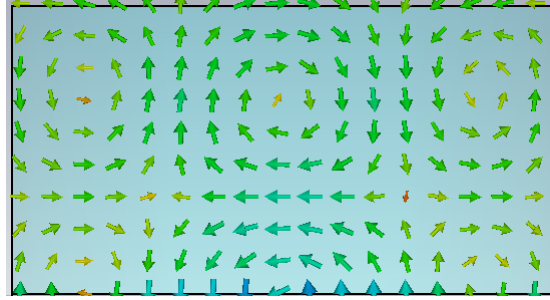


Fig. 3.49: Electric field distribution in the E-plane cross section of the resonator corresponding to the HEM_{133} mode (xz plane in Fig. 3.48).

shown that the ground plane size has considerable impact on the gain value in the broadside direction due to the edge diffraction. The size is therefore selected to provide maximum directivity whereas keeping the area as small as possible. Only the square footprint of the ground plane is considered even though the circular profile can further slightly increase the directivity. All the simulation results are given in the following section as well as the results of the measurements.

3.4.3 Prototype and Measurements

For manufacturing of the resonator, the 9K7 Green Tape from DuPont Microcircuit Materials [114] is used with electrical properties $\epsilon_r = 7.1$ and $\tan\delta = 0.0009$ at 10 GHz. For the resonator, 23 layers of the LTCC tape are needed. The final dimensions of the resonator, after lamination and firing process, are: height $h = 5.03$ mm, $d \approx 9.80$ mm. Due to the considerable height of the resonator and its layered structure, the diameter varies between 9.77 – 9.82 mm. Since the difference between the

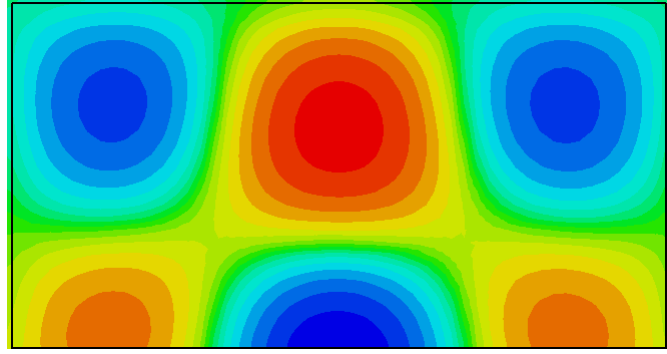


Fig. 3.50: Magnitude of magnetic field component H_y in the E-plane cross section of the resonator corresponding to the HEM_{133} mode (xz plane in Fig. 3.48).

dimensions of the designed and manufactured resonators cannot be neglected (almost 2 %), the simulations are carried out for the dimensions of the manufactured samples so that we have valid comparison between simulation and measurement. The size of the resonator in simulations is therefore adjusted to correspond to the size of the manufactured resonator.

The resonator is attached to the ground plane using special type of double-sided duct tape with height about $50 \mu\text{m}$ and relative permittivity $\epsilon_r \approx 3$. Due to the above-mentioned facts, the resonance frequency is shifted to 25.8 GHz.

For interfacing, end launch connector from Southwest Microwave is attached to the GCPW at the edge of the board. The fabricated antenna with the attached connector can be seen in Fig. 3.51.

The reflection coefficient comparison between simulation and measurement is depicted in Fig. 3.52. Radiation patterns in the principal planes at the frequency 25.8 GHz are finally compared in Fig. 3.53 and Fig. 3.54. Very good agreement in the value of realized gain can be observed as well as in the shape of the main lobe. The differences in side lobes in the E-plane between simulation and measurements are caused by very inaccurate model of the connector which was part of the simulations. Due to the nature of our measurement range, only patterns for one hemisphere are measured (i.e. $\theta = -90^\circ$ to 90°).

The simulated radiation efficiency of the antenna is 87 %; however, the value can be further increased by using lower loss material for the feeding structure compared to Arlon 25N which is used in our case. Based on very good agreement between simulation and measurement, we can assume that the real efficiency is not far from the simulated value.

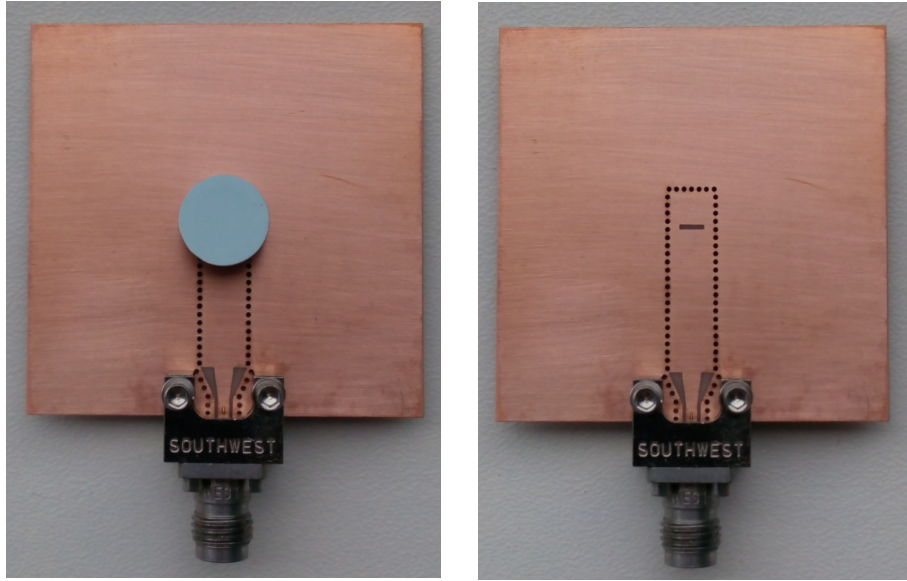


Fig. 3.51: Manufactured LTCC based DRA (on the left). Without attached dielectric resonator (on the right). The parameters of the antenna are: $h = 5.03$ mm, $d \approx 9.80$ mm, $\epsilon_r = 7.1$, $g = 34$ mm. And the feeding slot dimensions are $l_a = 2.75$ mm, $w_a = 0.46$ mm, $l_s = 4$ mm.

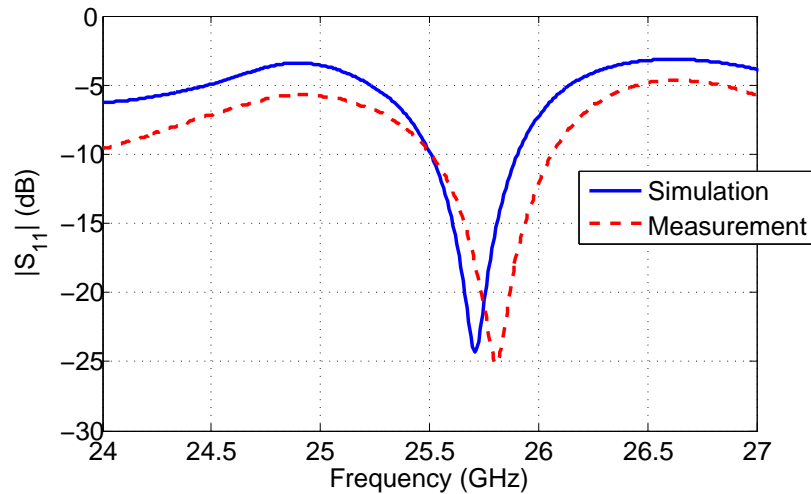


Fig. 3.52: Simulated and measured reflection coefficient magnitude as functions of frequency. The fractional bandwidth of the measured antenna is 2.15 %.

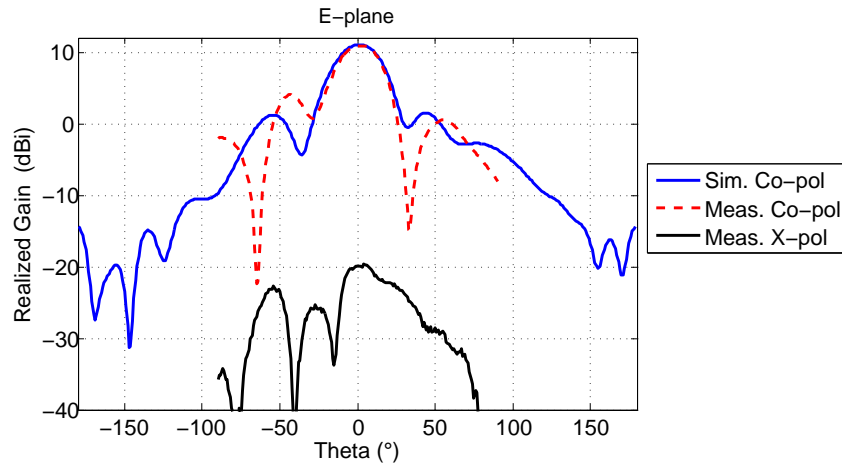


Fig. 3.53: Radiation patterns of the antenna in the E-plane, which corresponds to the xz plane according to the Fig. 3.48. Measured gain in the broadside direction is 10.8 dBi (10.9 dBi in simulations). Very good agreement inside the main lobe can be observed between the simulated and measured results, the side lobe level and in this plane, is mostly influenced by the presence of the 2.4 mm connector which is modeled in simulations only as a simple brick with similar outline dimensions as the real connector.

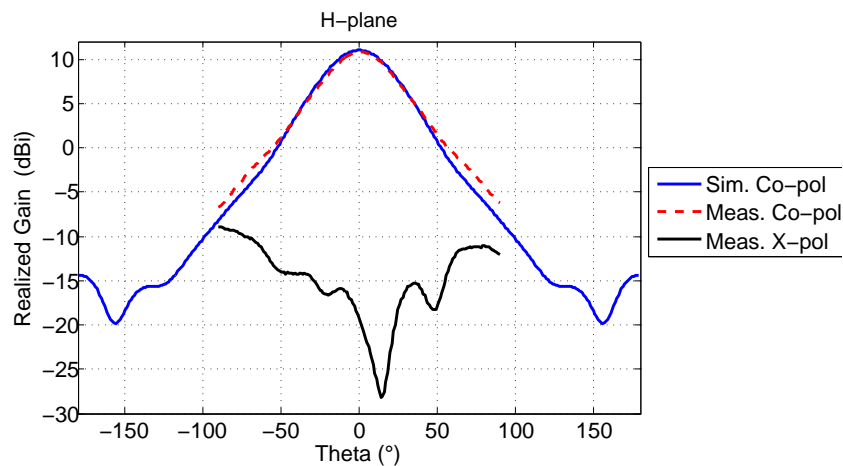


Fig. 3.54: H-plane radiation patterns (i.e. yz plane in Fig. 3.48). Since the influence of the connector in this plane is minimal, we can see excellent agreement between simulation and measurement.

3.5 Summary

One of the cornerstones of this dissertation lies in the gain enhancement of a single element DRAs by utilizing the properties of the higher-order modes excited in the simple shaped dielectric resonators. The accomplished work presented in this chapter has dealt with the design of a high gain rectangular and cylindrical DRAs for various frequency bands. The directive radiation pattern is obtained by excitation of higher order modes, dominantly TE_{133} mode in rectangular and HEM_{133} in cylindrical resonator, that increases the antenna's effective area, resulting in gain enhancement. The structure shows narrow impedance bandwidth, although sufficient to cover e.g. ISM frequency bands. Simultaneous excitation of other nearby modes can extend the impedance bandwidth (as in the case of square DRA); however gain bandwidth is not broadened by this approach.

The results of the manufactured antennas comply well with the simulations. We have also shown how a very electrically-small air gap introduced between the ground plane and resonator operating in HEM_{133} mode can further increase its peak gain from 11.6 dBi to 13.2 dBi and reducing significantly the side lobe levels.

Low temperature co-fired ceramics technology has turned out to be very advantageous to millimeter wave HO mode DRA design. We have demonstrated it on 25.8 GHz to produce directive DRA with high radiation efficiency. Since with LTCC it is possible to produce more accurate shapes compared to the technique of layering microwave substrates, the obtained measurement results agreed very well with the simulations.

Chapter 4

Mutual Coupling in Higher-Order Mode DRA Arrays

In this chapter, mutual coupling between two dielectric resonators is examined. Focus is drawn to resonators operating in higher-order modes for gain enhancement of single element dielectric resonator antennas. The modes comprise TE_{113} ($TE_{\delta 13}$) and TE_{115} ($TE_{\delta 15}$) of rectangular resonator, whose enhanced gain was described by Petosa et al. [57, 58] and mode proposed in this theses, i.e. TE_{133} [116] of rectangular resonator. However, the first subsection deals with mutual coupling between resonators excited with the low-order mode of broadside radiation in rectangular (i.e. TE_{111}) and cylindrical (mode HEM_{111}) resonator. We can assume the coupling level to be reduced in case of elements with higher directivity, since in case of excitation of certain element in planar array, the radiation in the array plane is decreased in order to enhance the directivity in the broadside direction. If the main purpose of the DRA array is to provide larger gain, we can increase the spacing between the elements compared to fundamental mode case without significantly increasing the side lobe levels, since lower amount of power is radiated towards the direction of possible grating lobes. Moreover, reduced coupling of DRA elements is of interest in dense array applications [117].

In general, mutual coupling among array elements can be responsible for radiation pattern distortions that cannot be predicted by array factor and pattern multiplication principle. Such distortions can be present in case of both, receiving and transmitting mode of the antenna array [25]. Moreover, it can alter the input impedance of array elements and thus cause impedance mismatch at the element terminals. The coupling level is influenced by properties of single elements (directivity, sidelobes etc.), feeding network and last, but not least, by the separation between neighboring elements s . In most designs of DRA arrays, the separation distance s between two adjacent elements lies between $0.5\lambda_0$ and $1\lambda_0$. Since the

coupling level is proportional to the separation distance s , a very simple solution to eliminate it is to increase the separation between the elements. Even though we are able to minimize all the negative effects of mutual coupling with this solution, the inter-element separation has also an influence on the generation of grating lobes and hence large separations are impractical if the large sidelobe levels are to be avoided. The selection of separation distance s is therefore a tradeoff between small mutual coupling and sidelobe levels.

The problem is analyzed using full-wave simulations in CST MWS. The methodology of analysis is verified on fundamental mode of rectangular resonators, for which the results are available in the open literature. The common approach to investigate the level of mutual coupling in antenna array is to analyze the interaction between only two elements. Two geometrical configurations of elements are taken into account. First, the elements are located next to each other so that the E-planes of the elements coincide (see Fig. 4.1). And second, the elements are placed so that their H-planes coincide (Fig. 4.2). Based on the configuration we speak about E-plane coupling or H-plane coupling. Both elements are located on top of an infinite ground plane and fed by apertures. These apertures are then driven by discrete ports according to Fig 4.1 and Fig 4.2. The discrete ports are used in order to simplify the numerical model, since in this case the feeding network is not part of the simulation model and thus we do not have to take care about the impedance matching. Moreover, any influence of the feeding network on coupling between elements is eliminated by this approach. Afterwards, the feeding networks for apertures are designed and together with elements fabricated in order to provide valid comparison between simulations and measurements. As a measure of mutual coupling we take inter-element isolation, or rather its inverse, which is the transmission coefficient between the discrete ports S_{21} .

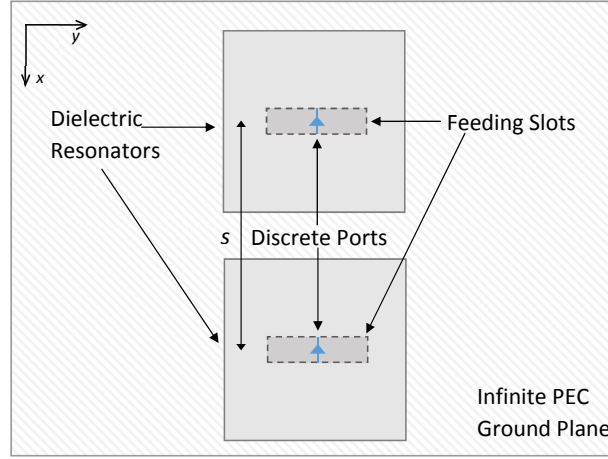


Fig. 4.1: Configuration of two aperture-fed dielectric resonators for analyzing coupling in the E-plane of the resonators (top view).

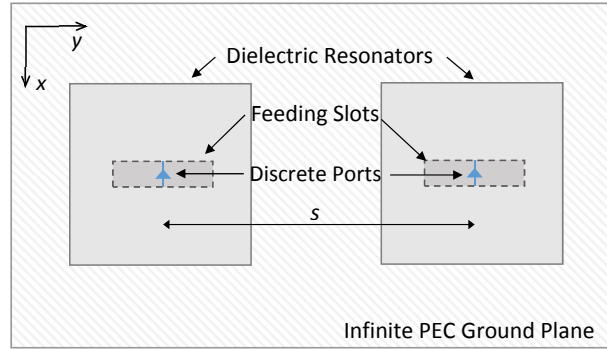


Fig. 4.2: Configuration of two aperture-fed dielectric resonators for analyzing coupling in the H-plane of the resonators (top view).

4.1 Mutual Coupling Between Dielectric Resonator Antennas Excited with Their Fundamental Modes

Since the mutual coupling among the elements can deteriorate the expected behavior of antenna array it must be often taken into account during the designing stage. Here, a review of results available in the open literature is presented. The coupling between the fundamental TE_{111} mode DRA elements is analyzed in section 5.3 and is not repeated here.

Mutual coupling between two DRA elements was studied for the first time in [62]. The authors theoretically derived mutual impedances and calculated mutual coupling for two hemispherical dielectric resonators operating in broadside TE_{111}

mode and fed by a probe. Since hemispherical DRA is the only shape for which analytical field solution exists, mutual coupling between rectangular and cylindrical DRAs has been studied only numerically and experimentally in numerous papers, where authors used either short current probe [63–66] or more frequently an aperture [67–71] for feeding the dielectric resonators. In this way, it was possible to account for other coupling mechanisms present in the experimental setup, most important the direct coupling between feeds of the resonators. In all the works, the resonators were excited with fundamental broadside radiated modes, i.e. HEM_{111} for cylindrical resonators and TE_{111} in case of rectangular resonators.

The results of the above mentioned investigations can be roughly generalized as follows. The coupling in the H-plane of the resonators is stronger, if the element spacing is smaller than approximately $s = 0.5\lambda_0$. With increasing the spacing, the E-plane coupling becomes stronger as it decays with spacing more steadily. At spacing $s = 0.5\lambda_0$ the transmission coefficient between two cylindrical aperture-fed dielectric resonators ($\epsilon_r \approx 10$) is approximately about -12 dB in the E-plane and about -15 dB in the H-plane [67, 68, 70]. At spacing $s = 1\lambda_0$ we can expect, for the same resonators, transmission coefficient of about -19 dB in the E-plane and about -30 dB in the H-plane [67, 68]. In case of probe-fed resonators [64] with separation distance $s = 0.5\lambda_0$ the transmission between resonators in their E-plane is -11.4 dB and in the H-plane -15.5 dB. At spacing $s = 1\lambda_0$ the transmission coefficient decreases to -17.8 dB for E-plane and -28.0 dB for the H-plane.

Since the introduction of DRAs as array elements, plethora of papers devoted to research and development of DRA arrays has been published, for references see section 1.4.

4.2 Mutual Coupling Between Rectangular Resonators Operating with TE_{113} and TE_{115} Mode

The directive radiation patterns of these modes were described by Petosa et al. in [57, 58]. For design, the authors used materials with relative permittivity of $\epsilon_r \approx 10$ and obtained broadside radiation patterns at 11 GHz with maximum gains 8.2 and 10.2 dBi with excitation of TE_{113} and TE_{115} , respectively. In this section, we analyze the mutual coupling between two identical resonators operating either with TE_{113} or TE_{115} mode. The outcomes of the analysis are supposed to give general guidelines for antenna array design, as we believe these elements are very promising in antenna array applications.

In [58], two peaks can be observed in the reflection coefficient frequency response in the frequency band of interest (resonances of two DRA modes), we optimize

the feeding and the resonator size, in order for only one resonance (of the desired mode) to occur around the frequency of interest. The nearby slot resonance (or another mode resonance) could influence the coupling factor value and it would be impossible to separate the coupling through analyzed DR mode and the coupling through another mechanism.

In the analysis of mutual coupling, we first design isolated elements operating with TE_{113} and TE_{115} modes. The simulation model is in this phase as simple as possible – resonator is placed on top of an infinite PEC ground plane and fed by a discrete port (Fig. 4.1). In order to get little closer to the manufacturable model without any substantial increase of model complexity, a layer of 1.524 mm thick Arlon 25N substrate with $\epsilon_r = 3.38$ is placed below the conducting ground plane. Moreover, the dielectric losses of all dielectrics are included in the material models. By this approach we can mitigate almost all the issues connected with the feeding network and we can use one symmetry plane in the model.

The geometry of the antenna can be seen in Fig 4.3 showing a single DR with a square footprint on top of a square ground plane. The internal magnetic fields (H_y field component) of TE_{113} and TE_{115} in the cross-section of the resonator (xz plane) are given in Fig. 4.4.

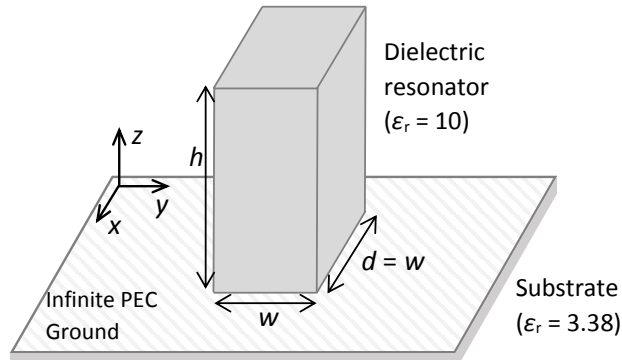


Fig. 4.3: Geometry of single DR element with square footprint.

4.2.1 Design and Performance of a Single TE_{113} and TE_{115} Mode Elements

Considering the design of DR operating with TE_{113} (and then TE_{115}) mode we use Arlon 1000 ($\epsilon_r = 10$) as dielectric material for element design and fabrication. Due to the limitations of our fabrication process (i.e. layering conventional microwave substrates), the center frequency of the design is not selected beforehand, but is

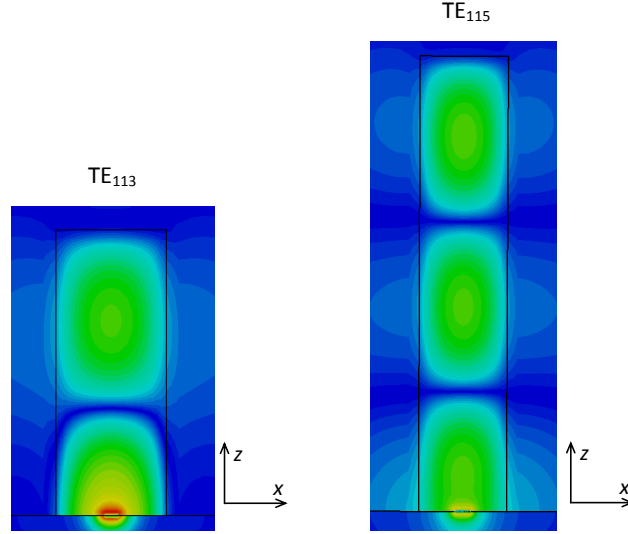


Fig. 4.4: H_y magnetic field component in the cross-section of the resonator.

arrived at in the design process. In case of the resonator design with $\epsilon_r = 10$, we fix the footprint size of the DR to be 6.35 mm x 6.35 mm (i.e. two layers of Arlon 1000 substrate) and optimize its height h in order to obtain maximum gain at resonant frequency as predicted by magnetic wall method. With this method, we obtain a set of several h values associated with their resonant frequencies. The analysis of coupling is performed only for the aspect ratio of the DRA element that provide the maximum gain. Aspect ratios are thus very similar to designs presented in [58]. We can further increase the impedance bandwidth of these antennas by using even lower dielectric constant material; however, the enhanced gain bandwidth is in this case more critical than the impedance bandwidth.

Since the discrete ports are used in the initial stage of our analysis, we must determine the input impedances in order to match the input ports accordingly. In first step, we excite the structure with 1 V signal at the input terminals and obtain its input impedance. Afterwards, we set this value for the port impedance so that we can calculate scattering parameters. The dimensions of the TE_{113} resonator that provide maximum gain (8.7 dBi) at 9.5 GHz are $w = 6.35$ mm, $d = 6.35$ mm and $h = 15.6$ mm and if the aperture length is $l_a = 6$ mm and its width is $w_a = 1.2$ mm, then the input port impedance is $(62 - j11.7)\Omega$. The situation is little different for TE_{115} resonator, where the maximum gain (10.3 dBi) occurs at 9 GHz with dimensions $w = 6.35$ mm, $d = 6.35$ mm and $h = 33$ mm and the aperture size $l_a = 6.3$ mm, $w_a = 1.26$ mm. In this case the input impedance is $(76.5 + j4.5)\Omega$.

The full-wave simulation results reveal (Fig. 4.6 and 4.8), as mentioned before, that the impedance bandwidth is not critical, if we use dielectric material with relative permittivity of 10 for fabrication. Furthermore, parasitic resonances in cases

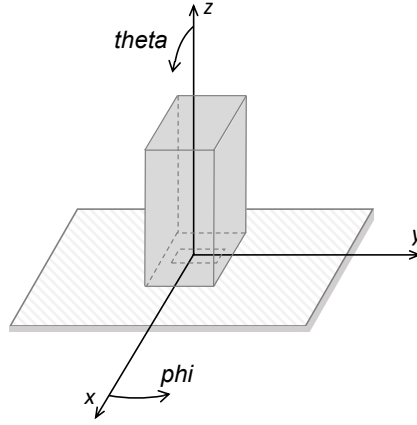


Fig. 4.5: Antenna orientation in spherical coordinate system.

of both modes can significantly broaden the impedance bandwidth. On the other hand, neither parasitic resonances nor lower permittivity material can broaden the enhanced gain frequency region, so the broadening the bandwidth does not make sense from the design point of view. Figure 4.6 also shows that the resonance frequency and frequency of the gain maximum of TE_{113} are not identical and the gain maximum is shifted to a little higher frequency. Such behavior is in agreement with published results of Petosa et al. [58]. It is interesting, that even a brute force optimization could not find dimensions (of the resonator and the slot) that would make resonant frequency and the frequency of the maximum gain coincide.

With TE_{113} mode, we are not able to avoid the higher resonance (TE_{115}) without sacrificing any of the advantages. However; we can assume that coupling through this mode can be neglected in analyzing coupling between antennas operating with TE_{113} mode. The frequency of interest (i.e. the resonant frequency of the resonators) is 9.23 GHz in case of TE_{113} mode and precisely 9 GHz in TE_{115} mode.

The magnetic and electric fields of the modes are visualized in Fig. 4.4. Results of single element reflection coefficient and frequency response of realized gain of both modes are on Fig. 4.6 and Fig 4.8 and finally, Fig. 4.7 and Fig. 4.9 present radiation patterns in principal planes. The antenna orientation in spherical coordinate system is given in Fig. 4.5.

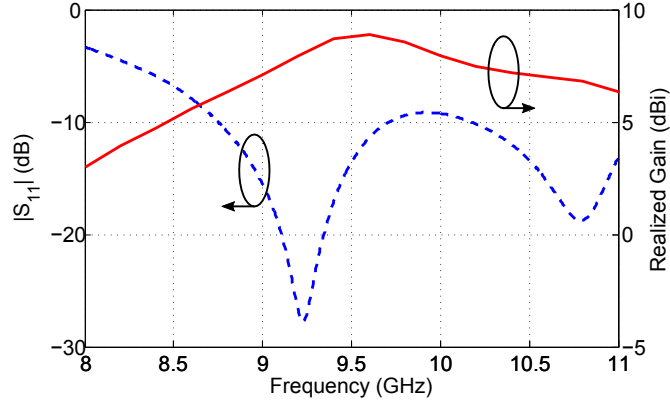


Fig. 4.6: Reflection coefficient and realized gain as function of frequency for resonator with TE_{113} mode. The TE_{113} mode resonance frequency occurs at 9.2 GHz. Realized gain at the resonance is 8.4 dBi. The gain maximum does not coincide with the resonance.

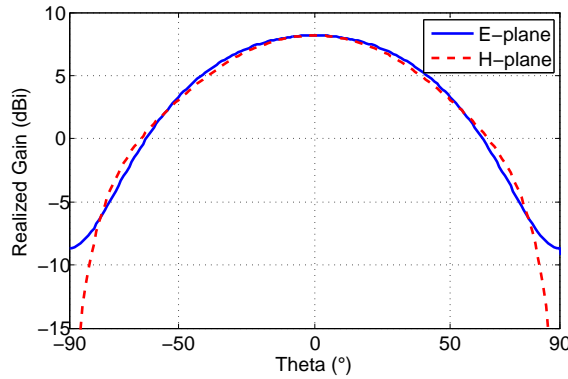


Fig. 4.7: Realized gain radiation patterns in E- and H- plane of the TE_{113} mode as obtained above infinite PEC ground plane at frequency 9.2 GHz.

4.2.2 Coupling Between the Resonators in TE_{113} Mode

The E-plane and H-plane arrangements of the resonators as given in Fig. 4.1 and Fig. 4.2 are used to determine the coupling level in between the two identical resonators operating with TE_{113} mode. However, small amount of coupling might be present in case of discrete port feeding due to surface waves in Arlon 25N substrate. We first evaluate this coupling mechanism for different inter slot distances in suitable numerical model (see Fig 4.10) in which the top half space of the model is filled with material with $\epsilon_r = 10$, and apertures are separated by PEC wall in the top half space, so that no coupling through this region is possible and at the same time, the effective permittivity around the slot stays approximately unchanged. The only coupling mechanism left is then the above mentioned surface wave trapped in the substrate with $h = 1.524$ mm and $\epsilon_r = 3.38$. Then, we sweep the distance between

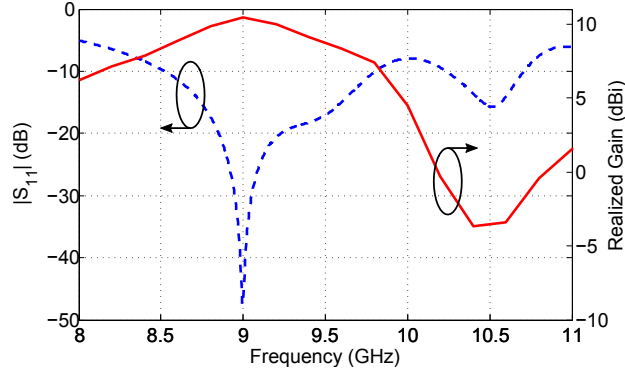


Fig. 4.8: Reflection coefficient and realized gain as function of frequency for resonator with TE_{115} mode. The TE_{115} mode resonance occurs at 9.0 GHz. Realized gain at the resonance is 10.4 dBi.

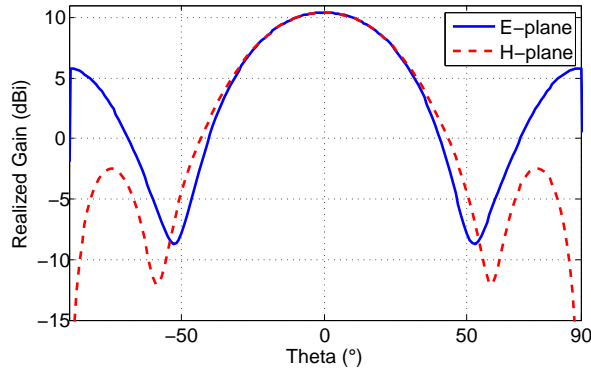


Fig. 4.9: Realized gain radiation patterns in E- and H- plane of the TE_{115} mode as obtained above infinite PEC ground plane. Side lobe levels in both planes are considerably higher than in the case of TE_{113} mode.

the slots and observe the values of the transmission coefficient. This coupling mechanism will occur if we feed the slots by microstrip lines or coplanar waveguides. Even in the case of series-fed array by a waveguide (SIW) we can anticipate similar coupling values. On the other hand, by using parallel SIW feeding we can significantly eliminate transmission between apertures through the common substrate layer.

Since the parameter s (inter-slot separation distance) is defined as the distance between the center points of the slots and not from their edges the values for parametric sweep are selected as follows. In the E-plane s ranges from $s = 2$ mm up to $s = 22$ mm and in the H-plane $s = 7$ to $s = 22$ mm. The numerical analysis is conducted on a model as described in above written paragraph with slots dimensions $l_a = 6$ mm and $w_a = 1$ mm and at the frequency 9 GHz. For small inter-slot separation distances, where the slots are very close to the PEC separation wall, the input impedance of the slots is slightly changed, thus input matching from the dis-

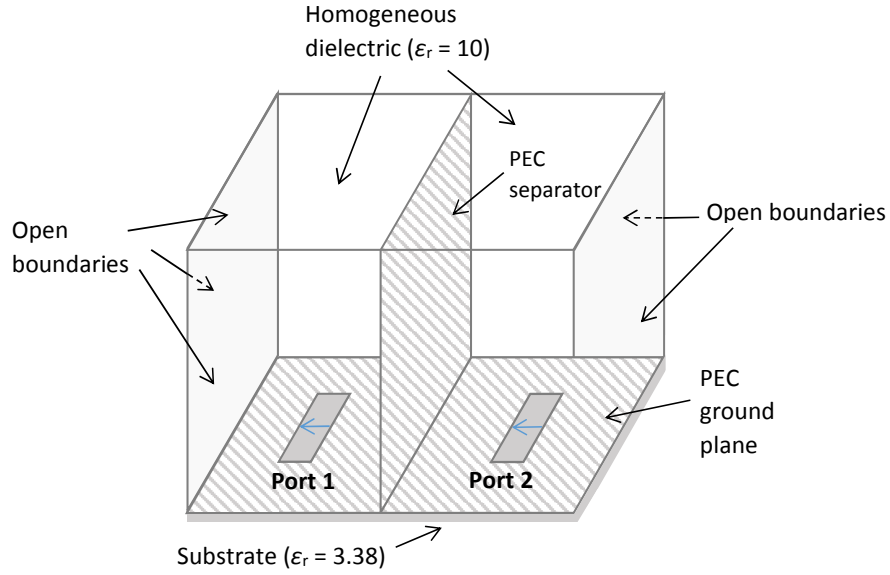


Fig. 4.10: Model for coupling evaluation due to substrate surface waves. The apertures in the upper half-space are separated by infinite PEC wall.

crete port to the slot is altered. However, in simulations the input port impedance is fixed to the constant value of 65.7Ω . Even though we manage to evaluate the coupling between apertures through the substrate layer and prove it to be negligible (Fig. 4.11), the direct aperture coupling above the ground plane still remains a part of the simulation results.

We proceed to simulations of two resonators as designed in section 4.2.1, the footprint of the resonators is of size $w \times w = 6.35 \text{ mm} \times 6.35 \text{ mm}$. Therefore, the minimum spacing s is selected to be $s = 6.5 \text{ mm}$ in the E-plane as well as in the H-plane. The spacing is varied from $s = 6.5 \text{ mm}$ up to 50 mm , what corresponds to electrical lengths $0.2\lambda_0 - 1.55\lambda_0$ at the 9.2 GHz resonant frequency. The input impedances of the ports are now matched to the input impedances of the resonators (only the real parts), i.e. 65.7Ω is set as the discrete port impedance. However, this is valid only for larger spacing values, since for small distances, the input impedance of the resonators is noticeably changed from the value of isolated element due to the mutual coupling. Real and imaginary part of the input port impedance as function of the inter element distance is thus shown in Fig. 4.12. On the other hand, the magnitude of the transmission coefficient between the resonators S_{21} as a function of s is shown in Fig. 4.13. Frequency responses of the input port impedance, transmission coefficient and reflection coefficient for two selected values of inter-element spacing s are given in Fig. 4.14. We select two values $s = 0.5\lambda_0$ and $s = 1\lambda_0$.

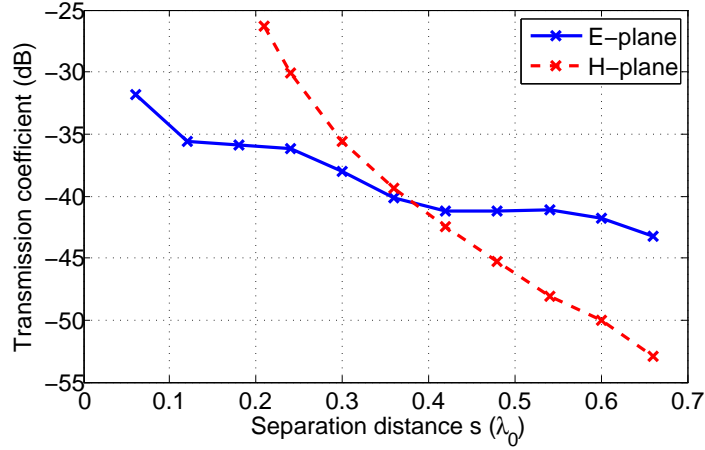


Fig. 4.11: Transmission coefficient between the apertures caused by transmission through underlying substrate layer (see Fig. 4.1 and Fig 3) at frequency 9 GHz. The apertures above the substrate are separated by PEC wall and the space above the ground plane is homogeneously filled with $\varepsilon_r = 10$ material, hence no transmission occurs in the region above the ground plane, where the coupling between the dielectric resonators is to be analyzed.

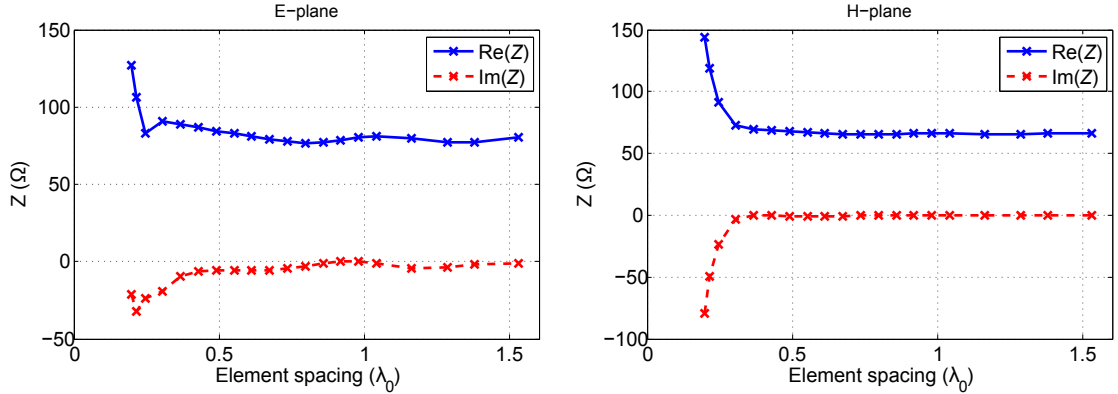


Fig. 4.12: Input impedance of a resonator for resonators arranged in the E-plane (left) and in the H-plane (right).

4.2.3 Coupling Between the Resonators in TE_{115} Mode

The same simulation approach as deployed in the previous section is used here to evaluate the coupling levels between two identical resonators operating in TE_{115} mode. The input port impedances are set to constant value 80Ω . Transmission coefficient in both principal planes as functions of inter element spacing s are given in Fig. 4.15. Moreover, real and imaginary parts of input impedance are given in Fig. 4.16. For two values of separation distance $s = 0.5\lambda_0$ and $s = 1\lambda_0$ the transmission, reflection coefficient and input impedance are given as a function of

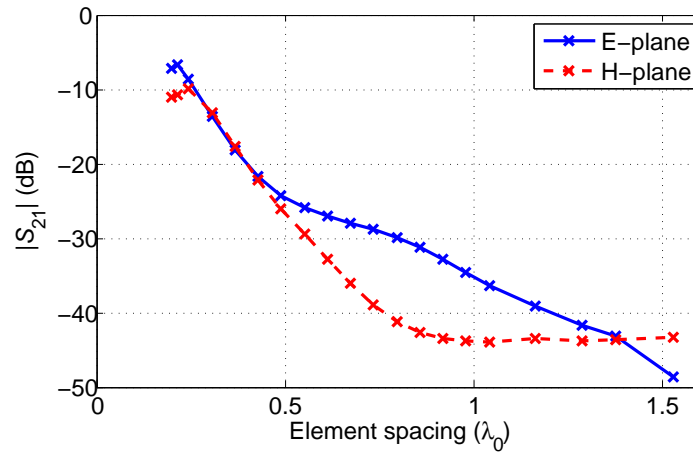


Fig. 4.13: Transmission coefficient as a function of element spacing in both principal planes for TE_{113} mode ($f = 9.2$ GHz).

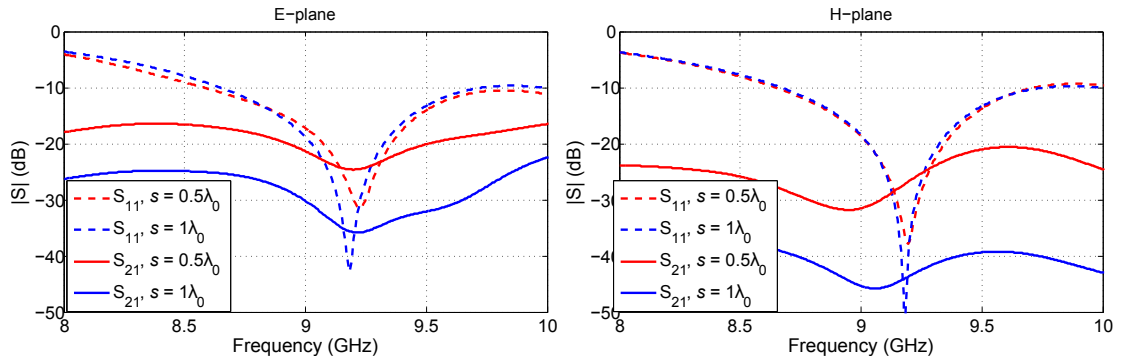


Fig. 4.14: Reflection and transmission coefficient for two spacings $s = 0.5\lambda_0$ and $s = 1\lambda_0$ in both principal planes.

frequency (see Fig. 4.17). The presence of larger side lobes in radiation patterns in H and E plane – assuming stronger coupling, as well we can assume stronger E plane coupling. Coupling reduction capability of this mode is thus not that efficient as with TE_{113} mode.

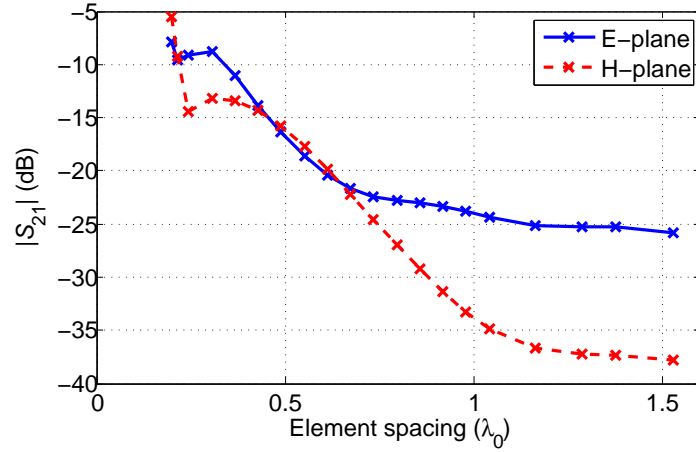


Fig. 4.15: Transmission coefficient as a function of element spacing in both principal planes for TE_{115} mode ($f = 9$ GHz).

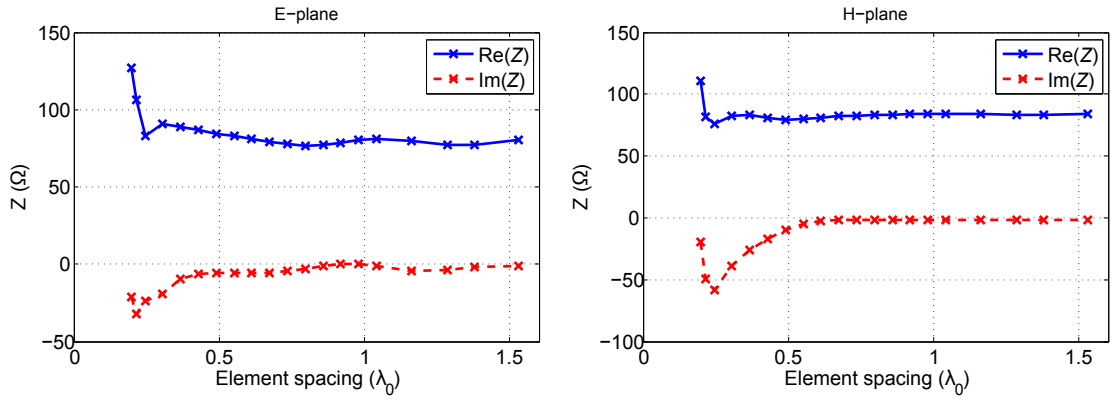


Fig. 4.16: Input impedance of a resonator for resonators arranged in the E-plane (left) and in the H-plane (right) for TE_{115} mode.

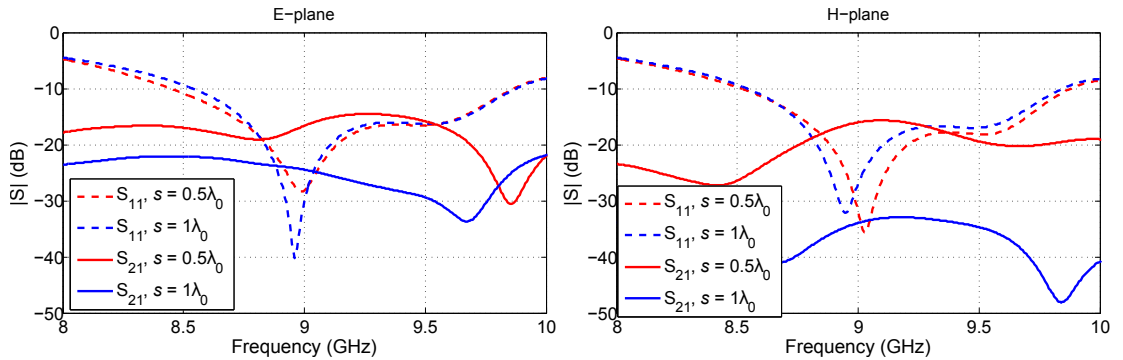


Fig. 4.17: Frequency response of reflection and transmission coefficient magnitude in the E-plane (left) and in the H-plane (right) of the resonators for two values of inter-element spacing, i.e. $s = \lambda_0/2$ and $s = \lambda_0$.

4.2.4 Designs for Experimental Verification

Although feeding the resonators by theoretical discrete ports provides quick insight into the mutual coupling and is very easy to implement in simulations, in order to validate the full-wave simulation results by measurements, we have to modify the model so that it corresponds to some manufacturable structure. This means, that it is necessary to substitute the discrete port feeding of the apertures by real transmission lines. We select microstrip lines for feeding the apertures, since they are very simple to implement in hardware. Therefore, direct coupling between the feeds is evaluated before performing the actual coupling analysis between the resonators. -using discrete ports we are able to explore coupling for very densely arranged resonators – in case of feeding network, the minimum spacing must conform to constraints (stub length in case of microstrip line etc.)

Each of the resonators has its own feeding line, so that we have two parallel-fed elements aligned either in their H-planes or their E-planes (see Fig. 4.18 and Fig. 4.19). Minimum possible spacing between the resonators arranged in E-plane is 12 mm and 10 mm in case of the H-plane arrangement.

In order to cut down the costs of the prototypes, we have fabricated only one feeds for TE_{113} and TE_{115} mode resonators, despite the fact, that each resonator requires slightly different feed dimensions to perform optimally. The aperture and the stub sizes are chosen as good compromise for impedance matching for both resonators. The aperture length is $l_a = 6$ mm and the stub length is $l_s = 5.4$ mm.

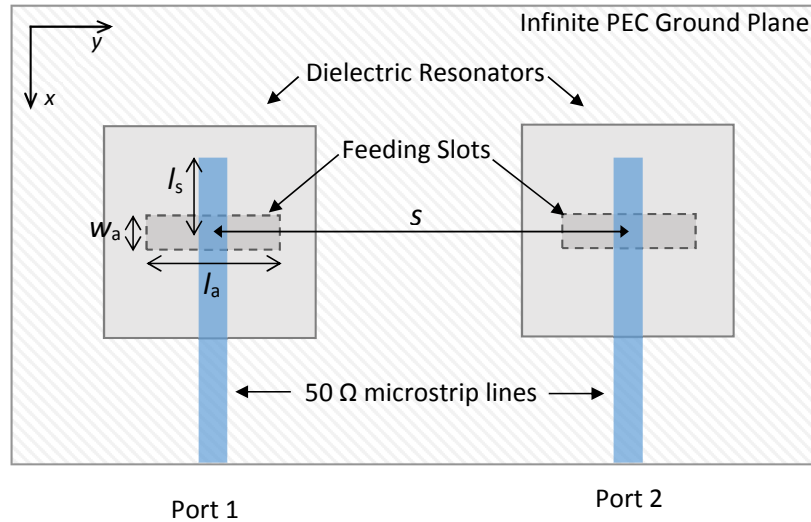


Fig. 4.18: Geometrical arrangement of microstrip line fed resonators for H-plane coupling analysis. The dimensions of the feeds and resonators are identical.

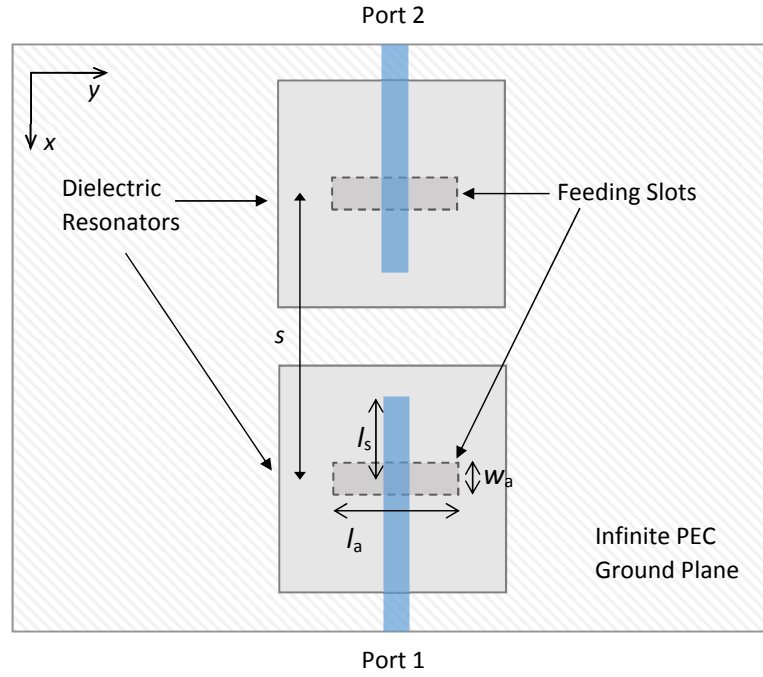


Fig. 4.19: Geometrical arrangement of microstrip line fed resonators for E-plane coupling analysis. The dimensions of the feeds and resonators are identical.

4.2.5 Experimental Verification

For experimental validation, the numerical models according to the Fig.4.18 and Fig.4.19 are simulated and transmission and reflection coefficients are determined for inter-element separation $s = 0.25\lambda_0$ to $s = 1\lambda_0$. However, to reduce the cost of the manufactured prototypes (for each distance s we need a separate PCB with feeding network) we measure the s-parameters only for two separation distances, i.e. $s \approx 0.5\lambda_0$ and $s \approx 1\lambda_0$. As expected the simulation results correspond to the characteristics given in Fig. 4.12 to Fig. 4.17, therefore we do not include them again.

The resonators operating with TE_{113} and TE_{115} modes are both build from two layers of Arlon 1000 substrate ($\epsilon_r = 10$, $\tan\delta=0.003$) and glued together. Ideally, the footprint size is supposed to be $d \times w = 6.35 \text{ mm} \times 6.35 \text{ mm}$ (as in the simulations); however, due to manufacturing tolerances and finite thickness of the glue, the final size of the manufactured resonators is approximately $d \times w = 6.4 \text{ mm} \times 6.8 \text{ mm}$. The size increase combined with relative permittivity tolerances of Arlon 1000 (ϵ_r is slightly higher - see section 5.3) result in frequency down-shift in all the resonators. In case of TE_{113} mode, the measured resonant frequency is approximately 8.85 GHz (9.18 GHz simulated) corresponding to relative shift of 3.7 %. In antennas operating with TE_{115} mode the frequency shift is little larger with 8.57 GHz measured and

9 GHz simulated resonant frequency, thus resulting in relative shift of about 4.9 %.

The measured scattering parameters can be found in Fig. 4.20 for TE_{113} mode and in Fig. 4.21 for TE_{115} mode. The measurement proved reduced coupling in both modes compared to fundamental TE_{111} mode. As simulations suggested, the coupling reduction is higher in TE_{113} mode.

Unfortunately, due to error during preparation of the models for fabrication, the inter-element separation distances s of manufactured antennas are 19.75 mm and 39.5 mm for antennas operating with both modes. These values do not correspond precisely to $0.5\lambda_0$ and $1\lambda_0$ as we have intended but rather to $0.58\lambda_0$ and $1.16\lambda_0$ for TE_{113} mode and to $0.56\lambda_0$ and $1.13\lambda_0$ for TE_{115} mode. Of course, this data is still relevant and we compare it to simulation results in section 4.4. The photographs of the antennas operating with both modes can be seen in Fig. 4.22.

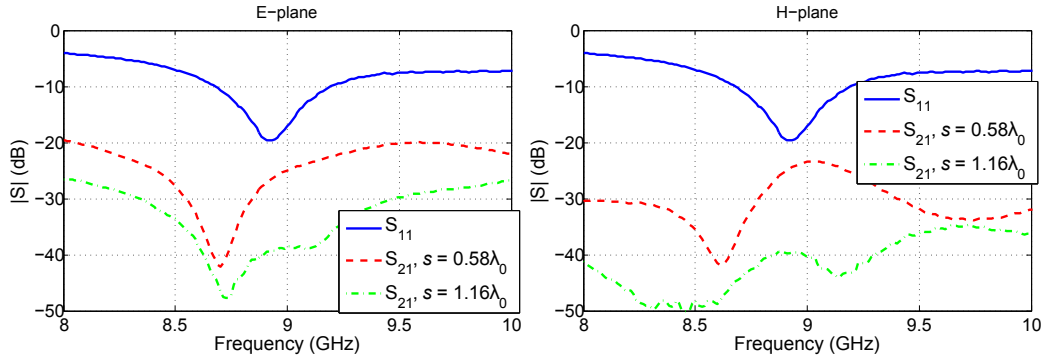


Fig. 4.20: Frequency response of reflection and transmission coefficient magnitude in the E-plane (left) and in the H-plane (right) of the resonators operating with TE_{113} mode for two values of inter-element spacing, i.e. $s = 0.58\lambda_0$ and $s = 1.16\lambda_0$.

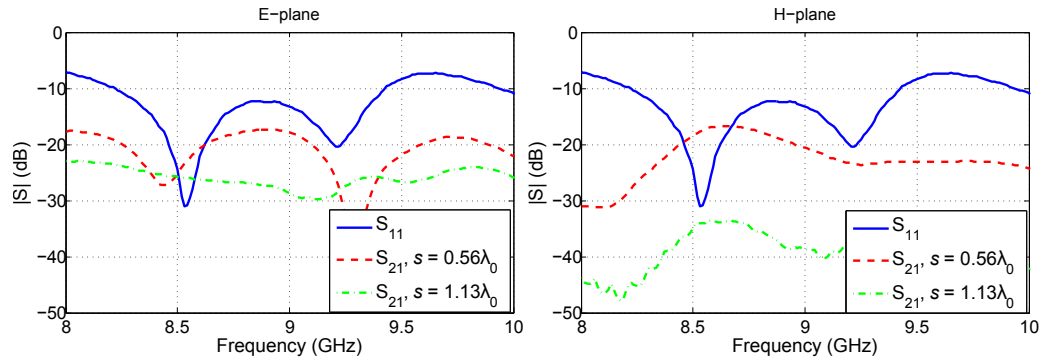


Fig. 4.21: Frequency response of reflection and transmission coefficient magnitude in the E-plane (left) and in the H-plane (right) of the resonators operating with TE_{115} mode for two values of inter-element spacing, i.e. $s = 0.56\lambda_0$ and $s = 1.13\lambda_0$.

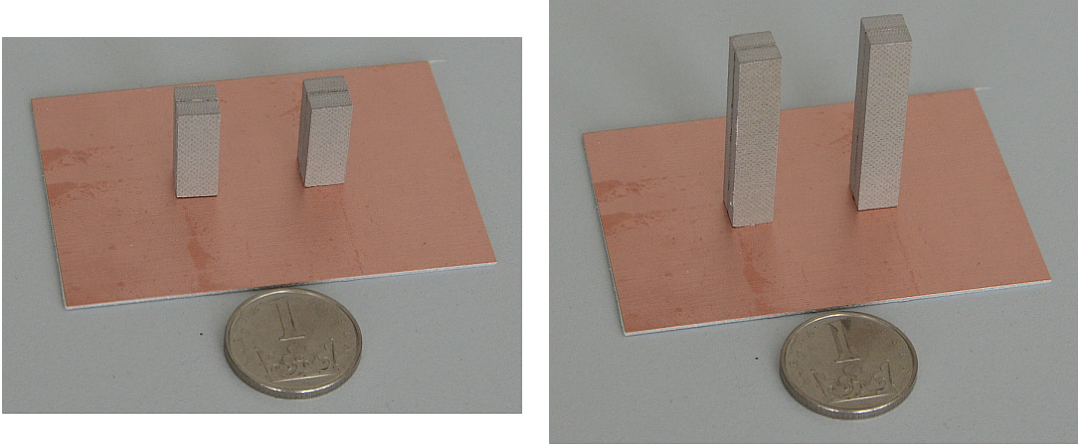


Fig. 4.22: Fabricated antennas operating with TE_{113} mode (left) and TE_{115} mode (right). The spacing between the antennas is in both cases $0.5\lambda_0$. The ground planes are identical.

4.3 Mutual Coupling Between Rectangular Resonators Operating with TE_{133} Mode

Finally, we evaluate mutual coupling between the resonators described in chapter 3. We use modified resonators with rectangular footprint. In section 3.1.5 it was shown, that in a resonator with square footprint, multiple modes can exist close to each other in spectrum, thus slightly expanding the bandwidth of the antenna. However, if coupling level is to be determined, we should avoid any undesirable radiation mechanism to be present in the resonator, in case it is not vital to the antenna operation principle. For this reason, we modify the shape of the resonator to be of rectangular footprint and we reduce that side of the resonator in which δ halfwave-cycles are expected, as the resonator parameters should be least sensitive in this dimension. Therefore, by reducing the size in this dimension, we can expect slight up-shift of the resonant frequency of the target TE_{133} mode. This design step results in the antenna impedance bandwidth reduction as well as in slight gain reduction. However, we can be sure that the dominant coupling mechanism between the resonators is that due of the desired mode.

The resonators are designed from material with relative permittivity $\epsilon_r = 6.15$ (Arlon 600) using magnetic wall model and subsequent optimization. The performance of the resonator is tuned approximately for 9.3 GHz resonant frequency. The electric size of the footprint of the resonator (see Fig. 4.23) is substantially larger as compared to the previously described resonators due to lower relative permittivity of the material used for resonator design as well as due to higher mode indices of our TE_{133} mode (in x -direction). The values for inter-element separation distances s

must be selected so that the two resonators do not overlap in space and also should not touch each other. The visualization of magnetic field component H_y in xz plane is given in Fig. 4.24

Due to the large sidelobe levels in the E-plane of the radiation pattern of TE_{133} mode DRA, we can assume much stronger coupling in this plane compared to the H-plane. The E-plane coupling can be even stronger than in the case of the fundamental broadside-radiating mode rectangular DRA due to the larger size of the TE_{133} resonators in the E-plane as well as due to increased directivity in the E-plane for directions $theta = 90^\circ$.

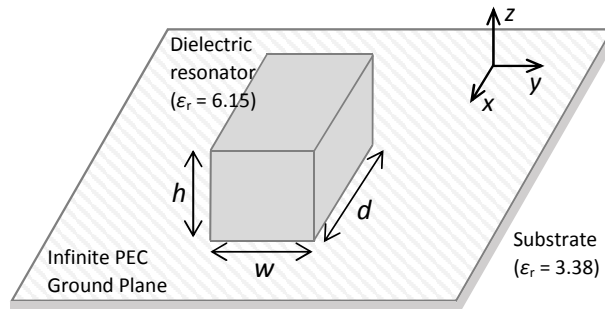


Fig. 4.23: Geometry of a TE_{133} mode DRA with a rectangular footprint. The resonator is aligned in spherical coordinate system according to the Fig. 4.5.

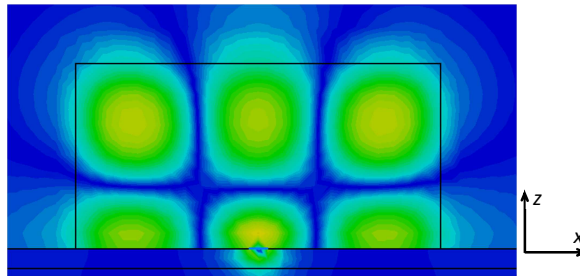


Fig. 4.24: Distribution of H_y field component in the cross-sectional view (plane xz).

4.3.1 Single Element Characteristics

To obtain single element isolated characteristics, the ground plane was extended to infinity and approximated by PEC. Such step modified the radiation characteristics predominantly in the E-plane and significantly increased the sidelobe levels (SLL). By using finite ground plane and small air gap between the resonator and the ground plane it is possible to considerably reduce the SLL. However, the finite ground plane would not affect the mutual coupling due to these extensive sidelobes ($\theta = -90^\circ$ and $\theta = 90^\circ$ in Fig. 4.26).

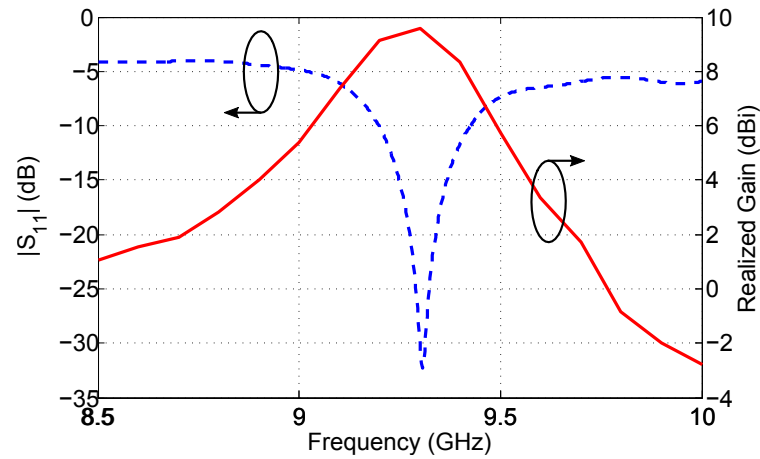


Fig. 4.25: Reflection coefficient and realized gain as functions of frequency for resonator with TE_{133} mode. The TE_{133} mode resonance occurs at 9.3 GHz.

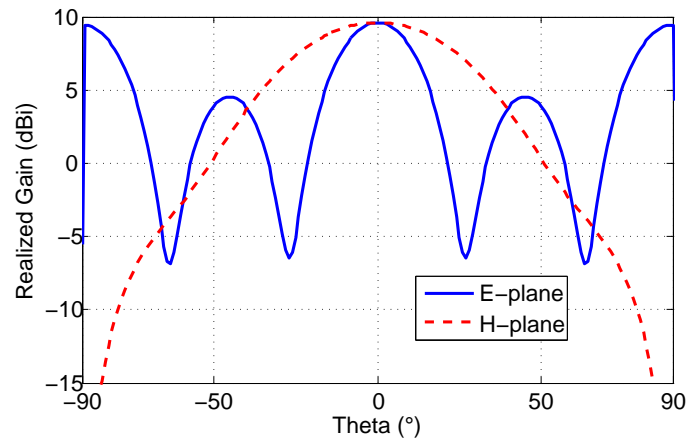


Fig. 4.26: Radiation patterns in the E- and H- plane of the TE_{133} mode as obtained above infinite PEC ground plane. Large SLL in the E-plane can be seen.

4.3.2 Coupling Between the Resonators in TE_{133} Mode

Once the single element model is prepared and its characteristics evaluated, two resonators operating with TE_{133} mode are aligned in their E- and H-planes according to the Fig. 4.1 and Fig. 4.2 and fed by discrete ports with input port impedance of 50Ω . Transmission coefficient is evaluated for inter-element separation distances $s = 0.4\lambda_0$ to $1.55\lambda_0$ in the H-plane and $s = 0.87\lambda_0$ to $s = 1.55\lambda_0$ in the E-plane. The reason why the separation distance in the E-plane does not start with a smaller value is caused by physical dimensions of the resonators, as it is impossible to achieve smaller s than about $s = 0.84\lambda_0$, at this value there is a connection between the walls of the resonators.

The large value of mutual coupling (i.e. -7.7 dB) in the E-plane at separation distance $1\lambda_0$ (Fig. 4.28) and the size restrictions suggest, the elements operating in TE_{133} mode are simply not suitable for arraying along their E-plane. Other techniques (e.g. finite ground plane, EBG structures for ground plane etc.) might be used to limit the sidelobe levels and increase the directivity in this plane. On the other hand, the dimensions and mutual coupling performance in the H-plane (Fig. 4.27 and Fig. 4.28) prove the possibility to use these elements for H-plane linear arrays.

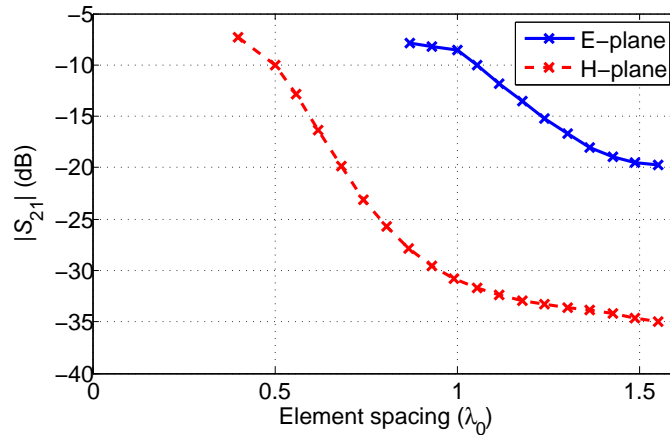


Fig. 4.27: Transmission coefficient as a function of element spacing in both principal planes for TE_{133} mode at 9.3 GHz.

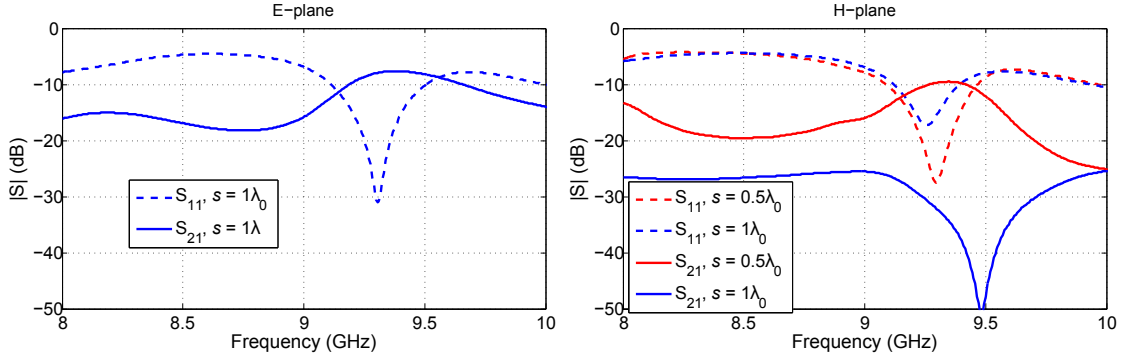


Fig. 4.28: Frequency response of reflection and transmission coefficient magnitude in the E-plane (left) and in the H-plane (right) of the resonators for two values of spacing, i.e. $s = \lambda_0/2$ and $s = \lambda_0$. The E-plane includes only the curves for $s = \lambda_0$.

4.3.3 Design for Experimental Verification

The same approach as described in the section 4.2.4 is utilized here to extend the model of aperture coupled DR antenna with microstrip line. In order to evaluate the mutual coupling, the resonators are aligned in their E and H planes according to the Fig. 4.18 and 4.19.

In this case, we also simulate the individual layers of substrate Arlon 600 with interleaved layers of glue with lower relative permittivity. It turns out that the inhomogeneous composition of the resonators has quite substantial influence on the reflection and transmission characteristics. Considering H-plane, with spacing $s = 0.5\lambda_0$, the transmission coefficient in resonance is decreased from -10 dB to -14 dB and for $s = 1\lambda_0$, $|S_{21}| = -34$ dB instead of -31 dB. In the E-plane, with spacing $s = 1\lambda_0$, $|S_{21}|$ is decreased to -8.5 dB from -8 dB.

4.3.4 Experimental Verification

In field simulations without the interleaved glue layers present, the resonant frequency is approximately 9.3 GHz; however, measured value is little higher 9.5 GHz. Lower relative permittivity and the air gaps between the layers of the resonator (9 layers in total for each resonator) cause the effective permittivity of the resonator to be somewhat lower than expected 6.15 of Arlon 600. As a result, the resonant frequency slightly rise. This frequency change correspond to relative frequency shift of 2.1 %. The photographs of the antennas operating with both modes can be seen in Fig. 4.30.

In summarizing table (see 4.3), we compare measured values and values simulated for bulk homogenous resonators, not the layered ones which results are much closer to the measured values.

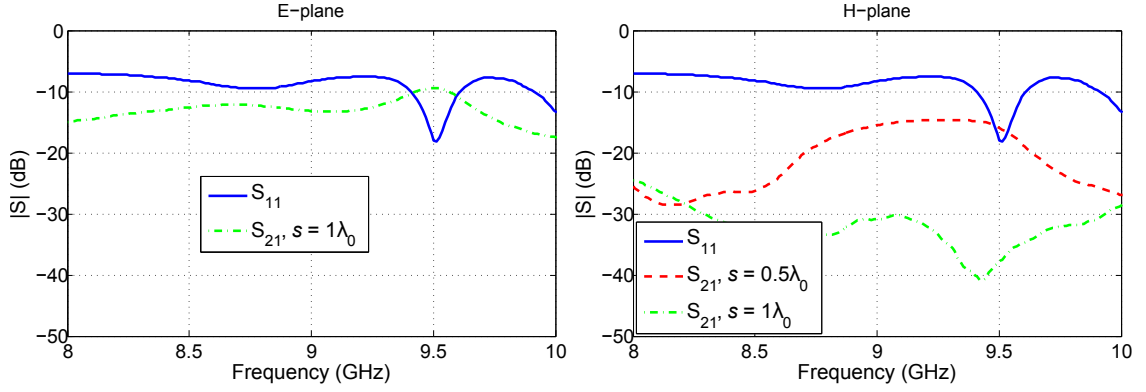


Fig. 4.29: Frequency response of reflection and transmission coefficient magnitude in the E-plane (left) and in the H-plane (right) of the resonators operating with TE_{133} mode for two values of inter-element spacing, i.e. $s = 0.5\lambda_0$ and $s = 1\lambda_0$.

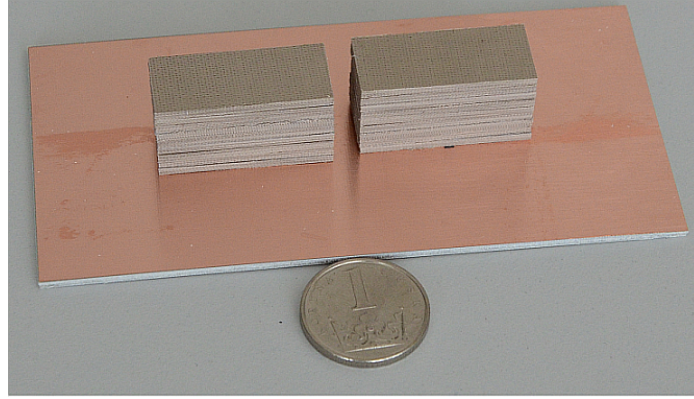


Fig. 4.30: Fabricated antennas operating with TE_{133} mode with separation distance $1\lambda_0$, aligned in the E-plane.

4.4 Summary

In our analysis, dielectric resonators operating with higher-order modes TE_{113} and TE_{115} turn out to be suitable elements for antenna array applications. According to simulations and measurements, both modes TE_{113} and TE_{115} are capable of decreasing the mutual coupling between the dielectric resonators in the E-plane as well as in the H-plane. The excitation of HO mode can thus be considered as a mutual coupling reduction technique. The obvious advantage is that there is no need for additional elements between or in the vicinity of the antennas [72]. The most important results are summed up in tables 4.1 and 4.2.

Due to considerably larger size of the TE_{133} mode resonators (larger footprint) and due to the large sidelobes in the E-plane, the coupling is stronger in this plane than in case of the fundamental TE_{111} mode. In the H-plane, the values are very

similar to the fundamental mode DRA. For this reason, TE_{133} is not suitable for coupling reduction; however, it can still be used for one dimensional H-plane antenna arrays design with very similar amounts of coupling among the elements as in case of TE_{111} mode antennas. The simulation and measurement results together with comparison with TE_{111} mode are given in table 4.3.

Tab. 4.1: Results of measurement and simulation of transmission coefficient between two resonators operating with HO modes, i.e. TE_{113} .

	$ S_{21} [-]$							
Plane	E-plane				H-plane			
$s [\lambda_0]$	0.58		1.16		0.58		1.16	
Meas./Sim.	M	S	M	S	M	S	M	S
TE_{113}	-27.3	-26.5	-39.4	-39.14	-27.4	-30	-41	-43.4

Tab. 4.2: Results of measurement and simulation of transmission coefficient between two resonators operating with HO modes, i.e. TE_{115} .

	$ S_{21} [-]$							
Plane	E-plane				H-plane			
$s [\lambda_0]$	0.56		1.12		0.56		1.12	
Meas./Sim.	M	S	M	S	M	S	M	S
TE_{115}	-21.4	-19.0	-26.0	-24.9	-17.7	-18.2	-34.1	-35.5

Tab. 4.3: Results of measurement and simulation of transmission coefficient between two resonators operating with HO modes, i.e. TE_{133} .

	$ S_{21} [-]$							
Plane	E-plane				H-plane			
$s [\lambda_0]$	0.5		1		0.5		1	
Meas./Sim.	M	S	M	S	M	S	M	S
TE_{133}	-	-	-9.4	-8	-15.9	-10	-35.7	-31
TE_{111} ¹	-13.3	-12.9	-19.1	-19.2	-	-	-	-

¹See section 5.3 for more details on this reference antenna operating with TE_{111} mode

Chapter 5

Perforated Dielectrics

As indicated in chapter 1, one of the main reasons why DRAs are not more widely used in the design of (sub-)mm wave antennas and arrays is the complexity of fabrication and mechanical adjustment of individual elements on the correct positions. Perforated dielectric structures can deal with this problem. However, in this as well as in other applications reviewed in section 1.5, the problem of effective relative permittivity calculation arise. In the open literature, the available formulas do not respect the anisotropic nature of perforated dielectric layers. The main focus of this chapter is therefore on the development of analytical model of perforated material capable to describe anisotropic properties for transverse electromagnetic waves as well as for surface waves propagating on perforated dielectric slabs.

The chapter is organized as follows. First, we deal with the theoretical model of perforated dielectric material, for this we use the effective medium concept and based on the quasi-static approach and the theory of anisotropic, more specifically uniaxial, media, we give formulas for polarization dependent effective permittivity of such dielectric mixtures. The uniaxiality of the material is proven by two independent numerical techniques, i.e. modal and time domain analysis. Here, we assume plane wave propagation in unbounded perforated dielectric material. Numerical verification of the applicability of the quasi-static formulas for microwave bands is done using TEM waveguide concept and time domain simulations. Description of several techniques for extraction of the effective relative permittivity is given; however we use the unit cell analysis as a reference solution.

Second, we deal with the surface wave excitation and propagation on perforated dielectric slabs and we determine effective relative permittivities for TE and TM modes (TE_0 and TM_0 modes) by solving modified dispersion equations based on data obtained from numerical unit cell analysis.

Last, we consider application of grounded perforated substrates to perforated dielectric resonator antennas. We evaluate the agreement between the actual per-

forated substrate and its homogenous equivalent. We analyze the performance of a perforated DRA operating with the broadside radiating mode of rectangular resonator (i.e. TE_{111}). We further focus on the radiation pattern alterations due to the perforated surrounding and on input impedance compared to isolated DRA element. The analysis is performed for various air filling factors. We can assume such structure to be more vulnerable to propagation of surface waves trapped in the perforated substrate due to substantial value of the effective relative permittivity compared to air. The surface waves can decrease the antenna efficiency, its gain and cause additional ripples on the radiation patterns. However, such analysis has not been described in the open literature yet. The isolated perforated DRA element is analyzed first on infinite perforated dielectric covered ground plane. And in the second case we take the edge effects into account by making the ground plane (and perforated substrate layer) finite. We again assume that the surface waves will increase the edge effects on the ripples of radiation patterns. Isolated element characteristics will be the first output of this chapter. The second important result will include the performance assessment of mutual coupling between two perforated DRA elements operating in fundamental broadside-radiating mode. Again, we can assume the surface waves to increase the level of mutual coupling between the resonators in both principal planes.

5.1 Perforated Dielectrics

From physical point of view, the perforated dielectric layers (substrates) are through-hole porous materials in which perforations (pores) operate in sub-wavelength regime in which it follows that the wavelength is much larger than the period of perforations (except of the EBG applications). Since the pores do not have to be filled with air, more general term “mixture” is sometimes used. The problem of porous media gained a lot of attention over the last decades in applied physics community with broad applications in material science, mechanical, civil, electrical and electronic engineering etc.

Porous materials are created by embedding pores (in our case through hole perforations) into a matrix medium (dielectric substrate in our case), thus forming a heterogeneous media of at least two constituents. The pores can have various shapes [118] and sizes including complex fractal shapes [119], [120] It follows that in certain cases the porous media can have anisotropic properties [121].

In porous media description, it is often desirable to determine the parameters of the homogenized material through the effective medium theory [122], [123]. The homogenized medium has the same macroscopic electromagnetic properties as the heterogeneous mixture of its constituents. Assuming a quasi-static approximation

in which the size (repetition period) of the pores is much larger (smaller) than the wavelength and by neglecting any scattering effects on the material discontinuities, the approximate effective media parameters can be analytically derived.

The problem of perforated dielectric layer to be solved is formulated in sections 5.1.2 together with the physical background and several theoretical models for estimation of effective relative permittivity of a two-phase mixture. The section 5.1.3 then gives an overview of mathematical description of anisotropic materials, what perforated dielectric layers undoubtedly are. Anisotropic nature of our structure is explained and the components of the effective relative permittivity tensor are derived for different electric field polarizations based on the quasi-static theoretical models. The main motivation is to find a polarization sensitive model of perforated dielectrics that gives better approximation than the simple model of volume averaging, currently utilized in antenna and propagation related topics that does not respect anisotropic properties of the perforated material.

5.1.1 Basic Nomenclature

Throughout the chapter, we consider time harmonic fields with $e^{-j\omega t}$ time variation. All the field quantities are thus phasors, which are functions of position \mathbf{r} only. For example, for instantaneous electric field intensity we can write:

$$\mathbf{E}(\mathbf{r}, t) = \Re \left\{ \mathbf{E}(\mathbf{r}) e^{-j\omega t} \right\}, \quad (5.1)$$

where ω [rad/s] is the angular frequency and $\mathbf{E}(\mathbf{r})$ is the electric field phasor and the same can be written for magnetic fields.

For uniform, plane waves propagating in a direction determined by a wave vector \mathbf{k} , the electric field $\mathbf{E}(\mathbf{r})$ is given as:

$$\mathbf{E}(\mathbf{r}) = \mathbf{E}(0) e^{-j\mathbf{k}\mathbf{r}}, \quad (5.2)$$

where $\mathbf{E}(0)$ is the electric field at a reference point. The wave vector magnitude is usually denoted as wavenumber and in general can be complex:

$$|\mathbf{k}| = k = \omega \sqrt{\tilde{\mu}\tilde{\varepsilon}}, \quad (5.3)$$

where $\tilde{\mu}$ and $\tilde{\varepsilon}$ are complex permeability and permittivity, respectively. In lossless case of nonmagnetic materials we can write:

$$k = \omega \sqrt{\mu_0 \varepsilon}, \quad (5.4)$$

where $\mu_0 = 4\pi \cdot 10^{-7}$ H/m is the permeability of vacuum and $\varepsilon = \varepsilon_0 \cdot \varepsilon_r$ is the permittivity of the lossless dielectric material with $\varepsilon_0 = 8.854 \cdot 10^{-12}$ F/m as permittivity

of vacuum and ε_r as relative permittivity. Since in general k is complex, it can be written as:

$$k = \beta - j\alpha, \quad (5.5)$$

In this form, the real part of the wavenumber β is called phase constant and the imaginary part α is the attenuation constant. In the literature, the form of k can be different due to slightly different form of eq. 5.2. In lossless case $\alpha = 0$, the wavenumber is real and identical to the phase constant $k = \beta$.

In transmission line theory, the propagation constant is again complex and given as $\gamma = \beta - j\alpha$, with β and α being phase and attenuation constant as given above. If the line is lossless $\alpha = 0$ the propagation constant is real and identical to the phase constant $\gamma = \beta$.

For lossless TEM transmission lines with no waveguide dispersion, the wavenumber and the propagation constant are identical $k = \gamma$. This is the case in section 5.1.5. For this reason we use terms propagation constant, phase constant and wavenumber interchangeably. However, this is not the case in section 5.2, where we deal with propagation of surface waves, since these waves are of TE/TM type, and the wavenumber and the propagation constant are different.

5.1.2 Porous Materials and the Theory of Homogenization

The theoretical foundation upon which the theory of porous dielectrics, in fact the theory of all dielectric mixtures, is based on the Lorenz internal field theory [122, 124], which describes the electric field inside a cavity (pore) embedded in a bulk dielectric material if external field \mathbf{E}_0 is applied. The external field \mathbf{E}_0 generates an average macroscopic field \mathbf{E} inside the bulk dielectric material, which includes the electric field \mathbf{E}_1 produced by the dielectric polarization \mathbf{P} due to the external field \mathbf{E}_0 and thus it follows $\mathbf{E} = \mathbf{E}_0 + \mathbf{E}_1$. The magnitude of \mathbf{E} is then given by:

$$|\mathbf{E}| = E = E_0 - \frac{P}{\varepsilon_0}, \quad (5.6)$$

since \mathbf{E}_1 has exactly the opposite direction as the field that generated it \mathbf{E}_0 .

The effect of the pores is introduced by a concept of local electric field \mathbf{E}_1 inside a cavity [125] that involves the depolarization field of a single scatterer \mathbf{E}_2 .

$$\mathbf{E}_1 = \mathbf{E} + \mathbf{E}_2 = \mathbf{E} + \frac{1}{\varepsilon} \overleftrightarrow{N} \cdot \mathbf{P}, \quad (5.7)$$

where ε is the permittivity of the background material, \overleftrightarrow{N} is the depolarization tensor (second order) that depends on the shape of a single pore. In suitably selected coordinate system \overleftrightarrow{N} becomes a diagonal matrix. The polarization per unit volume

\mathbf{P} depends on the dielectric properties, fractional volume and the polarizability of the constituents. It is given as

$$\mathbf{P} = n_0 \alpha_p \mathbf{E}_1, \quad (5.8)$$

where number of particles per unit volume is n_0 and the polarizability is denoted as α_p [121]. The polarizability is related to the permittivity by Clausius-Mossotti equation [125]. The total electric displacement field inside the material is

$$\mathbf{D} = \varepsilon \mathbf{E} + \mathbf{P}, \quad (5.9)$$

and finally, we define the effective permittivity of a heterogeneous material $\varepsilon_{\text{eff}} = \varepsilon_0 \varepsilon_{r,\text{eff}}$

$$\mathbf{D} = \varepsilon_{\text{eff}} \mathbf{E}. \quad (5.10)$$

The connection between the effective relative permittivity of the mixture $\varepsilon_{r,\text{eff}}$ and the polarizability is given by the Clausius-Mossotti equation, which under the assumptions of homogenous concentration of pores and identical polarizability of all pores inside the unit volume states:

$$\frac{\varepsilon_{r,\text{eff}} - 1}{\varepsilon_{r,\text{eff}} + 2} = \frac{n_0 \alpha_p}{3\varepsilon_0}. \quad (5.11)$$

Plethora of various mixing models to determine the effective permittivity of heterogenous mixtures has been published in the last decades, e.g. [121, 123, 126]; however, they are all (more or less) based on the famous Maxwell Garnett (MG) mixing rule [127, 128]. Our structure of parallel cylindrical perforations in the host dielectric is, from the viewpoint of MG rule, a two-dimensional structure. If we consider orientation of electric field perpendicular to the axis of perforations, the perforations create a two-dimensional grid of circular inclusions with depolarization factor $N = 1/2$ and the MG formula can be written as:

$$\varepsilon_{\text{eff}} = \varepsilon + 2f\varepsilon \frac{\varepsilon_i - \varepsilon}{\varepsilon_i + \varepsilon - f(\varepsilon_i - \varepsilon)}, \quad (5.12)$$

where ε_i is the permittivity of the inclusions, which in case of air perforations is $\varepsilon_i = \varepsilon_0$ and f denotes crucial parameter of the porous materials called *porosity* or simply a volume fraction. The porosity lies between 0 and 1 and is often given in percent.

Considering polarization parallel to the axis of perforations, the depolarization factor is $N = 0$ (there are actually no bounded pores in this case) and thus the effective permittivity [121] is determined:

$$\varepsilon_{\text{eff}} = f\varepsilon_i + (1 - f)\varepsilon. \quad (5.13)$$

Results of eq. 5.12 and eq. 5.13 are given in Fig. 5.1 for various values of porosity ranging between 0 % and 100 %. The largest difference can be observed if porosity is around 50 %.

Since N is zero in the case of field polarization parallel to the axis of perforations, this value of effective permittivity also represents the upper limit of the effective permittivity of the porous media. After some mathematical manipulation, it can be shown that this upper limit is actually a volumetric average of the permittivity of the matrix and inclusions (see eq. 5.32).

Our theoretical model of anisotropic perforated dielectric for TEM waves in unbounded space is therefore based on the equations 5.12 and 5.13 which were derived for the quasi-static approximation. In next sections, we verify applicability of this model for high frequency scenarios; however still in the sub-wavelength regime. In most of the simulations, we consider at least ten perforations per free-space wavelength. These values can then give good approximations of effective permittivity tensor for TE and TM waves propagating on perforated dielectric slabs. Since TE waves have only E field component perpendicular to the axis of perforations, we can assume that the effective permittivity should be given by eq. 5.12. On the other hand, as we show in section 5.2, TM waves have E-field component perpendicular as well as parallel to the axis of perforations and thus the effective permittivity should lie somewhere between the values given by eq. 5.12 and 5.13.

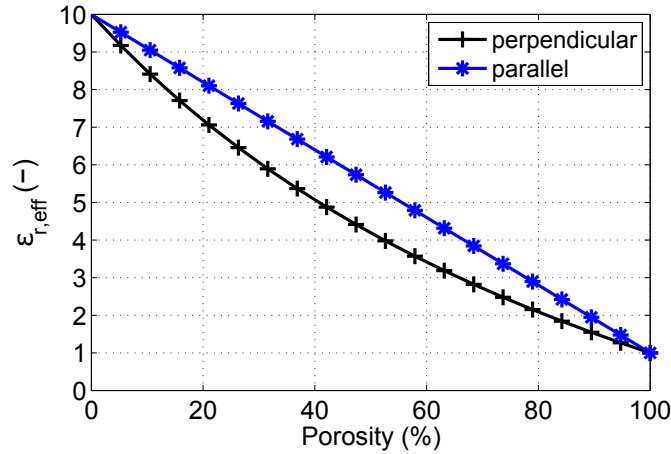


Fig. 5.1: Effective relative permittivity as a function of porosity based on Maxwell-Garnett mixing formula for E-field perpendicular and parallel to the axis of perforations.

5.1.3 Anisotropic Materials

In the previous section, it has been shown that the effective permittivity of the perforated dielectric slab depends on the \mathbf{E} field direction which makes the structure anisotropic (electrically anisotropic [129]). In anisotropic materials, the relation between \mathbf{E} and \mathbf{D} is no longer given by a scalar ε , but by a permittivity tensor $\overset{\leftrightarrow}{\varepsilon}$

$$\mathbf{D} = \overset{\leftrightarrow}{\varepsilon} \mathbf{E}, \quad (5.14)$$

that is, in Cartesian coordinates a 3 by 3 matrix relating all components of the fields together:

$$\begin{pmatrix} D_x \\ D_y \\ D_z \end{pmatrix} = \begin{pmatrix} \varepsilon_{11} & \varepsilon_{12} & \varepsilon_{13} \\ \varepsilon_{21} & \varepsilon_{22} & \varepsilon_{23} \\ \varepsilon_{31} & \varepsilon_{32} & \varepsilon_{33} \end{pmatrix} \times \begin{pmatrix} E_x \\ E_y \\ E_z \end{pmatrix} \quad (5.15)$$

In case of lossy dielectric, the elements correspond to complex permittivities and the permittivity tensor is Hermitian ($\varepsilon_{ij} = \varepsilon_{ji}^*$). In lossless case, the tensor becomes symmetric $\varepsilon_{ij} = \varepsilon_{ji}$ and thus for full characterization only 6 out of 9 components are necessary. Moreover, it implies that the tensor is diagonalizable by suitable selection of the coordinate system (i.e. rotation of the permittivity matrix) [130]. In this new coordinate system, the axes are called principal axes and the permittivity tensor is given by:

$$\overset{\leftrightarrow}{\varepsilon} = \begin{pmatrix} \varepsilon_x & 0 & 0 \\ 0 & \varepsilon_y & 0 \\ 0 & 0 & \varepsilon_z \end{pmatrix}. \quad (5.16)$$

If all three components of the permittivity tensor of anisotropic material are different from each other, such materials are called biaxial (i.e. $\varepsilon_x \neq \varepsilon_y \neq \varepsilon_z$). On the other hand, if all three principal components are identical, the material is isotropic ($\varepsilon_x = \varepsilon_y = \varepsilon_z$). The last group of anisotropic materials is uniaxial media. In uniaxial material two out of three components are identical and different from the third one, e.g. $\varepsilon_x = \varepsilon_y \neq \varepsilon_z$. In such case, axes x and y are called ordinary ($\varepsilon_x = \varepsilon_y = \varepsilon_o$) and the z axis is extraordinary, or in optics it is often called optical axis ($\varepsilon_z = \varepsilon_e$). As suggested in section 5.1.2 and demonstrated in section 5.1.4, the perforated substrates belong into the class of uniaxial media, for which the permittivity tensor has a form

$$\overset{\leftrightarrow}{\varepsilon} = \begin{pmatrix} \varepsilon_o & 0 & 0 \\ 0 & \varepsilon_o & 0 \\ 0 & 0 & \varepsilon_e \end{pmatrix}. \quad (5.17)$$

In a general lossless case, the propagation constant $\beta = |\boldsymbol{\beta}|$, where $\boldsymbol{\beta} = \beta_x \mathbf{a}_x + \beta_y \mathbf{a}_y + \beta_z \mathbf{a}_z$ (\mathbf{a}_x , \mathbf{a}_y and \mathbf{a}_z are unit vectors along Cartesian axes x , y , z) of a plane

electromagnetic wave propagating in this material is given by Fresnel's equation of wave normals and which can be written in the form [131]:

$$\frac{b_x^2}{\beta^2 - \omega^2 \mu \varepsilon_x} + \frac{b_y^2}{\beta^2 - \omega^2 \mu \varepsilon_y} + \frac{b_z^2}{\beta^2 - \omega^2 \mu \varepsilon_z} = \frac{1}{\beta^2} \quad (5.18)$$

however, more frequently used form of the eq. 5.18, particularly in the optics is [129]:

$$\frac{b_x^2}{v_p^2 - v_x^2} + \frac{b_y^2}{v_p^2 - v_y^2} + \frac{b_z^2}{v_p^2 - v_z^2} = 0, \quad (5.19)$$

where b_x, b_y, b_z are components of a unit vector \mathbf{b} perpendicular to the wavefront, $\beta = \beta \mathbf{b}$, v_p is a phase velocity in the direction of a unit vector \mathbf{b} , v_x, v_y , and v_z are principal phase velocities of propagation. The phase velocities are given as

$$v_p = \frac{\omega}{\beta}, \quad (5.20)$$

$$v_i = \frac{1}{\sqrt{\mu \varepsilon_i}}, \quad i = x, y, z. \quad (5.21)$$

The full forms of general both electrically and magnetically anisotropic materials can be found e.g. in [132].

According to [129], for uniaxial media, the two solutions to eq. 5.19 are given as

$$v_{p1}^2 = v_o^2, \quad (5.22)$$

$$v_{p2}^2 = v_o^2 \cos^2 \theta + v_e^2 \sin^2 \theta, \quad (5.23)$$

where v_o, v_e are principal phase velocities of ordinary and extraordinary wave and θ designates the angle between the wavefront normal and the optical axis z . The first solution v_{p1} corresponds to the ordinary wave propagating in the xy plane isotropically (provided x and y are ordinary axes) under conditions that the electric field vector \mathbf{E} is perpendicular to the direction of wave normal $\mathbf{b} \cdot \mathbf{E} = 0$ and \mathbf{E} is parallel to the xy plane (to both ordinary axes), i.e. $E_z = 0$. In this case \mathbf{E} and \mathbf{D} are parallel to each other and simplified relations hold true, $D_x = \varepsilon_x E_x, D_y = \varepsilon_y E_y$.

The second solution represents the extraordinary wave propagating anisotropically through the material and its phase velocity depends on the angle between the extraordinary axis z and the direction of wave normal \mathbf{b} . Interesting consequence of the equations 5.22 and 5.23 is that the phase velocity of the extraordinary wave equals the velocity of the ordinary wave if the wavefronts of the extraordinary wave are perpendicular to the optical axis z . Another consequence is that in xy plane the extraordinary wave can propagate isotropically as well, provided that $\theta = 90^\circ$.

The solutions in eq. 5.22 and 5.23 can be easily rewritten in terms of propagation constants instead of the phase velocities as

$$\beta_1 = \omega \sqrt{\mu \varepsilon_o}, \quad (5.24)$$

$$\beta_2 = \omega \sqrt{\frac{\mu \varepsilon_o \varepsilon_e}{\varepsilon_e \cos^2 \theta + \varepsilon_o \sin^2 \theta}}. \quad (5.25)$$

It follows that the material parameters as seen by propagating wave are decided by the polarization state of the wave as well as by the wave normal direction. By convenient selection of the wave vector direction and polarization we can extract ordinary ε_o and extraordinary ε_e permittivities from propagation constants. In case of anisotropic materials, we deliberately do not speak about propagation direction, since the wave vector is in general not parallel to the Poynting vector. They are parallel only for ordinary wave and for extraordinary wave propagating in $\theta = 90^\circ$ direction.

5.1.4 Classification of Perforated Substrates as Uniaxial Media

In the previous sections, based on the geometry, we suggested that the perforated dielectric slab is anisotropic, moreover that it is uniaxial with its extraordinary axis parallel to the axis of cylindrical perforations (axis z). If this is the case, then we should verify the requirement stated in previous chapter, $\varepsilon_x = \varepsilon_y \neq \varepsilon_z$.

Moreover, to simplify the simulations and to further demonstrate that the material is anisotropic, we perform simulations in order to prove the implications of eq. 5.22 and 5.23. We test scenarios corresponding to the combinations of wave normal directions \mathbf{b} and initial polarization directions \mathbf{E}_0 given in eq. 5.26 to 5.30 for material with $p = 3$ mm and $D = 2.5$ mm (see 5.10, $p = p_1$ in this figure). By considering the unit vectors of Cartesian coordinate system $\mathbf{a}_x, \mathbf{a}_y, \mathbf{a}_z$ we can write the requirements as:

$$\text{a) } \mathbf{b} \parallel \mathbf{a}_x, \quad \mathbf{E}_0 \parallel \mathbf{a}_y \quad (5.26)$$

$$\text{b) } \mathbf{b} \parallel \mathbf{a}_y, \quad \mathbf{E}_0 \parallel \mathbf{a}_x \quad (5.27)$$

$$\text{c) } \mathbf{b} \parallel \mathbf{a}_x, \quad \mathbf{E}_0 \parallel \mathbf{a}_z \quad (5.28)$$

$$\text{d) } \mathbf{b} \parallel \mathbf{a}_y, \quad \mathbf{E}_0 \parallel \mathbf{a}_z \quad (5.29)$$

$$\text{e) } \mathbf{b} \parallel \mathbf{a}_z, \quad \mathbf{E}_0 \parallel \mathbf{a}_x \quad (5.30)$$

In these cases we use simple method of time delay determination based on the time domain simulations is CST MWS (see section 5.1.5). From determined time delay and by knowing the lengths of the samples we can calculate approximate phase velocities corresponding to all these cases. More accurate data can be obtained from the unit cell analysis (see section 5.1.5) and we verify the time delay results with the unit cell results. In uniaxial media with z axis as extraordinary axis, it follows that the phase velocities in cases a) and b) are identical (ordinary waves). Next, in cases c) and d) the phase velocities are the same again, since extraordinary wave is propagating at angle $\theta = 90^\circ$ and last, the wave propagating under conditions e) must have the same phase velocity as in cases c) and d), since this situation corresponds to the extraordinary wave propagating along the extraordinary axis.

In order for the waveguide ports to work properly in x and y directions, we must add small sections of homogenous material at the beginning and end of the sample (see Fig. 5.9 for ports perpendicular to y axis). As these sections introduce apparent prolonging of the sample we shift the pulses in the time domain to compensate for the delay introduced by the homogenous sections. The length l_h is 0.5 mm and relative permittivity is adjusted to a value that gives the smallest level of reflection coefficient from the interface. In fact, this alone is one of the methods to determine the effective relative permittivity (see section 5.1.5).

Figures 5.2 to 5.4 suggest that all the conditions on uniaxial media are fulfilled since the time delays t_1 for ordinary waves are the same and delays t_2 for extraordinary waves are also almost identical. To further prove the material to be uniaxial, we analyze the unit cell for the situations given in eq 5.26 to 5.30. More detailed description on this analysis is given in section 5.1.5. The unit cell approach is more accurate than the time delay method due to periodic boundary conditions and absence of the homogenized sections. The results are dispersion diagrams corresponding to cases a) to e) given in Fig. 5.5 and 5.6.

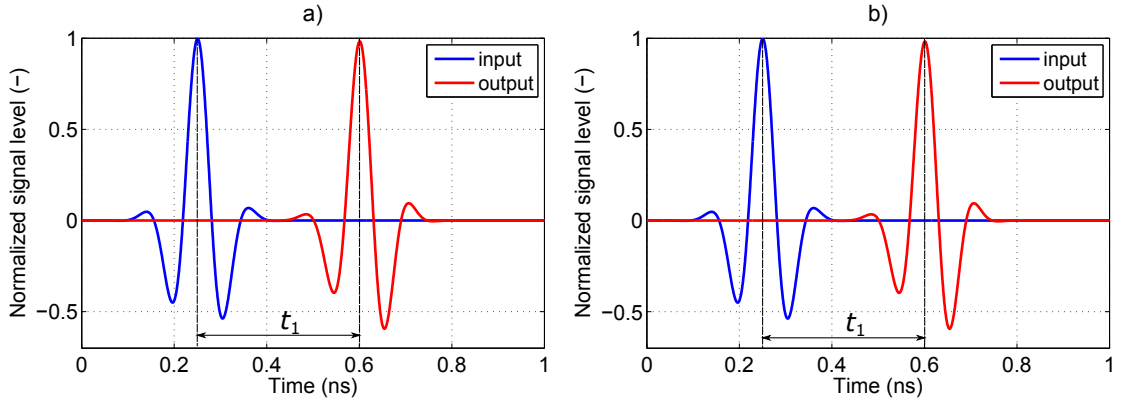


Fig. 5.2: Excitation pulses (blue) with frequency range 1-20 GHz and pulses as received at the end of a sample with length 57 mm. These cases correspond to ordinary wave propagation.

5.1.5 Determining Effective Relative Permittivity Tensor for Plane Waves

In this part, we deal with the propagation of plane EM waves in unbounded perforated dielectrics of certain dimensions and material properties. The unbounded medium is created as a fictional TEM rectangular waveguide in which the boundaries in y direction are set as either PEC (or PMC) and the boundaries in x direction are then PMC (PEC) (see Fig. 5.9). The goal of the work described in this section is to determine the propagation constant (phase constant, as we do not include losses) of perforated dielectrics as function of frequency and to subsequently calculate the effective relative permittivity of the homogenized substance. Homogenization can be understood simply as an approximation of the net material properties of a heterogeneous media with known properties of a single material. The heterogeneous material can then be substituted by homogenous substance of resolved material properties without any change to the wave propagation.

We start by describing the structure under test and we derive approximate analytical expression for effective relative permittivity based on the air filling of the material (the result is identical to eq. 5.13). We perform the analysis for two most basic arrangements of cylindrical perforations, i.e. triangular and square lattice, since the expressions are sometimes used incorrectly in the open literature [100, 133]. Afterwards, we proceed to brief description of several techniques for phase (amplitude) constant determination. Some of the techniques are only suitable for numerical simulations (time domain, frequency domain, modal analysis) and experimental verification would be rather difficult. In each case, the phase constant is used to calculate effective relative permittivity. The most precise method is based

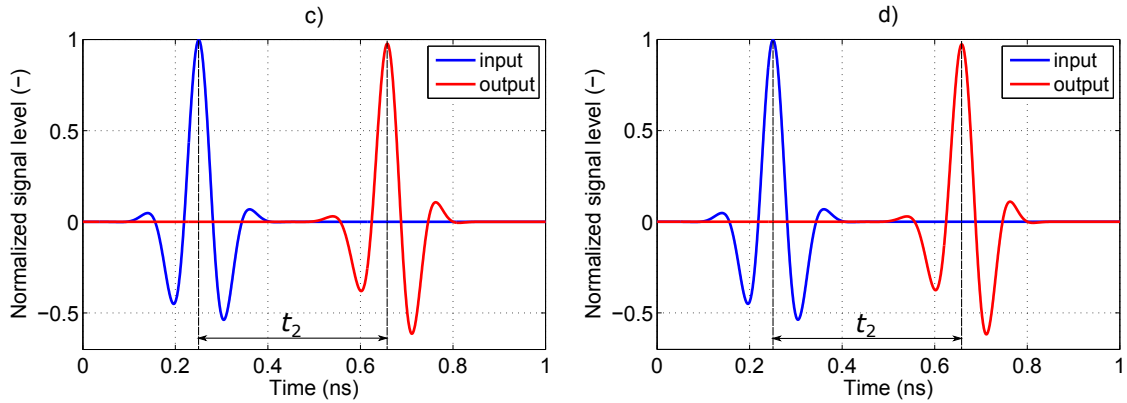


Fig. 5.3: Excitation pulses (blue) with frequency range 1-20 GHz and pulses as received at the end of a sample with length 57 mm. These cases correspond to extraordinary wave propagation in a plane perpendicular to the extraordinary axis. It can be seen that the time delay $t_2 > t_1$.

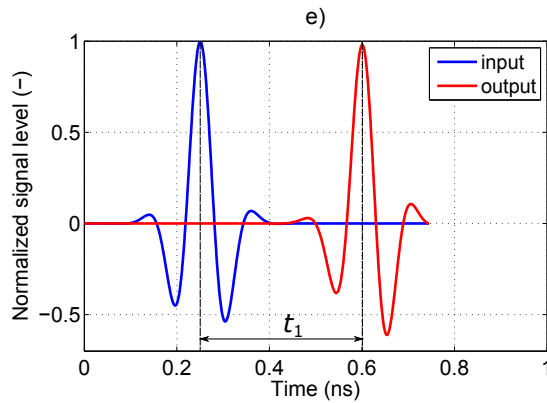


Fig. 5.4: Excitation pulse (blue) with frequency range 1-20 GHz and pulse received at the end of a sample with length 57 mm. This case corresponds to extraordinary wave with wavefront perpendicular to the extraordinary axis. The time delay between input and output pulse is the same as in case of ordinary wave which corresponds to uniaxial media property.

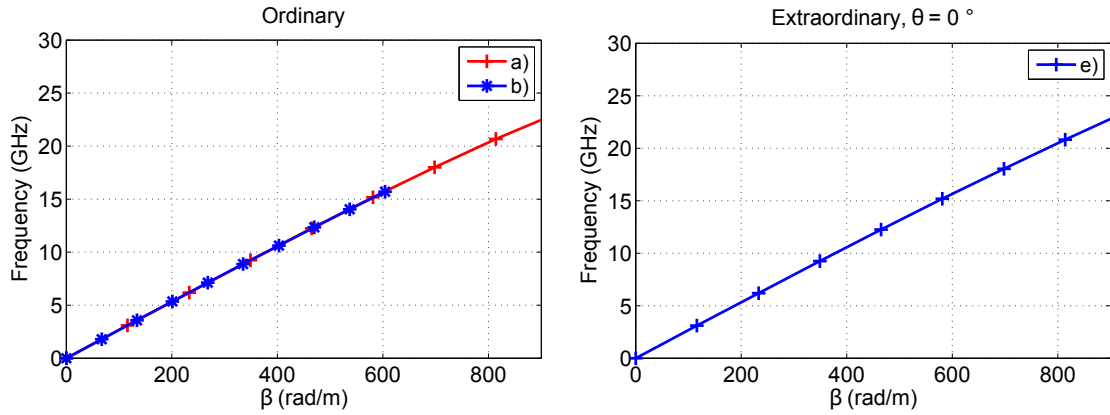


Fig. 5.5: Dispersion diagrams corresponding to cases a), b) (left) and e) (right). In uniaxial media, all these cases should give the same propagation constants influenced only by the ε_o term of permittivity tensor.

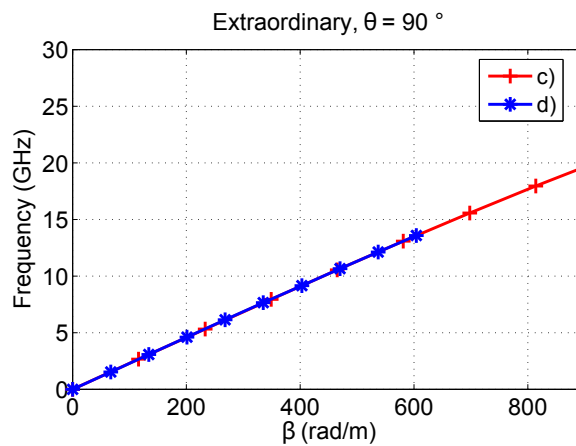


Fig. 5.6: Dispersion diagrams corresponding to cases c) and d). In uniaxial media, all these cases should give the same propagation constants influenced in this case only by the ε_e term of permittivity tensor.

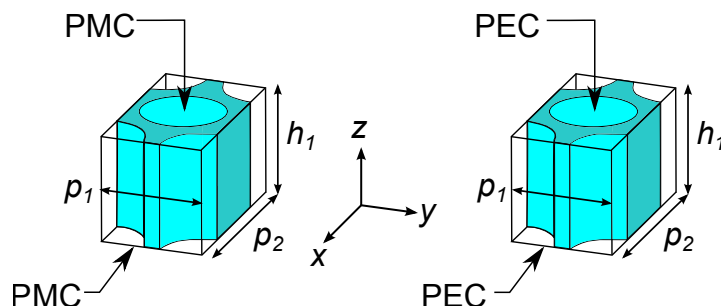


Fig. 5.7: Unit cell models for ordinary (left) and extraordinary (right) wave propagation perpendicular to the optical axis. If not stated otherwise, periodic boundaries are used.

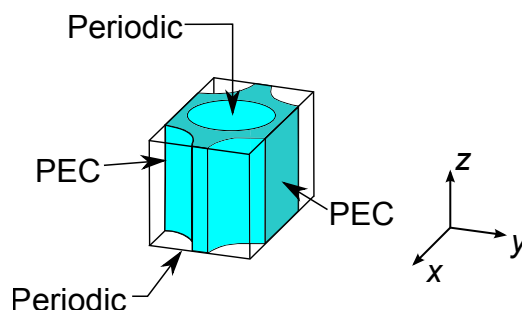


Fig. 5.8: Unit cell model for extraordinary wave propagation along the optical axis. If not stated otherwise, periodic boundaries are used.

on the unit cell analysis and hence the full results of only this method are provided.

The results of this section have connection mostly to the area of radio optics and transformation optics, where the properties of the perforated layers are determined by the polarization state and the direction of propagation.

Geometry and the unit cell

The general geometry of our macroscopic TEM waveguide structure is shown in Fig. 5.9. In here, we see a model prepared for TEM waveguide simulations, the section of perforated dielectric is extended by sections of homogenous dielectric with length l_h . These two sections are necessary for two reasons: first, the waveguide ports in field simulators require the structure to be longitudinally homogenous within at least 3 mesh cells after the port and second, by adjusting the relative permittivity of these parts, we can significantly improve the impedance matching between the port and the material under test. The structure to be analyzed is heterogeneous and composed of two dielectric media as explained before:

1. The bulk dielectric to be perforated (in material research denoted as matrix),
2. Air perforations (sometimes denoted as pores).

There are many possible shapes, orientations and distributions of the perforations given in the literature; however, we focus almost exclusively on triangular lattice of cylindrical perforations (square lattice is partially analyzed). The period of perforations in triangular lattice is p , but since the unit cell is to be of rectangular form, we introduce two periodicities p_x and $p_y = p$ (see 5.10). The diameter of each perforation is D and to satisfy mechanical robustness criterion, it follows that $D < p$ ($\max(D/p) = 1$). The case in which $D/p = 1$ is only theoretical; in such situation the structure loses its mechanical strength and cannot be fabricated by drilling holes into substrate.

The height of the profile h should be in case of TEM wave chosen so that the cutoff frequency of the first waveguide mode (TM_1/TE_1) is sufficiently high. We set $h = 2.5$ mm and the corresponding $f_c(\text{TM}_1) = 30$ GHz. Nevertheless, the shape of our structure should not give rise to any higher-order modes as long as they are not excited deliberately.

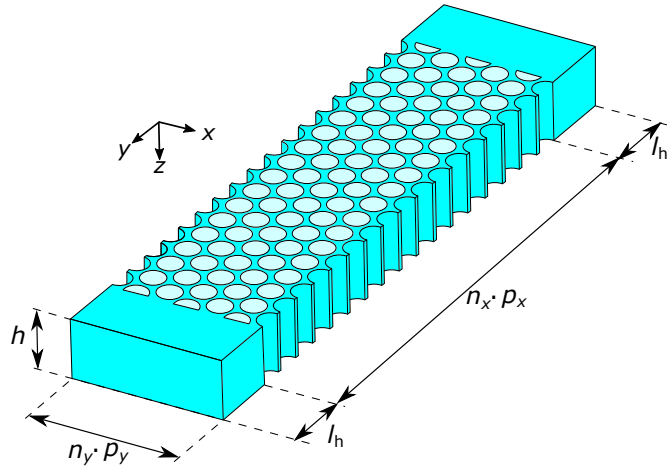


Fig. 5.9: Detail of the geometry. The structure is analyzed as a TEM waveguide with varying direction of propagation (homogenized sections, ports and boundary conditions are adjusting depending on the direction of propagation and polarization state). The length l_h of homogenous dielectrics sections at the beginning and the end of the waveguide is exaggerated in the drawing. The actual length is about 3 meshcells for the time domain simulations and the sections are absent in the frequency domain simulations. However, by adjusting the relative permittivity of these sections, improved impedance matching can be achieved.

Analytical derivation based on volume filling

The simplest theoretical model used to get an approximation of the static effective relative permittivity of a perforated medium is based on the volumetric average. It requires evaluation of the porosity f , which is a ratio between volumes of the unit cell and the dielectric material with ε_{rd} (i.e. matrix material). These models are used in microwave and antenna engineering [5, 78, 81, 82, 107]. In triangular lattice with period p (Fig.5.10) we get the effective relative permittivity as

$$\varepsilon_{\text{r,eff}} = \varepsilon_{\text{rd}} - \varepsilon_{\text{rd}} \frac{\pi D^2}{4p^2 \sin \frac{\pi}{3}} + \varepsilon_{\text{r,i}} \frac{\pi D^2}{4p^2 \sin \frac{\pi}{3}}, \quad (5.31)$$

where ε_{rd} is the relative permittivity of the initial dielectrics, $\varepsilon_{\text{r,i}}$ is the relative permittivity of the inclusions (in case of air perforations $\varepsilon_{\text{r,i}} = 1$), D is the diameter of perforations. The second term of eq. 5.31 decreases the effective permittivity due to the missing dielectric in the perforations. Additionally, the third term increases the permittivity by permittivity of the air in the perforations. After simple mathematical manipulation and evaluating for $\varepsilon_{\text{r,i}} = 1$, we get more common form of the equation 5.31

$$\varepsilon_{\text{r,eff}} = \varepsilon_{\text{rd}} - (\varepsilon_{\text{rd}} - 1) \frac{\pi D^2}{4p^2 \sin \frac{\pi}{3}} = \varepsilon_{\text{rd}} - (\varepsilon_{\text{rd}} - 1) f, \quad (5.32)$$

where f is porosity of the material. We can see that this is identical to the equation 5.13.

On the other hand, in case of a square lattice, the dielectric to air ratio is different and hence the effective permittivity expression is different as well. However, in some publications, the authors do not notice this difference, e.g. [100, 133]. The correct value of relative effective permittivity for square lattice is:

$$\varepsilon_{\text{r,eff}} = \varepsilon_{\text{rd}} - (\varepsilon_{\text{rd}} - 1) \frac{\pi D^2}{4p^2}. \quad (5.33)$$

One of the main problems with these formulas is that they do not respect the anisotropic nature of the perforated materials. If we recall the outcomes of the previous section, these formulas give quasi-static effective permittivity values for polarization parallel to the axis of perforations.

Time delay

One way to obtain the effective relative permittivity using time domain simulations is to determine the time delay Δt between transmitted and received pulse and by knowing the length of the sample $\Delta l = n_x \cdot p_x$, the phase velocity can be evaluated. The reference planes of the ports should be adjusted to positions, where homogenous

sections touch perforated sections, or the delay caused by the homogenous sections must be accounted for in the calculations. If the media is nondispersive the relative permittivity can be calculated from the obtained phase velocity $v_p = \Delta t / \Delta l$ as:

$$\varepsilon_{r,\text{eff}} = \left(c \frac{\Delta t}{\Delta l} \right)^2, \quad (5.34)$$

where c is the speed of light in vacuum. The disadvantage is that for a good resolution, narrow pulse is required; however, stronger dispersion degrades the time resolution in this case and if dispersion is present, this method is not suitable.

Phase delay

Determining the total phase delay caused by the sample of length $\Delta l = n_x \cdot p_x$ is another way of obtaining effective relative permittivity from simulations of single model. In this case, we must plot the phase of a suitable component of electric field \mathbf{E} or magnetic field \mathbf{H} (depends on the polarization and direction of propagation) over a curve of length Δl . We define a curve of length of Δl perpendicular to both, perforations and input/output ports and evaluate desired field component's phase over this curve (total phase). The results of this method might be deteriorated by certain reflections between homogenous and perforated sections and by exact position of the curve. This technique can also be used for surface wave analysis by considering suitable field component.

Standing wave pattern

By substituting the second port with PEC wall and removing the section of homogenous dielectric adjacent to the second port, we eliminate one partial reflection between homogenous and perforated sections and create interference of two waves. From interference pattern over a curve (as defined in previous section) we can measure the distance between two field minima. This distance then corresponds to a half of a wavelength in examined material $\lambda/2$. Effective relative permittivity can be calculated from:

$$\varepsilon_{r,\text{eff}} = \left(\frac{\lambda_0}{\lambda} \right)^2. \quad (5.35)$$

Two-line method

The two-line method requires simulations of two models with different lengths $\Delta l = l_l - l_s$, where l_l is the length of the longer and l_s of the shorter section. From S-parameters corresponding to these two models we first determine the phase

constant as [82]

$$\beta = \frac{|\arg S_{21}^l - \arg S_{21}^s|}{\Delta l} \quad (5.36)$$

and Δl should be an integer multiple of the lattice period p , in this case p_x . From known phase constant we get $\varepsilon_{r,\text{eff}}$ simply as:

$$\varepsilon_{r,\text{eff}} = \left(\frac{\beta \lambda_0}{2\pi} \right)^2, \quad (5.37)$$

where β is obtained as a phase difference between a longer and a shorter section divided by the length difference between these two models Δl .

Attenuation constant can be calculated from the magnitudes of the S_{21} parameters as [82]

$$|S_{21}^l| = e^{-\alpha \Delta l} |S_{21}^s|, \quad (5.38)$$

$$\alpha = -\frac{\ln(|S_{21}^l|/|S_{21}^s|)}{\Delta l}. \quad (5.39)$$

The advantage is that the influence of the reflections between homogenous and perforated sections can be mitigated and more accurate values of attenuation constant can be obtained. For this reason, we can use this technique to determine the attenuation constants of perforated materials in case of TEM wave as well as in case of TE/TM surface waves.

We use this technique later in section 5.2 to verify the results of the unit cell analysis in case of TM_0 surface waves on dielectric covered ground plane.

Reflection coefficient

Another straightforward technique to determine $\varepsilon_{r,\text{eff}}$ is to evaluate reflection coefficient Γ for a plane wave with normal incidence on a planar interface between free space and heterogeneous dielectric mixture

$$\Gamma = \frac{Z_1 - Z_0}{Z_1 + Z_0}, \quad (5.40)$$

where Z_0 and Z_1 are intrinsic impedances of free space and dielectric mixture under examination, respectively. In general, we can write for intrinsic impedance (and for lossless case):

$$Z = \sqrt{\frac{j\omega\mu}{\sigma + j\omega\varepsilon}} \stackrel{\text{lossless}}{\rightarrow} \sqrt{\frac{\mu}{\varepsilon}}. \quad (5.41)$$

This technique can be implemented numerically using TEM waveguide concept with suitable boundary conditions and effective dielectric constant is then evaluated using transmission line theory as in [134, 135].

Unit cell analysis

The perforated material can also be analyzed as a periodic structure, in which the unit cell is repeated in one or two dimensions indefinitely using periodic boundary conditions and Floquet theory. Full material characterization under these conditions requires only the analysis of a single unit cell. Even though the structure can be described by triangular grid with periodicity p , for our purpose the unit cell must be formed as a rectangle with two periodicities: p_x designates the periodicity in the x -direction and p_y periodicity in the y -direction (Fig.5.10). The extraordinary axis of the material is aligned with z – axis of the coordinate system.

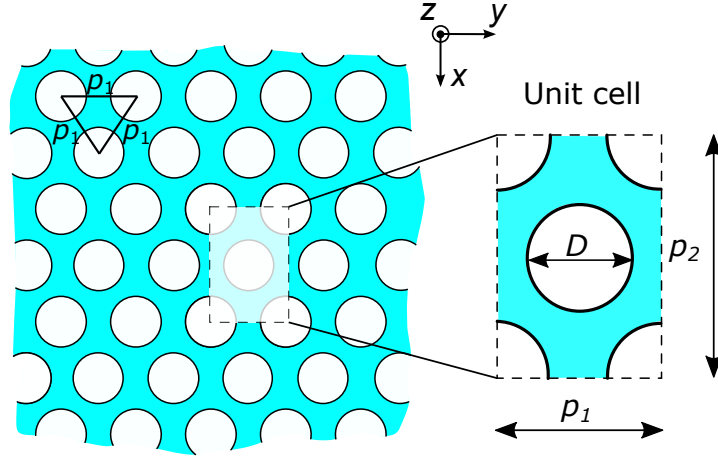


Fig. 5.10: Triangular lattice and the unit cell detail

From unit cell figure (Fig. 5.10) we can see that

$$p_y = p, \quad (5.42)$$

$$p_x = p\sqrt{3}. \quad (5.43)$$

Using modal analysis in CST Eigenmode solver we determine the dispersion diagrams of the unit cell for three electric field vector orientations (along the unit vectors). In case of \mathbf{E} aligned parallel with x -axis, we set top and bottom boundary condition to be PEC (Perfect Electric Conductors) and all four side walls are periodic boundary conditions. On periodic walls, perpendicular to y -axis we set zero phase difference (magnetic walls can be used for this polarization as well) and on the walls, perpendicular to z -axis we gradually set values from 0° to 180° (see Fig. 5.7). The results are eigenfrequencies corresponding to these phase shifts (Fig. 5.11 to 5.13).

This analysis is performed for three different values of period p ($p = 0.8$ mm, $p = 1.5$ mm, $p = 3$ mm) and for each period, three different diameters of perforations are considered, $D = p/2$, $D = 2p/3$, $D = 5p/6$ and $D = p$. For example, for period

$p = 3$ mm, the perforation diameters are 1.5, 2, 2.5 and 3 mm. It should be mentioned that the case in which $D = p$ is only theoretical and cannot be achieved in practical application, since the structure would lose its mechanical robustness. The exact values of the periods and diameters of perforations are selected to be approximately $\lambda_0/10$, $\lambda_0/20$ and $\lambda_0/37.5$ at frequency 10 GHz, with free space wavelength 30 mm.

Unit cell analysis does not allow us to receive attenuation constant of the material, only the phase constant can be obtained by considering total phase change over one meter. Knowing the phase difference over one unit cell $\Delta phase$ and the length of the unit cell l in the direction in which phase difference of $\Delta phase$ is applied, we can get the phase constant at calculated eigenfrequency as:

$$\beta = \frac{\Delta phase}{l}. \quad (5.44)$$

In this way, we repeat the simulations for TEM waves propagating in directions of axes x , y , z (principal axes) with two states of polarizations with respect to the structure geometry (if possible), i.e. electric field vector \mathbf{E} parallel to the axis of cylindrical perforations and \mathbf{E} perpendicular to the axis of perforations.

From theory, it follows that the propagation constant of a wave in anisotropic medium is determined by its polarization state with respect to the material's principal axes of anisotropy. In our situation, it means the propagation constant for TEM wave propagating in $\pm y$ direction is proved to be the same as the propagation constant of waves propagating in $\pm x$ or $\pm z$ directions with the \mathbf{E} field oriented perpendicular to the axis of perforations. The simulation results also show that the propagation constant in x and y directions are the same making the media uniaxial, despite the triangular lattice. This holds true for both polarization states (\mathbf{E} perpendicular and parallel to the axis of perforations). It means that the exact arrangement of the perforations is not relevant to the material properties and the same results, from the qualitative point of view would, be acquired in case of different lattices, e.g. square, honeycomb etc. In terms of uniaxial media, we call the axis of perforations (z axis in Fig. 5.10) extraordinary axis and the axes x and y ordinary axes. It should be noted that this holds true only in the sub-wavelength regime of the perforations.

The propagation constants at calculated eigenfrequencies are then used to evaluate equivalent effective relative permittivity tensor of homogenized dielectrics (eq. 5.17).

$$\beta = \frac{2\pi}{\lambda} = \frac{2\pi\sqrt{\varepsilon_{r,\text{eff}}}}{\lambda_0}, \quad (5.45)$$

$$\varepsilon_{r,\text{eff}} = \frac{\beta^2\lambda_0^2}{4\pi^2}, \quad (5.46)$$

where β is the phase constant, λ is the wavelength in homogenized perforated dielectric, λ_0 is the free space wavelength and $\varepsilon_{r,\text{eff}}$ is the effective relative permittivity of the homogenized perforated dielectric.

At higher frequencies, where the size of the period and perforations is closer to the wavelength, the material behaves as an Electromagnetic Band Gap structure [79, 80]. On top of the material dispersion of perforated dielectrics, the structure shows also waveguide dispersion and there is no sense in evaluation of the effective relative permittivity without taking waveguide dispersion into consideration. Due to our application, we decided to focus on dimensions that did not show bandgap behavior (i.e. sufficient number of perforations per wavelength) and where material homogenization can be utilized without any additional effects. The maximum frequency in the presented results is limited to approximately 40 GHz. The dispersion characteristics for all values of p and D are given in Fig. 5.11 to 5.13. The effective relative permittivities are then given in Fig. 5.14 to Fig. 5.16.

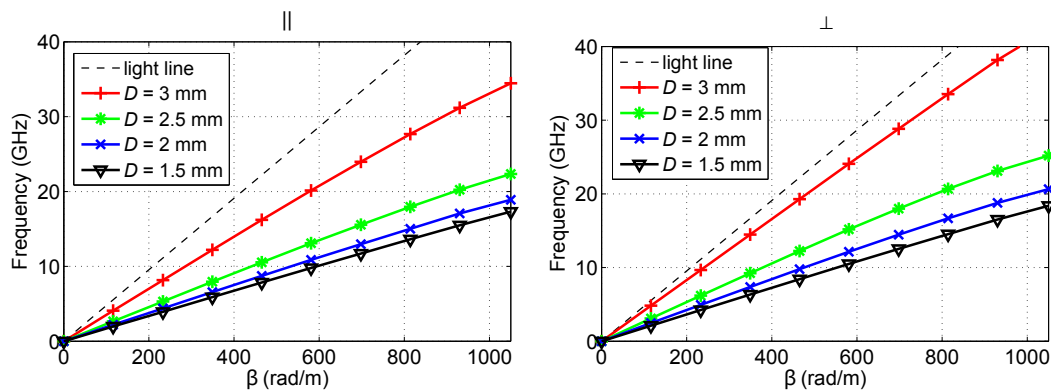


Fig. 5.11: Dispersion diagrams for unbounded perforated dielectric material with $p = 3$ mm for polarization parallel - extraordinary wave (left) and perpendicular - ordinary wave (right) to the axis of perforations.

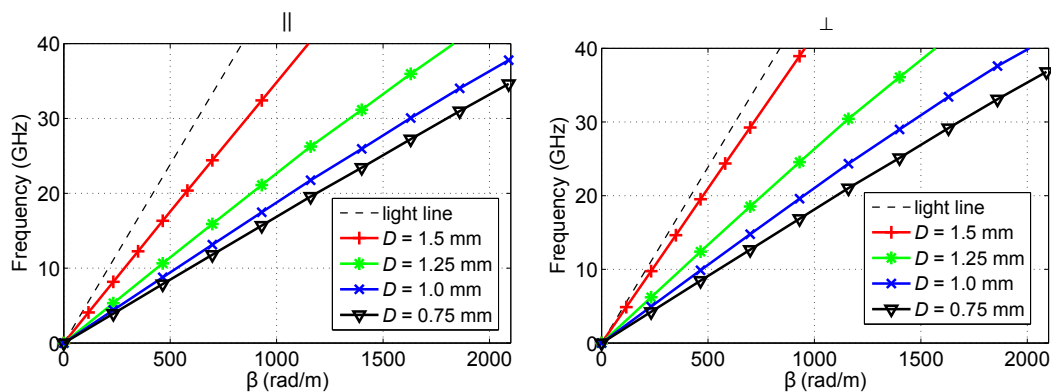


Fig. 5.12: Dispersion diagrams for unbounded perforated dielectric material with $p = 1.5$ mm for polarization parallel - extraordinary wave (left) and perpendicular - ordinary wave (right) to the axis of perforations.

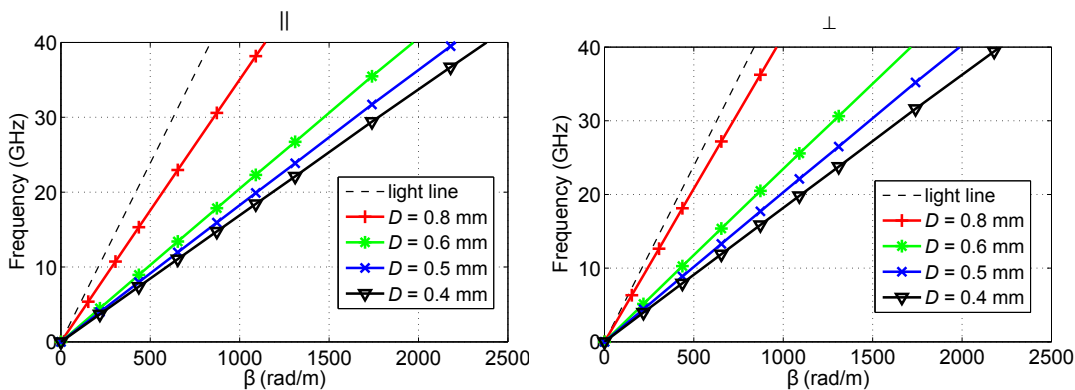


Fig. 5.13: Dispersion diagrams for unbounded perforated dielectric material with $p = 0.8$ mm for polarization parallel - extraordinary wave (left) and perpendicular - ordinary wave (right) to the axis of perforations.

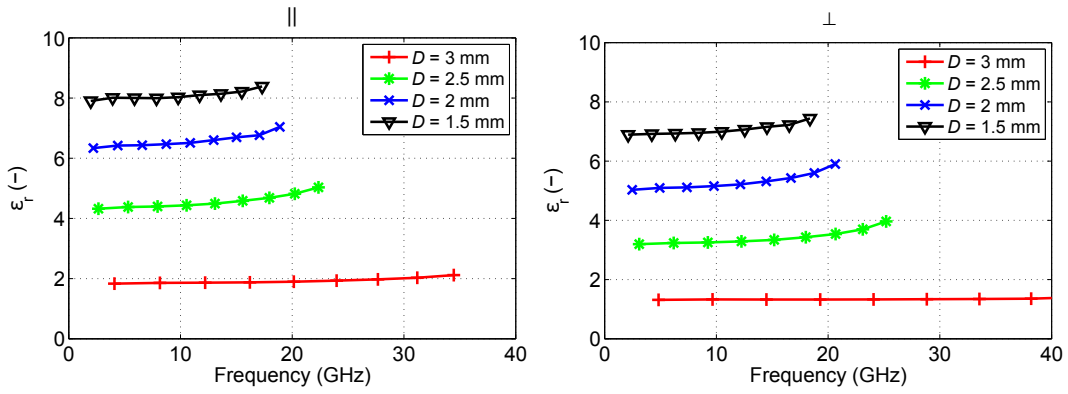


Fig. 5.14: Effective relative permittivities for extraordinary (left) and ordinary (right) wave in homogenized dielectric material with $p = 3$ mm.

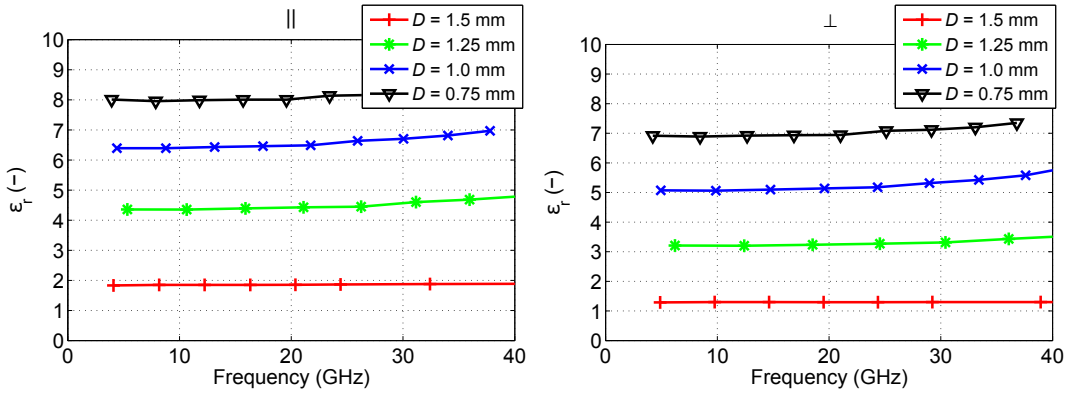


Fig. 5.15: Effective relative permittivities for extraordinary (left) and ordinary (right) wave in homogenized dielectric material with $p = 1.5$ mm.

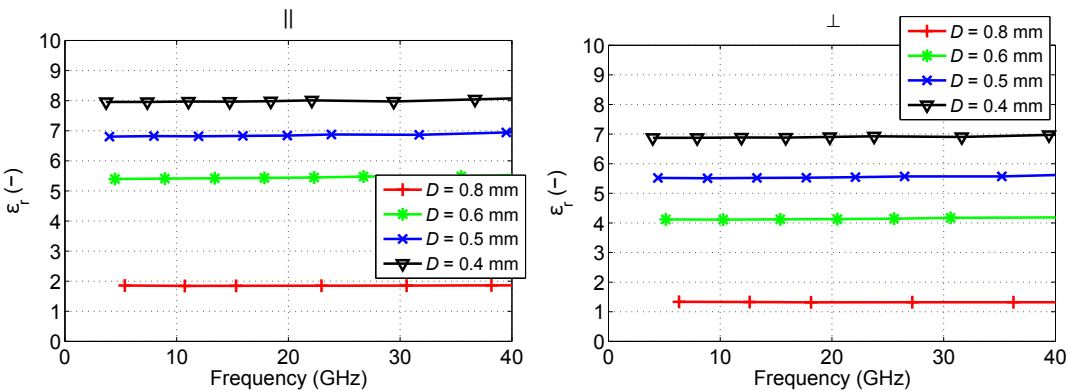


Fig. 5.16: Effective relative permittivities for extraordinary (left) and ordinary (right) wave in homogenized dielectric material with $p = 0.8$ mm.

5.1.6 Results

The absolute dimensions of the single perforations are not that important if we operate the structure at wavelengths much smaller than the period of perforations. Under this condition, the permittivity is controlled only by the D/p ratio (i.e. porosity f). The comparison between results of theoretical model based on Maxwell-Garnett mixing rules (eq. 5.12 and 5.13) and numerical simulations for period of perforations $p = 0.8$ mm is given in Fig. 5.17. The agreement at lower frequencies (10 GHz), where $p = \lambda_0/37.5$ is excellent, in addition, the theoretical model seems quite accurate even at 40 GHz, where $p = \lambda_0/9.4$.

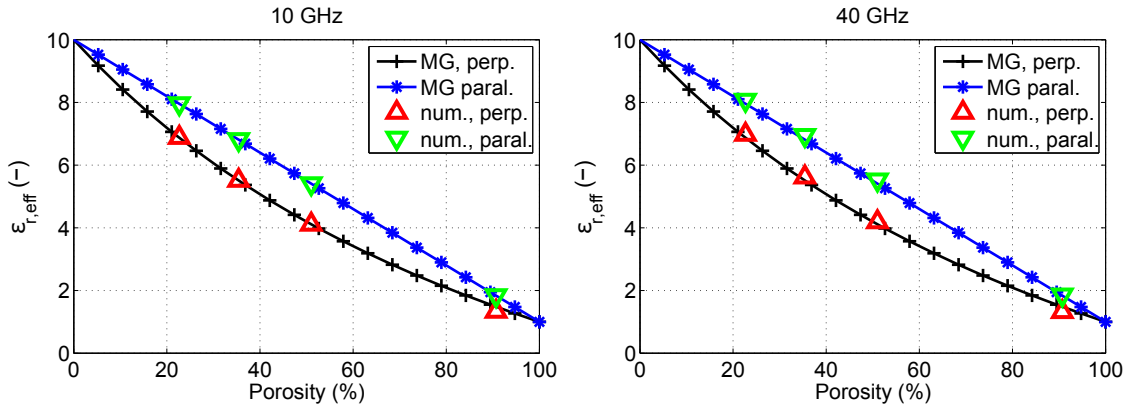


Fig. 5.17: Comparison between theoretical model based on Maxwell-Garnett mixing rules (solid lines) with simulation results (triangles) for $p = 0.8$ mm.

5.2 Surface Wave Propagation in Perforated Substrates

In the previous section, the anisotropy of unbounded perforated dielectrics for TEM wave propagation has been examined. Building on the results presented above, in this section we turn our attention to a little different problem. We deal with propagation of surface waves in perforated substrates, since as it has been shown in previous chapter, the relative permittivity of manufacturable structure (ratio $D/p < 1$) can be quite significant and starts between values 3-4. Again, we assume sub-wavelength regime of the perforations, in which the perforations are used only to decrease the effective relative permittivity of the substrate and not to serve as an EM band gap structure. The perforations with permittivity control function have been extensively used in transmission line and antenna research/design; however, to the author's knowledge, the evaluation of the surface wave phenomena in such cases has not been described in the open literature. As the thesis focuses on DRAs, the

main application is to determine how the surface waves in the perforated substrate influence the performance of a single element DRA and how it affects the mutual coupling between such elements. Moreover, we want to show that the anisotropy determined in previous section influences also the propagation constants of TE/TM surface wave modes. We thus derive effective relative permittivities as seen by transverse electric and transverse magnetic modes of surface waves. The outcomes can be applied to any other antenna/transmission line elements realized with perforated dielectrics (e.g. microstrip lines, dielectric waveguides, patch antennas, dielectric rod antennas, planar lenses etc.).

5.2.1 Surface Waves on Dielectric Slabs

Dielectric slab waveguide is one type of dielectric waveguides in which a wave can propagate without attenuation. The slab is a single layer of homogenous dielectric of certain permittivity ϵ_d (relative permittivity is ϵ_{rd} and relative permeability is assumed to be $\mu_{rd} = 1$) with height $2h$ surrounded from top and bottom by dielectric regions of smaller relative permittivity (mostly air). In such configuration and under certain conditions, electromagnetic waves can become trapped in between the interfaces due to the total internal reflection and propagate as surface waves of TM and/or TM type. Detailed descriptions based on modal analysis approach or ray tracing methods can be found in e.g. [1, 136, 137]. In here, we only give the most basic theoretical background that is required to determine the properties of perforated dielectrics with respect to surface waves propagation.

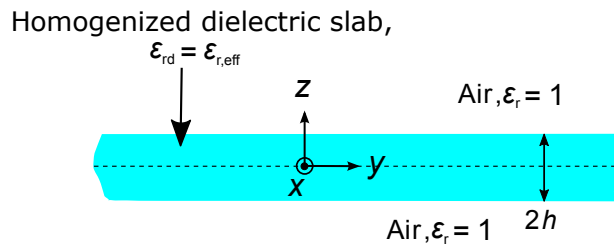


Fig. 5.18: Geometry of the dielectric slab with coordinate system.

The geometry of a general dielectric slab problem is given in Fig. 5.18. Under the assumption that the slab is infinite in the x direction, we can consider the problem to be two-dimensional, allowing no field variation in the x direction. The surface waves are then the waves TE/TM propagating along the slab in the y direction (or $-y$) and can be of two types: even and odd. The type is determined by the symmetry of the magnetic vector potential \mathbf{A} , which in this case, has only the $A_y = A$ component. In grounded slab waveguide in which one surface of the slab is covered by a conductor, even TM and odd TE modes do not satisfy boundary conditions and thus are not

supported by the structure. In our notation, the coordinate system is somewhat rotated with respect to common notation found in the literature, i.e. we have aligned the extraordinary axis of our geometry with z axis and the direction of propagation along the slab is thus y . Moreover, as our dielectric layer is heterogeneous, we assign it relative permittivity of homogenous equivalent $\varepsilon_{rd} = \varepsilon_{r,\text{eff}}$ and the propagation constant in homogenized dielectric is indicated as β_d .

In case of even modes, propagating in the $+y$ direction we can write for the dielectric region, i.e. for region $|z| < h$

$$A_d^e = B^e \cos(\beta_{zd}z)e^{-j\beta_y y}, \quad |z| < h, \quad (5.47)$$

and in the air regions

$$A_a^e = C^e e^{\alpha_{z0}|z|} e^{-j\beta_y y}, \quad |z| \geq h, \quad (5.48)$$

where B and C are constants, β_{zd} is propagation constant in the z direction in dielectrics, β_y is the propagation constant in the y -direction and α_{z0} is the attenuation constant in air, in z -direction.

Similarly, for the odd modes, we can write in the dielectric region:

$$A_d^o = B^o \sin(\beta_{zd}z)e^{-j\beta_y y}, \quad |z| < h, \quad (5.49)$$

and again for the air regions

$$A_a^o = C^o e^{-\alpha_{z0}|z|} e^{-j\beta_y y}, \quad z \geq h, \quad (5.50)$$

$$A_a^o = -C^o e^{\alpha_{z0}|z|} e^{-j\beta_y y}, \quad z \leq h, \quad (5.51)$$

From equations 5.47 to 5.51 it follows that the waves propagate in y direction without attenuation if both β_{zd} and α_{z0} are real; however, in the z direction, the field distribution is given either by sine or cosine function within the dielectric layer and decays exponentially in the air region, hence the waves in the z -direction in the air region are of evanescent nature.

The separation equation for dielectric region is

$$\beta_{zd}^2 + \beta_y^2 = \beta_d^2 = \omega^2 \mu_0 \varepsilon_d, \quad (5.52)$$

and in the air regions:

$$-\alpha_{z0}^2 + \beta_y^2 = \beta_0^2 = \omega^2 \mu_0 \varepsilon_0. \quad (5.53)$$

The separation equations hold true for all even and odd TE and TM modes.

The electric and magnetic fields in the air regions are not interesting for the further analysis and can be found in [1, 136]. On the other hand, the electric and

magnetic fields within the dielectric slab are then for even TM modes in rectangular coordinate system obtained from magnetic vector potential using [1]

$$E_x = -j \frac{1}{\omega \mu_0 \varepsilon_d} \frac{\partial^2 A_d^e}{\partial x \partial y}, \quad (5.54)$$

$$E_z = -j \frac{1}{\omega \mu_0 \varepsilon_d} \frac{\partial^2 A_d^e}{\partial z \partial y} = \frac{\beta_{zd} \beta_y}{\omega \mu_0 \varepsilon_d} B^e \sin(\beta_{zd} z) e^{-j \beta_y y}, \quad (5.55)$$

$$E_y = -j \frac{1}{\omega \mu_0 \varepsilon_d} \left(\frac{\partial^2}{\partial y^2} + \beta_d^2 \right) A_d^e = -j \frac{\beta_d^2 - \beta_y^2}{\omega \mu_0 \varepsilon_d} B^e \cos(\beta_{zd} z) e^{-j \beta_y y}, \quad (5.56)$$

$$H_x = \frac{1}{\mu_0} \frac{\partial A_d^e}{\partial z} = -\frac{\beta_{zd}}{\mu_0} B^e \sin(\beta_{zd} z) e^{-j \beta_y y}, \quad (5.57)$$

$$H_z = -\frac{1}{\mu_0} \frac{\partial A_d^e}{\partial x} = 0, \quad (5.58)$$

$$H_y = 0. \quad (5.59)$$

And for the odd TM modes:

$$E_x = -j \frac{1}{\omega \mu_0 \varepsilon_d} \frac{\partial^2 A_d^o}{\partial x \partial y} = 0, \quad (5.60)$$

$$E_z = -j \frac{1}{\omega \mu_0 \varepsilon_d} \frac{\partial^2 A_d^o}{\partial z \partial y} = -\frac{\beta_{zd} \beta_y}{\omega \mu_0 \varepsilon_d} B^o \cos(\beta_{zd} z) e^{-j \beta_y y}, \quad (5.61)$$

$$E_y = -j \frac{1}{\omega \mu_0 \varepsilon_d} \left(\frac{\partial^2}{\partial y^2} + \beta_d^2 \right) A_d^o = -j \frac{\beta_d^2 - \beta_y^2}{\omega \mu_0 \varepsilon_d} B^o \sin(\beta_{zd} z) e^{-j \beta_y y}, \quad (5.62)$$

$$H_x = \frac{1}{\mu_0} \frac{\partial A_d^o}{\partial z} = \frac{\beta_{zd}}{\mu_0} B^o \cos(\beta_{zd} z) e^{-j \beta_y y}, \quad (5.63)$$

$$H_z = -\frac{1}{\mu_0} \frac{\partial A_d^o}{\partial x} = 0, \quad (5.64)$$

$$H_y = 0. \quad (5.65)$$

The equations 5.54 to 5.65 demonstrate that the electric field vector of TM modes have components oriented in the y and z directions. It means the propagating TM wave on uniaxial perforated substrate (see Fig. 5.19) have electric field components parallel to the ordinary axis as well as to the extraordinary axis. The permittivity of the material should then lie somewhere between the values ε_e and ε_o determined in section 5.1.5.

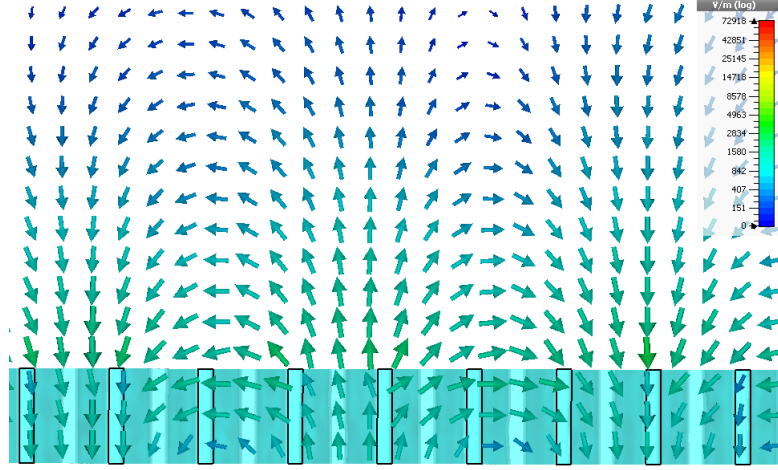


Fig. 5.19: Electric field distribution of TM_0 wave on grounded perforated substrate. The cut corresponds to yz plane according to the Fig. 5.18.

Using duality between the TM and TE mode formulation, for TE modes we would arrive at the conclusion, that the only non-zero electric field component of TE waves is the one oriented parallel to the x axis (E_x). The TE waves in perforated substrate thus have E-field oriented parallel to the ordinary axis of the anisotropic substrate and should be completely described by ϵ_o .

For the analysis and extraction of the effective permittivity of a perforated slab waveguide, we must define the dispersion relations. The detailed derivation of these formulas can be found in e.g. [1]. The dispersion relations for the TM and TE modes considering dielectric slab with permittivity $\epsilon_d = \epsilon_{rd}\epsilon_0$ and permeability $\mu_d = \mu_0$ surrounded by air with material properties ϵ_0, μ_0 are given by:

$$-\frac{1}{\epsilon_{rd}} (\beta_{zd}h) \cot(\beta_{zd}h) = \alpha_{z0}h \quad \text{even TM}, \quad (5.66)$$

$$\frac{1}{\epsilon_{rd}} (\beta_{zd}h) \tan(\beta_{zd}h) = \alpha_{z0}h \quad \text{odd TM}, \quad (5.67)$$

$$-(\beta_{zd}h) \cot(\beta_{zd}h) = \alpha_{z0}h \quad \text{even TE}, \quad (5.68)$$

$$(\beta_{zd}h) \tan(\beta_{zd}h) = \alpha_{z0}h \quad \text{odd TE}. \quad (5.69)$$

For unattenuated propagation of electromagnetic waves, all the three coefficients: β_{zd} , α_{z0} and β_y must be real. This holds true only if the following relation is satisfied:

$$\beta_0 < \beta_y < \beta_d. \quad (5.70)$$

The cutoff frequencies of the surface wave modes are then given for both TE_m and TM_m modes of even ($m = 1, 3, 5, \dots$) and odd ($m = 0, 2, 4, \dots$) type by equation 5.71.

$$f_c = \frac{m}{4h\sqrt{\mu_0\epsilon_0(\epsilon_{rd} - 1)}}. \quad (5.71)$$

In our analysis, we consider only the lowest order TE and TM modes, i.e. odd modes TM_0 and TE_0 to examine the behavior of surface waves on anisotropic substrate. For practical application to dielectric resonator antennas, only TM_0 mode is of interest as it has zero cutoff frequency. The propagation of TE_0 is not supported by a grounded dielectric slab and the lowest order TE mode is TE_1 .

5.2.2 Determining Effective Relative Permittivity for TM/TE Waves from Unit Cell Analysis

Usually, in the analysis and design of dielectric slab waveguides, one is familiar with the height of the slab $2h$ and with its material properties (ϵ_{rd} , μ_{rd}) and the cutoff frequencies and propagation constants are to be solved. For this reason, one must solve the transcendent dispersion equations (eq. 5.66 to 5.69). One of the methods to solve such equations is based on graphical numerical technique [137], which allows us to determine all propagating modes and their propagation constants.

However, we must proceed differently, since we are not interested in the propagation constants but rather in the material parameters of the slab. For simplicity, in the following text we denote the effective relative permittivity of the slab by ϵ_{rd} . The task now is to determine effective ϵ_{rd} of the perforated slab in TE_0 and TM_0 propagating wave from known propagation constant in the y direction β_y . We obtain β_y from unit cell analysis in eigenmode solver in CST MWS (see Fig. 5.20). In unit cell analysis, we proceed similarly like in the case of TEM wave in section 5.1.5. However, here we must add space above the dielectric slab, since the wave propagates partially in the air above the substrate. For TM_0 wave we set boundary condition at the bottom to PEC and for TE_0 mode to PMC, the boundaries at the top are then dual to those at the bottom. Nevertheless, if the height of the computational domain is sufficient and the fields decay to negligible values at the top boundary, the exact type of this boundary should not be relevant for the results (at least from some minimum phase shift). Ideally we would set the top boundary to some type of absorbing boundary; however in CST only PEC and PMC can be used in combination with the Eigenmode solver.

For TM_0 mode analysis ϵ_{rd} is rewritten in terms of β_{zd} and the final form of the

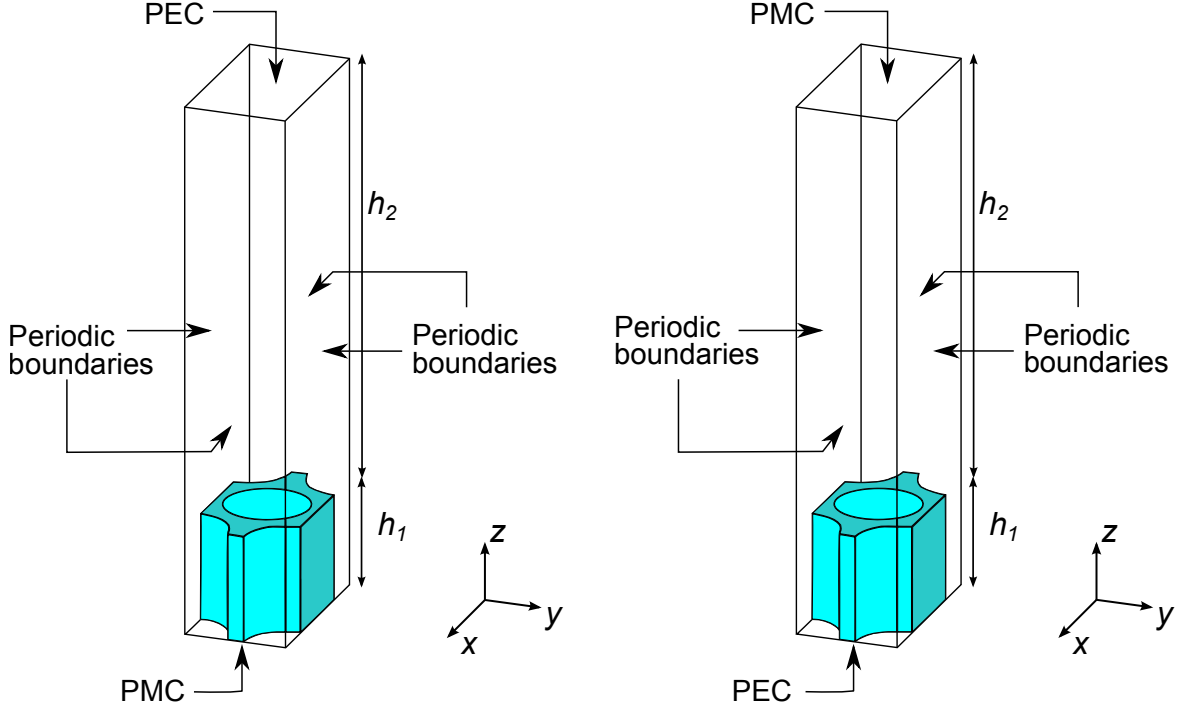


Fig. 5.20: Unit cell for TM_0 mode analysis (left) and for TE_0 mode analysis (right). Height of the substrate $h_1 = 3.175$ mm and height of the computational domain $h_2 = 20h_1$.

transcendent dispersion equation to be solved numerically is:

$$\frac{\beta_0^2}{\beta_{zd}^2 + \beta_y^2} (\beta_{zd}h) \tan(\beta_{zd}h) = \alpha_{z0}h, \quad (5.72)$$

where β_{zd} is our unknown. After obtaining β_{zd} we can calculate ϵ_{rd} for certain mode from modified eq. 5.73

$$\beta_{zd} = \pm \sqrt{\beta_d^2 - \beta_y^2} = \pm \sqrt{\epsilon_{rd}\beta_0^2 - \beta_y^2}, \quad (5.73)$$

since $\beta_d = \beta_0\sqrt{\epsilon_{rd}}$. On the other hand, α_{z0} is calculated by modifying separation equation eq. 5.53 in air region

$$\alpha_{z0} = \pm \sqrt{\beta_y^2 - \beta_0^2}. \quad (5.74)$$

In case of TE_0 mode, we solve eq. 5.75 for β_{zd} and again use eq. 5.76 to obtain ϵ_{rd}

$$\beta_{zd}h \tan(\beta_{zd}h) = \alpha_{z0}h. \quad (5.75)$$

Once the propagation constant β_{zd} is known, the effective relative permittivity for TE_0 mode $\epsilon_{rd,TE}$, and for TM_0 mode $\epsilon_{rd,TM}$ is then calculated as

$$\epsilon_{rd} = \frac{\beta_{zd}^2 + \beta_y^2}{\beta_0^2}. \quad (5.76)$$

The dispersion relations as obtained from eigenmode analysis of a single unit cell for three periods $p = 3$ mm, 1.5 mm and 0.8 mm are given for TM_0 and TE_0 modes in Fig. 5.21 to 5.23. For every period several diameters of perforations were selected ranging between $D = p/2$ and $D = p$.

Our hypothesis that the TE modes are less affected by propagating in perforated dielectric slab is confirmed. By observing the effective relative permittivity of the slabs with the same D/p ratios (for different p) we see that the values of effective ϵ_{rd} are very close to each other as well as to values of ϵ_{rd} as obtained for TEM wave propagation in unbounded media (ordinary wave). In case of TM_0 wave the situation is more complicated, as we have anticipated. The permittivity is slowly increasing with the frequency and the permittivity values lie in the range predicted by equations 5.12 and 5.13; however, much closer to the upper limit. The effective relative permittivities as functions of frequency are given in Fig. 5.24 to 5.26.

In Fig. 5.26 for $p = 0.8$ mm, we can see that for frequencies up to circa 17 GHz, the permittivity values follow steeper trend than in rest of the band. It must be verified by different and independent method if this behavior is caused by the structure or by the unsuitability of eigenmode analysis approach for such low frequencies. The reason for this suspicion stems from the boundary conditions of the unit cell, where the region is bounded from top by PMC boundary condition (see Fig. 5.20).

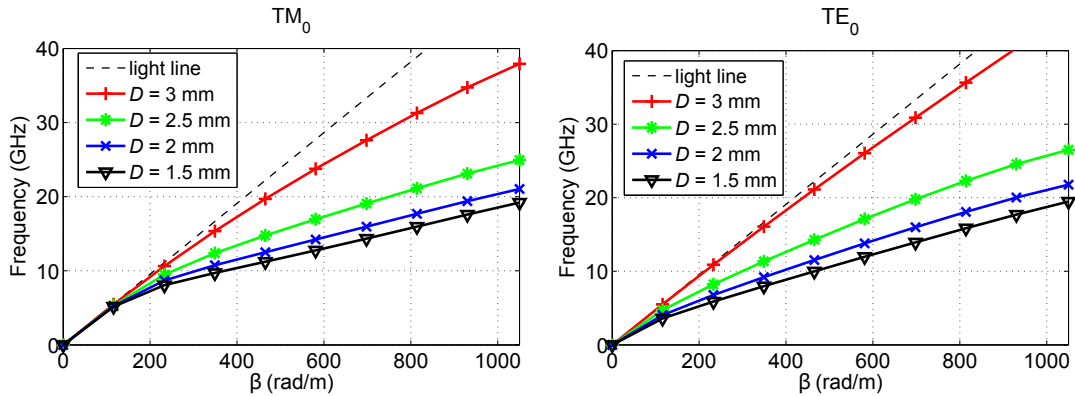


Fig. 5.21: Surface wave TM_0 (left) and TE_0 (right) mode dispersion diagrams for perforated dielectric layer with height $h = 3.175$ mm and period of perforations $p = 3$ mm.

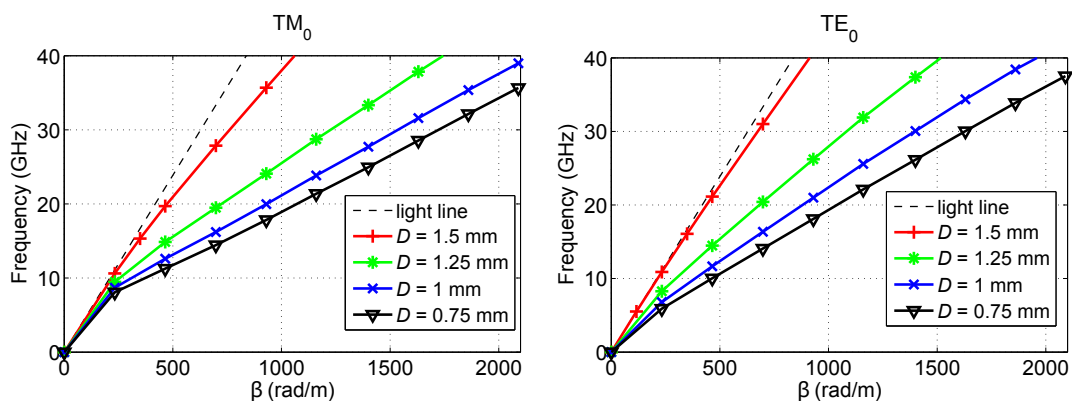


Fig. 5.22: Surface wave TM_0 (left) and TE_0 (right) mode dispersion diagrams for perforated dielectric layer with height $h = 3.175$ mm and period of perforations $p = 1.5$ mm.

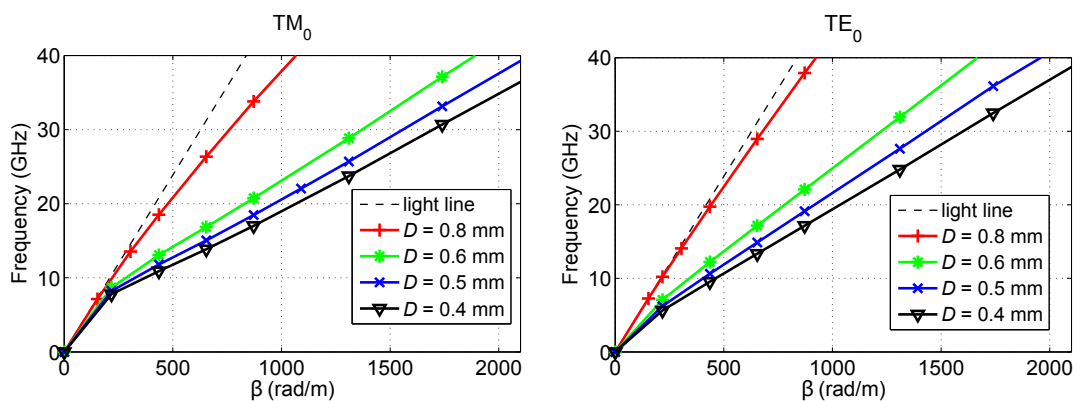


Fig. 5.23: Surface wave TM_0 (left) and TE_0 (right) mode dispersion diagrams for perforated dielectric layer with height $h = 3.175$ mm and period of perforations $p = 0.8$ mm.

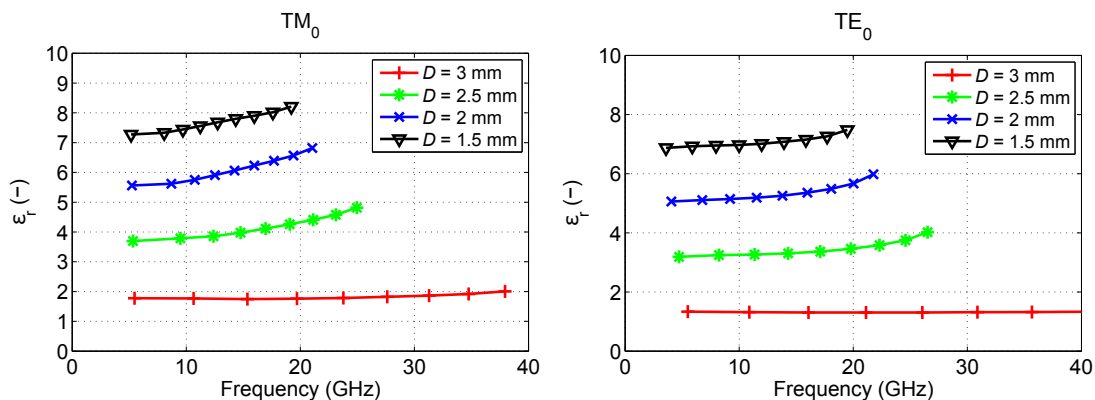


Fig. 5.24: Effective relative permittivities of homogenized equivalent dielectric layer as extracted for TM_0 (left) and TE_0 (right) mode surface wave propagating on perforated dielectric layer with height $h = 3.175$ mm and $p = 3$ mm.

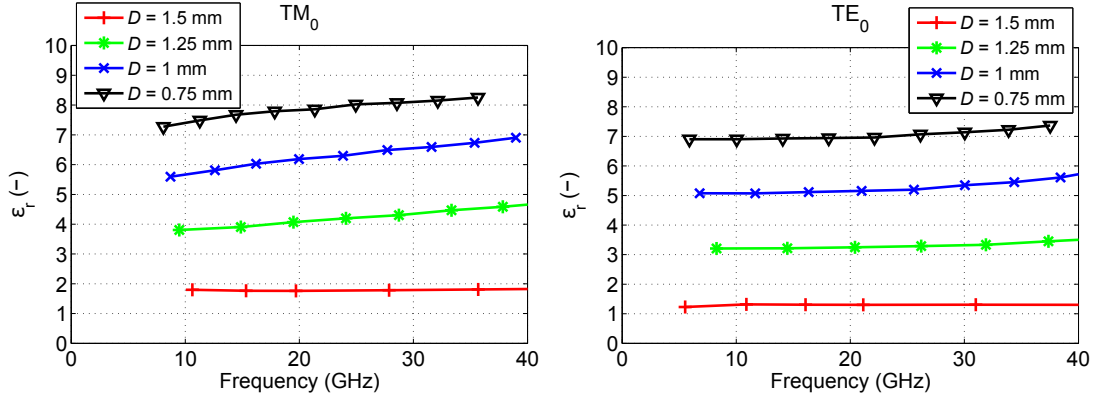


Fig. 5.25: Effective relative permittivities of homogenized equivalent dielectric layer as extracted for TM_0 (left) and TE_0 (right) mode surface wave propagating on perforated dielectric layer with height $h = 3.175$ mm and $p = 1.5$ mm.

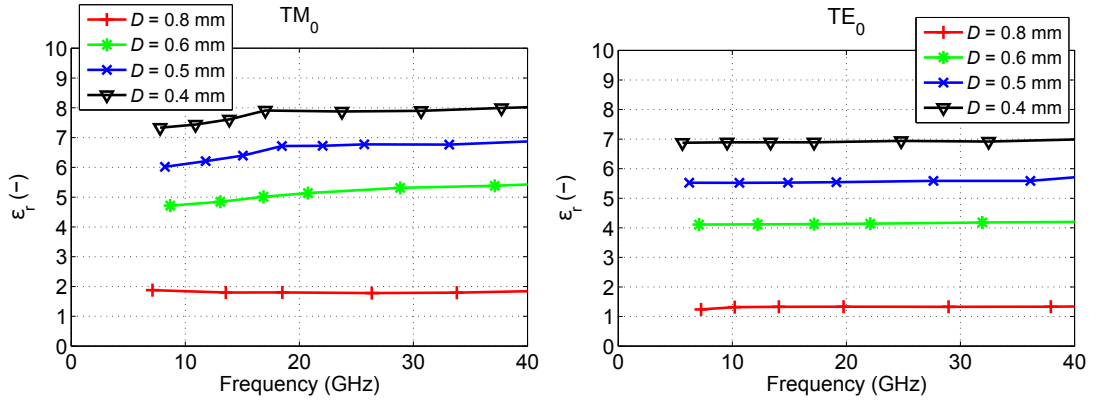


Fig. 5.26: Effective relative permittivities of homogenized equivalent dielectric layer as extracted for TM_0 (left) and TE_0 (right) mode surface wave propagating on perforated dielectric layer with height $h = 3.175$ mm and $p = 0.8$ mm.

5.2.3 Determining Effective Relative Permittivity for TM/TE Waves from Scattering Parameters of Macroscopic Model

To verify the outcomes of previous section, most importantly to verify the strange behavior of propagation constant and thereafter effective permittivity for TM_0 wave in the perforated material with $p = 0.8$ mm in frequency region up to 17 GHz (see Fig. 5.26), we deploy method based on comparison of scattering parameters of two samples with length difference described in section 5.1.5. The method compensates for negative effects of partial reflections between port parts and the structure under test. The results of the macroscopic model are influenced by boundary conditions, since open boundaries on three walls are used. Nevertheless, very good

agreement between independent simulation techniques is obtained (see Fig.5.27), which proves the decreasing effective permittivity toward lower frequencies as suggested in Fig.5.26.

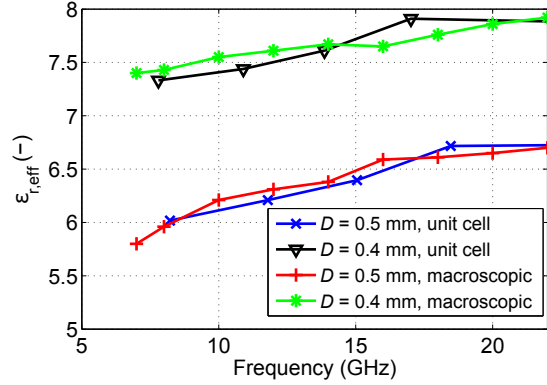


Fig. 5.27: Comparison of the effective relative permittivities of two selected geometries as obtained from unit cell analysis and from two sample comparison method.

5.2.4 Summary

The quasi-static theoretical model based on Maxwell-Garnett mixing rules tends to give useful results even for surface waves on dielectric slabs. As shown in Fig. 5.28 and 5.29, the effective relative permittivity as seen by TE_0 surface wave mode can be approximated with very good agreement by effective permittivity corresponding to polarization perpendicular to axis of perforations. The approximation is valid even for $p = \lambda_0/9.4$ (see Fig. 5.29(right)).

On the other hand, we predicted that the effective relative permittivity seen by propagating TM_0 mode to lie somewhere between the limits given by MG model for parallel and perpendicular polarization, since as has been shown, the TM_0 mode possesses electric field components both with parallel and perpendicular orientation with respect to axis of perforations. In Fig. 5.28(left) and 5.29 (left), we can see the $\epsilon_{r,eff}$ to be between the permittivity limits. However, it is interesting that as the frequency goes higher, the permittivity for parallel polarization prevails (see Fig. 5.29(right)).

The discrepancy between the theoretical model and simulation results at 20 GHz for period of perforations $p = 3$ mm and for porosities below circa 60 % (i.e. larger diameter of perforations D) in Fig. 5.28(left) can be assigned to electromagnetic bandgap behavior of the structure. At 20 GHz, the 3 mm period corresponds to electrical length about $\lambda_0/5$ and the effective media concept is no longer accurate.

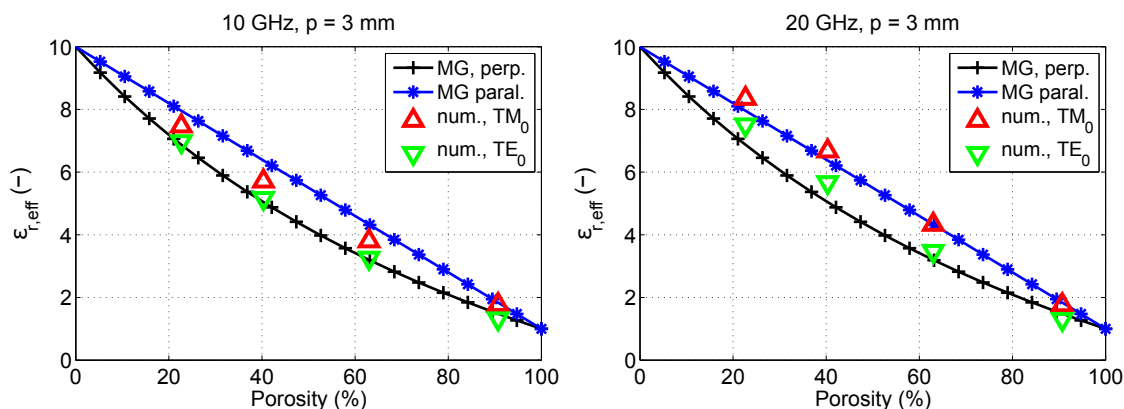


Fig. 5.28: Comparison between theoretical model based on Maxwell-Garnett approximation and effective relative permittivities as seen by surface wave modes at 10 GHz (left) and 20 GHz (right). Period of perforations $p = 3$ mm. The reason why for porosities below 50 % (at 20 GHz) the permittivity values for TM waves exceed the limits, is that the electromagnetic bandgap properties start to be present in the structure.

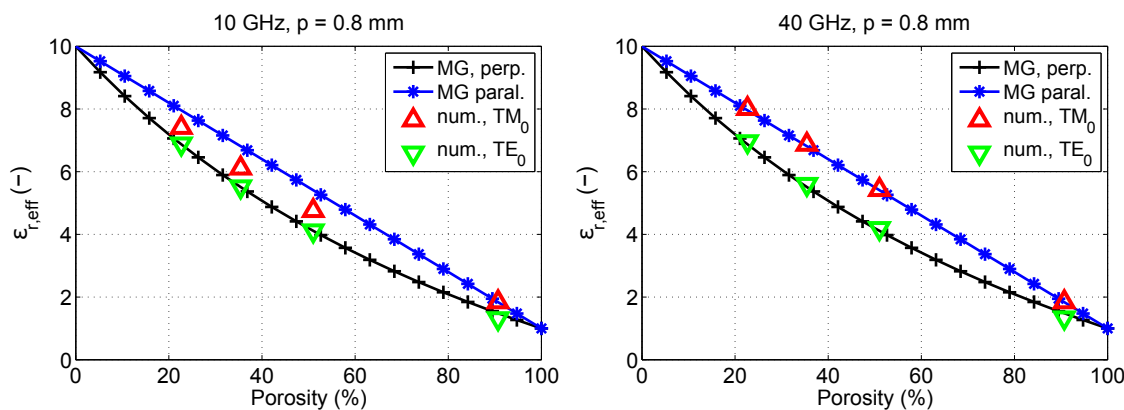


Fig. 5.29: Comparison between theoretical model based on Maxwell-Garnett approximation and effective relative permittivities as seen by surface wave modes at 10 GHz (left) and 40 GHz (right). Period of perforations $p = 0.8$ mm.

5.3 Perforated Dielectric Resonator Antennas

The last two sections dealt with perforated dielectric substrates from rather theoretical point of view, the effective relative permittivity as seen by various polarizations have been determined and simple quasi-static model for effective permittivity prediction has been proved valid also in the microwave region and in case of surface waves.

In this chapter, we focus on application of perforated substrate to single dielectric resonator antenna (DRA) elements, we investigate the influence of perforated walls on resonant frequency, bandwidth and radiation patterns of infinite and finite ground plane DRAs and we compare these results with homogenized models of perforated dielectrics, which are computationally much more efficient. We further deal with the mutual coupling increase between perforated DRA elements caused by excitation of surface waves on perforated dielectric layer and again we compare the outcomes with homogenized models as well as with conventional DRA elements operating at the same frequency.

5.3.1 Single Element Perforated DRA

For analysis of single element perforated dielectric resonator antennas we use rectangular shape of dielectric resonator with square footprint. As dielectric material, we consider dielectric with $\epsilon_r = 10$ and $h = 3.175$ mm.

We perform the testing for several structures with two different porosities and compare the results to conventional DRA as well as perforated DRA in which the perforated substrate is substituted by homogenous equivalent.

The triangular lattice provides larger porosity for certain D/p ratio compared to square lattice and since larger porosity transfers to smaller effective permittivity (see Fig. 5.30), the triangular lattice is superior to square lattice from this point of view. In spite of this fact, we decide to use square lattice in our analysis for the following reason. In triangular lattice, two of the four DRA's side walls are perturbed, meaning the boundaries of the dielectric "island" are not uniform and the perforations create kind of zig-zag pattern (see Fig. 5.31). As a result, the virtual size of the resonator is changed due to the interfaces with altered properties. If we consider perforated regions as homogenous equivalents of effective permittivity, the problem can be also seen as rippled interfaces between two dielectrics (DRA and its surrounding). In square lattice, this issue does not arise.

The dielectric resonators are created by cylindrical air perforations with diameter $D = 0.8$ mm and $D = 0.6$ mm. We examine the performance for period value $p = D = 0.8$ mm, revealing ratios $D/p = 1$ and $D/p = 0.75$, respectively. According

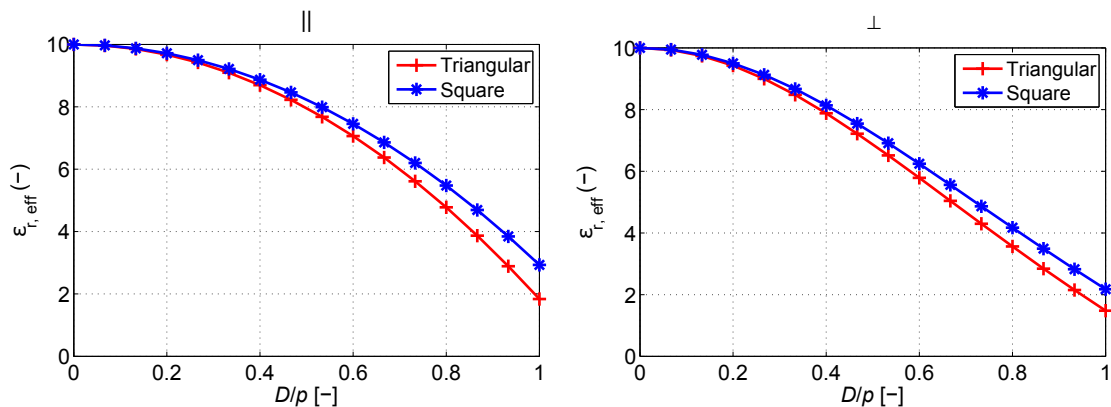


Fig. 5.30: Effective relative permittivity as a function of D/p ratio. Triangular lattice gives in general smaller effective permittivity compared to square lattice.

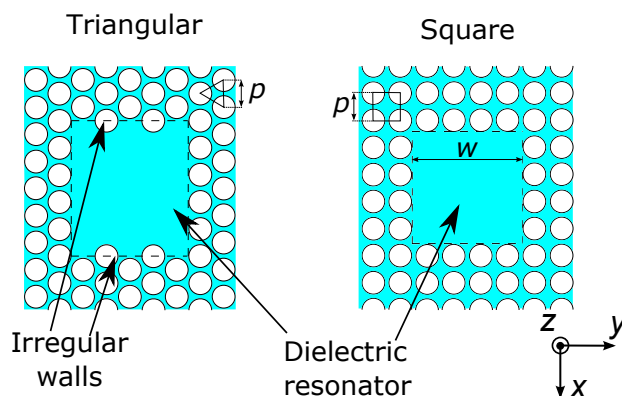


Fig. 5.31: Dielectric island (resonator) created by air perforations in triangular lattice (left) and square lattice (right). The ratio D/p is in both cases 0.833.

to theoretical model given in section 5.2, we can assume approximate values of effective relative permittivity for electric field orientation parallel to the axis of perforations to be $\epsilon_{r,eff} = 2.93$ and $\epsilon_{r,eff} = 5.08$. Triangular lattice would decrease these values to $\epsilon_{r,eff} = 1.84$ and $\epsilon_{r,eff} = 4.32$. For \mathbf{E} field perpendicular to the axis of perforations the approximate effective relative permittivities are $\epsilon_{r,eff} = 2.18$ and $\epsilon_{r,eff} = 3.83$, for $D/p = 1$ and $D/p = 0.833$, respectively. Again, the values in triangular lattice would be lower, $\epsilon_{r,eff} = 1.48$ and $\epsilon_{r,eff} = 3.2$.

The resonators are fed by short slots in the ground plane and for simplicity we use discrete ports with 50Ω impedance for feeding the slots. The length of the slot is in each case adjusted to provide best impedance matching. To have more realistic models, we use additional dielectric layer (Arlon 25n, $\epsilon_r = 3.38$, $h = 1.524$ mm). This layer is necessary from manufacturing point of view, where microstrip feeding network for feeding the slots is located here.

Infinite Ground Plane Performance

In analyzing the performance of perforated DRAs it might be convenient to start with models including not only infinite ground plane but also infinite perforated layer surrounding the island resonator. In this way, we can analyze the antenna elements without the interfering effects of edge diffraction (ground plane edge and end of perforated dielectric layer). Also, the comparison to traditional DRAs is simplified in this way.

For this reason, we use absorbing boundaries based on perfectly matched layers (open boundary in CST MWS) in directions x and y placed at the edges of the model (no space between edge and boundary condition). In $\pm z$ directions we use open boundaries with additional space between the structure and the boundary.

Directivity radiation patterns are given as it is not essential at this step to include material losses and reflection losses into account analyzing qualitatively the radiation characteristics of various configurations.

The size of the resonator's footprint is chosen so that the feeding aperture is completely hidden under the island of dielectrics and do not exceed to the perforated region. The structural difference between the holes of the perforated dielectric and homogenous effective dielectric would cause slight change in the input impedance of the antenna if the feeding slot exceeded to these areas. The comparison between perforated and homogenized dielectric would be in that case difficult. It also means that the antennas are not always perfectly matched to the input ports. For better matching, the slots would in some cases need to exceed the footprint of the resonator. The geometry of the DRA embedded in homogenized dielectric layer can be found in Fig. 5.32.

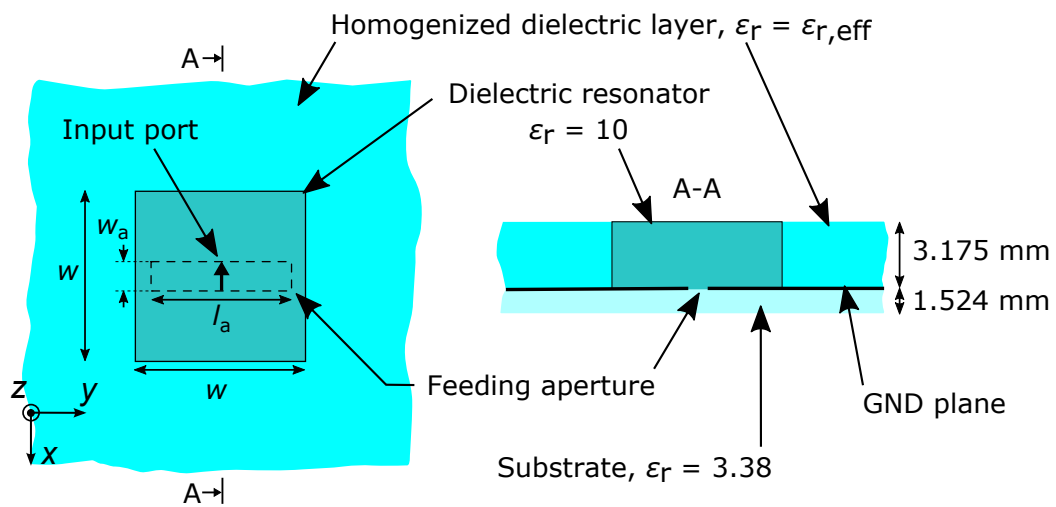


Fig. 5.32: Geometry of the DRA embedded in homogenized dielectric layer with equivalent properties to the perforated DRA in Fig. 5.31.

The first resonator to be analyzed is formed by a dielectric island of width $w = 5.6$ mm, i.e. $w = 7p$ with lattice parameters $D = p = 0.8$ mm, revealing approximate value of homogenous equivalent effective relative permittivity in the range of $\varepsilon_{r,\text{eff}} = 2.18 - 2.93$. It is shown that the homogenous model approximates the perforated substrate most accurately when $\varepsilon_{r,\text{eff}} = 2.85$. This result confirms the finding that the effective permittivity for the TM_0 wave is much closer to the upper limit of the permittivity range, since the TE_{111} mode of the dielectric resonator has very similar field distribution as a half period of TM_0 wave (\mathbf{E} field has component perpendicular and also parallel to the axis of perforations).

We proceed with slight change of lattice parameters to $D = 0.6$ mm and $p = 0.8$ mm, resulting in width of the dielectric island $w = 5.8$ mm (i.e. $7p + (p - D)$). The maximum $\varepsilon_{r,\text{eff}}$ for such lattice is 5.08, but the best match between perforated dielectric and its homogenous equivalent is observed for $\varepsilon_{r,\text{eff}} = 5.5$. This suggests, that the homogenous surrounding alone is not sufficient to explain the frequency shift of the resonance, but the shift is also caused by irregular walls created by the perforations which make the island somewhat larger in size, thus the frequency shift to lower frequencies can be explained as a combination of the effect of slightly enlarged resonator and the effect of surrounding material with certain material permittivity. However, these two effects cannot be separated and analyzed separately and they both increase the virtual size of the antenna (width w).

The reflection coefficients comparing perforated DRA and square DRA embedded in homogenous equivalent dielectric are given in Fig. 5.33. The effective permittivities of homogenous equivalents are found by comparison to the reference perforated DRA model, that is, we simply tune the relative permittivity of the homogenous dielectric layer up to the value, where the resonant frequency equals resonant frequency of the perforated DRA (identical dimensions of the feeding aperture are used). For shape simplification we proceed with smooth wall DRA embedded inside higher $\varepsilon_{r,\text{eff}}$ dielectric material.

Considering radiation patterns, the comparison for perforated and homogenized surrounding of the DRA element is given in Fig. 5.35 and 5.36 for E-plane and H-plane respectively. We see the homogenized model gives a difference about 0.2 dB in broadside direction and about 0.5 dB for endfire radiation ($\theta = \pm 90^\circ$) in the limit case $D/p = 1$. For manufacturable lattice in which D/p ratio is 0.75, the agreement is even better, 0.1 dB in broadside and 0.4 dB in the endfire direction. The radiation in the H-plane (see Fig. 5.36) is almost unaffected by the increased permittivity of the surrounding dielectric material. The antenna orientation within spherical coordinate system is given in Fig. 5.34.

We study the effects of homogenous equivalent surrounding the dielectric resonators on radiation patterns and resonant frequency, we start with $\varepsilon_{r,\text{eff}} = 1$, which

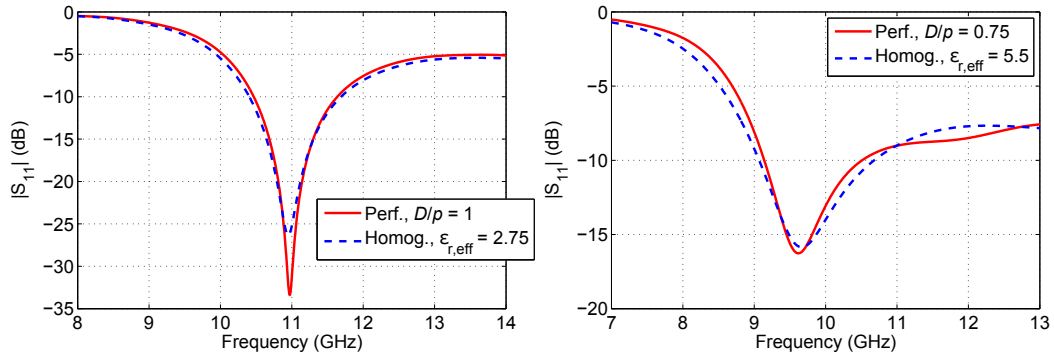


Fig. 5.33: Reflection coefficient for perforated DRA and DRA surrounded by homogenous dielectric. Theoretical limit in which $D/p = 1$ (left) and $D/p = 0.75$ (right).

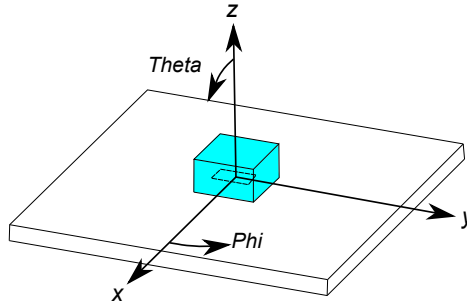


Fig. 5.34: Spherical coordinate system and antenna alignment.

corresponds to conventional air surrounded DRA element, we increase gradually the value up to $\epsilon_{r,\text{eff}} = 5$. By varying the relative permittivity $\epsilon_{r,\text{eff}}$ we are detuning the element at the same time. To have a valid comparison on the variation of resonant frequency with $\epsilon_{r,\text{eff}}$, we change the input port impedance to match the impedance of the detuned element for each $\epsilon_{r,\text{eff}}$ value. For completeness we also give the input impedance for each $\epsilon_{r,\text{eff}}$ value (see Fig. 5.37).

Finite Ground Plane Effects

In the analysis of perforated DRAs on infinite ground covered by infinite perforated dielectric layer, we can directly see how the energy is trapped in the substrate, creating two lobes in the plane of the ground (Fig. 5.35). Nevertheless in reality, the perforated dielectric layer as well as the conductive ground is terminated at some point and moreover, the size of those layers does not have to be identical. The trapped, surface waves are then sources of diffraction at the mentioned terminations.

The assumption here is that the perforated layer around the dielectric resonator highlights the ground plane effects, since more energy is directed towards the edges

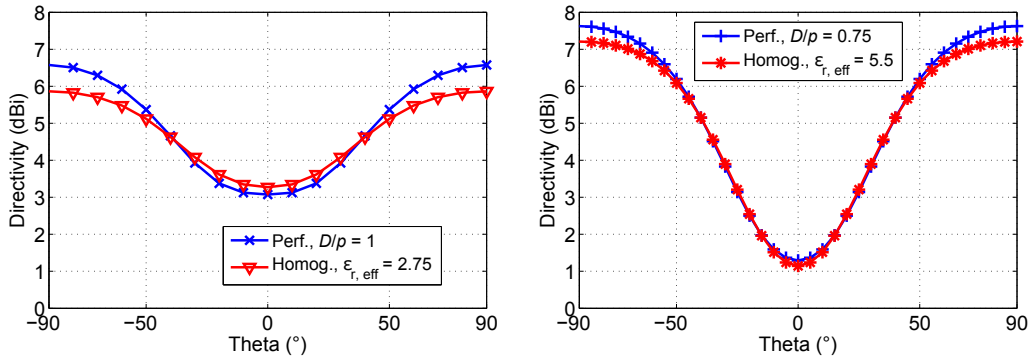


Fig. 5.35: E-plane radiation patterns for infinite ground plane for the case $D/p = 1$ (left) and $D/p = 0.75$ (right) comparing radiation patterns of perforated DRA and DRA surrounded by homogenized material.

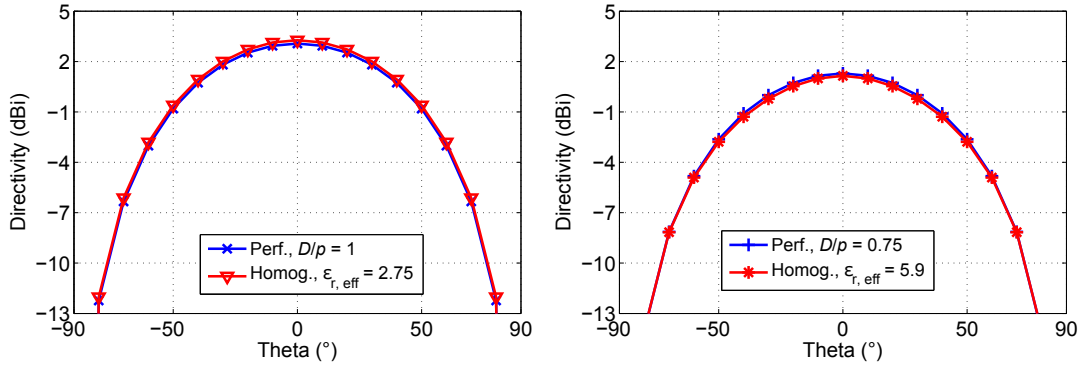


Fig. 5.36: H-plane radiation patterns for infinite ground plane for the case $D/p = 1$ (left) and $D/p = 0.75$ (right).

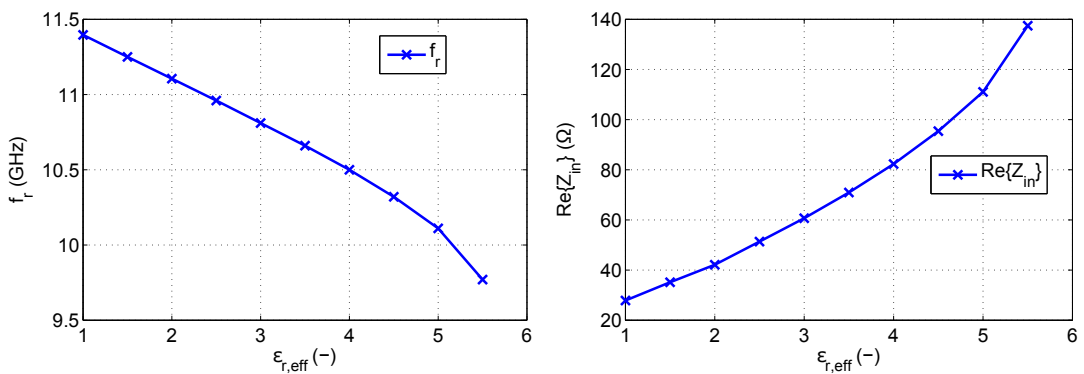


Fig. 5.37: Resonant frequency (left) and input resistance (right) as functions of effective relative permittivity $\epsilon_{r,\text{eff}}$ for DRA in homogenized dielectric model. Parameters of the structure are $w = 5.6$ mm, $l_a = 5$ mm, $w_a = 0.84$ mm

compared to the broadside direction (perpendicular to the ground). The level or ripples, particularly in the E-plane radiation pattern should be higher, than in case of conventional DRA. We do the comparison for several different sizes of the ground plane. In our simulations, the size of the perforated dielectric layer copies the size of the ground plane; however, in general the perforated dielectric layer can be smaller. The geometry of the DRA elements is the same as in previous section. We should mention that the finite ground plane can also influence the impedance characteristics of the antenna, however this happens only if the ground plane is not sufficiently large. As we choose the minimum ground plane size to be $gnd = 60$ mm, which is about $2\lambda_0$ we do not have to deal with this issue.

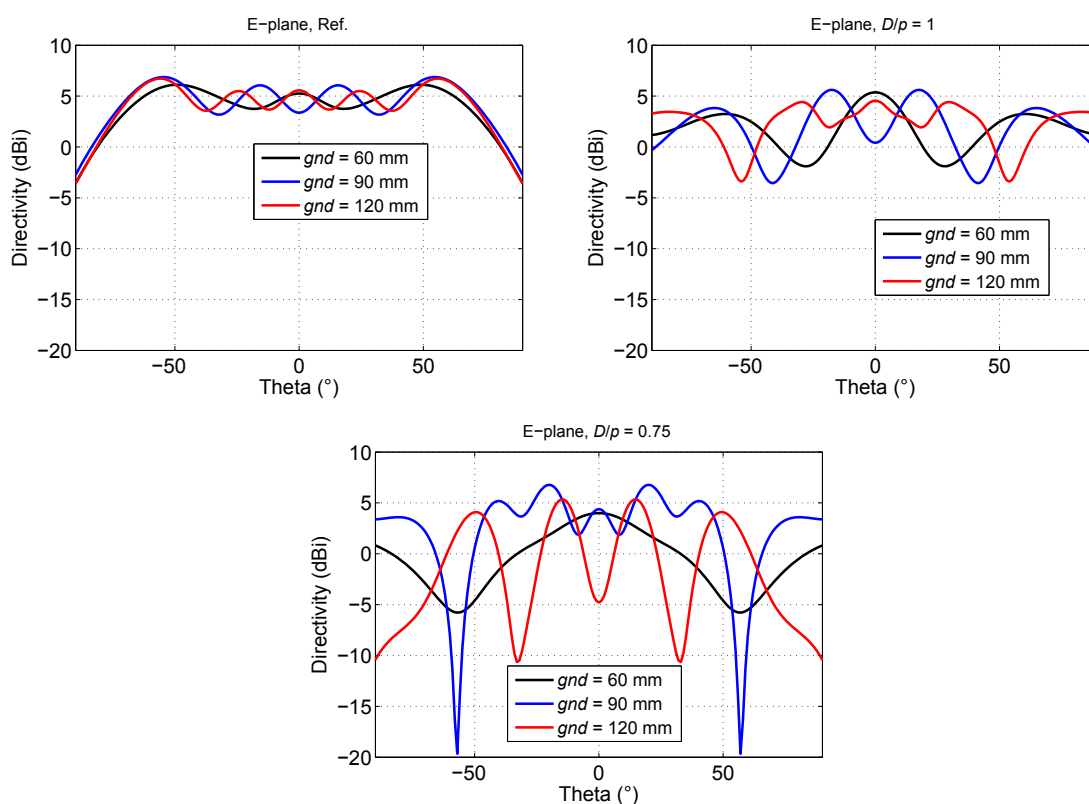


Fig. 5.38: E-plane radiation patterns (directivity) of finite ground plane DRA for the upper hemisphere ($-90^\circ < \theta < 90^\circ$) for conventional rectangular DRA (top left), perforated DRA with $D/p = 1$ (top right) and with $D/p = 0.75$ (bottom). As the effective permittivity of the surrounding is larger (smaller D/p ratio), more of the energy propagates along the substrate, towards the edges. The result is increased ripples in the far-field.

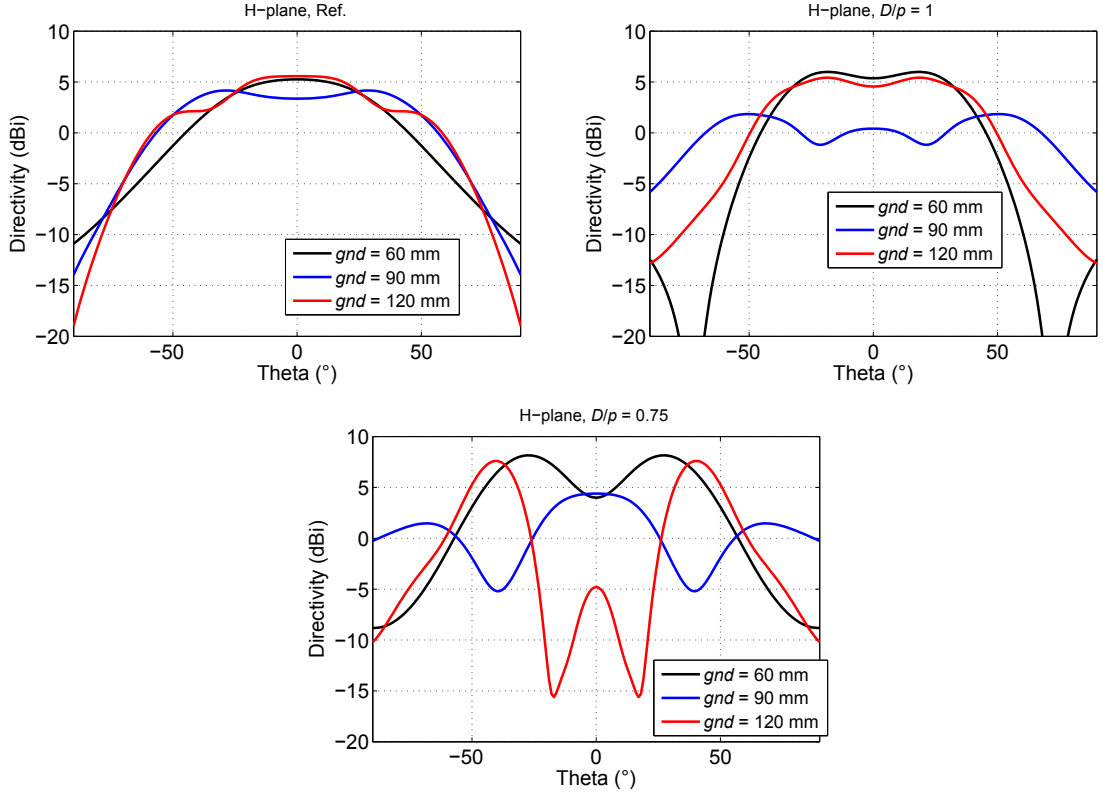


Fig. 5.39: H-plane radiation patterns (Directivity) of finite ground plane DRA for the upper hemisphere ($-90^\circ < \theta < 90^\circ$) for conventional rectangular DRA (top left), perforated DRA with $D/p = 1$ (top right) and with $D/p = 0.75$ (bottom).

5.3.2 Mutual Coupling Between Perforated DRA Elements

Mutual coupling between perforated DRA elements is studied through transmission coefficients between two elements. We evaluate the coupling in both E-plane and H-plane of the resonators and for this; we use models with perforations in dielectrics instead of homogenized models.

We examine the coupling for two sets of square lattice parameters, first D/p ratio is set to 1 ($f = 0.79$, $\varepsilon_{r,\text{eff},\parallel} = 2.93$) and then to 0.75 ($f = 0.44$, $\varepsilon_{r,\text{eff},\parallel} = 5.9$), which are the same values as have been used in single element characterization. The hole diameter and period in these cases are $D = 0.8$ mm and $p = 0.8$ mm for $D/p = 1$ mm and $D = 0.6$ mm and $p = 0.8$ mm for $D/p = 0.75$. The resonant frequency of dielectric resonators for $D/p = 1$ is $f_r = 10.95$ GHz and for $D/p = 0.75$ it is $f_r = 9.7$ GHz.

The absolute distance between adjacent walls of the resonators (see Fig. 5.40) is selected to be an integer multiple of perforation period $p = 0.8$ mm ($n \cdot p$, $n = 1, 2, 3, \dots$). For number of perforations between the elements we choose a range $n = 3$ to 33, i.e from $n \cdot p = 2.4$ mm to $n \cdot p = 26.4$ mm. The inter-element separation

s for certain number of perforations between the resonators n is then calculated as $s = w + n \cdot p$, where w is the width of the resonator (see Fig. 5.32), since s determines the distance between the centers of resonators and not between their edges. The separation distance s for resonators on lattice with $D/p = 1$ ($w = 5.6$ mm) thus ranges between 8 mm and 32 mm. Considering the center frequency 10.95 GHz, the separation distance in terms of free space wavelengths ($\lambda_0 = 27.4$ mm) is in the range $s = 0.29\lambda_0$ to $s = 1.17\lambda_0$.

For lattice ratio $D/p = 0.75$, the width of the resonators is slightly larger $w = 5.8$ mm and s is in the range 8.2 - 32.2 mm. Since the resonant frequency is lower for this lattice, i.e. $f_r = 9.7$ GHz, the free space wavelength is $\lambda_0 = 30.9$ mm and the range of s in wavelengths is $s = 0.27\lambda_0$ to $s = 1.04\lambda_0$.

As a reference structure, we use conventional DRA elements with $h = 3.175$ mm and $w = 5.6$ mm. The resonant frequency corresponding to these dimensions and dielectric material with $\epsilon_r = 10$ is $f_r = 12$ GHz. We do not tune the element to the same resonant frequency as perforated DRA, since this would mean changed aspect ratio, which we want to avoid.

As we use the same range of spacing as in case of perforated DRAs, the s ranges between $s = 0.32\lambda_0$ to $s = 1.28\lambda_0$. The results of transmission coefficient of resonators aligned in the E-plane for reference elements as well as for two different perforated elements can be found in Fig. 5.41. We can see that at spacing $s < 0.5\lambda_0$, there is no performance degradation in terms of mutual coupling, on the contrary, the mutual coupling is even reduced between perforated DRAs compared to standard DRAs. In the region $s < 0.5\lambda_0$ the transmission coefficient shows the lowest value in case of largest effective permittivity of the medium in between ($D/p = 0.75$). For approximately $s > 0.5\lambda_0$, the mutual coupling is getting larger as the perforations have smaller diameters (i.e. smaller D/p ratio). For elements separated by distance $s = 1\lambda_0$, causes the perforated substrate with $D/p = 0.75$ mutual coupling increase by 5.1 dB. Even the theoretical lattice with $D/p = 0.75$ increases the mutual coupling by more than 3 dB (also for $s = 1\lambda_0$).

We can sum up the results by stating, that in vary small arrays (e.g. 2x1, 2x2), the mutual coupling would not cause any significant degradation of the antenna array impedance characteristics. However, the radiation pattern would be still influenced because of the surface wave excitation and subsequent edge diffraction. On the other hand, for larger arrays, the mutual coupling between non-adjacent elements is significantly increased and the final gain of the antenna array can thus be reduced.

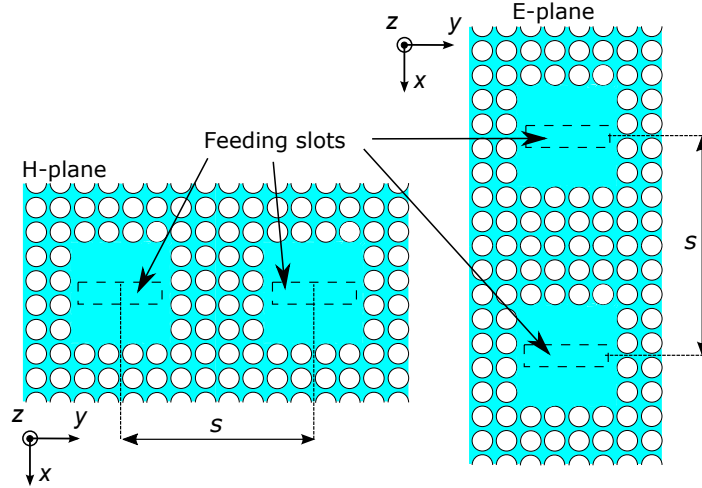


Fig. 5.40: Perforated dielectric resonators arranged in H-plane (left) and in E-plane (right). Separation distance s is the crucial parameter.

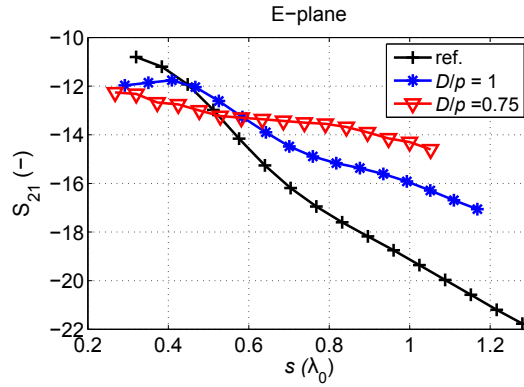


Fig. 5.41: Transmission coefficient between two resonators aligned in the E-plane comparing conventional DRA elements with $f_r = 12$ GHz (black), perforated DRAs with $D/p = 1$ $f_r = 10.95$ GHz (blue) and finally perforated DRAs with $D/p = 0.75$ $f_r = 9.7$ GHz (red). Inter-element distance s is plot in free space wavelengths at given resonant frequencies of individual antennas.

5.3.3 Design for Manufacturing

We slightly modify the perforated DRA models from previous section to conform to the manufacturing process. This means adjusting the grid parameters p and D and the dimensions of the resonators (i.e. w) accordingly. Also, in the previous section we considered the ground plane to be infinite; however, in final model we design the size of the ground plane so that it has negligible influence on the scattering parameters results. The ground plane edges are thus part of the simulation model.

The parameters of the perforations are $p = 1.15$ mm and $D = 1$ mm resulting in $D/p = 0.867$. This D/p ratio corresponds to porosity $f = 0.6$ and effective relative permittivity for parallel and perpendicular polarizations $\epsilon_{r,\text{eff},\parallel} = 4.59$ and

$\epsilon_{r,\text{eff},\parallel} = 3.4$, respectively. The width of the perforated square DRA is $w = 8.2$ mm and height $h = 3.175$ mm. The resonant frequency corresponding to this geometry is 8.45 GHz.

The reference structures (i.e. conventional square-footprint DRAs) possess the same aspect ratio as the perforated DRAs and since the possible height of the resonators is fixed (one substrate layer $h = 3.175$ mm), we select $w = 8.2$ mm. However, due to changed surrounding of the resonators (air in this case and perforated substrate in the previous case), the resonant frequency is shifted upward to 8.85 GHz.

The simulation results of reflection and transmission coefficient for the resonators aligned in the E-plane and with spacing $\lambda/2$ and λ can be found in Fig. 5.42 for perforated DRAs and in Fig. 5.43 for reference DRAs. The separation distances in wavelengths correspond to central frequencies of the structures; hence the absolute distances are not identical.

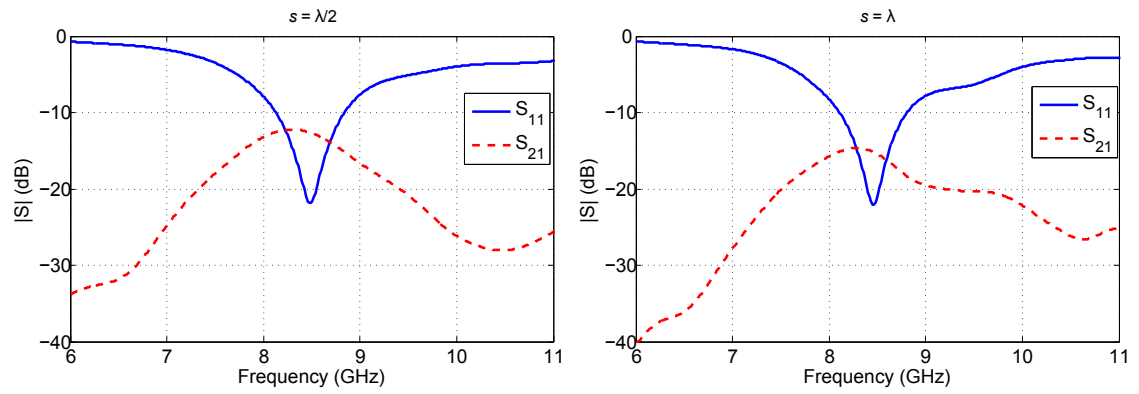


Fig. 5.42: Reflection and transmission coefficient for perforated DRAs aligned in their E-plane for two inter-element distances $s = \lambda/2$ (left) and $s = \lambda$ (right).

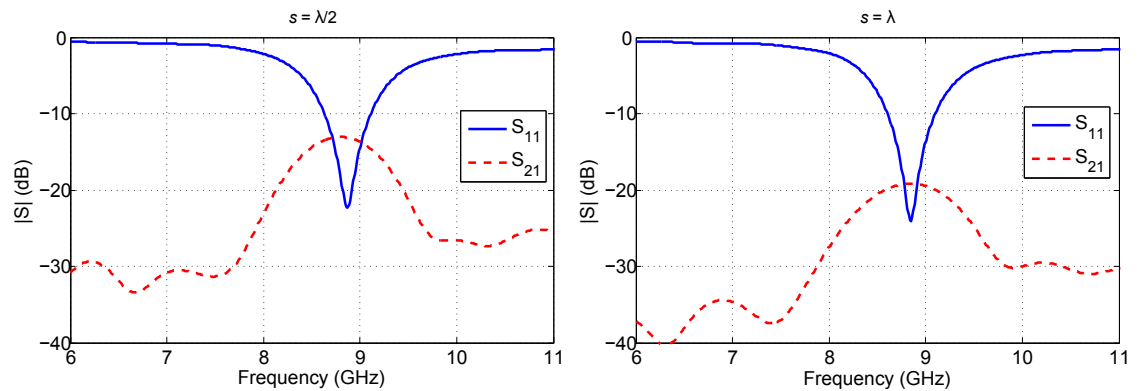


Fig. 5.43: Reflection and transmission coefficient for conventional DRAs aligned in their E-plane for two inter-element distances $s = \lambda/2$ (left) and $s = \lambda$ (right).

5.3.4 Experimental Validation

In experimental verification, we focus on the resonant frequency shift caused by the perforated walls around the resonator. But what is more important, we confirm by experiment the mutual coupling increase due to surface wave excitation on the perforated dielectric slab, which is formed by the perforated substrate between the elements. As a reference, we manufacture conventional DRAs with the same aspect ratios as have the perforated DRA elements and with little higher resonant frequency due to the absence of perforated material around the resonator. The comparison between transmission coefficients is then done on electrical distance basis, instead of absolute distance. It follows that we measure only scattering parameters and are not concerned with radiation patterns.

The samples of perforated DRAs are fabricated by perforating the microwave substrate Arlon 1000 with $\epsilon_r = 10$, $\tan\delta = 0.003$ and thickness $h = 3.175$ mm. The perforations are created by drilling into the substrate with drill hole of 1 mm and period of square lattice $p = 1.15$ mm revealing D/p ratio 0.869. The overall dimensions of the perforated dielectric layer are the same as the size of the ground plane, thus the ground plane is covered by perforated dielectric up to its edges.

We measure the transmission coefficient for two configurations of the resonators; the resonators are aligned in their E-planes, since coupling in this plane is critical compared to H-plane. The inter-element separation s must be an integer multiple of perforation period p (i.e. $s = n \cdot p$, $n = 1, 2, 3, \dots$). We select two separation s values so that we have approximately $s = \lambda_0/2$ and $s = \lambda_0$; this occurs for $n = 15$ and $n = 30$ considering 8.45 GHz central frequency ($\lambda_0 = 35.5$ mm). The exact separation distances in terms of free-space wavelengths are $0.486\lambda_0$ and $0.972\lambda_0$, respectively.

In manufacturing of the reference antennas we are not limited by the period of perforations, thus the separation distances are exactly $\lambda_0/2$ and λ_0 , at central frequency determined from simulations $f_r = 8.83$ GHz ($\lambda_0 = 34$ mm).

The measured results of reflection coefficients S_{11} , S_{22} and of transmission coefficient S_{21} of reference antennas show small down-shift in resonant frequency to 8.66 GHz, compared to the simulations 8.85 GHz (i.e. 2.2 %). This resonant frequency down-shift is more pronounced in perforated DRA elements, the measured resonant frequency is only 8.1 GHz, compared to simulated 8.45 GHz (i.e. 4.2 %).

Measurement results are given in Fig. 5.44 and 5.45 and comparison with simulation results of transmission coefficient in Fig. 5.46. Very good agreement between simulation and measurement can be seen.

Aside fabrication tolerances, this frequency shift can be explained by tolerances in relative permittivity of the dielectric layer. It would also explain, why the resonant

frequency shift is larger in perforated DRA structure, since in this case, the larger permittivity also affects the surrounding of the antenna (i.e. perforated dielectric). The photographs of the fabricated antennas are given in Fig. 5.47 to 5.49.

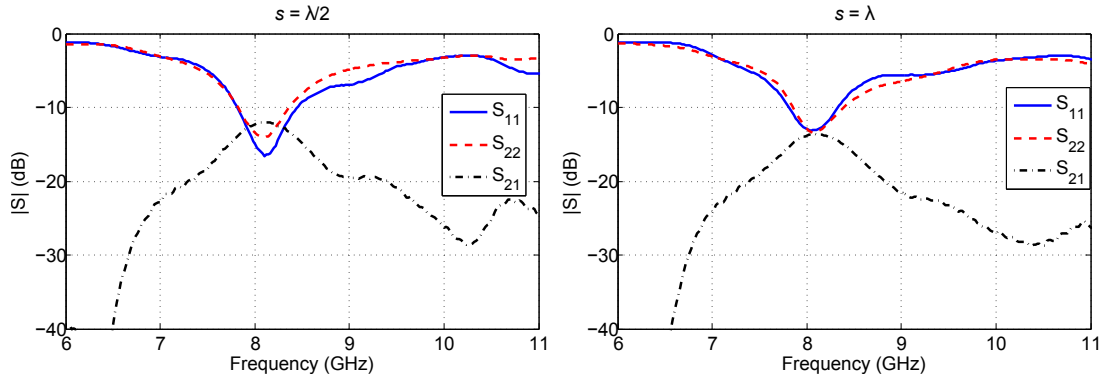


Fig. 5.44: Measured reflection and transmission coefficient for perforated DRAs aligned in the E-plane for two separation distances $s = \lambda/2$ (left) and $s = \lambda$ (right).

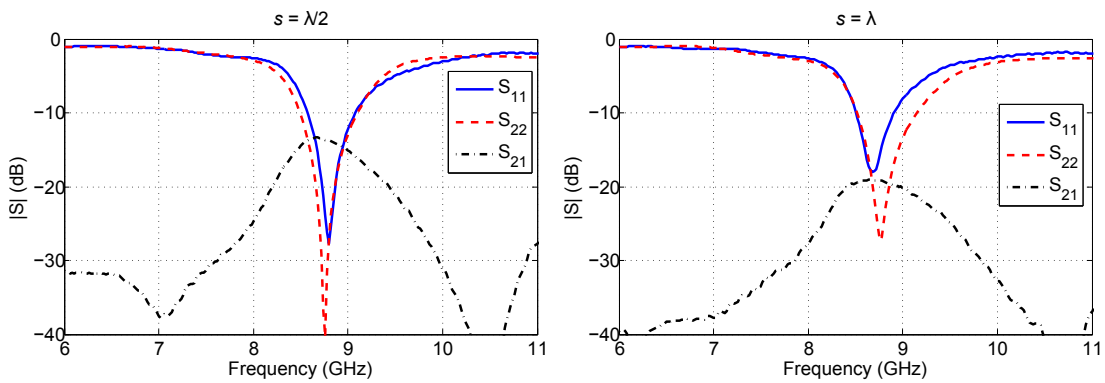


Fig. 5.45: Measured reflection and transmission coefficient for conventional DRAs aligned in their E-plane for two separation distances $s = \lambda/2$ (left) and $s = \lambda$ (right).

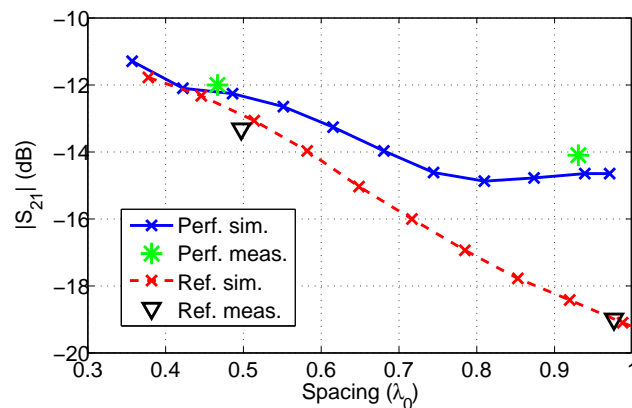


Fig. 5.46: Simulated and measured results of $|S_{21}|$, comparing conventional DRAs with perforated DRAs. Slight increase of $|S_{21}|$ in simulation results of perforated DRAs (blue) is caused by a standing surface wave excited in the perforated substrate.

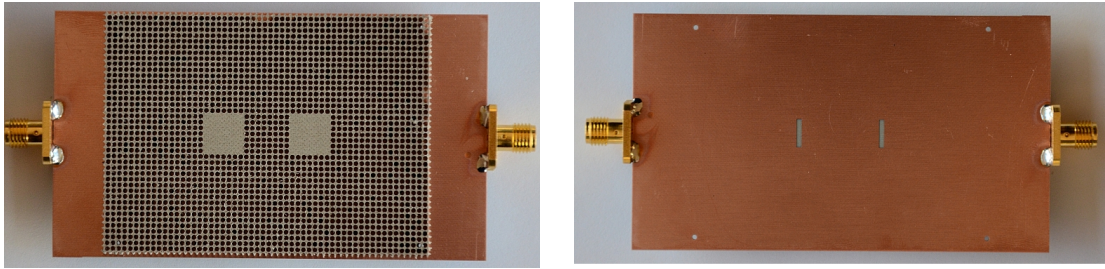


Fig. 5.47: Manufactured prototype of the perforated DRAs (left), with feeding apertures (right).

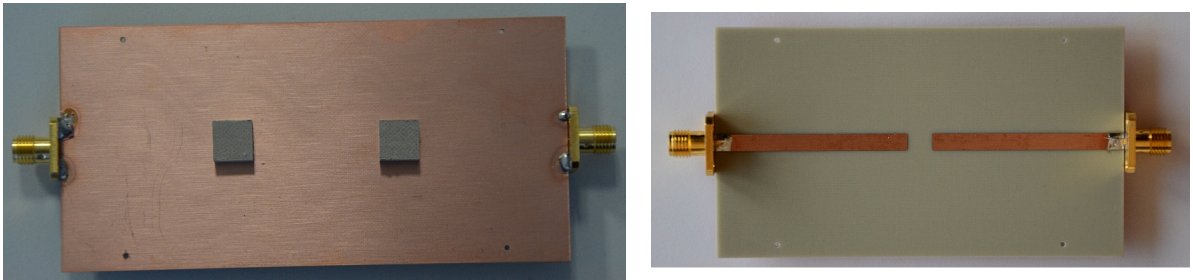


Fig. 5.48: Manufactured prototype of the reference DRAs with 1λ spacing (left), microstrip feeding lines (right).

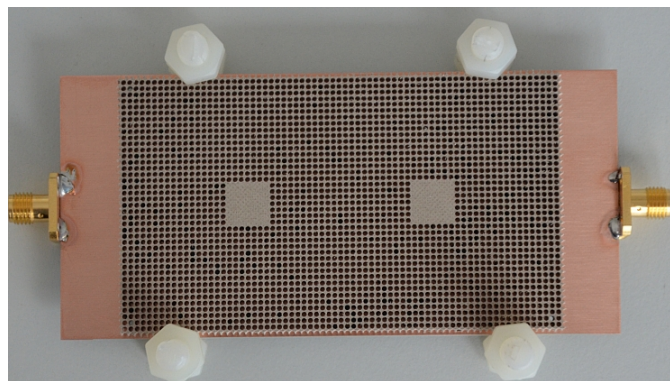


Fig. 5.49: Manufactured prototype of the perforated DRAs with 1λ spacing and with holding screws made from plastic (right).

5.3.5 Summary

Perforating a substrate layer and creating dielectric islands is a very interesting technique of manufacturing DRA arrays. We have shown, how the perforated substrate surrounding the resonator alters the performance of the single element antenna in terms of resonant frequency and radiation patterns. For the performance assessment we used two type of models, first, actual model of perforated material and second, the homogenized layer with effective permittivity determined by equations from previous sections.

Considering the mutual coupling, we can sum up the results of this section by stating, that in vary small arrays with small separation distance between the elements (e.g. 2x1, 2x2), the mutual coupling would not cause any significant degradation of the antenna array impedance characteristics. However, the radiation pattern would be still influenced because of the surface wave excitation and subsequent edge diffraction. On the other hand, for larger arrays, the mutual coupling between non-adjacent elements is significantly increased and the final gain of the antenna array can thus be reduced.

The perforated substrate with $D/p = 0.87$ used in the final simulations as well as in the experiments has shown approximate effective relative permittivity (parallel polarization) of $\varepsilon_{r,\text{eff},\parallel} = 4.6$. Due to this fact, the coupling between the elements aligned in the E-plane increased by 1 dB at separation distance $0.5\lambda_0$ and by 4.5 dB at separation distance $1\lambda_0$.

Conclusions

The original contributions of the thesis, as pointed out in the Chapter 2, lie in the areas of enhanced gain DRA elements based on the higher-order mode excitation, mutual coupling between HO mode resonators and last but not least, in the area of perforated dielectrics and perforated DRAs.

We have proposed rectangular and cylindrical DRA elements operating with modes TE_{133} and HEM_{133} , respectively. The antennas were configured as simple shaped resonators placed on top of a conductive ground plane. It turned out that the size of the ground plane had non-negligible influence on the maximum achievable gain. We optimized the antennas for maximum gain and we obtained optimum aspect ratios of the basic shapes that maximize the gain. Certain aspect ratios enabled simultaneous excitation of other HO modes thus improving the impedance bandwidth; however, it did not improve the bandwidth of the enhanced gain frequency region. With fabricated prototypes of proposed antennas we have achieved maximum gains of 11.6 dBi for cylindrical and 11.9 dB for rectangular DRAs, revealing about 5.6 dB and 5.9 dB gain improvement compared to fundamental, broadside radiating modes of given resonators.

By introducing a small air gap between the cylindrical resonator and its ground plane, we were able to further increase the gain from 11.6 dBi to 13.2 dBi. The common disadvantage of our HO mode solutions is their limited bandwidth. Even though the resonators were built from material with $\epsilon_r = 6.15$, the impedance bandwidth was only about 3 %. This bandwidth was extended by excitation of other HO modes in resonator with square footprint; however, the main limitation remained the reduced bandwidth of enhanced gain region.

The concept of cylindrical HEM_{133} mode antenna was utilized for design of mm-wave directive, SIW-fed DRA based on LTCC manufacturing technology at frequency about 26 GHz. Very low losses of the LTCC dielectrics resulted in high radiation efficiency of 87 %. Moreover, due to very good shape accuracy of LTCC technology we obtained excellent agreement between simulations and measurements.

In Chapter 4 we shifted our attention to the evaluation of mutual coupling between rectangular dielectric resonators operating with HO modes intended for gain

enhancement. We worked with modes TE_{113} , TE_{115} and finally with the TE_{133} . Resonators excited with TE_{113} , TE_{115} modes turned out to be suitable elements for antenna array applications. Moreover, both modes showed reduced coupling levels compared to fundamental mode DRAs, which makes them interesting for dense array applications. For example TE_{113} mode showed reduced mutual coupling by 12 dB factor in case of separation distance $0.5\lambda_0$ compared to fundamental TE_{111} mode. Excitation of HO mode can thus represent a new mutual coupling reduction technique. Considering TE_{133} mode, due to physical size and the large side-lobes in the E-plane, the element is not suitable for 2D antenna arrays; however, in case of 1D, H-plane antenna arrays, the element gives very similar mutual coupling levels as the fundamental mode DRAs (i.e. TE_{111}).

The third part (Chapter 5) of the thesis is focused on perforated dielectrics and perforated DRAs. Analytical model based on quasi-static approximation and on Maxwell-Garnett mixing rules is given and evaluated at microwave frequency bands for TEM wave. Compared to models in the open literature, our model respects the anisotropic properties of the perforated dielectrics and can be directly used to predict properties of perforated dielectrics in various antenna and propagation application areas, e.g. analysis and design of reflectarrays, transmitarrays, planar lenses and other transformation optics devices.

We extend the analysis to propagation of surface waves on perforated substrates. We determined the effective relative permittivities as seen by TM_0 and TE_0 surface wave modes and we successfully used the model derived for TEM wave to pose the limits for TM_0 and TE_0 mode relative permittivities of perforated substrate.

Last, we dealt with the perforated DRAs, we examine the behavior of single element radiators and we verify the usability of effective permittivity models. Resonant frequency shift due to the perforated surrounding of the DRA, instead of air, is investigated as well as the radiation pattern modification caused by edge diffraction of surface waves. We tested the mutual coupling between perforated DRs and we compared the results to conventional DRAs. For porosity of 87 % the mutual coupling increased by only 1 dB factor for perforated DRs $0.5\lambda_0$ apart; however, the increase was almost 5 dB for $1\lambda_0$ separation, which proved that the surface waves in perforated substrate increase the coupling levels among the elements of perforated antenna arrays.

Many interesting areas for a future research open up based on the work presented in this thesis. Considering the HO modes for gain enhancement, important issues are related to extending the bandwidth of the elements. One hint given in Chapter 3 is a controlled excitation of modes TE_{133} and TE_{115} close to each other in the frequency spectrum. Both modes can provide enhanced directivity if the aspect ratio is suitably selected. Another interesting research direction is the excitation

of dual linear polarization and eventually circular polarization in such resonators. Hybrid and reconfigurable designs might also be relevant.

In relation to Chapter 4 antenna array design with HO mode elements is very promising. Due to the directive radiation patterns of the single elements, limited use in scanning arrays seems also possible. If working with the TE_{133} mode, we can reduce the size of the array by factor of 4, since the HO mode provides about 6 dB higher gain compared to conventional TE_{111} mode DRA.

The analytical description of perforated dielectrics for permittivity reduction at microwave frequencies seems to be completely lacking in the open literature. Inclusion of the losses into the models deployed in this thesis would be very practical. The perforated dielectrics can be used for design of polarization sensitive devices (each polarization see slightly different relative permittivity). Investigation of different shapes and grids of perforations might also be interesting. Possible gain reduction of perforated DRA and DRA arrays due to surface waves should also be examined.

References

- [1] C.A. Balanis. *Advanced Engineering Electromagnetics*. Wiley, 2012. ISBN: 9780470589489.
- [2] D. Kajfez and P. Guillon. *Dielectric Resonators*. Artech House microwave library. Noble Publishing Corporation, 1998. ISBN: 9781884932052.
- [3] S. J. Fiedziuszko and S. Holmes. Dielectric resonators raise your high-q. *IEEE Microwave Magazine*, 2(3):50–60, Sep 2001. doi:10.1109/6668.951549.
- [4] S. Long, M. McAllister, and Liang Shen. The resonant cylindrical dielectric cavity antenna. *IEEE Transactions on Antennas and Propagation*, 31(3):406–412, May 1983. doi:10.1109/TAP.1983.1143080.
- [5] A. Petosa. *Dielectric Resonator Antennas Handbook*. Artech House Antennas and Propagation Library. Artech House Publishers, 2007. ISBN: 978-1596932067.
- [6] J.L. Volakis. *Antenna Engineering Handbook, 4e*. Electronics. McGraw-Hill Education, 2007. ISBN: 978-0071475747.
- [7] A. Petosa and A. Ittipiboon. Dielectric resonator antennas: A historical review and the current state of the art. *IEEE Antennas and Propagation Magazine*, 52(5):91–116, Oct 2010. doi:10.1109/MAP.2010.5687510.
- [8] K. M. Luk and K. W. Leung. *Dielectric Resonator Antennas*. Antennas. Research Studies Press, 2002. ISBN: 978-0863802638.
- [9] Sounik Kiran Kumar Dash, Taimoor Khan, and Asok De. Dielectric resonator antennas: An application oriented survey. *International Journal of RF and Microwave Computer-Aided Engineering*, 27(3):e21069–n/a, 2017. URL: <http://dx.doi.org/10.1002/mmce.21069>, doi:10.1002/mmce.21069.
- [10] R. Kumar Mongia and A. Ittipiboon. Theoretical and experimental investigations on rectangular dielectric resonator antennas. *IEEE Transactions on Antennas and Propagation*, 45(9):1348–1356, Sep 1997. doi:10.1109/8.623123.

-
- [11] M. W. McAllister and S. A. Long. Resonant hemispherical dielectric antenna. *Electronics Letters*, 20(16):657–659, August 1984. doi:10.1049/e1:19840450.
- [12] Kwok-Wa Leung, Kwai-Man Luk, K. Y. A. Lai, and Deyun Lin. Theory and experiment of an aperture-coupled hemispherical dielectric resonator antenna. *IEEE Transactions on Antennas and Propagation*, 43(11):1192–1198, Nov 1995. doi:10.1109/8.475090.
- [13] L. Z. Thamae and Z. Wu. Broadband bowtie dielectric resonator antenna. *IEEE Transactions on Antennas and Propagation*, 58(11):3707–3710, Nov 2010. doi:10.1109/TAP.2010.2071332.
- [14] Q. Rao, T. A. Denidni, and A. R. Sebak. Broadband compact stacked t-shaped dra with equilateral-triangle cross sections. *IEEE Microwave and Wireless Components Letters*, 16(1):7–9, Jan 2006. doi:10.1109/LMWC.2005.861360.
- [15] R. Chair, A. A. Kishk, K. F. Lee, and C. E. Smith. Wideband flipped staired pyramid dielectric resonator antennas. *Electronics Letters*, 40(10):581–582, May 2004. doi:10.1049/e1:20040402.
- [16] G. P. Junker, A. A. Kishk, A. W. Glisson, and D. Kajifez. Effect of air gap on cylindrical dielectric resonator antenna operating in tm₀₁ mode. *Electronics Letters*, 30(2):97–98, Jan 1994. doi:10.1049/e1:19940114.
- [17] Y. M. Pan and S. Y. Zheng. A low-profile stacked dielectric resonator antenna with high-gain and wide bandwidth. *IEEE Antennas and Wireless Propagation Letters*, 15:68–71, 2016. doi:10.1109/LAWP.2015.2429686.
- [18] S. Yarga, K. Sertel, and J. L. Volakis. A directive resonator antenna using degenerate band edge crystals. *IEEE Transactions on Antennas and Propagation*, 57(3):799–803, March 2009. doi:10.1109/TAP.2009.2013451.
- [19] S. Fakhte, H. Oraizi, and L. Matekovits. High gain rectangular dielectric resonator antenna using uniaxial material at fundamental mode. *IEEE Transactions on Antennas and Propagation*, 65(1):342–347, Jan 2017. doi:10.1109/TAP.2016.2627520.
- [20] S. Fakhte, H. Oraizi, L. Matekovits, and G. Dassano. Cylindrical anisotropic dielectric resonator antenna with improved gain. *IEEE Transactions on Antennas and Propagation*, 65(3):1404–1409, March 2017. doi:10.1109/TAP.2016.2647689.

-
- [21] S. Fakhte and H. Oraizi. Compact uniaxial anisotropic dielectric resonator antenna operating at higher order radiating mode. *Electronics Letters*, 52(19):1579–1580, 2016. doi:10.1049/e1.2016.2222.
- [22] J. T. H. St. Martin, Y. M. M. Antar, A. A. Kishk, A. Ittipiboon, and M. Cuhaci. Dielectric resonator antenna using aperture coupling. *Electronics Letters*, 26(24):2015–2016, Nov 1990. doi:10.1049/e1:19901302.
- [23] Z. C. Hao, W. Hong, A. Chen, J. Chen, and K. Wu. Siw fed dielectric resonator antennas (siw-dra). In *2006 IEEE MTT-S International Microwave Symposium Digest*, pages 202–205, June 2006. doi:10.1109/MWSYM.2006.249448.
- [24] Q. Lai, C. Fumeaux, W. Hong, and R. Vahldieck. 60 ghz aperture-coupled dielectric resonator antennas fed by a half-mode substrate integrated waveguide. *IEEE Transactions on Antennas and Propagation*, 58(6):1856–1864, June 2010. doi:10.1109/TAP.2010.2046852.
- [25] C.A. Balanis. *Antenna Theory, Analysis and Design*, 3e. Wiley, 2005. ISBN: 9780471667827.
- [26] Y. M. Pan, K. W. Leung, and K. Lu. Omnidirectional linearly and circularly polarized rectangular dielectric resonator antennas. *IEEE Transactions on Antennas and Propagation*, 60(2):751–759, Feb 2012. doi:10.1109/TAP.2011.2173122.
- [27] O. G. Avădănei, M. G. Banciu, and L. Nedelcu. Higher-order modes in high-permittivity cylindrical dielectric resonator antenna excited by an off-centered rectangular slot. *IEEE Antennas and Wireless Propagation Letters*, 13:1585–1588, 2014. doi:10.1109/LAWP.2014.2344860.
- [28] O. G. Avadanei, M. G. Banciu, I. Nicolaescu, and L. Nedelcu. Superior modes in high permittivity cylindrical dielectric resonator antenna excited by a central rectangular slot. *IEEE Transactions on Antennas and Propagation*, 60(11):5032–5038, Nov 2012. doi:10.1109/TAP.2012.2207692.
- [29] Bin Li and Kwok Wa Leung. Strip-fed rectangular dielectric resonator antennas with/without a parasitic patch. *IEEE Transactions on Antennas and Propagation*, 53(7):2200–2207, July 2005. doi:10.1109/TAP.2005.850745.
- [30] Y. M. Pan, S. Y. Zheng, and B. J. Hu. Design of dual-band omnidirectional cylindrical dielectric resonator antenna. *IEEE Antennas and Wireless Propagation Letters*, 13:710–713, 2014. doi:10.1109/LAWP.2014.2314745.

-
- [31] Xiaosheng Fang. *Designs of Dualband and Wideband Dielectric Resonator Antennas using Higher-order Modes*. PhD thesis, City University of Hong Kong, 2012. URL: <http://hdl.handle.net/2031/6946>.
- [32] Xiao Sheng Fang, Chi Kin Chow, Kwok Wa Leung, and Eng Hock Lim. New single-/dual-mode design formulas of the rectangular dielectric resonator antenna using covariance matrix adaptation evolutionary strategy. *IEEE Antennas and Wireless Propagation Letters*, 10:734–737, 2011. doi:10.1109/LAWP.2011.2162389.
- [33] Y. X. Sun and K. W. Leung. Dual-band and wideband dual-polarized cylindrical dielectric resonator antennas. *IEEE Antennas and Wireless Propagation Letters*, 12:384–387, 2013. doi:10.1109/LAWP.2013.2251993.
- [34] L. K. Hady, A. A. Kishk, and D. Kajfez. Dual-band compact dra with circular and monopole-like linear polarizations as a concept for gps and wlan applications. *IEEE Transactions on Antennas and Propagation*, 57(9):2591–2598, Sept 2009. doi:10.1109/TAP.2009.2024488.
- [35] Yong-Xin Guo, Kwai-Man Luk, and Kwok-Wa Leung. Mutual coupling between millimeter-wave dielectric-resonator antennas. *IEEE Transactions on Microwave Theory and Techniques*, 47(11):2164–2166, Nov 1999. doi:10.1109/22.798016.
- [36] W. M. Abdel Wahab, D. Busuioc, and S. Safavi-Naeini. Low cost planar waveguide technology-based dielectric resonator antenna (dra) for millimeter-wave applications: Analysis, design, and fabrication. *IEEE Transactions on Antennas and Propagation*, 58(8):2499–2507, Aug 2010. doi:10.1109/TAP.2010.2050443.
- [37] M. R. Nezhad-Ahmadi, M. Fakharzadeh, B. Biglarbegian, and S. Safavi-Naeini. High-efficiency on-chip dielectric resonator antenna for mm-wave transceivers. *IEEE Transactions on Antennas and Propagation*, 58(10):3388–3392, Oct 2010. doi:10.1109/TAP.2010.2055802.
- [38] W. M. Abdel-Wahab, S. Safavi-Naeini, and D. Busuioc. High gain/ efficiency 2d-dielectric resonator antenna array for low cost mm-wave systems. In *2011 IEEE International Symposium on Antennas and Propagation (APSURSI)*, pages 1682–1684, July 2011. doi:10.1109/APS.2011.5996628.

-
- [39] A. Perron, T. A. Denidni, and A. R. Sebak. High-gain hybrid dielectric resonator antenna for millimeter-wave applications: Design and implementation. *IEEE Transactions on Antennas and Propagation*, 57(10):2882–2892, Oct 2009. doi:10.1109/TAP.2009.2029292.
- [40] Q. Lai, G. Almpanis, C. Fumeaux, H. Benedickter, and R. Vahldieck. Comparison of the radiation efficiency for the dielectric resonator antenna and the microstrip antenna at ka band. *IEEE Transactions on Antennas and Propagation*, 56(11):3589–3592, Nov 2008. doi:10.1109/TAP.2008.2005551.
- [41] M. O. Sallam, M. Serry, S. Sedky, A. Shamim, W. De Raedt, G. A. E. Vandenbosch, and E. A. Soliman. Micromachined on-chip dielectric resonator antenna operating at 60 ghz. *IEEE Transactions on Antennas and Propagation*, 63(8):3410–3416, Aug 2015. doi:10.1109/TAP.2015.2439694.
- [42] Y. X. Guo and H. Chu. 60-ghz ltcc dielectric resonator antenna array. In *2013 IEEE Antennas and Propagation Society International Symposium (AP-SURSI)*, pages 1874–1875, July 2013. doi:10.1109/APS.2013.6711595.
- [43] Y. M. Pan, K. W. Leung, and K. M. Luk. Design of the millimeter-wave rectangular dielectric resonator antenna using a higher-order mode. *IEEE Transactions on Antennas and Propagation*, 59(8):2780–2788, Aug 2011. doi:10.1109/TAP.2011.2158962.
- [44] D. Hou, W. Hong, W. L. Goh, J. Chen, Y. Z. Xiong, S. Hu, and M. Madihian. D-band on-chip higher-order-mode dielectric-resonator antennas fed by half-mode cavity in cmos technology. *IEEE Antennas and Propagation Magazine*, 56(3):80–89, June 2014. doi:10.1109/MAP.2014.6867684.
- [45] P. Nayeri, M. Liang, R. Sabory-García, M. Tuo, F. Yang, M. Gehm, H. Xin, and A. Elsherbeni. High gain dielectric reflectarray antennas for thz applications. In *2013 IEEE Antennas and Propagation Society International Symposium (APSURSI)*, pages 1124–1125, July 2013. doi:10.1109/APS.2013.6711222.
- [46] Daniel Headland, Shruti Nirantar, Withawat Withayachumnankul, Philipp Gutruf, Derek Abbott, Madhu Bhaskaran, Christophe Fumeaux, and Sharath Sriram. Terahertz magnetic mirror realized with dielectric resonator antennas. *Advanced Materials*, 27(44):7137–7144, 2015. URL: <http://dx.doi.org/10.1002/adma.201503069>, doi:10.1002/adma.201503069.
- [47] D. Headland, T. Niu, E. Carrasco, D. Abbott, S. Sriram, M. Bhaskaran, C. Fumeaux, and W. Withayachumnankul. Terahertz reflectarrays and

- nonuniform metasurfaces. *IEEE Journal of Selected Topics in Quantum Electronics*, 23(4):1–18, July 2017. doi:10.1109/JSTQE.2016.2640452.
- [48] X. D. Deng, Y. Li, C. Liu, W. Wu, and Y. Z. Xiong. 340 ghz on-chip 3-d antenna with 10 dbi gain and 80efficiency. *IEEE Transactions on Terahertz Science and Technology*, 5(4):619–627, July 2015. doi:10.1109/TTHZ.2015.2424682.
- [49] Longfang Zou. *Dielectric resonator antennas : from multifunction microwave devices to optical nano-antennas*. PhD thesis, The University of Adelaide, 2013. URL: <http://hdl.handle.net/2440/82146>.
- [50] C. Fumeaux, C. Zou, D. Headland, S. Nirantar, P. Gutruf, L. Zou, M. Bhaskaran, S. Sriram, and W. Withayachumnankul. Terahertz and optical dielectric resonator antennas: Potential and challenges for efficient designs. In *2016 10th European Conference on Antennas and Propagation (EuCAP)*, pages 1–4, April 2016. doi:10.1109/EuCAP.2016.7481118.
- [51] L. Zou, W. Withayachumnankul, C. M. Shah, A. Mitchell, M. Klemm, M. Bhaskaran, S. Sriram, and C. Fumeaux. Efficiency and scalability of dielectric resonator antennas at optical frequencies. *IEEE Photonics Journal*, 6(4):1–10, Aug 2014. doi:10.1109/JPHOT.2014.2337891.
- [52] Ahmed A. Kishk. Directive yagi–uda dielectric resonator antennas. *Microwave and Optical Technology Letters*, 44(5):451–453, 2005. URL: <http://dx.doi.org/10.1002/mop.20664>, doi:10.1002/mop.20664.
- [53] Nasimuddin and K. P. Esselle. Antennas with dielectric resonators and surface mounted short horns for high gain and large bandwidth. *IET Microwaves, Antennas Propagation*, 1(3):723–728, June 2007. doi:10.1049/iet-map:20060120.
- [54] T. A. Denidni, Y. Coulibaly, and H. Boutayeb. Hybrid dielectric resonator antenna with circular mushroom-like structure for gain improvement. *IEEE Transactions on Antennas and Propagation*, 57(4):1043–1049, April 2009. doi:10.1109/TAP.2009.2015809.
- [55] Y. Coulibaly, M. Nedil, I. Ben Mabrouk, L. Talbi, and T. A. Denidni. High gain rectangular dielectric resonator for broadband millimeter-waves underground communications. In *2011 24th Canadian Conference on Electrical and Computer Engineering(CCECE)*, pages 001088–001091, May 2011. doi:10.1109/CCECE.2011.6030629.

-
- [56] M. Akbari, S. Gupta, M. Farahani, A. R. Sebak, and T. A. Denidni. Gain enhancement of circularly polarized dielectric resonator antenna based on fss superstrate for mmw applications. *IEEE Transactions on Antennas and Propagation*, 64(12):5542–5546, Dec 2016. doi:10.1109/TAP.2016.2623655.
- [57] A. Petosa, S. Thirakoune, and A. Ittipiboon. Higher-order modes in rectangular dras for gain enhancement. In *2009 13th International Symposium on Antenna Technology and Applied Electromagnetics and the Canadian Radio Science Meeting*, pages 1–4, Feb 2009. doi:10.1109/ANTEMURSI.2009.4805098.
- [58] A. Petosa and S. Thirakoune. Rectangular dielectric resonator antennas with enhanced gain. *IEEE Transactions on Antennas and Propagation*, 59(4):1385–1389, April 2011. doi:10.1109/TAP.2011.2109690.
- [59] D. Guha, A. Banerjee, C. Kumar, and Y. M. M. Antar. Higher order mode excitation for high-gain broadside radiation from cylindrical dielectric resonator antennas. *IEEE Transactions on Antennas and Propagation*, 60(1):71–77, Jan 2012. doi:10.1109/TAP.2011.2167922.
- [60] D. Guha, A. Banerjee, C. Kumar, and Y. M. M. Antar. New technique to excite higher-order radiating mode in a cylindrical dielectric resonator antenna. *IEEE Antennas and Wireless Propagation Letters*, 13:15–18, 2014. doi:10.1109/LAWP.2013.2294877.
- [61] D. Guha, A. Banerjee, C. Kumar, Y. M. M. Antar, and M. T. Sebastian. Design guidelines for the cylindrical dielectric resonator antenna using the recently proposed hem12d mode [antenna designer’s notebook]. *IEEE Antennas and Propagation Magazine*, 56(4):148–158, Aug 2014. doi:10.1109/MAP.2014.6931672.
- [62] Kwai-Man Luk, Wai-Kee Leung, and Kwok-Wa Leung. [5] mutual impedance of hemispherical dielectric resonator antennas. *IEEE Transactions on Antennas and Propagation*, 42(12):1652–1654, Dec 1994. doi:10.1109/8.362806.
- [63] G. P. Junker, A. A. Kishk, and A. W. Glisson. [6] multiport network description and radiation characteristics of coupled dielectric resonator antennas. *IEEE Transactions on Antennas and Propagation*, 46(3):425–433, Mar 1998. doi:10.1109/8.662662.
- [64] R. Chair, A. A. Kishk, and Kai-Fong Lee. [7] comparative study on the mutual coupling between different sized cylindrical dielectric resonators antennas and circular microstrip patch antennas. *IEEE Transactions on Antennas and Propagation*, 53(3):1011–1019, March 2005. doi:10.1109/TAP.2004.842682.

-
- [65] R. J. Dorris, R. T. Long, S. A. Long, M. A. Khayat, and J. T. Williams. [8] mutual coupling between cylindrical probe-fed dielectric resonator antennas. *IEEE Antennas and Wireless Propagation Letters*, 1(1):8–9, 2002. doi:10.1109/LAWP.2002.802575.
- [66] C. Fumeaux, G. Almpanis, K. Sankaran, D. Baumann, and R. Vahldieck. [9] finite-volume time-domain modeling of the mutual coupling between dielectric resonator antennas in array configurations. In *The Second European Conference on Antennas and Propagation, EuCAP 2007*, pages 1–4, Nov 2007. doi:10.1049/ic.2007.0909.
- [67] G. D. Loos and Y. M. M. Antar. [10] a new aperture-coupled rectangular dielectric resonator antenna array. *Microwave and Optical Technology Letters*, 7(14):642–644, 1994. URL: <http://dx.doi.org/10.1002/mop.4650071403>, doi:10.1002/mop.4650071403.
- [68] K. Y. Chow, K. W. Leung, K. M. Luk, and E. K. N. Yung. [11] cylindrical dielectric resonator antenna array. *Electronics Letters*, 31(18):1536–1537, Aug 1995. doi:10.1049/el:19951080.
- [69] K. W. Leung, H. Y. Lo, K. M. Luk, and E. K. N. Yung. [12] two-dimensional cylindrical dielectric resonator antenna array. *Electronics Letters*, 34(13):1283–1285, Jun 1998. doi:10.1049/el:19980931.
- [70] Yong-Xin Guo, Kwai-Man Luk, and Kwok-Wa Leung. [13] mutual coupling between millimeter-wave dielectric-resonator antennas. *IEEE Transactions on Microwave Theory and Techniques*, 47(11):2164–2166, Nov 1999. doi:10.1109/22.798016.
- [71] G. B. Gentili, M. Morini, and S. Selleri. [14] relevance of coupling effects on dra array design. *IEEE Transactions on Antennas and Propagation*, 51(3):399–404, March 2003. doi:10.1109/TAP.2003.809848.
- [72] A. Dadgarpour, B. Zarghooni, B. S. Virdee, T. A. Denidni, and A. A. Kishk. Mutual coupling reduction in dielectric resonator antennas using metasurface shield for 60-ghz mimo systems. *IEEE Antennas and Wireless Propagation Letters*, 16:477–480, 2017. doi:10.1109/LAWP.2016.2585127.
- [73] D. Guha, S. Biswas, T. Joseph, and M. T. Sebastian. [15] defected ground structure to reduce mutual coupling between cylindrical dielectric resonator antennas. *Electronics Letters*, 44(14):836–837, July 2008. doi:10.1049/el:20081189.

-
- [74] H. Chu and Y. X. Guo. A novel approach for millimeter-wave dielectric resonator antenna array designs by using the substrate integrated technology. *IEEE Transactions on Antennas and Propagation*, 65(2):909–914, Feb 2017. doi:10.1109/TAP.2016.2632702.
- [75] J. Lin, W. Shen, and K. Yang. A low-sidelobe and wideband series-fed linear dielectric resonator antenna array. *IEEE Antennas and Wireless Propagation Letters*, 16:513–516, 2017. doi:10.1109/LAWP.2016.2586579.
- [76] M. Su, L. Yuan, and Y. Liu. A linearly polarized radial-line dielectric resonator antenna array. *IEEE Antennas and Wireless Propagation Letters*, 16:788–791, 2017. doi:10.1109/LAWP.2016.2604287.
- [77] M. S. Sharawi, S. K. Podilchak, M. T. Hussain, and Y. M. M. Antar. Dielectric resonator based mimo antenna system enabling millimetre-wave mobile devices. *IET Microwaves, Antennas Propagation*, 11(2):287–293, 2017. doi:10.1049/iet-map.2016.0457.
- [78] J. S. Colburn and Y. Rahmat-Samii. Patch antennas on externally perforated high dielectric constant substrates. *IEEE Transactions on Antennas and Propagation*, 47(12):1785–1794, Dec 1999. doi:10.1109/8.817654.
- [79] R. Gonzalo, P. De Maagt, and M. Sorolla. Enhanced patch-antenna performance by suppressing surface waves using photonic-bandgap substrates. *IEEE Transactions on Microwave Theory and Techniques*, 47(11):2131–2138, Nov 1999. doi:10.1109/22.798009.
- [80] P. de Maagt, R. Gonzalo, Y. C. Vardaxoglou, and J. M. Baracco. Electromagnetic bandgap antennas and components for microwave and (sub)millimeter wave applications. *IEEE Transactions on Antennas and Propagation*, 51(10):2667–2677, Oct 2003. doi:10.1109/TAP.2003.817566.
- [81] A. Patrovsky and Ke Wu. Substrate integrated image guide (siig) - a low-loss waveguide for millimetre-wave applications. In *2005 European Microwave Conference*, volume 2, pages 4 pp.–, Oct 2005. doi:10.1109/EUMC.2005.1610071.
- [82] A. Patrovsky and Ke Wu. Substrate integrated image guide (siig)-a planar dielectric waveguide technology for millimeter-wave applications. *IEEE Transactions on Microwave Theory and Techniques*, 54(6):2872–2879, June 2006.
- [83] K. Ogusu. Numerical analysis of the rectangular dielectric waveguide and its modifications. *IEEE Transactions on Microwave Theory and Techniques*, 25(11):874–885, Nov 1977. doi:10.1109/TMTT.1977.1129235.

-
- [84] Song-Tsuen Peng and A. A. Oliner. Guidance and leakage properties of a class of open dielectric waveguides: Part i - mathematical formulations. *IEEE Transactions on Microwave Theory and Techniques*, 29(9):843–855, Sep 1981. doi:10.1109/TMTT.1981.1130465.
- [85] A. A. Oliner, Song-Tsuen Peng, Ting-Ih Hsu, and A. Sanchez. Guidance and leakage properties of a class of open dielectric waveguides: Part ii - new physical effects. *IEEE Transactions on Microwave Theory and Techniques*, 29(9):855–869, Sep 1981. doi:10.1109/TMTT.1981.1130466.
- [86] J. B. Muldavin and G. M. Rebeiz. Millimeter-wave tapered-slot antennas on synthesized low permittivity substrates. *IEEE Transactions on Antennas and Propagation*, 47(8):1276–1280, Aug 1999. doi:10.1109/8.791943.
- [87] A. Patrovsky and K. Wu. 94-ghz planar dielectric rod antenna with substrate integrated image guide (siig) feeding. *IEEE Antennas and Wireless Propagation Letters*, 5(1):435–437, Dec 2006. doi:10.1109/LAWP.2006.885014.
- [88] A. Patrovsky and K. Wu. Substrate integrated image guide array antenna for the upper millimeter-wave spectrum. *IEEE Transactions on Antennas and Propagation*, 55(11):2994–3001, Nov 2007. doi:10.1109/TAP.2007.908558.
- [89] P. Mondal and K. Wu. A leaky-wave antenna using periodic dielectric perforation for millimeter-wave applications. *IEEE Transactions on Antennas and Propagation*, 64(12):5492–5495, Dec 2016. doi:10.1109/TAP.2016.2621032.
- [90] K. Wu, Y. J. Cheng, T. Djerafi, and W. Hong. Substrate-integrated millimeter-wave and terahertz antenna technology. *Proceedings of the IEEE*, 100(7):2219–2232, July 2012. doi:10.1109/JPROC.2012.2190252.
- [91] A. Petosa, A. Ittipiboon, and S. Thirakoune. Perforated dielectric resonator antennas. *Electronics Letters*, 38(24):1493–1495, Nov 2002. doi:10.1049/e1:20021074.
- [92] A. Petosa, S. Thirakoune, and A. Ittipiboon. Array of perforated dielectric resonator antennas. In *IEEE Antennas and Propagation Society Symposium, 2004.*, volume 1, pages 1106–1109 Vol.1, June 2004. doi:10.1109/APS.2004.1329868.
- [93] A. Petosa, S. Thirakoune, M. Zuliani, and A. Ittipiboon. Comparison between planar arrays of perforated dras and microstrip patches. In *2005 IEEE Antennas and Propagation Society International Symposium*, volume 2A, pages 168–175 vol. 2A, July 2005. doi:10.1109/APS.2005.1551764.

-
- [94] Y. Zhang and A. A. Kishk. Analysis of dielectric resonator antenna arrays with supporting perforated rods. In *The Second European Conference on Antennas and Propagation, EuCAP 2007*, pages 1–5, Nov 2007. doi:10.1049/ic.2007.1421.
- [95] R. Chair, A. A. Kishk, and K. F. Lee. Experimental investigation for wideband perforated dielectric resonator antenna. *Electronics Letters*, 42(3):137–139, Feb 2006. doi:10.1049/el:20063987.
- [96] Y. X. Sun and K. W. Leung. Substrate-integrated two-port dual-frequency antenna. *IEEE Transactions on Antennas and Propagation*, 64(8):3692–3697, Aug 2016. doi:10.1109/TAP.2016.2565740.
- [97] Y. Li and K. M. Luk. Wideband perforated dense dielectric patch antenna array for millimeter-wave applications. *IEEE Transactions on Antennas and Propagation*, 63(8):3780–3786, Aug 2015. doi:10.1109/TAP.2015.2441118.
- [98] H. W. Lai, K. M. Luk, and K. W. Leung. Dense dielectric patch antenna; a new kind of low-profile antenna element for wireless communications. *IEEE Transactions on Antennas and Propagation*, 61(8):4239–4245, Aug 2013. doi:10.1109/TAP.2013.2260122.
- [99] K. Gong and X. H. Hu. Low-profile substrate integrated dielectric resonator antenna implemented with pcb process. *IEEE Antennas and Wireless Propagation Letters*, 13:1023–1026, 2014. doi:10.1109/LAWP.2014.2325033.
- [100] S. H. Zainud-Deen, S. M. Gaberand, and K. H. Awadalla. Transmitarray using perforated dielectric material for wideband applications. *Progress In Electromagnetics Research M*, 24:1–13, 2012. doi:10.2528/PIERM12020110.
- [101] M. Moeini-Fard and M. Khalaj-Amirhosseini. , inhomogeneous perforated reflect-array antennas. *Wireless Engineering and Technology*, 2:80–86, 2011. doi:10.4236/wet.2011.22011.
- [102] M. M. Tahseen and A. A. Kishk. High efficiency ka-band single layer air vias reflectarray: Design and analysis. In *2015 IEEE International Symposium on Antennas and Propagation USNC/URSI National Radio Science Meeting*, pages 2129–2130, July 2015. doi:10.1109/APS.2015.7305454.
- [103] A. Petosa, A. Ittipiboon, and S. Thirakoune. Investigation on arrays of perforated dielectric fresnel lenses. *IEE Proceedings - Microwaves, Antennas and Propagation*, 153(3):270–276, June 2006. doi:10.1049/ip-map:2005019.

-
- [104] C. S. Lee, S. W. Lee, R. Davis, and J. Tsui. Perforated dielectric lens. *Microwave and Optical Technology Letters*, 5(2):92–94, Feb 1992. doi:10.1002/mop.4650050214.
- [105] A. E. Mahmoud, W. Hong, Y. Zhang, and A. Kishk. W-band multilayer perforated dielectric substrate lens. *IEEE Antennas and Wireless Propagation Letters*, 13:734–737, 2014. doi:10.1109/LAWP.2014.2316144.
- [106] R. Yang, Z. Lei, L. Chen, Z. Wang, and Y. Hao. Surface wave transformation lens antennas. *IEEE Transactions on Antennas and Propagation*, 62(2):973–977, Feb 2014. doi:10.1109/TAP.2013.2291894.
- [107] Junhyun Kim, Dongheok Shin, Seungjae Choi, Do-Sik Yoo, Ilsung Seo, and Kyoungsik Kim. Meta-lens design with low permittivity dielectric materials through smart transformation optics. *Applied Physics Letters*, 107(10):101906, 2015. doi:10.1063/1.4930842.
- [108] IEEE standard for definitions of terms for antennas. *IEEE Std 145-2013 (Revision of IEEE Std 145-1993)*, pages 1–50, March 2014. doi:10.1109/IEEESTD.2014.6758443.
- [109] R. M. Baghaee, M. H. Neshati, and J. R. Mohassel. Rigorous analysis of rectangular dielectric resonator antenna with a finite ground plane. *IEEE Transactions on Antennas and Propagation*, 56(9):2801–2809, Sept 2008. doi:10.1109/TAP.2008.928768.
- [110] G. P. Junker, A. A. Kishk, A. W. Glisson, and D. Kajfez. Effect of an air gap around the coaxial probe exciting a cylindrical dielectric resonator antenna. *Electronics Letters*, 30(3):177–178, Feb 1994. doi:10.1049/e1:19940191.
- [111] G. P. Junker, A. A. Kishk, A. W. Glisson, and D. Kajfez. Effect of fabrication imperfections for ground-plane-backed dielectric resonator antennas with coaxial excitation. In *Symposium on Antenna Technology and Applied Electromagnetics [ANTEM 1994]*, pages 445–448, Aug 1994.
- [112] M. Ranjbar Nikkhah, J. Rashed-Mohassel, and A. A. Kishk. Compact wide-band rectangular dielectric resonator antenna with parasitic elements and air gaps. *Progress In Electromagnetics Research Letters*, 42:129–139, 2013. doi:10.2528/PIERL13071401.
- [113] M. Hassan Neshati F. Kazemi and F. Mohanna. Design of rectangular dielectric resonator antenna fed by dielectric image line with a finite ground

- plane. *International Journal of Communications, Network and System Sciences*, 3(7):620–624, 2010.
- [114] DuPont. Dupont green tape 951, low temperature ceramic system (online). Accessed: 26-4-2017. URL: http://ltcc.etsmtl.ca/documents/Dupont_951.pdf.
- [115] DuPont. Green tape low temperature co-fired ceramic system (online). Accessed: 26-4-2017. URL: http://www.dupont.com/content/dam/dupont/products-and-services/electronic-and-electrical-materials/documents/prodlib/GreenTape_Design_Layout_Guidelines.pdf.
- [116] M. Mrnka and Z. Raida. Linearly polarized high gain rectangular dielectric resonator antenna. In *2016 10th European Conference on Antennas and Propagation (EuCAP)*, pages 1–4, April 2016. doi:10.1109/EuCAP.2016.7481588.
- [117] P. S. Kildal, A. Vosoogh, and S. Maci. Fundamental directivity limitations of dense array antennas: A numerical study using hannan’s embedded element efficiency. *IEEE Antennas and Wireless Propagation Letters*, 15:766–769, 2016. doi:10.1109/LAWP.2015.2473136.
- [118] L. Gao and J. Z. Gu. Effective dielectric constant of a two-component material with shape distribution. *Journal of Physics D: Applied Physics*, 35(3):267–271, 2002. doi:<https://doi.org/10.1088/0022-3727/35/3/316>.
- [119] A. Mejdoubi and Ch. Brosseau. Finite-difference time-domain simulation of heterostructures with inclusion of arbitrarily complex geometry. *Journal of Applied Physics*, 99(6):0635021 – 06350214, March 2006. doi:<http://dx.doi.org/10.1063/1.2171771>.
- [120] A. Mejdoubi and Ch. Brosseau. Dielectric response of perforated two-dimensional lossy heterostructures: A finite-element approach. *Journal of Applied Physics*, 100(9):0941031 – 09410314, July 2006. doi:<http://dx.doi.org/10.1063/1.2171771>.
- [121] A. H. Sihvola and J. A. Kong. Effective permittivity of dielectric mixtures. *IEEE Transactions on Geoscience and Remote Sensing*, 26(4):420–429, July 1988. doi:10.1109/36.3045.
- [122] T. C. Choy. *Effective Medium Theory: Principles and Applications*, 2e. Oxford University Press, 2015. ISBN: 9780198705093.

-
- [123] Ch. Brosseau. Modelling and simulation of dielectric heterostructures: a physical survey from an historical perspective. *Journal of Physics D: Applied Physics*, 39(7):1277–1294, March 2006. doi:<https://doi.org/10.1088/0022-3727/39/7/S02>.
- [124] CH. Kittel. *Introduction to Solid State Physics, 8e*. Wiley, 2004. ISBN: 978-0-471-41526-8.
- [125] H. Föll. Electronic materials, chap. 3.2.6 local field and Clausius - Mosotti equation. Accessed: 25-4-2017. URL: https://www.tf.uni-kiel.de/matwis/amat/elmat_en/kap_3/backbone/r3_2_6.html.
- [126] Xing-Da Liu, Zhi-Ling Hou, Bao-Xun Zhang, Ke-Tao Zhan, Peng He, Kai-Lun Zhang, and Wei-Li Song. A general model of dielectric constant for porous materials. *Applied Physics Letters*, 108(10):1029021 – 1029024, March 2016. doi:<http://dx.doi.org/10.1063/1.4943639>.
- [127] J. C. Maxwell Garnett. Colours in metal glasses and in metallic films. *Philosophical Transactions of the Royal Society A*, 203(359-371):385–420, Jan 1904. doi:10.1098/rsta.1904.0024.
- [128] V. A. Markel. Introduction to the maxwell garnett approximation: tutorial. *Journal of the Optical Society of America A*, 33(7):1244–1256, 2016. doi:<https://doi.org/10.1364/JOSAA.33.001244>.
- [129] M. Born and E. Wolf. *Principles of Optics: Electromagnetic Theory of Propagation, Interference and Diffraction of Light, 7e*. Cambridge University Press, 1999. ISBN: 9780521642224.
- [130] H. J. Eom. *Electromagnetic Wave Theory for Boundary-Value Problems*. Springer-Verlag Berlin Heidelberg, 2004. ISBN: 978-3-540-21266-9.
- [131] National Taipei University of Technology. Plane wave in anisotropic media – lecture materials (online). Accessed: 25-4-2017. URL: <http://www.cc.ntut.edu.tw/~juiching/EWE7.pdf>.
- [132] N. Damaskos, A. Maffett, and P. Uslenghi. Dispersion relation for general anisotropic media. *IEEE Transactions on Antennas and Propagation*, 30(5):991–993, Sep 1982. doi:10.1109/TAP.1982.1142905.
- [133] Y. Zhang and A. A. Kishk. Analysis of dielectric resonator antenna arrays with supporting perforated rods. In *The Second European Conference on Antennas and Propagation, EuCAP 2007*, pages 1–5, Nov 2007. doi:10.1049/ic.2007.1421.

-
- [134] K. K. Karkkainen, A. H. Sihvola, and K. I. Nikoskinen. Effective permittivity of mixtures: numerical validation by the fdtd method. *IEEE Transactions on Geoscience and Remote Sensing*, 38(3):1303–1308, May 2000. doi:10.1109/36.843023.
- [135] O. Pekonen, K. Karkkainen, A. Sihvola, and K. Nikoskinen. Numerical testing of dielectric mixing rules by FDTD method. *Journal of Electromagnetic Waves and Applications*, 13(1):67–87, 1999. doi:http://dx.doi.org/10.1163/156939399X01618.
- [136] R.F. Harrington. *Time Harmonic Electromagnetic Fields*. Wiley-IEEE Press, 2001. ISBN: 978-0-471-20806-8.
- [137] R.E. Collin. *Field Theory of Guided Waves, 2e*. Wiley-IEEE Press, 1990. ISBN: 978-0-87942-237-0.
- [138] M. Mrnka and Z. Raida. Enhanced-gain dielectric resonator antenna based on the combination of higher-order modes. *IEEE Antennas and Wireless Propagation Letters*, 15:710–713, 2016. doi:10.1109/LAWP.2015.2470099.

List of Figures

3.1	General geometry of a DRA including a feeding aperture. Orientation of the aperture determines if TE_{mnp}^x or TE_{mnp}^y mode is excited. In this case the excitation of TE_{mnp}^y modes would be supported. For simplification, we first assume ground plane to be infinite $g \rightarrow \infty$. . .	26
3.2	Detail on the aperture feeding of the resonator. The input impedance of the discrete port in the simulations is set to 50Ω	28
3.3	Electric and magnetic fields in A-A cross section of the resonator (see Fig. 3.1).	29
3.4	Electric field distribution on the top wall of the resonator.	29
3.5	Magnetic field distribution (H_y component) in the B-B cross section of the resonator.	29
3.6	Input port reflection coefficients showing resonances of the TE_{133} mode for resonators height $h = 11$ mm. As the footprint's shape of the resonator approaches square, the resonant frequency of TE_{133} mode varies more slowly (right). The resonance on the right for $w = 15$ mm is TE_{115} mode.	31
3.7	Input port reflection coefficients showing resonances of TE_{133} mode and some additional higher modes for resonators height $h = 12$ mm. We can see that the additional resonances increase the impedance bandwidth of the antenna (right).	31
3.8	Input port reflection coefficients showing resonances of TE_{133} mode $h = 13$ mm.	31
3.9	Input port reflection coefficients showing resonances of TE_{133} mode for resonators height $h = 14$ mm.	32
3.10	Input port reflection coefficients showing resonances of TE_{133} mode $h = 15$ mm.	32
3.11	Maximum gain corresponding to the TE_{133} mode as function of resonator's width w for various heights of the resonator (frequencies according to Fig. 3.6 to 3.10).	32

3.12	Radiation patterns for resonator with height $h = 11$ mm and for various widths w . For frequencies see TE ₁₃₃ mode resonances in Fig. 3.6.	33
3.13	Radiation patterns for resonator with height $h = 13$ mm and for various widths w . For frequencies see Fig. 3.8.	33
3.14	Radiation patterns for resonator with height $h = 15$ mm and for various widths w . For frequencies see Fig. 3.10. In this case, the excitation of TE ₁₁₅ is the strongest, we can see it by reduced sidelobes in the E-plane at $theta = \pm 90^\circ$ and increased sidelobes in the H-plane at circa $\pm 70^\circ$	33
3.15	Realized gain in direction $theta = 0^\circ$ as a function of the ground plane size g at frequency 10 GHz. The period corresponds to approximately $2\lambda_0$	34
3.16	E-plane radiation patterns at 10 GHz for four ground plane sizes $g = 30, 75, 100$ and 300 mm. With increasing g , the patterns are getting more rippled – i.e. interference between direct and diffracted waves.	35
3.17	H-plane radiation patterns at 10 GHz for four ground plane sizes $g = 30, 75, 100$ and 300 mm. We can see the H-plane patterns are less sensitive to the ground plane size.	35
3.18	Reflection coefficient for various ground plane sizes. We can see that only extremely small g can influence the reflection coefficient.	35
3.19	Detail of the microstrip fed antenna.	36
3.20	Frequency response of the reflection coefficient of both resonators. The TE ₁₃₃ mode resonates at about 10.25 GHz.	38
3.21	E-plane (left) and H-plane (right) radiation patterns of both resonators at frequency 10.25 GHz.	38
3.22	Dielectric resonator created by several layers of dielectric substrate with interleaved glue layers. The proportions in the figure are exaggerated, glue layers are only circa $50 \mu\text{m}$ thick.	39
3.23	Top view of the fabricated DR antenna with SMA connector.	39
3.24	Comparison between simulated and measured reflection coefficient. The measured results varied from simulated due to inaccurate fabrication.	40
3.25	Measured realized gain frequency response. Maximum achieved gain is 11.9 dBi.	41

3.26	Normalized radiation patterns in both principal planes (E-plane on the left, H-plane on the right). The absence of the measured back lobe (compared to simulations) is given by the nature of our measurement range. The shape of the cross-polarization pattern in the E-plane suggest slight misalignment of the antenna during measurements.	41
3.27	Geometry of the aperture-fed cylindrical DRA and its alignment in the spherical coordinate system.	44
3.28	Manufactured prototype of the high gain cylindrical DRA	44
3.29	E-field and H-field distributions of the HEM_{133} mode as obtained by the modal analysis and the same field components as excited in our DRA at 5.8 GHz. The phase difference between the visualized E and H-field is 180° . For plane cuts see Fig. 3.31.	45
3.30	E-field and H-field distributions of the HEM_{123} mode as obtained by the modal analysis and the same field components as excited in our DRA at 5.8 GHz. The phase difference between the visualized E and H-field is 180° . Moreover, the fields have 90° phase shift as compared to the fields in Fig. 3.29. For plane cuts see Fig. 3.31.	45
3.31	Detail of the antenna geometry and the dimensions.	47
3.32	Reflection coefficient vs. frequency for several diameters of the resonator.	48
3.33	Realized peak gain in the broadside direction vs. frequency for several diameters of the resonator.	48
3.34	Realized peak gain in the broadside direction vs. frequency with ground plane diameter as a parameter.	48
3.35	Comparison between simulated and measured magnitude of the reflection coefficient.	49
3.36	Realized gain frequency response in the broadside direction – simulation vs. measurement.	49
3.37	Simulated and measured radiation patterns at 5.82 GHz in the E-plane, which corresponds to xz plane in Fig. 3.31.	49
3.38	Simulated and measured radiation patterns at 5.82 GHz in the H-plane, which corresponds to yz plane in Fig. 3.31.	50
3.39	The configuration of the examined DRA with incorporated air gap between the ground plane and the resonator.	52
3.40	Variation of the reflection coefficient with increasing the height of the air gap.	53
3.41	Variation of the gain (IEEE gain) with increasing the size of the air gap.	53

3.42	Measured reflection coefficient for several thicknesses of the air gap between the ground plane and the resonator.	54
3.43	Measured realized gain for two values of air gap height between the ground plane and the resonator. Gain boost of 1.6 dB can be seen.	54
3.44	E-plane radiation patterns (co- and cross-polarization) of the antenna for two different heights of the air gap at frequency 5.85 GHz.	54
3.45	H-plane radiation patterns (co- and cross-polarization) of the antenna for two different heights of the air gap at frequency 5.85 GHz.	55
3.46	DRA prototype with air gap introduced by stripes of duct tape on the left and right side of the resonator.	55
3.47	Manufactured LTCC resonators for 24 GHz resonant frequency of HEM ₁₃₃ mode from DuPont Green Tape 951.	57
3.48	Configuration of the proposed directive LTCC dielectric resonator antenna fed by an aperture in SIW.	59
3.49	Electric field distribution in the E-plane cross section of the resonator corresponding to the HEM ₁₃₃ mode (xz plane in Fig. 3.48).	59
3.50	Magnitude of magnetic field component H_y in the E-plane cross section of the resonator corresponding to the HEM ₁₃₃ mode (xz plane in Fig. 3.48).	60
3.51	Manufactured LTCC based DRA (on the left). Without attached dielectric resonator (on the right). The parameters of the antenna are: $h = 5.03$ mm, $d \approx 9.80$ mm, $\epsilon_r = 7.1$, $g = 34$ mm. And the feeding slot dimensions are $l_a = 2.75$ mm, $w_a = 0.46$ mm, $l_s = 4$ mm.	61
3.52	Simulated and measured reflection coefficient magnitude as functions of frequency. The fractional bandwidth of the measured antenna is 2.15 %.	61
3.53	Radiation patterns of the antenna in the E-plane, which corresponds to the xz plane according to the Fig. 3.48. Measured gain in the broadside direction is 10.8 dBi (10.9 dBi in simulations). Very good agreement inside the main lobe can be observed between the simulated and measured results, the side lobe level and in this plane, is mostly influenced by the presence of the 2.4 mm connector which is modeled in simulations only as a simple brick with similar outline dimensions as the real connector.	62
3.54	H-plane radiation patterns (i.e. yz plane in Fig. 3.48). Since the influence of the connector in this plane is minimal, we can see excellent agreement between simulation and measurement.	62

4.1	Configuration of two aperture-fed dielectric resonators for analyzing coupling in the E-plane of the resonators (top view).	66
4.2	Configuration of two aperture-fed dielectric resonators for analyzing coupling in the H-plane of the resonators (top view).	66
4.3	Geometry of single DR element with square footprint.	68
4.4	H_y magnetic field component in the cross-section of the resonator. . .	69
4.5	Antenna orientation in spherical coordinate system.	70
4.6	Reflection coefficient and realized gain as function of frequency for resonator with TE_{113} mode. The TE_{113} mode resonance frequency occurs at 9.2 GHz. Realized gain at the resonance is 8.4 dBi. The gain maximum does not coincide with the resonance.	71
4.7	Realized gain radiation patters in E- and H- plane of the TE_{113} mode as obtained above infinite PEC ground plane at frequency 9.2 GHz. .	71
4.8	Reflection coefficient and realized gain as function of frequency for resonator with TE_{115} mode. The TE_{115} mode resonance occurs at 9.0 GHz. Realized gain at the resonance is 10.4 dBi.	72
4.9	Realized gain radiation patters in E- and H- plane of the TE_{115} mode as obtained above infinite PEC ground plane. Side lobe levels in both planes are considerably higher than in the case of TE_{113} mode.	72
4.10	Model for coupling evaluation due to substrate surface waves. The apertures in the upper half-space are separated by infinite PEC wall.	73
4.11	Transmission coefficient between the apertures caused by transmission through underlying substrate layer (see Fig. 4.1 and Fig 3) at frequency 9 GHz. The apertures above the substrate are separated by PEC wall and the space above the ground plane is homogeneously filled with $\epsilon_r = 10$ material, hence no transmission occurs in the region above the ground plane, where the coupling between the dielectric resonators is to be analyzed.	74
4.12	Input impedance of a resonator for resonators arranged in the E-plane (left) and in the H-plane (right).	74
4.13	Transmission coefficient as a function of element spacing in both principal planes for TE_{113} mode ($f = 9.2$ GHz).	75
4.14	Reflection and transmission coefficient for two spacings $s = 0.5\lambda_0$ and $s = 1\lambda_0$ in both principal planes.	75
4.15	Transmission coefficient as a function of element spacing in both principal planes for TE_{115} mode ($f = 9$ GHz).	76
4.16	Input impedance of a resonator for resonators arranged in the E-plane (left) and in the H-plane (right) for TE_{115} mode.	76

4.17	Frequency response of reflection and transmission coefficient magnitude in the E-plane (left) and in the H-plane (right) of the resonators for two values of inter-element spacing, i.e. $s = \lambda_0/2$ and $s = \lambda_0$	76
4.18	Geometrical arrangement of microstrip line fed resonators for H-plane coupling analysis. The dimensions of the feeds and resonators are identical.	77
4.19	Geometrical arrangement of microstrip line fed resonators for E-plane coupling analysis. The dimensions of the feeds and resonators are identical.	78
4.20	Frequency response of reflection and transmission coefficient magnitude in the E-plane (left) and in the H-plane (right) of the resonators operating with TE_{113} mode for two values of inter-element spacing, i.e. $s = 0.58\lambda_0$ and $s = 1.16\lambda_0$	79
4.21	Frequency response of reflection and transmission coefficient magnitude in the E-plane (left) and in the H-plane (right) of the resonators operating with TE_{115} mode for two values of inter-element spacing, i.e. $s = 0.56\lambda_0$ and $s = 1.13\lambda_0$	79
4.22	Fabricated antennas operating with TE_{113} mode (left) and TE_{115} mode (right). The spacing between the antennas is in both cases $0.5\lambda_0$. The ground planes are identical.	80
4.23	Geometry of a TE_{133} mode DRA with a rectangular footprint. The resonator is aligned in spherical coordinate system according to the Fig. 4.5.	81
4.24	Distribution of H_y field component in the cross-sectional view (plane xz).	81
4.25	Reflection coefficient and realized gain as functions of frequency for resonator with TE_{133} mode. The TE_{133} mode resonance occurs at 9.3 GHz.	82
4.26	Radiation patterns in the E- and H- plane of the TE_{133} mode as obtained above infinite PEC ground plane. Large SLL in the E-plane can be seen.	82
4.27	Transmission coefficient as a function of element spacing in both principal planes for TE_{133} mode at 9.3 GHz.	83
4.28	Frequency response of reflection and transmission coefficient magnitude in the E-plane (left) and in the H-plane (right) of the resonators for two values of spacing, i.e. $s = \lambda_0/2$ and $s = \lambda_0$. The E-plane includes only the curves for $s = \lambda_0$	84

4.29	Frequency response of reflection and transmission coefficient magnitude in the E-plane (left) and in the H-plane (right) of the resonators operating with TE_{133} mode for two values of inter-element spacing, i.e. $s = 0.5\lambda_0$ and $s = 1\lambda_0$	85
4.30	Fabricated antennas operating with TE_{133} mode with separation distance $1\lambda_0$, aligned in the E-plane.	85
5.1	Effective relative permittivity as a function of porosity based on Maxwell-Garnett mixing formula for E-field perpendicular and parallel to the axis of perforations.	92
5.2	Excitation pulses (blue) with frequency range 1-20 GHz and pulses as received at the end of a sample with length 57 mm. These cases correspond to ordinary wave propagation.	97
5.3	Excitation pulses (blue) with frequency range 1-20 GHz and pulses as received at the end of a sample with length 57 mm. These cases correspond to extraordinary wave propagation in a plane perpendicular to the extraordinary axis. It can be seen that the time delay $t_2 > t_1$	98
5.4	Excitation pulse (blue) with frequency range 1-20 GHz and pulse received at the end of a sample with length 57 mm. This case corresponds to extraordinary wave with wavefront perpendicular to the extraordinary axis. The time delay between input and output pulse is the same as in case of ordinary wave which corresponds to uniaxial media property.	98
5.5	Dispersion diagrams corresponding to cases a), b) (left) and e) (right). In uniaxial media, all these cases should give the same propagation constants influenced only by the ε_o term of permittivity tensor.	99
5.6	Dispersion diagrams corresponding to cases c) and d). In uniaxial media, all these cases should give the same propagation constants influenced in this case only by the ε_e term of permittivity tensor.	99
5.7	Unit cell models for ordinary (left) and extraordinary (right) wave propagation perpendicular to the optical axis. If not stated otherwise, periodic boundaries are used.	100
5.8	Unit cell model for extraordinary wave propagation along the optical axis. If not stated otherwise, periodic boundaries are used.	100

5.9	Detail of the geometry. The structure is analyzed as a TEM waveguide with varying direction of propagation (homogenized sections, ports and boundary conditions are adjusting depending on the direction of propagation and polarization state). The length l_h of homogenous dielectrics sections at the beginning and the end of the waveguide is exaggerated in the drawing. The actual length is about 3 meshcells for the time domain simulations and the sections are absent in the frequency domain simulations. However, by adjusting the relative permittivity of these sections, improved impedance matching can be achieved.	101
5.10	Triangular lattice and the unit cell detail	105
5.11	Dispersion diagrams for unbounded perforated dielectric material with $p = 3$ mm for polarization parallel - extraordinary wave (left) and perpendicular - ordinary wave (right) to the axis of perforations. . . .	108
5.12	Dispersion diagrams for unbounded perforated dielectric material with $p = 1.5$ mm for polarization parallel - extraordinary wave (left) and perpendicular - ordinary wave (right) to the axis of perforations. . . .	108
5.13	Dispersion diagrams for unbounded perforated dielectric material with $p = 0.8$ mm for polarization parallel - extraordinary wave (left) and perpendicular - ordinary wave (right) to the axis of perforations. . . .	108
5.14	Effective relative permittivities for extraordinary (left) and ordinary (right) wave in homogenized dielectric material with $p = 3$ mm. . . .	109
5.15	Effective relative permittivities for extraordinary (left) and ordinary (right) wave in homogenized dielectric material with $p = 1.5$ mm. . . .	109
5.16	Effective relative permittivities for extraordinary (left) and ordinary (right) wave in homogenized dielectric material with $p = 0.8$ mm. . . .	109
5.17	Comparison between theoretical model based on Maxwell-Garnett mixing rules (solid lines) with simulation results (triangles) for $p = 0.8$ mm.	110
5.18	Geometry of the dielectric slab with coordinate system.	111
5.19	Electric field distribution of TM_0 wave on grounded perforated substrate. The cut corresponds to yz plane according to the Fig. 5.18. . . .	114
5.20	Unit cell for TM_0 mode analysis (left) and for TE_0 mode analysis (right). Height of the substrate $h_1 = 3.175$ mm and height of the computational domain $h_2 = 20h_1$	116
5.21	Surface wave TM_0 (left) and TE_0 (right) mode dispersion diagrams for perforated dielectric layer with height $h = 3.175$ mm and period of perforations $p = 3$ mm.	117

5.22	Surface wave TM_0 (left) and TE_0 (right) mode dispersion diagrams for perforated dielectric layer with height $h = 3.175$ mm and period of perforations $p = 1.5$ mm.	118
5.23	Surface wave TM_0 (left) and TE_0 (right) mode dispersion diagrams for perforated dielectric layer with height $h = 3.175$ mm and period of perforations $p = 0.8$ mm.	118
5.24	Effective relative permittivities of homogenized equivalent dielectric layer as extracted for TM_0 (left) and TE_0 (right) mode surface wave propagating on perforated dielectric layer with height $h = 3.175$ mm and $p = 3$ mm.	118
5.25	Effective relative permittivities of homogenized equivalent dielectric layer as extracted for TM_0 (left) and TE_0 (right) mode surface wave propagating on perforated dielectric layer with height $h = 3.175$ mm and $p = 1.5$ mm.	119
5.26	Effective relative permittivities of homogenized equivalent dielectric layer as extracted for TM_0 (left) and TE_0 (right) mode surface wave propagating on perforated dielectric layer with height $h = 3.175$ mm and $p = 0.8$ mm.	119
5.27	Comparison of the effective relative permittivities of two selected geometries as obtained from unit cell analysis and from two sample comparison method.	120
5.28	Comparison between theoretical model based on Maxwell-Garnett approximation and effective relative permittivities as seen by surface wave modes at 10 GHz (left) and 20 GHz (right). Period of perforations $p = 3$ mm. The reason why for porosities below 50 % (at 20 GHz) the permittivity values for TM waves exceed the limits, is that the electromagnetic bandgap properties start to be present in the structure.	121
5.29	Comparison between theoretical model based on Maxwell-Garnett approximation and effective relative permittivities as seen by surface wave modes at 10 GHz (left) and 40 GHz (right). Period of perforations $p = 0.8$ mm.	121
5.30	Effective relative permittivity as a function of D/p ratio. Triangular lattice gives in general smaller effective permittivity compared to square lattice.	123
5.31	Dielectric island (resonator) created by air perforations in triangular lattice (left) and square lattice (right). The ratio D/p is in both cases 0.833.	123

5.32	Geometry of the DRA embedded in homogenized dielectric layer with equivalent properties to the perforated DRA in Fig. 5.31.	124
5.33	Reflection coefficient for perforated DRA and DRA surrounded by homogenous dielectric. Theoretical limit in which $D/p = 1$ (left) and $D/p = 0.75$ (right).	126
5.34	Spherical coordinate system and antenna alignment.	126
5.35	E-plane radiation patterns for infinite ground plane for the case $D/p = 1$ (left) and $D/p = 0.75$ (right) comparing radiation patterns of perforated DRA and DRA surrounded by homogenized material.	127
5.36	H-plane radiation patterns for infinite ground plane for the case $D/p = 1$ (left) and $D/p = 0.75$ (right).	127
5.37	Resonant frequency (left) and input resistance (right) as functions of effective relative permittivity $\varepsilon_{r,\text{eff}}$ for DRA in homogenized dielectric model. Parameters of the structure are $w = 5.6$ mm, $l_a = 5$ mm, $w_a = 0.84$ mm	127
5.38	E-plane radiation patterns (directivity) of finite ground plane DRA for the upper hemisphere ($-90^\circ < \theta < 90^\circ$) for conventional rectangular DRA (top left), perforated DRA with $D/p = 1$ (top right) and with $D/p = 0.75$ (bottom). As the effective permittivity of the surrounding is larger (smaller D/p ratio), more of the energy propagates along the substrate, towards the edges. The result is increased ripples in the far-field.	128
5.39	H-plane radiation patterns (Directivity) of finite ground plane DRA for the upper hemisphere ($-90^\circ < \theta < 90^\circ$) for conventional rectangular DRA (top left), perforated DRA with $D/p = 1$ (top right) and with $D/p = 0.75$ (bottom).	129
5.40	Perforated dielectric resonators arranged in H-plane (left) and in E-plane (right). Separation distance s is the crucial parameter.	131
5.41	Transmission coefficient between two resonators aligned in the E-plane comparing conventional DRA elements with $f_r = 12$ GHz (black), perforated DRAs with $D/p = 1$ $f_r = 10.95$ GHz (blue) and finally perforated DRAs with $D/p = 1$ $f_r = 9.7$ GHz (red). Inter-element distance s is plot in free space wavelengths at given resonant frequencies of individual antennas.	131
5.42	Reflection and transmission coefficient for perforated DRAs aligned in their E-plane for two inter-element distances $s = \lambda/2$ (left) and $s = \lambda$ (right).	132

5.43	Reflection and transmission coefficient for conventional DRAs aligned in their E-plane for two inter-element distances $s = \lambda/2$ (left) and $s = \lambda$ (right).	132
5.44	Measured reflection and transmission coefficient for perforated DRAs aligned in the E-plane for two separation distances $s = \lambda/2$ (left) and $s = \lambda$ (right).	134
5.45	Measured reflection and transmission coefficient for conventional DRAs aligned in their E-plane for two separation distances $s = \lambda/2$ (left) and $s = \lambda$ (right).	134
5.46	Simulated and measured results of $ S_{21} $, comparing conventional DRAs with perforated DRAs. Slight increase of $ S_{21} $ in simulation results of perforated DRAs (blue) is caused by a standing surface wave excited in the perforated substrate.	134
5.47	Manufactured prototype of the perforated DRAs (left), with feeding apertures (right).	135
5.48	Manufactured prototype of the reference DRAs with 1λ spacing (left), microstrip feeding lines (right).	135
5.49	Manufactured prototype of the perforated DRAs with 1λ spacing and with holding screws made from plastic (right).	135

List of Tables

3.1	Comparison between the resonant frequency results of theoretical DWM and eigenmode analysis in CST. Relative permittivity of the resonator $\epsilon_r = 6.15$, $h = 10$ mm.	26
3.2	Final dimensions of the antenna.	39
4.1	Results of measurement and simulation of transmission coefficient between two resonators operating with HO modes, i.e. TE_{113}	86
4.2	Results of measurement and simulation of transmission coefficient between two resonators operating with HO modes, i.e. TE_{115}	86
4.3	Results of measurement and simulation of transmission coefficient between two resonators operating with HO modes, i.e. TE_{133}	86

List of symbols, physical constants and abbreviations

DR	Dielectric Resonator
DRA	Dielectric Resonator Antenna
DWM	Dielectric Waveguide Model
EBG	Electromagnetic Band Gap
EM	Electromagnetic
ε_r	relative permittivity
$\varepsilon_{r,\text{eff}}$	effective relative permittivity
ε_i	permittivity of inclusions
f_r	Resonant Frequency
G	Gain
HEM	Hybrid Electromagnetic
k	wavenumber
\mathbf{k}	wave vector
λ	wavelength
LTCC	Low Temperature Co-fired Ceramics
PEC	Perfect Electric Conductor
μ	permeability
PMC	Perfect Magnetic Conductor
P	Dielectric polarization
\mathbf{r}	position vector
TEM	Transverse Electro-Magnetic
TE	Transverse Electric
TM	Transverse Magnetic
s	inter-element separation distance
SIW	Substrate Integrated Waveguide
SLL	Sidelobe Level
ω	angular frequency

Michal Mrnka

Poznaňská 2

e-mail: xmrnka@gmail.com

616 00 Brno

Phone 1: +420 776 498 767

Czech Republic

Phone 2: +421 948 046 957

Education

- 2013 - current **Brno University of Technology** - Brno, Czech Republic
Ph.D. in Radio electronics.
Research Topic: Higher-order modes in dielectric resonator antennas, perforated dielectrics
- 2010-2013 **Brno University of Technology** - Brno, Czech Republic
MSc, Electronics and Communication.
Graduated summa cum laude
- 2010-2011 **Tampere University of Technology** - Tampere, Finland
Erasmus exchange student (2 semesters)
- 2007-2010 **Brno University of Technology** - Brno, Czech Republic
BSc, Electronics and Communication.

Working experience and research stays

- 2015-current **ERA a.s.** - Pardubice, Czech Republic
R&D Antenna engineer.
Fields: Antenna design for VHF and L band radars, antenna placement modelling, radar cross section analysis
- 10/2015 **Technical University of Kosice** - Košice, Slovakia
Visiting PhD student.
Topic: Low Temperature Co-Fired Ceramic (LTCC) based dielectric resonator antennas for millimeter wave applications.
- 11/2014 **Graz University of Technology** - Graz, Austria
Visiting PhD student.
Topic: Wide-band dielectric resonator antennas for energy harvesting applications

-
- 09/2013 to 07/2014 **Max Planck Institute for Radio Astronomy** - Bonn, Germany
Intern with microwave technology group.
Topics: Microwave measurements, LabVIEW programming, development of waveguide components for Ka band
- 02/2012 to 08/2013 **ERA a.s.** - Pardubice, Czech Republic
Master Thesis internship.
Topic: Design of a range illuminating antenna in L-band, preparation of the technical documentation and performance verification by measurements.
- 08/2011 to 05/2013 **FEI Company** - Brno, Czech Republic
Electronics intern.
Topics: PCB layouting, simple circuits design, electronic measurements, technical support of the development group.

Industrial, basic and applied research projects

- 2014 -2016 **Mm-wave electromagnetic structures for biomedical research**
Czech Grant Agency project GACR P102/12/1274
Reconfigurable hybrid dielectric resonator antennas and directive dielectric resonator antennas for on-body and off-body communications.
- 2015 -2016 **Wireless Power Transmission for Sustainable Electronics**
European Project COST WiPE IC1301
Antennas for energy harvesting, Low Temperature Co-Fired Ceramic materials for efficient millimeter-wave dielectric resonator antennas.
- 9/2015 to 3/2016 **Volkswagen** - Industrial project
Development of a methodology for in-car electromagnetic field modeling.
- 1/2015 to 6/2015 **Antenna Toolbox for MATLAB**
Technological Agency of Czech Republic project TA04010457
Cooperation on 1D Method of Moments implementation for wire antennas.

Awards

- 06/2013 **Dean's award for Master's thesis**
Topic: Transmitting Antenna With Dual Circular Polarization For
Indoor Antenna Measurement Range
- 06/2010 **Dean's award for Master's thesis**
Topic: Study of Gel Electrolytes by Magnetic Resonance Methods

Languages

English
Fluent (C1)

German
Intermediate (A2)

Software skills

CST, HFSS, MATLAB, Ansys, Comsol, AWR Microwave Office, Ansoft Designer, Agilent EMpro, PSpice, DxDesigner, PADS, LabVIEW, Microsoft Office etc.

Additional education

- 08/2016 **Antenna Arrays and Reflectarrays**
course within the European School of Antennas framework, Catholic
University of Leuven, Belgium
- 07/2015 **Antenna Imaging Techniques**
course within the European School of Antennas framework, Delft
University of Technology, The Netherlands
- 07/2014 **Summer school on Microwaves and Lightwaves**
Technical University of Denmark
- 09/2012 **Summer school on Nanotechnology**
Ege University and Izmir Institute of Technology, Turkey
- 07/2011 **Summer school on Radar/SAR**
Fraunhofer Institute for High Frequency Physics and Radar Tech-
niques FHR in Bonn, Germany

List of Selected Publications

- [1] M. Mrnka, Z. Raida and J. Grosinger. Wide-band dielectric resonator antennas for RF energy harvesting. *2015 Conference on Microwave Techniques (COMITE)*, April 2015. p 1 - 4.
- [2] M. Mrnka and Z. Raida. Rectangular dielectric resonator antenna with switchable radiation pattern. *2015 IEEE-APS Topical Conference on Antennas and Propagation in Wireless Communications (APWC)*, Sept 2015. p 272 - 275.
- [3] M. Mrnka and Z. Raida. Enhanced-Gain Dielectric Resonator Antenna Based on the Combination of Higher-Order Modes. *IEEE Antennas and Wireless Propagation Letters*, 15, 2016. p 710 - 713.
- [4] M. Mrnka, P. Vasina, M. Kufa, V. Hebelka and Z. Raida. The RF Energy Harvesting Antennas Operating in Commercially Deployed Frequency Bands: A Comparative Study. *International Journal of Antennas and Propagation*, vol. 2016. p 710 - 713.
- [5] M. Mrnka and Z. Raida. Linearly polarized high gain rectangular dielectric resonator antenna. *2016 10th European Conference on Antennas and Propagation (EuCAP)*, April 2016. p 1 - 4.
- [6] M. Mrnka, M. Pavlovic and Z. Raida. Antenna Range Illuminator Based on a Septum Polarizer and a Dual-Mode Horn [Measurements Corner]. *IEEE Antennas and Propagation Magazine*, 58(4) Aug 2016. p 82 - 86.
- [7] M. Mrnka and Z. Raida. Gain improvement of higher order mode dielectric resonator antenna by thin air gap. *2016 International Conference on Broadband Communications for Next Generation Networks and Multimedia Applications (CoBCom)*, Sept 2016. p 1 - 3.
- [8] M. Mrnka, M. Cupal, Z. Raida, A. Pietrikova, D. Kocur. Millimeter-wave directive dielectric resonator antenna based on LTCC. *2016 Loughborough Antennas Propagation Conference (LAPC)*, Nov 2016. p 1 - 4.